UNIVERSITÀ DEGLI STUDI DI NAPOLI
FEDERICO II

ICTH PhD

UNIVERSITÀ DEGLI STUDI DI NAPOLI FEDERICO II

PH.D. THESIS

IN

INFORMATION AND COMMUNICATION TECHNOLOGY FOR HEALTH

MULTIFUNCTIONAL HYBRID NANORESONATORS FOR BIOSENSING APPLICATIONS: DESIGN, FABRICATION, AND CHARACTERIZATION

BRUNO MIRANDA

TUTOR: PROF. CARLO FORESTIERE

CO-TUTOR: DR. LUCA DE STEFANO

COORDINATOR: PROF. DANIELE RICCIO

XXXV CICLO

SCUOLA POLITECNICA E DELLE SCIENZE DI BASE
DIPARTIMENTO DI INGEGNERIA ELETTRICA E TECNOLOGIE DELL'INFORMAZIONE

. . . to my family and my friends
without their love and encouragement
this would not have been possible . . .

Abstract

Nanophotonics, bridging together nanoscience and photonics, is becoming a key enabling technology in biomedicine showing great promises in early diagnosis and less-invasive therapies. In this context, the unique features of plasmonic and dielectric nanoresonators to localize and/or enhance light at the nanoscale are greatly contributing to biosensing and enhanced spectroscopies. Properly engineered metallic and dielectric nanoresonators, exhibiting tunable resonant behavior, can provide an unprecedented level of control over the light in subwavelength spatial regions. The resonances of these objects strongly depend on their size, shape, composition, and surrounding media. Therefore, their effective electromagnetic modeling and its continuous cross-talk with experimental observations represent the best way to meet the demand for standardized, easy-to-use, large-scale, and low-cost optical devices for biomedical applications.

From the theoretical perspective, the growing efforts of scientists to provide a complete framework for the description of both metallic and dielectric nanostructures has resulted in powerful tools, in particular spectral theories, in which the resonant object is described by means of all its resonant modes.

From the experimental perspective, instead, scientific and technological advances are operating a deep translation of the typical industrial microfabrication approaches to the nanoscale to meet the demand for metallic and dielectric nanostructured devices to be operated in all the fields of science, including biomedicine.

Both top-down (from bulk materials to nanomaterials) and bottom-up (from the molecular scale to nanoscale) approaches have been proposed for the fabrication of plasmonic and all-dielectric nanoresonators, which have been largely applied in biomedicine for biosensing applications. However, finding an optimal trade-off between performance and fabrication cost still represents the bottleneck of their employment in everyday life. The pandemic outbreak of Covid-19 has in fact highlighted the necessity of rapid, simple-to-use, affordable, and accurate biosensing platforms for the screening of the population on a large scale. Such devices do not need expensive and time-consuming analytical techniques that require experienced staff and

long waiting times.

In this context, a winning strategy for the design and application of optical nanoresonators in biomedicine could be exploiting the continuous interplay between theoretical predictions and experimental observations. This approach could enable the achievement of fully-predictable systems that can be fabricated on a large scale, with good reproducibility and satisfactory performance.

Motivated by this necessity, in this thesis, a novel paradigm in the design of multifunctional hybrid nanoresonators is proposed and experimentally validated. This paradigm could lead to the fabrication and characterization of novel nanosystems, which could find large applications in biosensing.

In Chapter 1, the recent highlights in the applications of metallic and dielectric nanoresonators in biomedicine and their fabrication approaches are reviewed. Moreover, due to the more standardized bottom-up approaches for their synthesis, plasmon-based optical biosensors are thoroughly described, in which hybrid nanoparticles with multiple functionalities are introduced as optical transducers.

In Chapter 2, the theoretical background of the electromagnetic scattering of optically small objects is carefully reviewed, with particular emphasis on the Mie Theory. Moreover, a spectral scattering theory is introduced and applied to the most important building blocks of plasmonic and dielectric nanoresonators, mainly constituted by spherical nanoparticles and thin nanowires, respectively. The spectral theory enables the understanding of the scattering of these homogeneous nanostructures in the framework of the electroquasistatic and magnetoquasistatic approximations of the Maxwell equations, guaranteeing the good prediction of the resonance position and quality factor of their modes.

In Chapter 3, the concept of hybrid nanoparticles is introduced. The Maxwell Garnett homogenization theory is introduced briefly. This theory describes the effective dielectric permittivity of a composite medium with inclusions. The composition of these hybrid systems is found by means of a reverse engineering approach based on the genetic optimization, the Maxwell Garnett theory, and the Mie theory. Moreover, the Mie-Kerker theory is also used for the description of the electromagnetic scattering from coated hybrid nanoparticles. The validation of the obtained model is proposed starting from standard hybrid plasmonic nanoparticles synthesized *via* bottom-up approaches.

In Chapter 4, a novel hybrid drug delivery nanosystem is presented. It is based on porous biosilica nanoparticles and *in-situ* synthesized gelatin/gold nanoparticles. The composition of the gelatin-stabilized plasmonic nanoparticles is found by genetic optimization. The obtained hybrid nanosystem is further coated with gelatin shells

of increasing thicknesses. Then, a theoretical model is introduced that allows, from simple spectroscopic measurements, to determine the shell degradation and consequent drug release. The proposed nanosystem could represent a valid alternative for the*in-vivo* monitoring of the drug release from a nanocarrier.

In Chapter 5, novel hybrid nanocomposites based on polyethylene glycol diacrylate hydrogels and citrate-capped gold nanoparticles are proposed. The optimization of the fabrication technique takes advantage of the high reproducibility, large scalability, and simplicity of an all-solution fabrication strategy. The optical properties of the obtained nanocomposites can be easily predicted within the hybrid nanoparticles framework. The mechanical properties of hydrogels with different molecular weights result to have an effect on the optical features of the hybrid nanocomposites. These features are exploited to obtain devices with different transduction mechanisms. The obtained devices exhibit excellent performances in the selective and sensitive detection of a model target molecule. The presented devices direct find applications in wearable biosensors, and food and environmental monitoring. Moreover, they could be easily integrated within more complex microfluidic and microelectronic components due to the intrinsic flexible nature of the polymeric matrix in which the nanoparticles are embedded.

Contents

Chapter 1

Introduction

In the last decades, nanotechnology has been finding large interest in the scientific community, driving researchers from all over the world towards a technological transition from macro- to nano-scale in all the fields of application [1].

In particular, the combination of nanotechnology and photonics, namely *nanophotonics*, has emerged as a multidisciplinary field, whose aim is the study of the complex interactions between light and matter at the sub-wavelength scale for a plethora of applications, including nonlinear optics, condensed-matter physics, light harvesting, near-field/far-field optics, biomedical imaging, nanophotonic design, and optical biosensors [2].

In this context, the unprecedented optical properties of plasmonic and dielectric nanomaterials have largely contributed to the deep understanding and application of this field to life sciences [3].

On the one hand, noble metal nanostructures, generally made of silver (Ag) and gold (Au), with negative dielectric constants, exhibit coherent oscillations of their free electron plasma, known as localized surface plasmon resonances (LSPRs), generating a strong enhancement of the electromagnetic field in their surroundings in the visible and near-infrared regions of the spectrum.

On the other hand, dielectric objects of small dimensions compared to the free-space wavelength can exhibit the so-called *Mie Resonances* proven that their relative dielectric permittivity is sufficiently high ($\epsilon_R \gg 1$) [4, 5].

Dielectric resonators could represent a good alternative to noble metals for several applications. However, due to the possibility of exciting magnetic modes and the presence of multimodal interference, their design is more complex than the plasmonic counterpart and still requires careful theoretical investigations. While metal nanostructures suffer from high losses, due to their intrinsic absorption, dielectric nanostructures exhibit modest losses, but lower field enhancement.

Therefore, a promising approach could be the combination of both materials, namely hybrid metal-dielectric nanostructures to take advantage of both low losses and high field enhancement. However, the fabrication of these hybrid materials, is generally expensive and time-consuming, which limits their applications to real-case studies.

A winning strategy for the design and application of optical resonators in biomedicine is exploiting the continuous interplay between theoretical predictions and experimental observations. This approach could enable the achievement of fully-predictable systems that can be fabricated on a large scale, with good reproducibility and satisfactory performance, thus boosting their production at an industrial level, which is nowadays the bottleneck of their employment in everyday life.

1.1 Metallic and dielectric nanoresonators for biomedical applications

A nanoresonator is a photonic structure enabling the localization of the incident electromagnetic wave in a volume with characteristic dimensions much smaller than the operating wavelength. In particular, metallic objects support plasmonic resonances, which can be described within the electroquasistatic (EQS) approximation of the Maxwell equations if the resonator is very small compared to the operating wavelength [6, 7, 8, 9, 10].

High localized electric fields can be achieved by means of EQS mechanisms, including tip-shape effects in objects with sharp edges or capacitive coupling in closely spaced metal objects [11]. Radiative effects can be also exploited to further enhance the local electric field, even though they usually play a minor role [12]. The most simple plasmonic nanoresonator is represented by spherical gold or silver nanoparticles (NPs).

Plasmonic resonances, falling in the visible region of the optical spectrum, were first described by Gustav Mie in 1908 [13] while trying to explain the typical reddish coloration of gold NPs. Since then, the great development of nanotechnology has led to advanced and engineered nanosystems with tunable LSPR, whose applications in biomedicine span from biosensing to bioimaging, and from photothermal therapy (PTT) to drug release monitoring [14, 15].

LSPR, apart from the size, shape, and composition of the plasmonic nanoresonator, is strongly affected by the dielectric permittivity, or refractive index, of the surrounding medium [16]. This feature can be exploited to design refractive index-

based optical biosensors, in which the LSPR position undergoes a concentration-dependent red-shift when a molecule of interest is immobilized on the NPs' surface [17].

Moreover, colloidal NPs aggregation can be engineered to achieve significant colorimetric variations detectable to the naked eye, in the so-called colorimetric biosensors [18].

In addition, due to the electromagnetic field enhancement in their surroundings, plasmonic NPs can be used as nanoantennas for the amplification of external signals. For example, they can act as antennas for fluorescent dyes to amplify their emission in the so-called Plasmon-(or Metal-) enhanced fluorescence mechanism (P(M)EF) [19, 20], they can strongly enhance the Raman signal of molecules associated with their vibrational modes, in the so-called Surface-Enhanced Raman Scattering (SERS) mechanism [21, 22, 23, 24], or, similarly, they can amplify the Infrared Absorption of molecules associated with their vibrational modes in the Surface-Enhanced Infrared Absorption (SEIRA) mechanism [25]. By acting as external signal amplifiers, nanoantennas can boost the sensitivity and limit of detection of these commonly used techniques in the biosensing community, down to single-molecule levels [14, 26, 24, 27].

Concerning bioimaging, plasmonic nanoresonators generally exhibit $10^5 - 10^6$ times stronger scattered light intensity than that of a fluorescein molecule. They do not undergo photobleaching when exposed to external light. Therefore, they have found large interest as contrast agents [28, 29]. More precisely, bigger NPs exhibit stronger scattering efficiency than smaller NPs and can be detected *via* two principal techniques: optical coherence tomography (OCT, mostly used for *in-vivo* imaging) and dark field confocal imaging (DFCI, mostly used for *in-vitro* imaging). Plasmonic NPs can be made *site-specific*, thus becoming able to recognize only specific targeted sites [28].

Moreover, for the treatment of cancer, plasmonic photothermal therapy (PPTT) could represent a winning strategy compared to the classical PTT since the high absorption efficiency of plasmonic NPs causes their localized heating. The photothermal properties of gold NPs were first studied by Link and El-Sayed [30], who demonstrated that the photo-excitation of plasmonic NPs results in fast energy conversion and dissipation into heat. The dissipated energy is available for the heating of the local environment. The used light radiation must be at a frequency that strongly overlaps with the LSPR absorption band of the NPs. Therefore, by introducing NPs of the opportune size and shape within the invisible range of tissues (NIR) it is possible to locally heat the malignant cells and destroy them with external laser sources [31].

Finally, another interesting biomedical application of plasmonic NPs is the spectroscopic monitoring of the release of a drug immobilized on the NPs surface. In fact, by opportunely designing the plasmonic resonances, it is possible to correlate the release of a drug molecule with the variations in the local effective dielectric constants of the surrounding medium. When the drug is released, a decrease in the effective dielectric constant is observed, which induces a blue shift in the LSPR position [32, 33].

More recently, high-index, or all-dielectric, nanoresonators are emerging as alternative optical devices [34, 35, 36, 37, 38]. Contrarily to plasmonic nanoresonators, the resonances in high-index nanoresonators, with sizes much smaller than the operating wavelength, can be modeled by the magnetoquasistatic (MQS) approximation of the Maxwell equations, where the normal component of the displacement current density vanishes on the surface of the object [39].

Among the many types of all-dielectric structures, thin wires may constitute a promising building block of high-permittivity nanoresonators since they could play the same important role as conducting thin wires [40]. For instance, at optical frequencies, periodic arrangements of high-permittivity nano-wires have been already proposed [41, 42] as magnetic media. The design of complex networks made of high-index thin wires benefits from the MQS approximation of the Maxwell equations [39, 43, 44], since it represents a fast method, with low computational costs, that provide an accurate prediction of the dielectric resonances and quality factors.

Despite being much more recent than their plasmonic counterpart, high-index nanoresonators have been already investigated for biomedical applications, in particular for chirality and refractive index-based biosensors [45]. For instance, silicon nanoresonators, arranged in both periodic and non-periodic arrays have been already proposed as diagnostic platforms for the screening of cancer biomarkers [46, 47], and for the design of sensing platforms to detect the molecular chirality (*i.e.*, the absence of superposition under mirror reflection exhibited by many molecules exploited in drug research) [48, 49].

More recently, some theranostic applications of high-index NPs have been also proposed, even though they are still in their early stages [50, 51].

In this thesis, the main theoretical background describing the electromagnetic scattering of optically small objects is presented. Moreover, some analytical tools, falling in the framework of the EQS and MQS approximations of the Maxwell equations are introduced. These tools allow the prediction of the resonance positions and quality factors of plasmonic and dielectric nanoresonators.

1.2 From top-down to bottom-up fabrication strategies

Historically, the introduction of the term nanotechnology is attributed to the Nobel-laureate Richard Feynman, who gave a talk called *"There's Plenty of Room at the Bottom"* at an American Physical Society meeting, in 1959 [52]. With his visionary talk, Feynman discussed both *top-down* and *bottom-up* approaches to produce materials in the range between 1 and 100 nm, most of which are still relevant today [53]. Therefore, nanofabrication methods can be classified into two groups: the top-down and bottom-up approaches. The top-down approach relies on the etching of bulk material to achieve the required smaller characteristic dimensions of the object, which is generally achieved by lithographic techniques [54]. In contrast, in the bottom-up approach, the structures are condensed into nanomaterials atom by atom or molecule by molecule through covalent or supramolecular interactions [55].

The top-down approaches for the fabrication of nanostructured materials are dominantly used in the semiconductor industry for all the electronic components of modern technologies. With these techniques, the desired structures are imprinted or deposited on silica/silicon, but also flexible substrates *via* lithography-based procedures.

One of them is the *photolithography* or optical lithography [56]. This technique is based on a projection printing system where the features of the desired structures are projected, through a photomask, onto a substrate that has been pre-spun with a photoresist (light-sensitive) material using UV light. If the photoresist is positive, the regions of the photoresist that are exposed to UV light become soluble in a particular developing solvent. These *excess* regions are washed away during the developing step, leaving a pattern of raised features on the wafer identical to the dark regions on the mask. Conversely, for a negative resist, the regions of the photoresist that are exposed to UV light become insoluble to a particular developing solvent, and only the unexposed regions are washed away during the developing step, leaving a pattern of raised features on the wafer identical to the clear regions on the mask [57].

Another very common top-down approach is the *electron-beam* (E-beam) *lithography* (EBL). It allows the drawing of customized geometries on substrates coated with an electron-sensitive resist. A sub-10 nm resolution can be obtained with this technique. This fabrication procedure can be carried out with a traditional scanning electron microscope (SEM) integrated with a control unit. Also in this case, the crucial step is the exposure of the resist, which is done maskless, in this case, by an

E-beam. The non-exposed resist, generally a polymer, is dissolved in an appropriate solvent, thus leaving the patterned area. Finally, the combination with other complementary processes, such as dry or wet etching, lift-off of evaporated material, and/or electro-deposition is exploited to terminate the nanofabrication [58].

In both lithographic approaches, the *E-beam* or *thermal* evaporation are the most common techniques to deposit a plasmonic (*e.g.*, gold and/or silver) or a dielectric (*e.g.*, silicon and/or germanium) material on the patterned substrate. E-beam evaporation is a common physical vapor deposition (PVD) process, in which a beam of high-energy electrons is used to vaporize a material. The vaporized material condenses onto the selected substrate to form a thin film. E-beam evaporation is often used to deposit thin films of metals and alloys with high purity and good adhesion to the substrate. This type of evaporation is performed using an electron beam that scans the sample's surface and then evaporates or sublimates the material just from its surface without melting it in the crucible (bulk material container). Analogously, thermal evaporation is a type of PVD process, but, in this case, the material is vaporized using heat. A crucible containing the material is heated to a high temperature, causing the material to vaporize and condense onto a substrate, forming a thin film.

The main limitations of these fabrication procedures, at the laboratory level, but also for large-scale production, are associated with the costs and maintenance of the required equipment. Moreover, time-consuming protocols are required to achieve the desired nanostructures. Concerning optical lithography, one of the main limitations is associated with the desired size, which for a common UV light can be brought to a resolution not lower than 50 nm. There exist UV-light sources working in the deep UV (wavelength in between $10 - 50$ nm), but they are very expensive and require sophisticated cooling systems. In addition, the chemical nature of the prepared nanostructures cannot be finely tuned, and this represents a critical issue in the preparation of optical biosensors.

The currently known and commonly adopted bottom-up fabrication strategies have been inspired by nature, in which biological atoms and molecules are preprogrammed to self-assemble and organize driven by supramolecular interactions into ordered and functional structures [53]. For example, hydrogen bonding, Van der Waals interactions, electrostatic interactions, and so on ..., represent an extremely useful tool that combines the concepts of self-assembly and molecular recognition for the fabrication of 1D, 2D, and 3D nanomaterials. Inspired by nature, scientists have, therefore, proposed bottom-up synthesized nanomaterials by exploiting the responsivity of atoms and molecules to external *stimuli* (*e.g.*, electric field, chemical/biochemical interactions, temperature, and light). Ultra-fine NPs, nanoshells,

and nanotubes, can be prepared with tunable size, shape, size distribution, and density.

The main advantages of this type of approach are the high throughput, low costs, and good control of the surface chemistry of the final nanostructures, which, for biosensing applications, enables ease of functionalization with biomolecules for the production of specific and selective platforms for clinical and environmental applications [59, 14]. On the contrary, the main limitations arise from the poor control of their final optical properties, their assembly on a rigid substrate, and on their chemical stability for relatively long times. These limitations can be overcome by carefully studying the kinetics of nucleation and growth processes of the nanoparticles, by using all-solution fabrication strategies, and adopting stabilizing or coating organic/inorganic materials, respectively [60].

While the bottom-up fabrication of plasmonic NPs is a well-established and adopted methodology, for all-dielectric nanoresonators, the application of this approach is still an active research field.

The quest for large-scale, low-cost, and highly reproducible optical devices for biosensing applications has become of large interest in recent years, caused also by the pandemic outbreak of Covid-19 [61]. To this aim, bottom-up techniques, or at most mixed techniques (the tools offered by the top-down methods are used for the large-scale production of plasmonic substrates), could be a winning strategy. Therefore, for the scope of this thesis, all the experimental parts, are focused on bottom-up synthesized plasmonic NPs for biosensing applications.

1.3 Plasmonic optical biosensors

A *sensor* is a device used for the detection of a physical variable (*e.g.*, temperature, mass, light, pressure, ...) and for its conversion into a universal signal, such as an electrical signal. The component responsible for this conversion is the *transducer*. The transduced signal is generally an analog signal, which is converted into a digital one from an analog-to-digital converter. The converted signal is finally transmitted to a microprocessor.

Three are the main parameters that are used to evaluate the performance of a sensor [62]:

- the limit of detection (LOD), which is the lowest measurable input signal;
- the sensitivity, which is the variation of the output signal with respect to the input;

- the selectivity, which is the capability of a sensor to discriminate the input signal among many other signals.

The term *biosensor* denotes a type of chemical sensor, in which the detection is performed by means of a biochemical or biological mechanism. Therefore, a biosensor has a biological element placed on top of the transducing element, namely a *biorecognition layer* or *bioreceptor*. While the bioreceptor recognizes a specific analyte, the target, the transducer translates this recognition into a readable and measurable output signal [63]. In the last decade, biosensors are becoming a fast and cheap alternative to the generally expensive, time-consuming, standard laboratory analytical methods based on chromatography, and biochemical or microbiological techniques.

Optical biosensors exploit light in different spectral regions (from UV to IR) to obtain quantitative information on the concentration of a specific target analyte. These devices do not require instrumentation in direct contact with the sample. In fact, the transducer can be located relatively far from both the source and detector.

In particular, in this thesis, hybrid plasmonic NPs are adopted as optical transducers of biomolecular interactions. Opportunely functionalized plasmonic NPs give rise to plasmonic optical biosensors, whose analytical performance can be evaluated according to the selected transducing mechanism.

Plasmonic optical biosensors can be based on inherent oscillations of the free-plasma electrons (LSPR) and characterized by optical spectroscopy (refractive-index-based or absorption-based), in which the position of the LSPR undergoes a shift or an intensity variation as a function of the molecular concentration [60, 64, 65, 16], or based on external signal amplification, in which fluorescence, Raman signal, or infrared absorption intensity variations can be correlated to the molecular concentration [66, 14, 59].

Gold and silver nanoresonators have been adopted as platforms for plasmonic optical biosensors, however, the ones made of gold (AuNPs) are usually preferred to silver ones (AgNPs) for their higher chemical stability.

Specifically, AgNPs suffer from oxidative susceptibility when they come in contact with solvents and biomolecules, thus requiring further treatments to improve their stability [67, 68]. Moreover, many surface chemistry approaches have been introduced and refined to improve the biocompatibility of AuNPs[69] and to hook a probe on them, this latter being crucial in the design of optical biosensors[70, 71].

Inherent LSPR-based biosensors typically exploit two different transduction mechanisms: NPs aggregation and the refractive index change [72]. The choice between these two approaches depends on several factors, such as the nanofabrication strategy, the surface chemistry, and the specificity/non-specificity of binding events.

The aggregation-driven sensing mechanism is based on the strong colorimetric variation of colloidal plasmonic NPs when they are functionalized with two binding molecules, which cause the aggregation and a prominent red-shift of the LSPR in the absorbance spectrum (visible to the naked eye).[73, 74, 75] Unfortunately, this technique requires several stabilization procedures and trials to avoid the non-specific aggregation of NPs. For example, citrate AuNPs can be destabilized by salts (i.e. PBS buffer, NaCl solutions), strong basic or acidic pH, and some organic solvents with a subsequent spontaneous aggregation and/or degradation.[76, 77, 78] Moreover, NPs aggregation sensing mechanisms can be developed only when the AuNPs are in their colloidal form, strongly limiting their application to laboratory analysis.

To meet the increasing demand for fast, easy-to-use, cost-effective, selective, and sensitive platforms for the rapid screening of diseases and food quality analysis, several research groups introduced innovative fabrication techniques of either transparent or reflective substrates with immobilized nanoparticles on their surface acting as refractive index optical sensors [79, 80, 26, 81, 82]. For such devices, top-down methods are usually preferred in order to achieve ordered periodic arrays with ultra-high sensitivity and ultra-low limits of detection (LODs) [83, 84, 85].

Other fabrication strategies have been proposed, which rely on the random, or quasi-random, immobilization of AuNPs. These strategies only require a simple bottom-up synthesis onto rigid and polymeric substrates. This is a very promising direction to obtain low-cost, easy-to-fabricate, and large-scale optical platforms[86, 87]. Despite the continuous improvement of low-cost 2D platforms in the last few years, they still exhibit poor analytical performance, reduced surface area, reduced surface area-to-volume ratio, and the instability of immobilized biorecognition layers.

These limitations can be overcome by considering 3D platforms, where three-dimensional arrays of AuNPs are embedded into polymeric substrates. In fact, 3D optical biosensors are becoming the *new paradigm in biosensing technologies* with applications in the direct sensing within 3D architectures, such as implantable devices (scaffolds and patches) as well as *in vitro* analytical models (cell cultures, artificial tissues, and organoids) [88]. The combination of polymers with plasmonic NPs could be applied in the field of point-of-care (POC) and wearable sensing devices, which are still in their early stages, mainly due to the very accurate fabrication procedures required and the lower mechanical robustness compared to their electrical/electrochemical analogs. Polymers ensure high flexibility, adaptability to non-planar surfaces, and ease of integration within more complex systems, such as microelectronics and microfluidics, without compromising high sensitivity and mass production [59, 89].

In this dissertation, novel approaches for the design, fabrication, and characterization of large-scale, low-cost, and hybrid plasmonic NPs are proposed for application in biochemical sensing and are introduced with a careful description of the selected substrates and stabilizing materials.

1.4 Hybrid nanoparticles with multiple functionalities

The concept of *hybrid* plasmonic NPs is generally adopted to describe heterogeneous NPs consisting of a plasmonic metal and, at least, one other material. As a classical example, core–shell NPs are NPs with a core of typically gold, or silver, encapsulated inside a shell of various materials. The shell layer can be made of polymers or inorganic materials that are generally exploited to enhance chemical and colloidal stability, biocompatibility, and anti-fouling properties. Furthermore, it is selected to load and release drugs upon chemical external *stimuli* [90].

The incorporation of other functional materials within/onto a plasmonic NP can also introduce other physicochemical properties/functionalities, such as magnetism, stimuli-responsiveness, ... [91, 92]. The combination of two or more molecular compounds can lead to multifunctional hybrid NPs with enhanced performances, which take advantage of the facile synthesis, surface chemistry, and functionalization of plasmonic NPs [93]. The recent advances in chemical reduction and 3D nanofabrication techniques offer new promise in the production of complex hybrid NPs, which opens up unprecedented opportunities in their biomedical applications.

Unfortunately, Mie description of the electromagnetic scattering of plasmonic NPs did not consider the heterogeneity of hybrid NPs occurring during their bottom-up synthesis. Stabilizers (*e.g.*, polyethylene glycol [94], sodium citrate [95], gelatin [96]) are generally involved in the chemical synthesis of colloidal NPs, which possess their own refractive index. The stabilizers affect the effective dielectric constant of the hybrid NP, and, as a direct consequence, their optical properties, making difficult an accurate description of their absorption spectra. To this aim, Maxwell Garnett homogenization theory represents a validated and generally accepted tool to include inhomogeneities and impurities in the optical characterization of materials. The combination of Mie Theory and Maxwell Garnett approximation enables the prediction of the absorption and scattering cross-sections of hybrid NPs [97, 98].

Hydrogels, a particular class of polymers, are becoming the most studied materials, not only for the coating of plasmonic hybrid NPs, but also as 3D immobilization

matrices, due to their hydrophilicity, swelling capability, ease of integration within more complex microsystems [99], and for their capability of preserving active and functional structures of enzymes and other biomolecules, [100]. Furthermore, the properties of hydrogels can be easily engineered, since the cross-linking density of the polymer can be opportunely tuned to control the diffusion of biomolecules with a specific molecular weight [101, 102]. A hydrogel/hybrid NPs nanocomposite with a specific molecular and architectural design provides novel bio-responsive functionalities, controllable interaction between the biological species and the matrix, and preservation of the activity and functionality of the immobilized bioreceptor [103, 104, 105].

In this thesis, hybrid NPs with multiple functionalities are introduced. First, the design, fabrication, and characterization of a gelatin-capped hybrid diatomite/AuNPs colloidal nanosystem are proposed for application in drug release monitoring. Here, multifunctionality arises from the combination of AuNPs with diatomite, providing the system with a transducing element to monitor the polymer shell formation and degradation, as well as, indirect monitoring of the drug release. Then, a hybrid nanocomposite made of citrate-AuNPs and polyethylene-glycol diacrylate (PEGDA) hydrogel is proposed as a plasmonic transducer for biosensing monitoring. In these systems, multifunctionality arises, instead, from the mechanical properties of the hydrogel, which allow their exploitation in both refractive-index-based and swelling-dependent optical biosensors. Depending on the hydrogel molecular weight, the proposed hybrid nanosystems enable the biosensing of both small and big molecules with high accuracy and relatively low LODs. Moreover, the simple, low-cost, large-scale fabrication of this nanocomposite can be applied in all fields of biomedicine since its chemical and optical properties can be tailored to specific applications.

1.5 Author's main contribution

Major contributions

- Maxwell Garnett approximation for the accurate prediction of the electromagnetic scattering, absorption, and extinction of hybrid NPs by Mie and Kerker theories: numerical implementation, data analysis, and interpretation of the results (included in Chapters 3,4, and 5);

- Gelatin-capped plasmonic/diatomite colloidal nanoparticles for drug release monitoring: design, optical characterization, data analysis, and interpretation of the results [106] (included in Chapter 4);

- PEGDA/AuNPs nanocomposites for biosensing applications: design, fabrication, optical characterization, functionalization, data analysis, and interpretation of the results [60, 66, 107, 108] (included in Chapter 5);
- Plasmonic nanosensors in biomedicine: a review of the current state of the art [14] (included in Chapter 1);
- Flexible optical biosensors for life-sciences applications: a review of the current state of the art [59] (included in Chapter 1 and Chapter 5);
- Hollow microneedle-based plasmonic sensor for on patch detection of molecules in dermal interstitial fluid: design, fabrication, optical characterization, functionalization, data analysis, and interpretation of the results (not included in this thesis, under-review paper)
- Plasmonic bimetallic nanoislands arranged in random arrays for antibody functionality assessment: fabrication, optical characterization, functionalization, data analysis, and interpretation of the results (not included in this thesis, manuscript in preparation)

Contributions

- Electromagnetic scattering by networks of high-permittivity thin wires: numerical simulations by Comsol Multiphysics, implementation of the model, data analysis, and interpretation of the results [44] (included in Chapter 2);
- One-shot fabrication of polymeric hollow microneedles by standard photolithography: numerical simulation by Comsol Multiphysics, data analysis, and interpretation of the results [109] (not included in this thesis);
- Oxygen indicator films of PEGDA and Titania (TiO_2) NPs with tunable response times: optical characterization, data analysis, and interpretation of the results [110] (not included in this thesis);
- Porous silicon-based optical sensors [111] for electroluminescence: design, fabrication, optical characterization, and data analysis (not included in this thesis).

Acknowledgements

All the theoretical work of this Ph.D. was carried out at the Department of Electrical Engineering and Information Technology (DIETI) of the University of Naples Federico II, under the guidance of Prof. Carlo Forestiere. All the experimental studies

were performed at the Institute of Applied Science and Intelligent Systems - Naples Unit (ISASI-NA) of the National Research Council, under the guidance of Dr. Luca De Stefano, and in collaboration with Dr. Ilaria Rea, for spectroscopic ellipsometry measurements, Dr. Principia Dardano, for scanning electron microscopy, from ISASI-NA, Dr. Stefania Dello Iacono for the mechanical tests, from the Institute of Polymers, Composites, and Biomaterials (IPCB) of Naples, and Dr. Marinella Pirozzi for transmission electron microscopy, from the Institute for Experimental Endocrinology and Oncology (IEOS) of Naples.

Chapter 2

Plasmonic and Dielectric modes of optically small objects

2.1 Mie Theory: Absorption and Scattering of light by small particles

The treatment of absorption and scattering of light by arbitrary objects is a fundamental problem in optics, which is quite complex and large to be treated in a general way. Therefore, for the aims of this thesis dissertation, it will be limited to isolated, optically small particles within the framework of classical electromagnetic theory.

When an electromagnetic wave illuminates an obstacle (*e.g.*, an electron, an atom, a molecule, or a particle), its electric charges start to oscillate due to the interaction with the electric field of the incident wave. From this oscillatory motion of the electric charges, the electromagnetic energy is radiated in all directions; this *secondary radiation* goes under the name of *scattering*, which is the sum of excitation and re-radiation. In addition, part of the incident wave electromagnetic energy can be converted into another form, such as thermal energy, in a process called *absorption*. Scattering and absorption, which are not mutually independent processes, are the main subject of this paragraph.

2.1.1 Basics of Electromagnetic Theory

The description of the macroscopic electromagnetic field in matter is provided by Maxwell equations, which can be expressed as:

$$\nabla \cdot \mathbf{D} = \rho_F, \tag{2.1}$$

$$\nabla \times \mathbf{E} + \frac{\partial \mathbf{B}}{\partial t} = \mathbf{0}, \tag{2.2}$$

$$\nabla \cdot \mathbf{B} = 0 \tag{2.3}$$

$$\nabla \times \mathbf{H} = \mathbf{J}_F + \frac{\partial \mathbf{D}}{\partial t}, \tag{2.4}$$

where $\mathbf{E}$ and $\mathbf{D}$ are the electric field and the electric displacement, respectively, and $\mathbf{B}$ and $\mathbf{H}$ are the magnetic induction and magnetic field, respectively; ρ_F and $\mathbf{J}_F$ are the charge and current densities associated with the free charges. In particular, $\mathbf{D}$ and $\mathbf{H}$ are expressed as

$$\mathbf{D} = \varepsilon_0 \mathbf{E} + \mathbf{P}, \tag{2.5}$$

$$\mathbf{H} = \frac{\mathbf{B}}{\mu_0} - \mathbf{M}, \tag{2.6}$$

with $\mathbf{P}$ being the electric polarization and $\mathbf{M}$ being the magnetization, representing the average electric and magnetic dipole moments per unit volume. ε_0 and μ_0 are the permittivity and permeability of the free space, respectively. The set of equations from 2.1 to 2.6 must be completed with the so-called *constitutive relations*, which strongly depend on the medium under consideration. If we assume a linear, homogeneous, and isotropic medium, they can be expressed as:

$$\mathbf{J}_F = \sigma \mathbf{E}, \tag{2.7}$$

$$\mathbf{B} = \mu \mathbf{H}, \tag{2.8}$$

$$\mathbf{P} = \varepsilon_0 \chi \mathbf{E}, \tag{2.9}$$

where σ is the conductivity, μ the permeability, and χ the electric susceptibility of the considered material. For noble metals, such as silver and gold, these constitutive relations hold true; however, there are many classes of materials for which these relations are not valid; therefore they must not be taken as universal laws of nature.

2.1.2 General Formulation

The evaluation of the absorption and scattering of an arbitrary particle can be performed by solving a very general problem in which the size, shape, and optical properties of the particles are specified and the electromagnetic field within and outside the particle must be determined. The particle illumination is assumed as made by a monochromatic and arbitrarily polarized plane wave for simplicity. [13].

The scattering-absorption problem, schematized in Figure 2.1, can be solved by exploiting the superposition principle. In this dissertation, the particle's inner field is

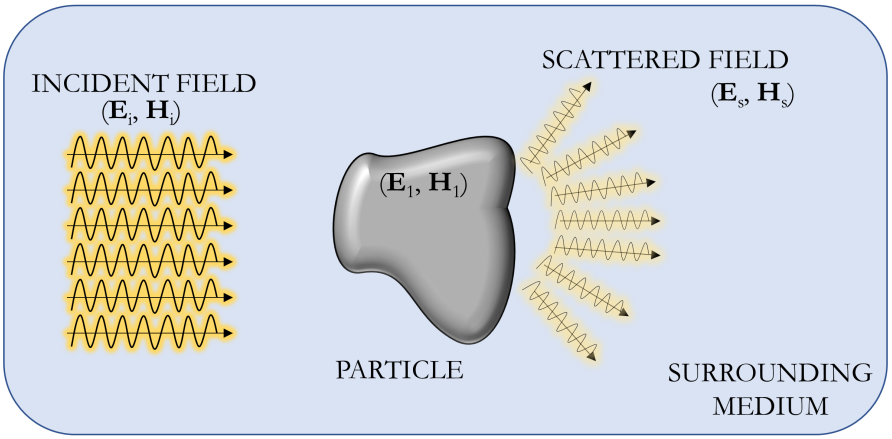

Figure 2.1: Schematic representation of the field within the particle $(\mathbf{E}_1, \mathbf{H}_1)$ and scattered field $(\mathbf{E}_s, \mathbf{H}_s)$in the surrounding medium caused by the incident field $(\mathbf{E}_i, \mathbf{H}_i)$.

denoted by $(\mathbf{E}_1, \mathbf{H}_1)$, while the field outside the particle (in the surrounding medium) is denoted by $(\mathbf{E}_2, \mathbf{H}_2)$ and can be expressed as

$$\mathbf{E}_2 = \mathbf{E}_i + \mathbf{E}_s, \qquad \mathbf{H}_2 = \mathbf{H}_i + \mathbf{H}_s. \tag{2.10}$$

Therefore, the superposition principle applies to the field outside the particle and is given by the summation of the scattered field $(\mathbf{E}_s, \mathbf{H}_s)$ and the incident field $(\mathbf{E}_i, \mathbf{H}_i)$. Specifically, being a plane wave, and given the wave vector $\mathbf{k}$ in the surrounding medium, the incident field is evaluated as:

$$\mathbf{E}_i = \mathbf{E}_0 \exp(i\mathbf{k} \cdot \mathbf{x} - i\omega t), \qquad \mathbf{H}_i = \mathbf{H}_0 \exp(i\mathbf{k} \cdot \mathbf{x} - i\omega t). \tag{2.11}$$

The fields $(\mathbf{E}, \mathbf{H})$ satisfy the time-harmonic Maxwell equations in the points in which ε and μ are continuous:

$$\nabla \cdot \mathbf{E} = 0, \tag{2.12}$$

$$\nabla \cdot \mathbf{H} = 0 \tag{2.13}$$

$$\nabla \times \mathbf{E} = i\omega\mu\mathbf{H}, \tag{2.14}$$

$$\nabla \times \mathbf{H} = -i\omega\varepsilon\mathbf{E}. \tag{2.15}$$

If the curl operator is applied to equations 2.14 and 2.15, the following equations are obtained:

$$\nabla \times (\nabla \times \mathbf{E}) = i\omega\mu\nabla \times \mathbf{H} = \omega^2\varepsilon\mu\mathbf{E}, \tag{2.16}$$

$$\nabla \times (\nabla \times \mathbf{H}) = -i\omega\varepsilon\nabla \times \mathbf{E} = \omega^2\varepsilon\mu\mathbf{H}, \tag{2.17}$$

which, in turn, can be rewritten as:

$$\nabla^2\mathbf{E} + k^2\mathbf{E} = 0 \qquad \nabla^2\mathbf{H} + k^2\mathbf{H} = 0. \tag{2.18}$$

Therefore, $\mathbf{E}$ and $\mathbf{H}$ do satisfy the *vector wave equation* in which, given the generic vector $\mathbf{A}$, $\nabla^2\mathbf{A} = \nabla \cdot (\nabla\mathbf{A})$ and $k^2 = \omega^2\varepsilon\mu$. Equations 2.18 are obtained from the vector identity:

$$\nabla \times (\nabla \times \mathbf{A}) = \nabla(\nabla \cdot \mathbf{A}) - \nabla \cdot (\nabla\mathbf{A}). \tag{2.19}$$

To take into account the discontinuities (transition regions with thicknesses much smaller than the particle size) of ε and μ due to the crossing of the boundaries between the particle and its surrounding medium, the following conditions must be imposed on the fields:

$$\begin{aligned} [\mathbf{E}_2(\mathbf{x}) - \mathbf{E}_1(\mathbf{x})] \times \hat{\mathbf{n}} = \mathbf{0}, \\ [\mathbf{H}_2(\mathbf{x}) - \mathbf{H}_1(\mathbf{x})] \times \hat{\mathbf{n}} = \mathbf{0}, \end{aligned} \qquad \mathbf{x} \quad on \quad S \tag{2.20}$$

where $\hat{\mathbf{n}}$ is the unit vector normally directed outward the surface S of the particle.

2.1.3 Absorption, Scattering and Extinction

Suppose that one or more particles are exposed to an electromagnetic radiation beam and that a detector D is placed downstream from the particles. In presence of the particles, the detector receives an electromagnetic power U, while in absence of the particles, the electromagnetic energy is received at a rate denoted as U_0, with $U_0 > U$. This means that the presence of the particles causes an *extinction* of the incident light. The difference $U_o - U$ is referred to as the *absorption* and *scattering* of the particles if the medium in which they are embedded is non-absorbing. The two phenomena are strongly affected by the particles' size, shape, orientation, composition, and density, by the surrounding medium optical properties, and by the incident field polarization and frequency.

For a single particle, illuminated by a plane wave and placed within a non-absorbing medium, it is always possible to construct an imaginary sphere of radius r and surface A around the particle (Figure 2.2). The net rate of the electromagnetic energy crossing A is

$$W_a = -\int_A \mathbf{S} \cdot \hat{\mathbf{e}}_r dA.$$

For this dissertation, no energy is created after the interaction of an electromag-

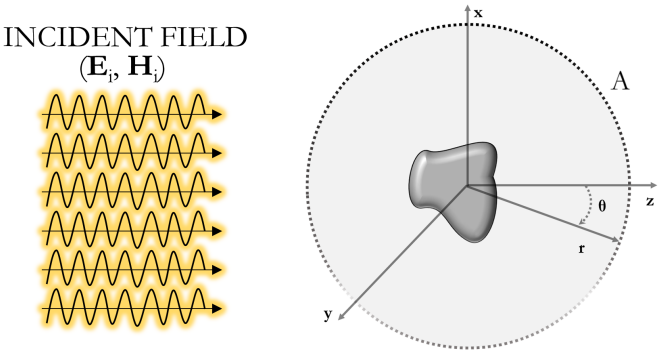

Figure 2.2: Extinction by a single particle.

netic wave with a particle, therefore W_a is assumed as always positive ($W_a > 0$), meaning that energy is absorbed within the imaginary sphere, but since the medium is non-absorbing, the absorbed contribution can only be addressed to the particle.

Starting from the derivation of the time-averaged Poynting vector in the points outside the particle, written as the following summation:

$$\mathbf{S} = \frac{1}{2}\Re e\{\mathbf{E}_2 \times \mathbf{H}_2^*\} = \mathbf{S}_i + \mathbf{S}_s + \mathbf{S}_{ext} \tag{2.21}$$

where

$$\mathbf{S}_i = \frac{1}{2}\Re e\{\mathbf{E}_i \times \mathbf{H}_i^*\}, \quad \mathbf{S}_s = \frac{1}{2}\Re e\{\mathbf{E}_s \times \mathbf{H}_s^*\}, \quad \mathbf{S}_{ext} = \frac{1}{2}\Re e\{\mathbf{E}_i \times \mathbf{H}_s^* + \mathbf{E}_s \times \mathbf{H}_i^*\},$$

it is possible to write W_a as

$$W_a = W_i - W_s + W_{ext}, \tag{2.22}$$

with

$$\mathbf{W}_i = -\int_A \mathbf{S}_i \cdot \hat{\mathbf{e}}_r dA, \quad \mathbf{W}_s = \int_A \mathbf{S}_s \cdot \hat{\mathbf{e}}_r dA, \quad \mathbf{W}_{ext} = -\int_A \mathbf{S}_{ext} \cdot \hat{\mathbf{e}}_r dA. \tag{2.23}$$

Since W_i is the result of an integral on a non-absorbing symmetric surface it goes identically to 0. Therefore, W_{ext} is nothing but the sum of energy absorbing and scattering rates, respectively:

$$W_{ext} = W_a + W_s. \tag{2.24}$$

It is convenient to assume the incident electric field to be polarized along the x-axis $\mathbf{E}_i = E\hat{\mathbf{e}_x}$, and the wave vector $\mathbf{k}$ directed along $\hat{\mathbf{e}_z}$. Considering that the

medium is non-absorbing, the energy absorption rate is independent of the radius r, which, accordingly, can be assumed as sufficiently large to be in the far-field region in a way that:

$$\mathbf{E}_s \sim \frac{e^{ik(r-z)}}{-ikr}\mathbf{X}E, \quad \mathbf{H}_s \sim \frac{k}{\omega\mu}\hat{\mathbf{e}_r} \times \mathbf{E}_s, \tag{2.25}$$

and $\hat{\mathbf{e}_r} \cdot \mathbf{X} = 0$. To remind that the symbol $\mathbf{X}$ denotes the *vector scattering amplitude* [112] related to the scalar amplitude scattering matrix in the following relationship:

$$\mathbf{X} = (S_2 \cos\phi + S_3 \sin\phi)\hat{\mathbf{e}}_{\parallel s} + (S_4 \cos\phi + S_1 \sin\phi)\hat{\mathbf{e}}_{\perp s}. \tag{2.26}$$

After some algebraic calculations:

$$\begin{aligned} W_{ext} = \frac{-k}{2\omega\mu}|\mathbf{E}|^2 \Re e\Big\{ & \frac{e^{-ikr}}{ikr}\int_A e^{ikz}\hat{\mathbf{e}}_x \cdot \mathbf{X}^* dA \\ & -\frac{e^{ikr}}{ikr}\int_A e^{-ikz}\cos\theta\hat{\mathbf{e}}_x \cdot \mathbf{X} dA \\ & +\frac{e^{ikr}}{ikr}\int_A e^{-ikz}\sin\theta\cos\phi\hat{\mathbf{e}}_z \cdot \mathbf{X} dA\Big\} \end{aligned} \tag{2.27}$$

It can be shown that, as $kr \to \infty$, the limiting value of W_{ext} can be evaluated as:

$$W_{ext} = I_i \frac{4\pi}{k^2}\Re e\{(\mathbf{X} \cdot \hat{\mathbf{e}}_x)_{\theta=0}\} \tag{2.28}$$

where I_i is the irradiance of the incident field. Therefore, from the *ratio* of W_{ext} and I_i, the *extinction cross section* C_{ext} can be obtained:

$$C_{ext} = \frac{W_{ext}}{I_i} = \frac{4\pi}{k^2}\Re e\{(\mathbf{X} \cdot \hat{\mathbf{e}}_x)_{\theta=0}\}. \tag{2.29}$$

From Eq. 2.22, it is now obvious to write:

$$C_{ext} = C_{sca} + C_{abs}, \tag{2.30}$$

where $C_{sca} = W_s/I_i$ and $C_{abs} = W_a/I_i$. The *scattering cross section* C_{sca} can be derived from Eqs. 2.23 and 2.25:

$$C_{sca} = \int_0^{2\pi}\int_0^{\pi} \frac{|\mathbf{X}|^2}{k^2}\sin\theta d\theta d\phi = \int_{4\pi} \frac{|\mathbf{X}|^2}{k^2} d\Omega. \tag{2.31}$$

The quantity $|\mathbf{X}|^2/k^2$ is denoted as *differential scattering cross section*, $dC_{sca}/d\Omega$. Physically, it denotes the angular distribution of the scattered light. In the scattering theory the quantity $\mathbf{X}^2/k^2C_{sca}$ represents the *phase function* p, which can be

normalized as:

$$\int_{4\pi} p d\Omega = 1.$$

Moreover, it is possible to define the average cosine of the scattering angle known as *asymmetry parameter* g with the following:

$$g = \langle \cos\theta \rangle = \int_{4\pi} p \cos\theta d\Omega.$$

Particularly, when the particle *isotropically* scatters light or when the scattering is symmetric about a right angle (90°), $g = 0$.A positive g value denotes a higher forward scattering ($\theta = 0°$), while a negative g value denotes a higher backscattering ($\theta = 180°$). It is possible to define extinction, scattering, and absorption *efficiencies* as:

$$Q_{ext} = \frac{C_{ext}}{G}, \quad Q_{sca} = \frac{C_{sca}}{G}, \quad Q_{abs} = \frac{C_{abs}}{G},$$

where G is the particle cross-section projected onto a plane perpendicular to the incident field. Eq. 2.29 represents a particular form of *the optical theorem*, which states that the extinction only depends on the scattering in the forward ($\theta = 0°$) direction. This means that the extinction is nothing but the combined effect of the absorption in the particle and the scattering in all directions by the particle [113].

2.1.4 Absorption and Scattering by a Sphere

In the theory of scattering and absorption, one of the most relevant problems is related to small spherical particles with arbitrary size and optical constants, which are soluble in a closed form. The solution to this problem is historically attributed to Gustav Mie, which, in 1908, formulated his theory starting from the observation of the brilliant colors exhibited by small colloidal particles of gold.

In this section, the mathematics behind Mie Theory is reported starting from a time-harmonic electromagnetic field ($\mathbf{E}$, $\mathbf{H}$), which is a linear, homogeneous, and isotropic medium must satisfy Eq. 2.18, and the Maxwell equation (Eqs. 2.12-2.15), meaning that it must be divergence-free and that the electric and magnetic fields must be dependent. Since it is always possible to construct a vector function $\mathbf{M}$ for which

$$\mathbf{M} = \nabla \times (\mathbf{c}\psi)$$

where ψ is a scalar function and $\mathbf{c}$ an arbitrary constant vector, and since the divergence of the curl of any vector function is null ($\nabla \cdot \mathbf{M} = 0$), by applying some vector

identities, it is possible to obtain:

$$\nabla^2\mathbf{M} + k^2\mathbf{M} = \nabla \times [\mathbf{c}(\nabla^2\psi + k^2\psi)].$$

Therefore, only if ψ is a solution of the *scalar* wave equation

$$\nabla^2\psi + k^2\psi = 0,$$

$\mathbf{M}$ identically satisfies the *vector* wave equation, where $\mathbf{M}$ results to be perpendicular to $\mathbf{c}$ ($\mathbf{M} = -\mathbf{c} \times \nabla\psi$). Moreover, it is possible to define another vector $\mathbf{N}$ with vanishing divergence and satisfying the vector wave equation:

$$\mathbf{N} = \frac{\nabla \times \mathbf{M}}{k} \qquad \nabla^2\mathbf{N} + k^2\mathbf{N} = 0.$$

Due to these considerations, the problem of finding the solutions to the field equations can be simplified to the solution of the scalar wave equation. In fact, $\mathbf{M}$ and $\mathbf{N}$ are arbitrary fields having all the requirements to describe an electromagnetic field, since they are divergence-free, non-independent, and satisfy the vector wave equation. In this context, ψ is generally denoted as *generating function* of $\mathbf{M}$ and $\mathbf{N}$ *vector harmonics*, and $\mathbf{c}$ as the *pilot* or *guiding* vector.

Since the scattering by a sphere is the problem of this section, it is convenient to choose a generating function ψ and a *guiding* vector $\mathbf{c}$ in a way that ψ satisfies the scalar wave equation in polar spherical coordinates and $\mathbf{M}$ is a solution of the vector wave equation in the same coordinates ($\mathbf{r}$, θ, ϕ), as schematized in Figure 2.3. To do

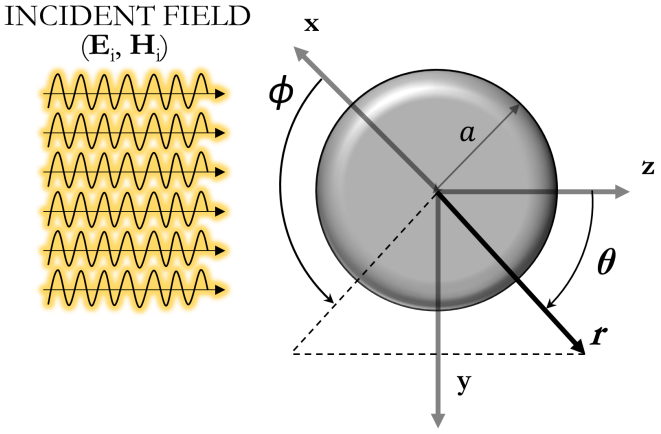

Figure 2.3: Extinction by a single particle.

this, **c** must be the radius vector **r**:

$$\mathbf{M} = \nabla \times (\mathbf{r}\psi). \tag{2.32}$$

Therefore, **M** is everywhere tangential to the arbitrary sphere of constant radius **r**. The scalar wave equation can be expressed in spherical polar coordinates as:

$$\frac{1}{r^2}\frac{\partial}{\partial r}\left(r^2\frac{\partial\psi}{\partial r}\right) + \frac{1}{r^2\sin\theta}\frac{\partial}{\partial\theta}\left(\sin\theta\frac{\partial\psi}{\partial\theta}\right) + \frac{1}{r^2\sin\theta}\frac{\partial^2\psi}{\partial\phi^2} + k^2\psi = 0. \tag{2.33}$$

It is possible to seek solutions to the Eq.2.33 with the formulation

$$\psi(r,\theta,\phi) = R(r)\Theta(\theta)\Phi(\phi),$$

which leads to three different equations:

$$\frac{d^2\Phi}{d\phi^2} + m^2\Phi = 0, \tag{2.34}$$

$$\frac{1}{\sin\theta}\frac{d}{d\theta}\left(\frac{d\Theta}{d\theta}\right) + \left[n(n+1) - \frac{m^2}{\sin^2\theta}\right]\Theta = 0, \tag{2.35}$$

$$\frac{d}{dr}\left(r^2\frac{dR}{dr}\right) + [k^2r^2 - n(n+1)]R = 0, \tag{2.36}$$

where m and n are known as *separation constants*, which can be obtained by imposing some conditions to ψ.

Concerning Eq.2.34, for a given m, Φ_m is a solution, while Φ_{-m} is not a linear independent solution.

$$\Phi_e = \cos m\phi, \qquad \Phi_o = \sin m\phi,$$

are instead linearly independent solutions, with e and o subscripts are used to indicate *even* and *odd*. It is necessary that ψ is a *single-valued* scalar function of the angle *phi* (azimuthal angle):

$$\lim_{\nu\to 2\pi}\psi(\phi+\nu) = \psi(\phi) \tag{2.37}$$

for all the azimuthal angles at interior points of homogeneous regions (boundaries are excluded from this treatment). The condition in Eq.2.37 forces the m values to be zero or integers, and, in particular, positive integers are the only ones needed to generate all the linearly independent solutions to Eq.2.34.

Concerning Eq.2.35, it can be shown that the solutions that are finite at $\theta = 0$ and $\theta = \pi$ are nothing but the *associated Legendre functions* of the first kind $P_n^m\cos(\theta)$, having degree n and order m, with $n = m, m+1, ...$ [114]. It can be shown that these

functions are orthogonal:

$$\int_{-1}^{1} p_n^m(\cos\theta) p_{n'}^m(\cos\theta) d\cos\theta = \delta_{n'n} \frac{2}{2n+1} \frac{(n+m)!}{(n-m)!}, \tag{2.38}$$

where $\delta_{n'n}$ is the Kronecker delta

$$\delta_{n'n} = \begin{cases} 1, & \text{if } n = n', \\ 0, & \text{if } n \neq n'. \end{cases}$$

It should be noticed that when $m = 0$, the *associate Legendre functions* become the *Legendre polynomials* P_n.

Finally, concerning Eq.2.36, it is possible to introduce the dimensionless variable $\rho = kr$ and define the function $Z = R\sqrt{\rho}$ in such a way that:

$$\rho \frac{d}{d\rho}\left(\rho \frac{dZ}{d\rho}\right) + \left[\rho^2 - \left(n + \frac{1}{2}\right)^2\right] Z = 0. \tag{2.39}$$

Eq.2.39 has linearly independent solutions that are known as *Bessel functions* of the first and second kind J_ν and Y_ν (or N_ν), with $\nu = n + 1/2$. In the spherical polar coordinates, these solutions are the *spherical* Bessel functions

$$j_n(\rho) = \sqrt{\frac{\pi}{2\rho}} J_{n+1/2}(\rho), \tag{2.40}$$

$$y_n(\rho) = \sqrt{\frac{\pi}{2\rho}} Y_{n+1/2}(\rho), \tag{2.41}$$

which, given the generic z_n associable with either j_n or y_n, satisfy the following recurrence relations:

$$z_{n-1}(\rho) + z_{n+1}(\rho) = \frac{2n+1}{\rho} z_n(rho) \tag{2.42}$$

$$(2n+1)\frac{d}{d\rho} z_n(rho) = n z_{n-1}(\rho) - (n+1) z_{n+1}(\rho) \tag{2.43}$$

Therefore, provided the first two orders functions,

$$j_0(\rho) = \frac{sin\rho}{\rho}, \qquad j_1\rho = \frac{\sin(\rho)}{\rho^2} - \frac{\cos(\rho)}{\rho},$$
$$y_0(\rho) = -\frac{cos\rho}{\rho}, \qquad y_1\rho = -\frac{\cos(\rho)}{\rho^2} - \frac{\sin(\rho)}{\rho},$$

higher-order ones can be derived by recurrence. For all n, $y_n(kr)$ becomes infinite as r approaches zero.

Although not limited to real values of $\rho = kr$, in Figure 2.4, the spherical Bessel functions as a function of real-valued kr are reported for $n = 0, 1, 2, 3, 4$. Any linear combination of the Bessel functions is also a solution of Eq. 2.36. Of particular utility will be the spherical *Hankel functions* or *spherical Bessel equations of the third kind*, which can be obtained by two linear combinations of j_n and y_n:

$$h_n^{(1)}(\rho) = j_n(\rho) + iy_n(\rho), \tag{2.44}$$

$$h_n^{(2)}(\rho) = j_n(\rho) + iy_n(\rho). \tag{2.45}$$

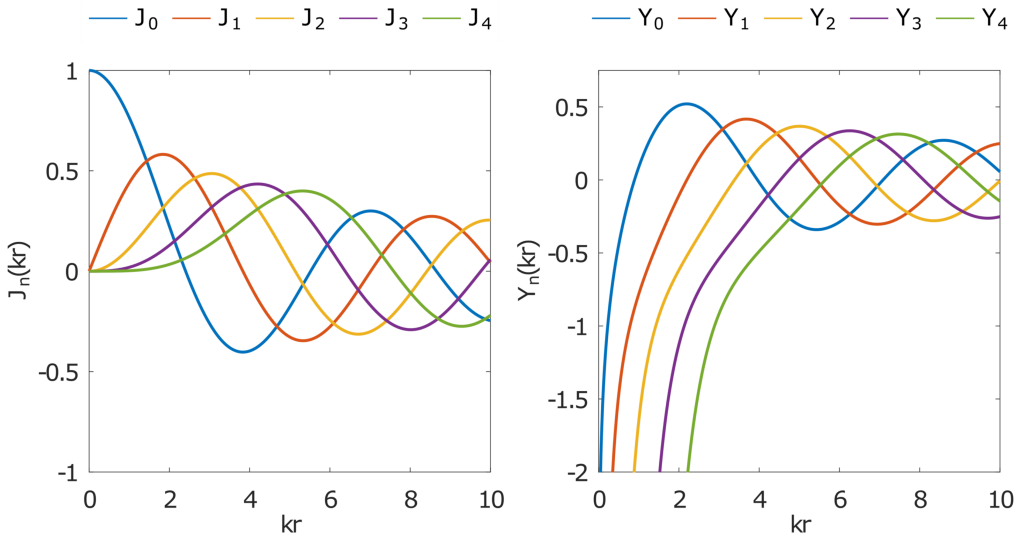

Figure 2.4: Spherical Bessel functions of the first ($j_n(kr)$) and second $y_n(kr)$ kinds for n =0 (blue), 1 (orange), 2 (yellow), 3 (purple), 4 (green).

Considering all the three separated equations from Eq. 2.34 to Eq. 2.36, it is now possible to build up the generating functions that satisfy the scalar wave equation in spherical polar coordinates:

$$\psi_{emn} = \cos(m\phi)P_n^m(cos\theta)z_n(kr), \tag{2.46}$$

$$\psi_{omn} = \sin(m\phi)P_n^m(cos\theta)z_n(kr), \tag{2.47}$$

with z_n being any of the spherical Bessel functions herein defined. Reminding Eq.

2.32, and the definition of the vector $\mathbf{N}$, the following is obtained:

$$\begin{aligned} \mathbf{M}_{emn} &= \nabla \times (\mathbf{r}\psi_{emn}), \qquad \mathbf{M}_{omn} = \nabla \times (\mathbf{r}\psi_{omn}), \\ \mathbf{N}_{emn} &= \frac{\nabla \times \mathbf{M}_{emn}}{k}, \qquad \mathbf{N}_{omn} = \frac{\nabla \times \mathbf{M}_{omn}}{k}. \end{aligned} \tag{2.48}$$

Eqs. 2.48 can be always written in component form as follows

$$\begin{aligned} \mathbf{M}_{emn} = \frac{-m}{\sin\theta} \sin(m\phi) P_n^m(\cos\theta) z_n(\rho) \\ hat\mathbf{e}_\theta \\ - \cos(m\phi) \frac{dP_n^m(\cos\theta)}{d\theta} z_n(\rho) \hat{\mathbf{e}}_\phi, \end{aligned} \tag{2.49}$$

$$\begin{aligned} \mathbf{M}_{omn} = \frac{m}{\sin\theta} \cos(m\phi) P_n^m(\cos\theta) z_n(\rho) \hat{\mathbf{e}}_\theta \\ - \sin(m\phi) \frac{dP_n^m(\cos\theta)}{d\theta} z_n(\rho) \hat{\mathbf{e}}_\phi, \end{aligned} \tag{2.50}$$

$$\begin{aligned} \mathbf{N}_{emn} = \frac{z_n(\rho)}{\rho} \cos(m\phi) n(n+1) P_n^m(\cos\theta) \hat{\mathbf{e}}_r \\ + \cos(m\phi) \frac{dP_n^m(\cos\theta)}{d\theta} \frac{1}{\rho} \frac{d}{d\rho} [\rho z_n(\rho)] \hat{\mathbf{e}}_\theta \\ -m \sin(m\phi) \frac{P_n^m(\cos\theta)}{\sin\theta} \frac{1}{\rho} \frac{d}{d\rho} [\rho z_n(\rho)] \hat{\mathbf{e}}_\phi \end{aligned} \tag{2.51}$$

$$\begin{aligned} \mathbf{N}_{omn} = \frac{z_n(\rho)}{\rho} \sin(m\phi) n(n+1) P_n^m(\cos\theta) \hat{\mathbf{e}}_r \\ + \sin(m\phi) \frac{dP_n^m(\cos\theta)}{d\theta} \frac{1}{\rho} \frac{d}{d\rho} [\rho z_n(\rho)] \hat{\mathbf{e}}_\theta \\ +m \cos(m\phi) \frac{P_n^m(\cos\theta)}{\sin\theta} \frac{1}{\rho} \frac{d}{d\rho} [\rho z_n(\rho)] \hat{\mathbf{e}}_\phi, \end{aligned} \tag{2.52}$$

and any solutions of the field equations, in the problem of the scattering by an arbitrary sphere, can be expanded in an infinite series of these functions. To do this, the determination of the coefficients of the series is required and can be faced starting from a plane wave polarized along the x-axis, which in spherical coordinates turns into:

$$\mathbf{E}_i = E_0 e^{ikr\cos\theta} \hat{\mathbf{e}}_x, \tag{2.53}$$

with

$$\hat{\mathbf{e}}_x = \sin\theta\cos\phi\hat{\mathbf{e}}_r + \cos\theta\cos\phi\hat{\mathbf{e}}_\theta - \sin\phi\hat{\mathbf{e}}_\phi. \tag{2.54}$$

The expansion of Eq. 2.53 into vector spherical harmonics can be written as:

$$\mathbf{E}_i = \sum_{m=0}^{\infty}\sum_{n=m}^{\infty}(\mathbf{B}_{emn}\mathbf{M}_{emn} + \mathbf{B}_{omn}\mathbf{M}_{omn} + \mathbf{A}_{emn}\mathbf{N}_{emn} + \mathbf{A}_{omn}\mathbf{N}_{omn}). \tag{2.55}$$

Since $\sin(m\phi)$ and $\cos(m'\phi)$ are orthogonal, also $\mathbf{M}_{emn}$ and $\mathbf{M}_{omn}$ are orthogonal

$$\int_0^{2\pi}\int_0^{\pi}\mathbf{M}_{em'n'}\cdot\mathbf{M}_{omn}\sin\theta d\theta d\phi = 0 \qquad (\forall m, m', n, n'). \tag{2.56}$$

The same mutual orthogonality applies for the sets of functions ($\mathbf{N}_{omn}$, $\mathbf{N}_{emn}$), ($\mathbf{M}_{omn}$,$\mathbf{N}_{omn}$), and ($\mathbf{M}_{emn}$, $\mathbf{N}_{emn}$). Due to this, it is possible to show that the coefficients in the expansion can be expressed as:

$$\mathbf{B}_{emn} = \frac{\int_0^{2\pi}\int_0^{2\pi}\mathbf{E}_i\cdot\mathbf{M}_{emn}\sin\theta d\theta d\phi}{\int_0^{2\pi}\int_0^{2\pi}|\mathbf{M}_{emn}|^2\sin\theta d\theta d\phi}. \tag{2.57}$$

Also the coefficients $\mathbf{B}_{omn}$, $\mathbf{A}_{emn}$, and $\mathbf{A}_{omn}$ have similar expressions.

With this expression of the coefficients, it is simple to show that, due to Eqs. 2.49, 2.52, and 2.54, and following the mutual orthogonality of the sine and cosine functions, $\mathbf{B}_{emn} = \mathbf{A}_{omn} = 0$. For the same reasons, $\mathbf{B}_{omn} = \mathbf{A}_{emn} = 0$ with exception from the case $m = 1$. Since the incident field $\mathbf{E}_i$ is finite in the origin, $j_n(kr)$ must be the appropriate Bessel function in ψ_{o1n} and ψ_{e1n}. Therefore, the expansion of the incident field can be written as follows:

$$\mathbf{E}_i = \sum_{n=1}^{\infty}(\mathbf{B}_{o1n}\mathbf{M}^{(1)}_{o1n} + \mathbf{A}_{e1n}\mathbf{N}^{(1)}_{e1n}), \tag{2.58}$$

where the superscript (1) denotes that the radial dependence of the generating function is achieved by using only $j_n(kr)$.

The coefficients of the expansion can be derived by proving the orthogonality of the component of the vector spherical harmonics, by applying Gegenbauer's generalization of the integral of Poisson and some algebraic considerations [13]. Finally, the following expansion coefficients are obtained:

$$\mathbf{B}_{o1n} = i^n E_0\frac{2n+1}{n(n+1)} \tag{2.59}$$

$$\mathbf{A}_{e1n} = -iE_0 i^n\frac{2n+1}{n(n+1)}. \tag{2.60}$$

Therefore, Eq. 2.58 can be rewritten as:

$$\mathbf{E}_i = E_0 \sum_{n=1}^{\infty} i^n \frac{2n+1}{n(n+1)} (\mathbf{M}_{o1n}^{(1)} - i\mathbf{N}_{e1n}^{(1)}) \tag{2.61}$$

and provides the expansion of a plane wave (electric incident field) in spherical harmonics.

Analogously, the corresponding magnetic field is obtained by simply applying Maxwell equations (Eq. 2.14). Therefore,

$$\mathbf{H}_i = \frac{-k}{\omega\mu} E_0 \sum_{n=1}^{\infty} i^n \frac{2n+1}{n(n+1)} (\mathbf{M}_{o1n}^{(1)} - i\mathbf{N}_{e1n}^{(1)}). \tag{2.62}$$

Also the field within the sphere ($\mathbf{E}_1$, $\mathbf{H}_1$) and the scattered field ($\mathbf{E}_s$, $\mathbf{H}_s$) can be expanded in vector spherical harmonics.

First, the boundary condition (Eq. 2.20) between the sphere and its surrounding medium must be applied, which leads to:

$$(\mathbf{E}_i + \mathbf{E}_s - \mathbf{E}_1) \times \hat{\mathbf{e}}_r = (\mathbf{H}_i + \mathbf{H}_s - \mathbf{H}_1) \times \hat{\mathbf{e}}_r = 0. \tag{2.63}$$

Then, by combining Eq. 2.63 with the orthogonality of the vector harmonics and the expansion of the incident field, it is possible to show that the coefficients are, also in this case, different from zero only when $m = 1$. Again, since the incident field is finite in the origin, the spherical Bessel function in the generating functions must be of the type $j_n(k_1 r)$, where k_1 represents the wave number within the sphere. Therefore, for the internal fields,

$$\begin{aligned} \mathbf{E}_1 &= \sum_{n=1}^{\infty} E_n (c_n \mathbf{M}_{o1n}^{(1)} - i d_n \mathbf{N}_{e1n}^{(1)}), \\ \mathbf{H}_1 &= \frac{-k_1}{\omega\mu_1} \sum_{n=1}^{\infty} E_n (d_n \mathbf{M}_{e1n}^{(1)} + i c_n \mathbf{N}_{o1n}^{(1)}), \end{aligned} \tag{2.64}$$

where μ_1 is the permeability of the sphere and $E_n = i^n E_0 (2n+1)/[n(n+1)]$.

For the scattered fields, both j_n and y_n must be considered since, outside the sphere, y_n does not diverge. Therefore, Hankel functions are considered for this treatment. In particular, only the Hankel function associated with an outgoing wave at large distances from the sphere must be considered in the generating functions; its expression is asymptotically given by:

$$h_n^{(1)}(kr) \sim \frac{(-i)e^{ikr}}{ikr}, \qquad kr \gg n^2. \tag{2.65}$$

Starting from this asymptotic identity, the scattered field can be expanded as:

$$\begin{aligned}\mathbf{E}_s &= \sum_{n=1}^{\infty} E_n(ia_n\mathbf{n}_{e1n}^{(3)} - b_n\mathbf{M}_{o1n}^{(3)}),\\ \mathbf{H}_s &= \frac{k}{\omega\mu}\sum_{n=1}^{\infty} E_n(ib_n\mathbf{n}_{o1n}^{(3)} + a_n\mathbf{M}_{e1n}^{(3)}),\end{aligned} \tag{2.66}$$

where the superscript (3) denotes that the radial dependence of the generating functions is obtained by using Hankel functions.

To write the vector spherical harmonics components in the expansions of the internal and scattered field in a more concise form, it is convenient to define the angle-dependent functions π_n and τ_n:

$$\pi_n = \frac{P_n^1}{\sin\theta}, \qquad \tau_n = \frac{dP_n^1}{d\theta}. \tag{2.67}$$

These functions are even and odd functions of $\cos\theta$, respectively, and are obtained by upward recurrence from the following relations:

$$\begin{aligned}\pi_n &= \frac{2n-1}{n-1}\cos(\theta)\pi_{n-1} - \frac{n}{n-1}\pi_{n-2},\\ \tau_n &= n\cos(\theta)\pi_n - (n+1)\pi_{n-1},\end{aligned} \tag{2.68}$$

with $\pi_0 = 0$ and $\pi_1 = 1$. It can be shown that, despite not being mutually orthogonal nor orthogonal, the functions $\pi_n + \tau_n$ and $\pi_n - \tau_n$ are orthogonal. Therefore,

$$\int_0^{\pi}(\tau_n + \pi_n)(\tau_m + \pi_m)\sin\theta d\theta = \int_0^{\pi}(\tau_n - \pi_n)(\tau_m - \pi_m)\sin\theta d\theta \quad (m \neq n). \tag{2.69}$$

Starting from these considerations the internal (Eqs. 2.64) and scattered (Eqs. 2.66) fields can be now written as:

$$\begin{aligned}\mathbf{M}_{o1n} &= \cos\phi\pi_n(\cos\theta)z_n(\rho)\hat{\mathbf{e}}_\theta - \sin\phi\tau_n(\cos\theta)z_n(\rho)\hat{\mathbf{e}}_\phi,\\ \mathbf{M}_{e1n} &= -\sin\phi\pi_n(\cos\theta)z_n(\rho)\hat{\mathbf{e}}_\theta - \cos\phi\tau_n(\cos\theta)z_n(\rho)\hat{\mathbf{e}}_\phi,\\ \mathbf{N}_{o1n} &= \sin\phi n(n+1)\sin\theta\pi_n(\cos\theta)\frac{z_n(\rho)}{\rho}\hat{\mathbf{e}}_r\\ &+ \sin\phi\tau_n(\cos\theta)\frac{[\rho z_n(\rho)]'}{\rho}\hat{\mathbf{e}}_\theta + \cos\phi\pi_n(\cos\theta)\frac{(\rho z_n(\rho)]'}{\rho}\hat{\mathbf{e}}_\phi,\\ \mathbf{N}_{e1n} &= \cos\phi n(n+1)\sin\theta\pi_n(\cos\theta)\frac{z_n(\rho)}{\rho}\hat{\mathbf{e}}_r\\ &+ \cos\phi\tau_n(\cos\theta)\frac{[\rho z_n(\rho)]'}{\rho}\hat{\mathbf{e}}_\theta - \sin\phi\pi_n(\cos\theta)\frac{(\rho z_n(\rho)]'}{\rho}\hat{\mathbf{e}}_\phi.\end{aligned} \tag{2.70}$$

The vector spherical harmonics $\mathbf{M}_n$ and $\mathbf{N}_n$ in which the scattered fields are expressed as an infinite series represent the *normal modes* of the sphere. The total scattered field is always traceable to a superposition of normal modes weighted by the coefficients a_n and b_n. For sake of clarity, the diagrams of the electric field lines associated with the first four modes on a sphere, are reported in Figure 2.5 [13, 115]. For each n, two types of modes are observable: the *transverse magnetic modes*, also denoted as *electric type* modes or *E-waves*, in which the radial magnetic field component vanishes, and the *transverse electric modes*, also denoted as *magnetic type* mode or *H-waves*, in which the radial electric field component vanishes.

At this stage, it is possible to understand how absorption, scattering, and extinction of the sphere vary with its size and optical properties, and also with the optical properties of the surrounding medium. To do this, the explicit expression of the *scattering coefficients* a_n and b_n involved in Eq. 2.66 must be derived.

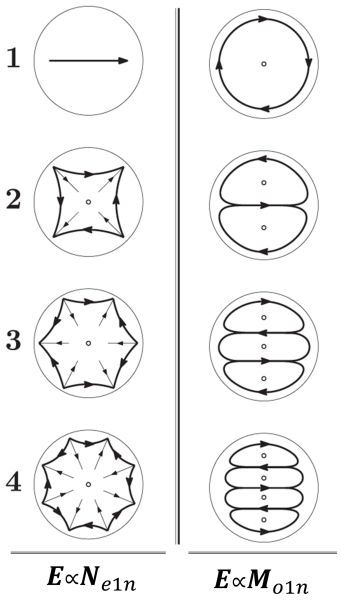

Figure 2.5: Stylized version of the electric field patterns associated with the first four ($n = 1, 2, 3, 4$) normal modes (TM, on the left, and TE, on the right) of a sphere. Adapted from Ref. [115].

For any given n, the boundary conditions (Eq. 2.63) in component form, lead to four independent equations, which can be used to find not only a_n and b_n, but also c_n and d_n involved in Eq. 2.64:

$$\begin{aligned} E_{i\theta} + E_{s\theta} &= E_{1\theta}, \qquad & E_{i\phi} + E_{s\phi} &= E_{1\phi}, \\ H_{i\theta} + H_{s\theta} &= H_{1\theta}, \qquad & H_{i\phi} + H_{s\phi} &= H_{1\phi} \end{aligned} \tag{2.71}$$

for all $r = a$. By applying the orthogonality of $\cos\phi$ and $\sin\phi$, the orthogonality between $\pi_n + \tau_n$ and $\pi_n - \tau_n$, the derived expansions of the incident, scattered, and internal fields (Eqs. 2.58, 2.66, and 2.64) and the boundary conditions, four linear equations are obtained:

$$\begin{aligned} j_n(mx)c_n = h_n^{(1)}(x)b_n = j_n(x), \\ \mu[mxj_n(mx)]'c_n + \mu_1[xh_n^{(1)}(x)]'b_n = \mu_1[xj_n(x)]', \\ \mu m j_n(mx)d_n + \mu_1 h_n^{(1)}(x)a_n = \mu_1 j_n(x), \\ [mxj_n(mx)]'d_n + m[xh_n^{(1)}(x)]'a_n = m[xj_n(x)]', \end{aligned} \tag{2.72}$$

where 'indicates the differentiation with respect to the argument indicated in the parentheses, while the parameter x and m are the *size parameter* and the *relative refractive index*, respectively, obtained as:

$$x = ka = \frac{2\pi N a}{\lambda}, \qquad m = \frac{k_1}{k} = \frac{N_1}{N}. \tag{2.73}$$

In this formulation, N_1 and N are the refractive indices of the sphere and surrounding medium, respectively. The solution to the four linear equations leads to the coefficients c_n and d_n within the sphere:

$$\begin{aligned} c_n &= \frac{\mu_1 j_n(x)[xh_n^{(1)}(x)]' - \mu_1 h_n^{(1)}(x)[xj_n(x)]'}{\mu_1 j_n(mx)[xh_n^{(1)}(x)]' - \mu h_n^{(1)}(x)[mxj_n(mx)]'}, \\ d_n &= \frac{\mu_1 m j_n(x)[xh_n^{(1)}(x)]' - \mu_1 m h_n^{(1)}(x)[xj_n(x)]'}{\mu m^2 j_n(mx)[xh_n^{(1)}(x)]' - \mu_1 h_n^{(1)}(x)[mxj_n(mx)]'}, \end{aligned} \tag{2.74}$$

and to the scattering coefficients a_n and b_n:

$$\begin{aligned} a_n &= \frac{\mu m^2 j_n(mx)[xj_n(x)]' - \mu_1 j_n(x)[mxj_n(mx)]'}{\mu m^2 j_n(mx)[xh_n^{(1)}(x)]' - \mu_1 h_n^{(1)}(x)[mxj_n(mx)]'}, \\ b_n &= \frac{\mu_1 j_n(mx)[xj_n(x)]' - \mu j_n(x)[mxj_n(mx)]'}{\mu_1 j_n(mx)[xh_n^{(1)}(x)]' - \mu h_n^{(1)}(x)[mxj_n(mx)]'}. \end{aligned} \tag{2.75}$$

The couples of coefficients (c_n, b_n) and (a_n, d_n) exhibit identical denominators. This means that, if the frequency, (or the radius) has a value for which one of the denominators is very small, its corresponding normal mode is dominant of the scattered field. For example, a_n mode dominates the scattered field when the following

condition is satisfied:

$$\frac{[xh_n^{(1)}(x)]'}{h_n^{(1)}} \simeq \frac{\mu_1[mxj_n(mx)]'}{\mu m^2 j_n(mx)}, \tag{2.76}$$

while b_n mode dominates if:

$$\frac{[xh_n^{(1)}(x)]'}{h_n^{(1)}} \simeq \frac{\mu[mxj_n(mx)]'}{\mu_1 j_n(mx)}. \tag{2.77}$$

The exact satisfaction of the conditions expressed in Eqs. 2.76 and 2.77 require that the frequencies are *complex* and the corresponding modes are *virtual*; such frequencies are denoted as *natural* frequencies of the sphere [116]. By assuming the same permeability for the particle and its surrounding medium and introducing the following *Riccati-Bessel* functions,

$$\psi_n(\rho) = \rho j_n(\rho), \qquad \xi_n(\rho)h_n^{(1)}(\rho),$$

it is possible to simplify the scattering coefficients in Eq. 2.75 as:

$$a_n = \frac{m\psi_n(mx)\psi_n'(x) - \psi_n(x)\psi_n'(mx)}{m\psi_n(mx)\xi_n'(x) - \xi_n(x)\psi_n'(mx)}, \tag{2.78}$$

$$b_n = \frac{\psi_n(mx)\psi_n'(x) - m\psi_n(x)\psi_n'(mx)}{\psi_n(mx)\xi_n'(x) - m\xi_n(x)\psi_n'(mx)}. \tag{2.79}$$

Of course, when $m = 1$, meaning that the spherical particle is *transparent* compared to its surrounding medium (*i.e.*, same refractive index), the scattering coefficients a_n and b_n vanish identically (no scattering occurs).

Due to the particle spherical symmetry, all the expressions derived for an x-polarized wave can be generalized to any polarization state. This means that, once the scattering coefficients are known, all the relative measurable quantities (*e.g.*, cross sections, and scattering matrix elements) can be derived. The cross sections of a sphere of radius a can be obtained starting from the expressions reported in Section 2.1.3. Starting from the optical theorem, for which

$$W_a = W_{ext} - W_s,$$

and considering the surface of an arbitrary concentric sphere of radius $r \geq a$, the expression of the net rate of the extinct and scattered electromagnetic energy can be

written as

$$W_{ext} = \frac{1}{2}\Re e\Big\{ \int_0^{2\pi} \int_0^{\pi} (E_{i\phi}H^*_{s\phi} - E_{s\theta}H^*_{s\phi} - E_{s\theta}H^*_{i\phi} + E_{s\phi}H^*_{i\theta}) r^2 \sin\theta d\theta d\phi \Big\},$$
$$W_s = \frac{1}{2}\Re e\Big\{ \int_0^{2\pi} \int_0^{\pi} (E_{s\theta}H^*_{s\phi} - E_{s\phi}H^*_{s\theta}) r^2 \sin\theta d\theta d\phi \Big\}. \tag{2.80}$$

These two quantities are independent of the polarization state, so if an x-polarized incident wave is assumed, the electric and magnetic incident wave components in the first integral can be expressed as:

$$E_{i\theta} = \frac{\cos\phi}{\rho} \sum_{n=1}^{\infty} E_n(\psi_n \pi_n - i\psi'_n \tau_n), \qquad H_{i\theta} = \frac{k}{\omega\mu} \tan\phi E_{i\theta},$$
$$E_{i\phi} = \frac{\sin\phi}{\rho} \sum_{n=1}^{\infty} E_n(i\psi'_n \pi_n - \psi_n \tau_n), \qquad H_{i\phi} = \frac{-k}{\omega\mu} \cot\phi E_{i\phi}.$$

Then, the corresponding scattering field components are:

$$E_{s\theta} = \frac{\cos\phi}{\rho} \sum_{n=1}^{\infty} E_n(i a_n \xi'_n \tau_n - b_n \xi_n \pi_n),$$
$$E_{s\phi} = \frac{\sin\phi}{\rho} \sum_{n=1}^{\infty} E_n(b_n \xi_n \tau_n - a_n \xi'_n \pi_n),$$
$$H_{s\theta} = \frac{k}{\omega\mu}\frac{\sin\phi}{\rho} \sum_{n=1}^{\infty} E_n(i b_n \xi'_n \tau_n - a_n \xi_n \pi_n), \tag{2.81}$$
$$H_{s\phi} = \frac{k}{\omega\mu}\frac{\cos\phi}{\rho} \sum_{n=1}^{\infty} E_n(i b_n \xi'_n \pi_n - a_n \xi_n \tau_n).$$

By substituting the scattered field components and integrating the second of Eqs. 2.80:

$$W_s = \frac{\pi |E_0|^2}{k\omega\mu} \sum_{n=1}^{\infty} (2n+1) \Re e\{g_n\} (|a_n|^2 + |b_n|^2), \tag{2.82}$$

where $g_n = -i\xi^*_n \xi'_n$. Given the Riccati-Bessel function $\chi_n = -\rho y_n(\rho)$, and $\xi_n = \psi_n - i\chi_n$, g_n can be written as:

$$g_n = (\chi^*_n \psi'_n - \psi^*_n \chi'_n) - i(\psi^*_n \psi'_n - \chi^*_n \chi'_n).$$

ψ_n and χ_n are real functions for real argument and by considering the Wronskian relation

$$\chi_n \psi'_n - \psi_n \chi'_n = 1, \tag{2.83}$$

the scattering cross section is finally derived as:

$$C_{sca} = \frac{W_s}{I_i} = \frac{2\pi}{k^2} \sum_{n=1}^{\infty} (2n+1)(|a_n|^2 + |b_n|^2). \tag{2.84}$$

Analogously, the extinction cross-section is finally derivable:

$$C_{ext} = \frac{W_{ext}}{I_i} = \frac{2\pi}{k^2} \sum_{n=1}^{\infty} (2n+1)\Re e\{a_n + b_n\}, \tag{2.85}$$

2.2 Quasistatic approximations

There are two main mechanisms for which, in the linear regime, a homogeneous and nonmagnetic object, small compared to the incident wavelength in a vacuum, may resonate:

- when the particle's dielectric permittivity is negative, *e.g.* metals near their plasma frequency, the resonance arises from the interplay between the kinetic energy of the free electrons and the energy stored in the electric field;
- when the particle's dielectric permittivity is high and positive, the resonance arises from the interplay between the polarization energy stored in the particle and the energy stored in the magnetic field.

The first type of resonances, also known as *plasmonic* resonances, is generally very well described by the electro-quasistatic approximation of the Maxwell equations [117, 118], while the second one is very well described by the magneto-quasistatic approximations of the Maxwell equations [39]. In this regime of the Maxwell equations, it is possible to define a radiation quality factor Q that represents the link between the stored energy and the energy radiated in the surrounding medium. When the modes are non-interacting and intense enough, Q is nothing but the inverse of the fractional bandwidth.

In this section, the electro-quasistatic and magneto-quasistatic modes and resonances of linear, nonmagnetic, homogeneous, and isotropic objects are introduced using the integral formulation of the Maxwell equations. These approximations are the ones behind the modeling of capacitors and inductors and are completed with radiation corrections by means of a perturbation approach, starting from the size parameter of the object defined as:

$$x = \frac{k_0}{\ell_c}$$

where k_0 is the wave number and ℓ_c is the characteristic length of the object. From the proposed formulation, it is possible to derive analytical expressions of the relative resonance shift and quality factor as a function of their radiative corrections [43].

2.2.1 Induced current density field in 3D objects

First, a linear material occupying a domain Ω, bounded by a closed surface $\partial\Omega$ with normal $\hat{\mathbf{n}}$, is assumed nonmagnetic, isotropic, homogeneous, nondispersive in space, time-dispersive, with relative dielectric permittivity ε_R, and surrounded by vacuum. A time-harmonic electromagnetic wave ($\Re e\{E_i(\mathbf{r})e^{-i\omega t}\}$) illuminates the object (Figure 2.6).

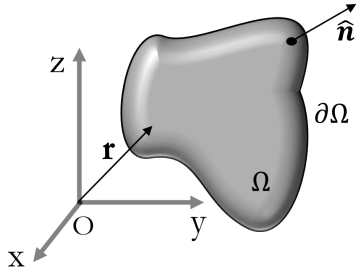

Figure 2.6: A three-dimensional domain Ω, with normal $\hat{\mathbf{n}}$.

Herein, the problem of scattering is faced by considering as unknown the current density field $\mathbf{J}(\mathbf{r})$ induced in the object. The current density field can be particularized into:

- conduction current, in metals at frequencies below interband transitions;
- polarization current, in dielectrics at both microwaves and optical frequencies;
- sum of conduction and polarization currents, in metals at frequencies in which interband transitions occur.

Therefore, $\mathbf{J}(\mathbf{r}) = -i\omega\varepsilon_0\chi\mathbf{E}(\mathbf{r})$, where $\mathbf{E}$ is the sum of the induced and incident electric field, ε_0 is the vacuum permittivity, and $\chi = (\varepsilon_R - 1)$ is the electric susceptibility. Both the vector fields $\mathbf{J}$ and $\mathbf{E}$ exhibit zero-divergence in Ω, since the considered object is homogeneous and isotropic. The current density $\mathbf{J}$ is governed by the full-wave volume integral equation [119, 120, 121]:

$$\frac{\mathbf{J}(\mathbf{r})}{\chi} + \nabla \oint_{\partial\Omega} \mathbf{J}(\mathbf{r}') \cdot \hat{\mathbf{n}}' G(\mathbf{r}-\mathbf{r}')dS' - k_0^2 \int_{\Omega} \mathbf{J}(\mathbf{r}')G(\mathbf{r}-\mathbf{r}')dV' = -i\omega\varepsilon_0 E_i(\mathbf{r}), \quad \forall \mathbf{r} \in \Omega, \tag{2.86}$$

with $k_0 = \omega/c_0$, c_0 the speed of light in vacuum, and $G(\mathbf{r}-\mathbf{r}') = e^{ik_0|\mathbf{r}-\mathbf{r}'|}/4\pi|\mathbf{r}-\mathbf{r}'|$ the Green function in vacuum.

In Equation 2.86, the surface integral brings the contribution of the scalar potential to the induced electric field, while the volume integral the contribution of the vector potential [119]. As stated above, it is possible to define the dimensionless size parameter x as:

$$x = \frac{\omega}{c_0}\ell_c, \tag{2.87}$$

where ℓ_c is the characteristic length of the region Ω. For example, a characteristic dimension of an arbitrarily shaped object could be the smallest radius of a sphere containing the object.

By normalizing the spatial coordinates by ℓ_c ($\tilde{\mathbf{r}} = \mathbf{r}/\ell_c$), it is now possible to rewrite Equation 2.86 as:

$$\frac{\mathbf{J}(\tilde{\mathbf{r}})}{\chi} - \mathcal{L}\left\{\mathbf{J}\right\}(\tilde{\mathbf{r}}) = -i\omega\varepsilon_0\,\mathbf{E}_i(\tilde{\mathbf{r}}), \quad \forall\tilde{\mathbf{r}} \in \tilde{\Omega}, \tag{2.88}$$

with

$$\mathcal{L}\left\{\mathbf{W}\right\}(\tilde{\mathbf{r}}) = -\tilde{\nabla}\oint_{\partial\tilde{\Omega}} \mathbf{W}(\tilde{\mathbf{r}}')\cdot\hat{\mathbf{n}}' g(\Delta r, x)dS' + x^2\int_{\tilde{\Omega}} \mathbf{W}(\tilde{\mathbf{r}}')g(\Delta r, x)dV'. \tag{2.89}$$

In Equations 2.88 and 2.89, $\tilde{\Omega}$ now denotes the scaled domain, $\tilde{\nabla}$ the scaled gradient operator, and $g(\Delta r, x)$ the dimensionless scalar Green's function in vacuum defined as:

$$g(\Delta r, x) = \frac{e^{ix\Delta r}}{4\pi\Delta r}, \tag{2.90}$$

with $\Delta r = |\tilde{\mathbf{r}} - \tilde{\mathbf{r}}'|$.

The solution of Equation 2.88 can be now derived in the quasistatic limit, meaning that the dimensionless size parameter $x \to 0$. A complete representation of the unknown $\mathbf{J}(\tilde{\mathbf{r}})$ is obtained from the union of two orthogonal sets [39]. The first set $\{\mathbf{j}_h^{||}\}$ is obtained by solving the following eigenvalue problem

$$\mathcal{L}_e\left\{\mathbf{j}_h^{||}\right\}(\tilde{\mathbf{r}}) = \frac{1}{\chi_h^{||}}\mathbf{j}_h^{||}(\tilde{\mathbf{r}}), \quad \forall\tilde{\mathbf{r}} \in \tilde{\Omega}, \tag{2.91}$$

with $\mathcal{L}_e$ being the *electrostatic integral operator*, which provides the electrostatic field as a function of the surface charge density [118]:

$$\mathcal{L}_e\{\mathbf{W}\}(\tilde{\mathbf{r}}) = -\nabla\oint_{\partial\Omega} \mathbf{W}(\tilde{\mathbf{r}}')\cdot\hat{\mathbf{n}}' g_0(\Delta r)dS', \tag{2.92}$$

where $g_0(\Delta r)$ is the dimensionless Green function in vacuum, defined as:

$$g_0(\Delta r) = \frac{1}{4\pi\Delta r} \tag{2.93}$$

It can be shown that the spectrum of $\mathcal{L}_e$ is countable infinite [118] and that the eigenfunctions $\{\mathbf{j}_h^{||}\}_{h\in\mathbb{N}}$ are *longitudinal* vector fields, namely they are both div-free and curl-free in $\tilde{\Omega}$, but have a nonzero normal component to $\partial\tilde{\Omega}$ [117]. Moreover, since $\mathcal{L}_e$ is definite negative and self-adjoint, the eigenvalues $\chi_h^{||}$ are real and negative, and the corresponding eigenfunctions are orthogonal according to the following scalar product

$$\langle \mathbf{A}, \mathbf{B} \rangle = \int_\Omega \mathbf{A} \cdot \mathbf{B} dV. \tag{2.94}$$

Then, by assuming this set to be orthonormal, the following relation is obtained:

$$\langle \mathbf{j}_h^{||}, \mathbf{j}_k^{||} \rangle_{\tilde{\Omega}} = \delta_{h,k}. \tag{2.95}$$

The second set of is given by the *transverse* vector fields $\{\mathbf{j}_h^{\perp}\}$, which are divergence-free in $\tilde{\Omega}$ and have null normal components to $\partial\tilde{\Omega}$

$$j_h^{\perp} \cdot \hat{\mathbf{n}}|_{\partial\tilde{\Omega}} = 0. \tag{2.96}$$

These fields are solutions to the following eigenvalue problem in the weak form:

$$\mathcal{L}_m\{\mathbf{j}_h^{\perp}\}(\tilde{\mathbf{r}}) = \frac{1}{k_h^{\perp}}(\tilde{\mathbf{r}})\mathbf{j}_h^{\perp}(\tilde{\mathbf{r}}), \quad \forall\tilde{\mathbf{r}} \in \tilde{\Omega}. \tag{2.97}$$

In this case, $\mathcal{L}_m$ denotes the *magnetostatic integral operator* and is defined as

$$\mathcal{L}_m\{\mathbf{W}\}(\tilde{\mathbf{r}}) = \int_{\tilde{\Omega}} \mathbf{W}(\tilde{\mathbf{r}}')g_0(\Delta r)dV'. \tag{2.98}$$

Moreover, as $\mathcal{L}_e$, $\mathcal{L}_m$ has a countable infinite spectrum and is self-adjoint, but differently from $\mathcal{L}_e$, it is definite positive. Therefore, the eigenvalues $\{k_h^{\perp}\}_{h\in\mathbb{N}}$ are real and positive, and the eigenfunctions $\{\mathbf{j}_h^{\perp}\}_{h\in\mathbb{N}}$ are orthogonal, according to the scalar product reported in Equation 2.94, and assumed orthonormal, according to the following expression:

$$\langle \mathbf{j}_h^{\perp}, \mathbf{j}_k^{\perp} \rangle_{\tilde{\Omega}} = \delta_{h,k}. \tag{2.99}$$

By definition, the two sets of eigenfunctions $\{\mathbf{j}_h^{\perp}\}$ and $\{\mathbf{j}_h^{||}\}$ are orthogonal. and are material and size independent. They only depend on the shape of the object. From the union of the two sets of eigenfunctions, the current density $\mathbf{J}$ in the quasistatic

regime ($x \to 0$) can be finally expressed as

$$\mathbf{J}(\tilde{\mathbf{r}}) = -i\omega\varepsilon_0\chi \sum_{h=1}^{\infty} \left[\frac{\chi_h^{||}}{\chi_h^{||} - \chi} \langle \mathbf{j}_h^{||}, \mathbf{E}_i \rangle_{\tilde{\Omega}} \mathbf{j}_h^{||}(\tilde{\mathbf{r}}) + \frac{k_h^{\perp}}{k_h^{\perp} - x^2\chi} \langle \mathbf{j}_h^{\perp}, \mathbf{E}_i \rangle_{\tilde{\Omega}} \mathbf{j}_h^{\perp}(\tilde{\mathbf{r}}) \right]. \tag{2.100}$$

In this expansion, the dependence on the material is removed by introducing polynomial functions of χ, while the dependence on the geometry is hidden in the material-independent eigenvalue-eigenfunction systems [122]. The expression of the current density $\mathbf{J}$ in Equation 2.100, brings to light two distinct resonance conditions for the polynomial function of χ. The two conditions arise from the two different resonance mechanisms highlighted previously in this section. The first condition is:

$$\Re e\{\chi\} = \chi_h^{||}, \tag{2.101}$$

obtained by putting in resonance the eigenfunctions $\mathbf{j}_h^{||}$; the second one is

$$\Re e\{\chi\} = \frac{k_h^{\perp}}{x^2}, \tag{2.102}$$

where the eigenfunctions $\mathbf{j}_h^{\perp}$ are put in resonance.
Therefore, the eigenfunctions sets $\{\mathbf{j}_h^{||}\}$ and $\{\mathbf{j}_h^{\perp}\}$ represent the *density current modes* of the small object in the quasistatic regime, while $\{\chi_h^{||}\}$ and $\{\chi_h^{\perp}/x^2\}$ the corresponding *eigen-susceptibilities*. Finally, the scalar products in Equation 2.100, $\langle \mathbf{j}_h^{||}, \mathbf{E}_i \rangle_{\tilde{\Omega}}$ and $\langle \mathbf{j}_h^{\perp}, \mathbf{E}_i \rangle_{\tilde{\Omega}}$, provide the description of the coupling of the modes with the incident field.

2.2.2 Electro-quasistatic modes and resonances

The detailed investigation of the electro-quasistatic resonances associated with the eigenfunctions $\mathbf{j}_h^{||}$ and the eigenvalues $\chi_h^{||}$ within the electrostatic integral operator $\mathcal{L}_e$ in Equation 2.91 is herein provided. As stated in previous subsection, $\mathbf{j}_h^{||}$ are the electro-quasistatic (EQS) current modes, while $\chi_h^{||}$ are the electro-quasistatic susceptibilities. The EQS current modes represent longitudinal vector fields that are square integrable in $\tilde{\Omega}$, namely $\mathbf{j}_h^{||} \in \mathbf{L}^2(\tilde{\Omega})$. Moreover, they are both divergence- and curl-free within $\tilde{\Omega}$, while they have nonzero normal component to $\partial\tilde{\Omega}$,

$$\mathbf{L}_{||}^2(\tilde{\Omega}) = \left\{ \mathbf{L}^2(\tilde{\Omega}) \,|\, \tilde{\nabla} \cdot \mathbf{j}^{||} = 0, \tilde{\nabla} \times \mathbf{j}^{||} = \mathbf{0} \text{ in } \tilde{\Omega} \setminus \partial\tilde{\Omega} \right\}. \tag{2.103}$$

The normal component of $\mathbf{j}_h^{||}$ to the object boundary $\partial\tilde{\Omega}$ depends on the induced surface charge density on $\partial\tilde{\Omega}$, and must satisfy the *charge-neutrality* condition, ex-

pressed as

$$\oint_{\partial\tilde{\Omega}} \mathbf{j}_h^{||} \cdot \hat{\mathbf{n}} dS = 0. \tag{2.104}$$

A useful property of the spectrum of $\mathcal{L}_e$, which does not depend on the shape of the object, must be recalled: its eigenvalues $\chi_h^{||}$ have a finite limit in their unique accumulation point ($h \to \infty$) [117], namely

$$\lim_{h\to+\infty} \chi_h^{||} = -2, \tag{2.105}$$

This means that, for a time-dispersive metal, well-described by the Drude model [64] as follows:

$$\chi = -\frac{\omega_p^2}{\omega(\omega + i\nu)}, \tag{2.106}$$

the resonance frequencies corresponding to the eigen-susceptibilities $\chi_h^{||}$ accumulate at $\omega_p/\sqrt{2}$, where ω_p and $\nu \ll \omega_p$ are the plasma and collision angular frequencies of the metal, respectively.

Recalling Equation 2.95, which is nothing but the norm induced by the scalar product in Eq.2.94, $||\mathbf{j}_h^{||}|| = 1$, the scaled electrostatic energy of the h-th EQS current mode $\mathbf{j}_h^{||}$ can be expressed as

$$\mathcal{W}_e\left\{\mathbf{j}_h^{||}\right\} = -\frac{1}{2\varepsilon_0}\oint_{\partial\tilde{\Omega}}\oint_{\partial\tilde{\Omega}} g_0(\Delta r)\sigma_h(\tilde{\mathbf{r}})\sigma_h(\tilde{\mathbf{r}}')dS'dS = \frac{1}{2\varepsilon_0}\frac{1}{\left(-\chi_h^{||}\right)}, \tag{2.107}$$

where $\sigma_h = \mathbf{j}_h^{||} \cdot \hat{\mathbf{n}}$ is the surface charge density of the h-th EQS current mode. From the scaled electrostatic energy $\mathcal{W}_e$, the electrostatic energy W_e can be obtained by the simple following expression:

$$W_e\left\{\mathbf{j}_h^{||}\right\} = \frac{\ell_c^3}{\omega^2}\mathcal{W}_e\left\{\mathbf{j}_h^{||}\right\}$$

It is possible to define the electric dipole moment $\mathbf{P}_h$ of the EQS current mode $\mathbf{j}_h^{||}$ as

$$\mathbf{P}_h = \int_{\tilde{\Omega}} \mathbf{j}_h^{||} dV = \oint_{\partial\tilde{\Omega}} \mathbf{r}\left(\mathbf{j}_h^{||} \cdot \hat{\mathbf{n}}\right) dS. \tag{2.108}$$

If the electric dipole moment $\mathbf{P}_h$ vanishes, the associated mode $\mathbf{j}_h^{||}$ is a *dark* mode, otherwise, it is denoted as *bright* mode. When the density current mode exhibited by the object is spatially uniform in the particle scaled domain $\tilde{\Omega}$, and directed along a direction $\mathbf{c}$, the orthogonality condition in Equation 2.95 suggests that all the

remaining current modes have no electric dipole moment along that specific direction:

$$\int_{\tilde{\Omega}} \mathbf{c} \cdot \mathbf{j}_h^{||} dV = \mathbf{c} \cdot \mathbf{P}_k = 0. \tag{2.109}$$

This is what happens for a sphere or a spheroid. As mentioned above, the EQS operator $\mathcal{L}_e$ is definite negative and its eigen-susceptibilities are negative. This means that, due to the resonance condition in Equation 2.101, the corresponding current modes $\{\mathbf{j}_h^{||}\}$ are resonantly excited only when the object has negative dielectric permittivity.

For example, in metal nanoparticles at frequencies near their plasma frequency, the current modes correspond to the resonant plasmon modes and derive from the interplay between the kinetic energy of the free electrons and the energy stored in the electric field [118].

2.2.3 Magneto-quasistatic modes and resonances

The detailed investigation of the magneto-quasistatic resonances associated with the eigenfunctions $\mathbf{j}_h^{\perp}$ and the eigenvalues $k_h^{\perp}$ within the magnetostatic integral operator $\mathcal{L}_m$ in Equation 2.97 is herein provided.

First, a brief demonstration to prove that the eigenfunctions $\mathbf{j}_k^{\perp}$ are source-free solutions of the Maxwell equations in small dielectric objects ($x \ll 1$) with high-permittivity ($\varepsilon_R \gg 1$).

Under these conditions, the electromagnetic field can be determined, in first approximation, by the displacement current density field $\mathbf{J}$ within the object [123]. Thus, we seek the values of the parameter $\beta = (x/\ell_c)^2\chi$ for which a nontrivial solution of the source-free magneto-quasistatic (MQS) problem can be found [124]:

$$\nabla \times \mathbf{A} = \mu_0 \mathbf{H}, \tag{2.110a}$$

$$\nabla \times \mathbf{H} = \mathbf{J}, \tag{2.110b}$$

with the following constitutive relation

$$\mathbf{J} = \frac{\beta}{\mu_0} \mathbf{A}\Pi_\Omega, \tag{2.111}$$

where $\chi = (\varepsilon_R - 1)$ is the electric susceptibility, Π_Ω is the characteristic function on the set Ω, *i.e.*, $\Pi_\Omega = 1$ for $\mathbf{r} \in \Omega$ and 0 otherwise, and μ_0 is the magnetic permeability in vacuum.

The MQS vector potential $\mathbf{A}$ satisfies the Coulomb gauge ($\nabla \cdot \mathbf{A} = 0$) in Ω and $\mathcal{R}^3 \setminus \Omega$, and both $\mathbf{A}$ and the magnetic field $\mathbf{H}$ are regular at infinity. Equation 2.111

does not take into account the effects of the displacement current density field in a vacuum. Since the normal component of the current density field $\mathbf{J}$ at the boundary is equal to zero, the current density field $\mathbf{J}$ is div-free everywhere in $\mathcal{R}^3$; on the contrary, the normal component of the vector potential at $\partial\Omega$ may be discontinuous. Since $\mathbf{J}$ has a vanishing normal component on $\partial\Omega$, also the normal component of the polarization current density field must be zero. For the sake of simplicity, also here a scaling of the spatial coordinates by the characteristic length ℓ_c ($\tilde{\mathbf{r}} \to \mathbf{r}/\ell_c$) is performed, and the problems in Equations 2.110 and 2.111 can be solved by expressing the vector potential $\mathbf{A}$ as a function of the current density $\mathbf{J}$ as follows

$$\mathbf{A}(\tilde{\mathbf{r}}) = \mu_0 \ell_c^2 \mathcal{L}_m \{\mathbf{J}\}(\tilde{\mathbf{r}}). \tag{2.112}$$

$\mathcal{L}_m$ is the MQS integral operator reported in Equation 2.98, where the Green function g_0 arises from the neglected displacement current density in the vacuum. Finally, the linear eigenvalue problem is obtained from the combination of Equations 2.111 and 2.112,

$$\mathcal{L}_m \{\ \mathbf{J}\}(\tilde{\mathbf{r}}) = \frac{1}{k^\perp}\ \mathbf{J}(\tilde{\mathbf{r}}), \quad \forall \tilde{\mathbf{r}} \in \tilde{\Omega}, \tag{2.113}$$

where

$$\mathbf{J} \cdot \hat{\mathbf{n}}|_{\partial\tilde{\Omega}} = 0, \tag{2.114}$$

and $k^\perp = x^2\chi$. Therefore, the eigenvalue problem in Equation (2.97) with the constraint in Equation (2.96) is derived.

After this brief demonstration, the eigenfunctions $\mathbf{j}_h^\perp$ can now be denoted as *MQS current modes*, and the eigenvalues $k_h^\perp/x^2$ as the MQS eigen-susceptibilities. At this stage, it is possible to remind also that Equation (2.113) holds in the weak form in the functional space. This space is equipped with the inner product 2.94 and constituted by the *transverse* vector fields, these being square-integrable and div-free in $\tilde{\Omega}$ with vanishing normal component to $\partial\tilde{\Omega}$ [39]. Therefore,

$$\mathbf{L}^2_\perp(\tilde{\Omega}) = \left\{\mathbf{L}^2(\tilde{\Omega}) \,|\, \tilde{\nabla} \cdot \mathbf{j}^\perp = 0,\ \text{in } \tilde{\Omega} \setminus \partial\tilde{\Omega} \text{ and } \mathbf{j}^\perp \cdot \hat{\mathbf{n}} = \mathbf{0} \text{ on } \partial\tilde{\Omega}\right\}. \tag{2.115}$$

The integral operator $\mathcal{L}_m$ is compact, positive definite, and self-adjoint. Therefore, Equation 2.97 admits a countable set of eigenvalues $\left\{k_h^\perp\right\}_{h\in\mathbb{N}}$ real and positive, which, differently from the EQS eigenvalues $\chi_h^{||}$, accumulate at infinity:

$$\lim_{h\to+\infty} k_h^\perp = +\infty, \tag{2.116}$$

independently from the shape of the object. The integral operator $\mathcal{L}_m$, and its eigen-

values, depend on the chosen spatial coordinates normalization. Specifically, the eigenvalues $k_h^{\perp}$ show a quadratic proportionality with the characteristic size of the object ℓ_c. Differently from the EQS modes, all the MQS current modes $\mathbf{j}_h^{\perp}$ are *dark* modes, since they exhibit zero electric dipole moment (by definition in Equation 2.108). Assuming the current modes to be unit vectors ($||\mathbf{j}_h^{\perp}|| = 1$), the scaled magnetostatic energy of the h-th MQS current mode can be expressed as:

$$\mathcal{W}_m\{\mathbf{j}_h^{\perp}\} = \frac{1}{2}\int_{\tilde{\Omega}} \mathbf{j}_h^{\perp} \cdot \mathbf{A}\{\mathbf{j}_h^{\perp}\} dV = \frac{\mu_0}{8\pi}\int_{\tilde{\Omega}} \mathbf{j}_h^{\perp}(\tilde{\mathbf{r}}) \cdot \int_{\tilde{\Omega}} \frac{\mathbf{j}_h^{\perp}(\tilde{\mathbf{r}'})}{\Delta r} dV' dV = \frac{\mu_0}{2}\frac{1}{k_h^{\perp}}. \tag{2.117}$$

From the scaled magnetostatic energy $\mathcal{W}_m$, the non-scaled magnetostatic energy W_m is obtained by the simple relation:

$$W_m = (\ell_c)^5 \, \mathcal{W}_m \tag{2.118}$$

The magnetic dipole moment $\mathbf{M}_h$ of the h-th MQS current mode $\mathbf{j}_h^{\perp}$ is:

$$\mathbf{M}_h = \frac{1}{2}\int_{\tilde{\Omega}} \tilde{\mathbf{r}} \times \mathbf{j}_h^{\perp} dV. \tag{2.119}$$

If the dielectric supports a mode for which $\mathbf{j}_h^{\perp} = \hat{\tilde{\mathbf{r}}} \times \mathbf{c}$, where $\mathbf{c}$ is a constant vector, due to the orthogonality condition (2.99) all the remaining current modes $\mathbf{j}_k^{\perp}$ have a vanishing magnetic dipole moment along $\mathbf{c}$, *i.e.*,

$$\frac{1}{2}\int_{\tilde{\Omega}} \mathbf{j}_k^{\perp} \cdot (\tilde{\mathbf{r}} \times \mathbf{c}) dV = \mathbf{c} \cdot \mathbf{M}_k = 0. \tag{2.120}$$

Among the set of MQS current modes, there exists a subset of modes, which generate a transverse vector potential $\mathbf{A}\{\mathbf{j}_h^{\perp}\}$ with no normal component to $\partial\tilde{\Omega}$:

$$\hat{\mathbf{n}} \cdot \mathbf{A}\{\mathbf{j}_h^{\perp}\}\Big|_{\partial\tilde{\Omega}} = 0. \tag{2.121}$$

A MQS mode belonging to this subset is a particular mode denoted as $\mathcal{A}^{\perp}$-mode. The $\mathcal{A}^{\perp}$-modes are solutions to the problem in Equation (2.113) also in a strong form (in the space of square-integrable vector fields). The resonance angular frequencies ω_h are expressed as

$$\omega_h = \frac{c_0}{\ell_c}\sqrt{\frac{k_h^{\perp}}{\chi}}. \tag{2.122}$$

and they accumulate at infinity. Moreover, given the radius of a sphere a, the follow-

ing bound on the eigenvalues holds:

$$k_h^{\perp} \geq \frac{\sqrt{3}}{4\pi}\frac{1}{a^2}, \qquad \forall h \in \mathbb{N}, \tag{2.123}$$

Equation (2.123) is obtained by multiplying both members of Equation (2.113) by normalized $\mathbf{j}_h^{\perp}$ (according to Equation (2.99)), then by integrating over Ω and using the Cauchy-Schwartz inequality and the inequality in Ref.[125]:

$$\int_{\tilde{\Omega}} \frac{1}{|\mathbf{r}-\mathbf{r}'|^2} dV' \leq \int_{B_a} \frac{1}{|\mathbf{r}'|^2} dV' = 4\pi a, \qquad \forall \mathbf{r} \in \Omega. \tag{2.124}$$

where B_a has the same volume of Ω. Therefore, given Equation (2.123) and the resonance condition in Equation (2.102), the MQS current modes $\{\mathbf{j}_h^{\perp}\}$ can be put in resonance in electrically small objects ($x \ll 1$) only with highly positive dielectric permittivities ($\varepsilon_R \gg 1$).

The MQS resonances in dielectrics arise from the energy oscillations between the polarization energy of the dielectric and the magnetic energy. It is possible to demonstrate this resonance condition by combining Equations (2.117) and (2.122),

$$\frac{(\ell_c)^3}{\omega_h^2}\mathcal{W}_m\{\mathbf{j}_h^{\perp}\} = \frac{(\ell_c)^3}{2\varepsilon_0}\frac{\|\mathbf{j}_h^{\perp}\|_{\tilde{\Omega}}^2}{\omega_h^2\,\chi}. \tag{2.125}$$

On the left, the energy stored in the magnetic field associated with the current mode $\mathbf{j}_h^{\perp}$, on the right, the energy stored in the dielectric in the form of polarization energy, at the resonance frequency ω_h, are reported, respectively.

2.3 Case Studies

In this section, two case studies are considered: plasmonic spheres and dielectric thin wires.

On the one hand, nanospheres (or nanoparticles) made of a Drude metal (*e.g.*, gold or silver) are the simplest and most studied plasmonic nanoresonators whose fundamental mode is the electric dipole. A proper assembly of plasmonic nanospheres (array) could lead to predictable optical responses for the design of optical devices.

On the other hand, high permittivity thin wires could represent the dual elementary geometry for the design of complex dielectric networks with repeating resonances in different regions of the spectrum.

2.3.1 Plasmonic Spheres

As a first case study, the plasmonic resonances of an electrically small sphere of radius R are considered. The object characteristic length ℓ_c is chosen equal to the radius R, and, as a consequence, the size parameter x becomes

$$x = \frac{\omega}{c_0} R.$$

The formulas of the radiative corrections here presented are extrapolated by perturbing the denominators of the Mie coefficients in Equations 2.75 in the neighborhood of their EQS resonances, or they can be directly obtained from the Padè expansion of the Mie coefficients found in Refs. [126, 127].

In particular, the EQS eigenvalues of a sphere and their relative radiative corrections are:

$$\chi_n^{\parallel} = -\frac{2n+1}{n}, \tag{2.126a}$$

$$\chi_n^{(2)} = -\frac{2}{n^2} \frac{(n+1)(2n+1)}{(3+2n)(2n-1)}, \tag{2.126b}$$

$$\chi_n^{(2n+1)} = -i \frac{(n+1)}{[n(2n-1)!]^2}, \tag{2.126c}$$

where $n \in \mathbb{N}$, and $(2n-1)! = 1 \times 3 \times 5 \times \cdots \times (2n-1)$. The index n is the mode multipolar order: the modes with $n = 1$ are dipolar, $n = 2$ quadrupolar, and so on.

Each eigenvalue $\chi_n^{\parallel}$ is associated with a set of $2n+1$ degenerate current modes $\mathbf{j}_{pmn}^{\parallel}$ with $m = 0, 1, 2, \ldots, n$. By recalling the polar spherical coordinates $\mathbf{r} = (r, \theta, \phi)$ (see also Fig.2.3) and normalizing them by the characteristic length $\ell_c = R$ (*i.e.*, $\tilde{\mathbf{r}} \to \mathbf{r}/R$) and hence $r \in [0, 1]$, the analytical expression of the EQS modes of a sphere are:

$$\mathbf{j}_{\substack{e \\ o}mn}^{\parallel}(r, \theta, \phi) = \frac{1}{\sqrt{\alpha_{mn}}} \left[\begin{pmatrix} \cos m\phi \\ \sin m\phi \end{pmatrix} n P_n^m(\cos\vartheta)\, \hat{\boldsymbol{r}} + \begin{pmatrix} \cos m\phi \\ \sin m\phi \end{pmatrix} \frac{dP_n^m(\cos\vartheta)}{d\vartheta} \hat{\boldsymbol{\vartheta}} + \begin{pmatrix} -\sin m\phi \\ +\cos m\phi \end{pmatrix} m \frac{P_n^m(\cos\vartheta)}{\sin\vartheta} \hat{\boldsymbol{\phi}} \right] r^{n-1}, \tag{2.127}$$

where the subscript p can be e for even modes and o for odd modes according to the azimuthal variable. P_n^m are instead the Legendre functions of the first kind having degree n and order m as stated in the first section of this chapter. Finally, the prefactor α_{mn} is needed to guarantee that $\|\mathbf{j}_{\substack{e \\ o}}\|^2 = 1$ and therefore, given the Kronecker

delta δ_m, its expression is:

$$\alpha_{mn} = 2\pi n(\delta_m + 1)\frac{(m+n)!}{(2n+1)(n-m)!} \tag{2.128}$$

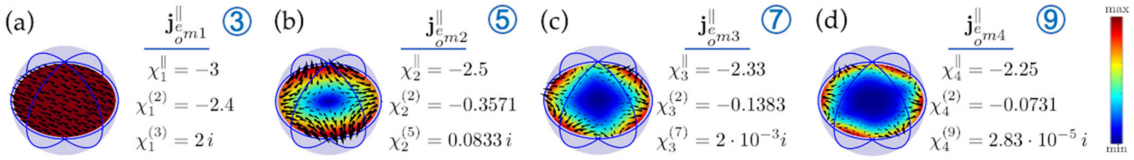

Figure 2.7: Catalog of the EQS modes of a plasmonic sphere. The EQS modes $\mathbf{j}^{\parallel}_{e_{o}mn}$ with $n = 1, 2, 3, 4$ are ordered according to their eigenvalues $\chi_n^{\parallel}$. The second order correction $\chi_n^{(2)}$ and the first non-vanishing imaginary correction $\chi_n^{(n_i)}$ of the order n_i are shown on the right of each field plot. The numbers in the blue circles denote the order n_i of the first non-vanishing imaginary correction. Adapted from Ref. [43].

The *catalog* of resonances of a plasmonic sphere having radius R is reported in Figure 2.7 [43]. The sphere exhibits three degenerate EQS modes $\mathbf{j}^{\parallel}_{e_{o}m1}$ with $m = 0, 1$, namely $\mathbf{j}^{\parallel}_{e01}$, $\mathbf{j}^{\parallel}_{e11}$, and $\mathbf{j}^{\parallel}_{o11}$), which are associated to the lowest eigenvalue $\chi_1^{\parallel} = -3$ (Figure 2.7 a). These modes are bright modes and represent the three electric dipoles (fundamental modes) oriented along mutual orthogonal directions.

2.3.2 Dielectric Networks

As stated in previous sections, within the framework of the magneto-quasistatic approximation, the induced polarization density field is solenoidal in the object and its normal component to the surface of the object vanishes identically [128]. These properties pave the way for the research of new geometries for which high-permittivity dielectric resonators could be treated as lumped networks when their size is smaller or comparable to the wavelength of operation. In this context, possible candidates are represented by arbitrary interconnections of high-permittivity dielectric thin wires, denoted as *high-permittivity dielectric networks* in this section.

Although many other structures have been proposed as high permittivity optical devices, thin wires may constitute a building block of all-dielectric nanoresonators by assuming the same role achieved by conducting thin wires in the last century. Moreover, the prediction of the optical properties (electromagnetic scattering) of high-permittivity dielectric networks could be simplified through opportune reasoning, thus reducing computational costs. A wire is denoted as *thin* if the linear dimension of its cross-section is much smaller than its length. The background provided in the

previous sections is exploited to achieve the full prediction on the catalog of resonance frequencies and quality factors of high-permittivity thin wires networks starting from the expansion of the Maxwell equations in terms of the MQS modes and applying the radiative corrections, but with a lumped element-based description, which simplifies the problem and reduces computational costs [44, 43].

Before passing to high-permittivity networks, a simple dielectric loop made of a high permittivity thin wire of uniform cross-section and area Σ and having axis Γ with tangent vector $\hat{\mathbf{t}}$ is considered. Γ is used also to represent the loop length. Therefore, the volume Ω occupied by the loop can be computed as $\Omega = \Sigma \times \Gamma$. As shown in [39], the geometry described up to now exhibits the lowest eigenvalue $k_1^{\perp}$ associated with the fundamental mode $\mathbf{j}_1^{\perp}(\tilde{\mathbf{r}})$ far away from all the other modes of the structure. The more the cross-section of the wire reduces, the more separated the fundamental mode of the structure from the other ones is. Therefore, for $x \leq 1$, only the fundamental MQS mode $\mathbf{j}_1^{\perp}(\tilde{\mathbf{r}})$ is effectively excited. Therefore, in this case, the expression of the induced polarization current density 2.100 simplifies in:

$$\mathbf{J}\left(\tilde{\mathbf{r}}\right) = i\omega\chi\varepsilon_0 \frac{1}{1 - x^2\chi/k_1^{\perp}} \langle \mathbf{j}_1^{\perp}, \mathbf{E}_i \rangle \mathbf{j}_1^{\perp}(\tilde{\mathbf{r}}). \tag{2.129}$$

The fundamental mode $\mathbf{j}_1^{\perp}(\tilde{\mathbf{r}})$ of a loop with finite cross-section is directed along the wire axis $\hat{\mathbf{t}}$, almost uniform in the cross-section, and with uniform module along the wire axis, and almost uniform in the cross section [39].

$$\mathbf{j}_1^{\perp}(\tilde{\mathbf{r}}) = \begin{cases} \hat{\mathbf{t}}(\tilde{\mathbf{r}})/\sqrt{\tilde{\Omega}} & \text{in } \tilde{\Omega}, \\ \mathbf{0} & \text{otherwise.} \end{cases} \tag{2.130}$$

The normalization condition in Equation 2.95 can be applied leading to $\langle \mathbf{j}_1^{\perp}, \mathbf{j}_1^{\perp} \rangle = 1$. The corresponding eigenvalue $k_1^{\perp}$ is provided by Equation 2.97, namely

$$\frac{\tilde{\Omega}}{k_1^{\perp}} = \frac{1}{4\pi} \int_{\tilde{\Omega}} \int_{\tilde{\Omega}} \frac{\hat{\mathbf{t}}(\tilde{\mathbf{r}}) \cdot \hat{\mathbf{t}}(\tilde{\mathbf{r}})'}{|\tilde{\mathbf{r}} - \tilde{\mathbf{r}}'|} dV' dV, \tag{2.131}$$

where $\tilde{\Omega}$ is the scaled volume of the object ($\tilde{\Omega} = \Gamma \times \Sigma/\ell_c^3$). It must be now noticed that apart from the multiplicative constant $(\ell_c^5/\Sigma^2)\mu_0$, the integral of the right-hand side is nothing but the *self-inductance of the loop L*. Therefore, it is possible to relate the fundamental eigenvalue $k_1^{\perp}$ to the self-inductance of the thin wire loop as:

$$k_1^{\perp} = \frac{\ell_c \Gamma}{\Sigma} \frac{\ell_c \mu_0}{L}. \tag{2.132}$$

Lumped element model for a single loop

Equation 2.129 can be explained starting from the polarization current density field **J** induced in the loop, which is

$$\mathbf{J} = i\omega\varepsilon_0\chi\left(\mathbf{E} + \mathbf{E}_i\right) \tag{2.133}$$

where **E** is the induced electric field. From the line integral along Γ on both sides of Equation 2.133, the following relation derives:

$$\frac{1}{\chi}\frac{1}{i\omega C}I = \mathcal{E}_i + \mathcal{E} \tag{2.134}$$

where I is the intensity of the polarization current induced in the wire,

$$C = \varepsilon_0\frac{\Sigma}{\Gamma}, \tag{2.135}$$

$\mathcal{E}$ is the induced voltage along the loop

$$\mathcal{E} = \oint_\Gamma \mathbf{E}\cdot\hat{\mathbf{t}}\,dl, \tag{2.136}$$

and $\mathcal{E}_i$ is the applied voltage

$$\mathcal{E}_i = \oint_\Gamma \mathbf{E}_i\cdot\hat{\mathbf{t}}\,dl. \tag{2.137}$$

On the other hand, by applying the Neumann-Faraday law the following relation holds:

$$\mathcal{E} = -i\omega LI \tag{2.138}$$

where L is the self-inductance of the loop. By substituting Equation 2.138 in Equation 2.134, it is possible to derive the equation of the equivalent circuit in Figure 2.8, as:

$$\left(i\omega L + \frac{1}{\chi}\frac{1}{i\omega C}\right)I = \mathcal{E}_i. \tag{2.139}$$

Moreover, from Equations 2.132 and 2.135

$$\frac{1}{\omega_c^2 k_1^\perp} = LC, \tag{2.140}$$

the solution of equation 2.139 becomes:

$$I = i\omega C\chi\frac{1}{1-\left(\omega/\omega_c\right)^2\chi/k_1^\perp}\mathcal{E}_i. \tag{2.141}$$

This expression is nothing but the polarization current intensity obtained from Equation 2.129 written in a different form. The quasi-static resonance frequency, solution of the following equation [39]:

$$x_h^{\perp} = \frac{\omega_h^{\perp}}{c_0}\ell_c = \sqrt{\frac{k_h^{\perp}}{\Re e\{\chi\}}},, \tag{2.142}$$

is the value of ω that minimizes the following relationship:

$$\left|1 - (\omega/\omega_c)^2 \chi/k_1^{\perp}\right|.$$

The derived model can be directly applied also in the case of complex susceptibilities. Precisely, when the χ is a complex quantity, the capacitance χC reported in Figure 2.8 becomes complex. Thus, the corresponding impedance will have a non-vanishing real part (in circuitry, this corresponds to a resistance).

Radiative corrections

In the case of the considered dielectric loop the radiative corrections $k_h^{(2)}$ and $k_h^{(3)}$ have the following expressions [43]:

$$k_1^{(2)} = \frac{\left(k_1^{\perp}\right)^2}{8\pi}\int_{\tilde{\Omega}}\int_{\tilde{\Omega}} |\tilde{\mathbf{r}} - \tilde{\mathbf{r}}'|\, \mathbf{j}_1^{\perp}(\tilde{\mathbf{r}}) \cdot \mathbf{j}_1^{\perp}(\tilde{\mathbf{r}}) dV' dV, \tag{2.143}$$

$$k_0^{(3)} = -i\frac{\left(k_1^{\perp}\right)^2}{24\pi}\int_{\tilde{\Omega}}\int_{\tilde{\Omega}} |\tilde{\mathbf{r}} - \tilde{\mathbf{r}}'|^2\, \mathbf{j}_1^{\perp}(\tilde{\mathbf{r}}) \cdot \mathbf{j}_1^{\perp}(\tilde{\mathbf{r}}) dV' dV. \tag{2.144}$$

By using Equation 2.130, Equation 2.143 simplifies to:

$$k_1^{(2)} = -2\pi\frac{\Sigma}{\Gamma^2}\left(k_1^{\perp}\right)^2\Delta \tag{2.145}$$

where

$$\Delta = -\frac{1}{8\pi}\oint_{\tilde{\Gamma}}\oint_{\tilde{\Gamma}} \hat{\mathbf{t}}(\tilde{\mathbf{r}}) \cdot \hat{\mathbf{t}}(\tilde{\mathbf{r}}) |\tilde{\mathbf{r}} - \tilde{\mathbf{r}}'| dl' dl > 0; \tag{2.146}$$

and where the choice $\ell_c = \Gamma/2\pi$ has been done. By using Equation 2.130, and the Binet–Cauchy identity [129], Equation 2.144 becomes:

$$k_1^{(3)} = i\left(k_1^{\perp}\right)^2 \frac{1}{6\pi}\left\|\mathbf{M}_1\right\|^2, \tag{2.147}$$

where $\mathbf{M}_1$ is the magnetic dipole moment of the fundamental mode $\mathbf{j}_1^{\perp}$ in the scaled object (Equation 2.119). The radiation Q_1 factor of the fundamental mode $\mathbf{j}_1^{\perp}$ is instead given by

$$Q_1 = \frac{6\pi}{k_1^{\perp} \left\|\mathbf{M}_1\right\|^2} \frac{1}{x_1^3}, \tag{2.148}$$

where $x_1 = \omega_1/\omega_c$ and ω_1 is the resonance frequency that takes into account the radiative shift [43]. These corrections well-describe the position of the resonance frequency and the quality factor for $x \lesssim 1$.

The induced polarization current in the loop with the radiative corrections can be finally obtained by substituting $k_1^{\perp}$ with $k_1 = k_1^{\perp} + k_1^{(2)} x^2 + k_1^{(3)} x^3$ into expression 2.141.

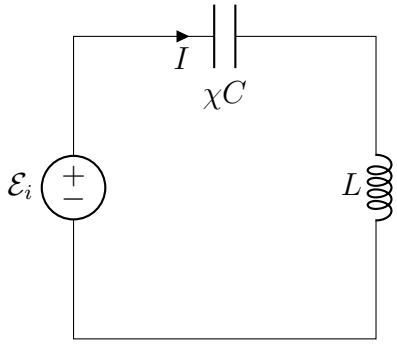

Figure 2.8: Lumped element circuit for a high-permittivity loop.

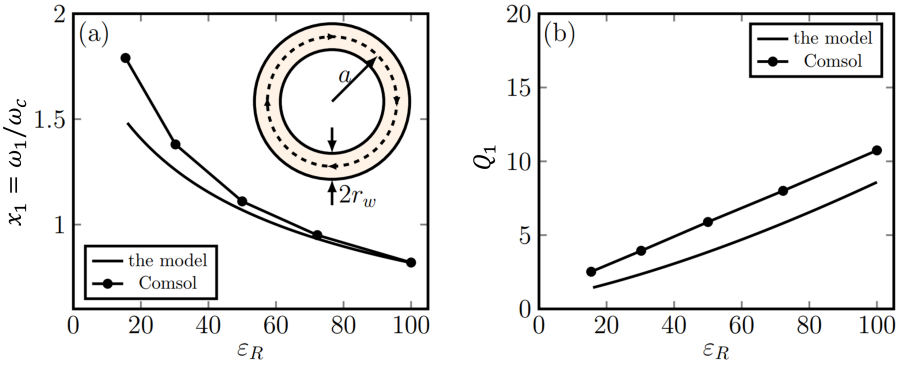

Figure 2.9: Comparison between the proposed model and Comsol: (a) Resonance frequency normalized to $\omega_c = c_0/a$, that is $x_0 = \omega_0/\omega_c$, and (b) radiative quality factor Q of a high-permittivity circular loop with major radius a and minor radius $r_w = 0.1a$ as a function of the permittivity ε_R. Adapted from Ref. [44].

Circular loop

The illustration of the formulas above can be made by considering a circular loop with a circular cross-section (namely, torus), major radius a, and minor radius r_w. This is the starting point since the circular loop was the structure where the dielectric resonances have been proposed for the first time [130], and its modes were studied in Ref. [131, 39]. For a circular loop, the expression of $k_1^{\perp}$ is

$$k_1^{\perp} = \frac{2a^2}{r_w^2}\frac{a\mu_0}{L}, \tag{2.149}$$

where L is the inductance of the loop [132],

$$L = \mu_0\sqrt{a\left(a-r_{\mathrm{w}}\right)}\left[\left(\frac{2}{k}-k\right)K(k^2)-\frac{2}{k}E(k^2)\right]+\frac{\mu_0}{4}a, \tag{2.150}$$

$$k = \sqrt{\frac{4a\left(a-r_{\mathrm{w}}\right)}{\left(2a-r_{\mathrm{w}}\right)^2}}, \tag{2.151}$$

$K(\cdot)$ and $E(\cdot)$ are the complete elliptic integrals of the first and second kind [133]. The term $\mu_0/4a$ in Equation 2.150 is the internal inductance of the loop [132]. The expression of the second order correction follows from Eq. 2.145:

$$k_1^{(2)} = -\frac{2}{3}\frac{2a^2}{r_w^2}\left(\frac{a\mu_0}{L}\right)^2. \tag{2.152}$$

Therefore, for a non-dispersive material, the resonance frequency is obtained starting from the derivation in Ref. [43]:

$$\omega_1 = \frac{c_0}{a}\left(\sqrt{\frac{r_w^2}{2a^2}\left(\frac{L}{a\mu_0}\right)\mathrm{Re}\left\{\chi\right\}+\frac{2}{3}\left(\frac{a\mu_0}{L}\right)}\right)^{-1}. \tag{2.153}$$

The expression of the radiative quality factor Q_1 is given by:

$$Q_1 = \frac{6}{\pi}\left(\frac{L}{a\mu_0}\right)\frac{1}{x_1^3}. \tag{2.154}$$

Equations 2.153 and 2.154 were validated against Comsol Multiphysics (Wave Optics package) considering a high-permittivity loop with $r_w = 0.1a$. Specifically, in Figure 2.9 (a) the resonance position obtained $x_1 = \omega_1/\omega_c$ derived from the model was compared with the resonance peak position of the scattering spectrum derived by Comsol numerical simulations, upon excitation of the loop by an electric point dipole

source, located at a distance $3a$ from the center of the loop, and oriented along the toroidal direction $\hat{\mathbf{t}}$. For very high permittivities ($\varepsilon_R \to 100$), a very good agreement between the model and numerical simulations was achieved. For smaller, but still positive, ε_R the error slightly deteriorates due to the blue-shift of the resonance wavelength becoming comparable to the dimensions of the object.

Figure 2.9 (b) shows instead the Q_1 factor obtained from Equation 2.154 against the inverse of the fractional bandwidth, namely the ratio of the full width at half maximum to the peak frequency, obtained in Comsol. Also for the quality factor, a good agreement between the model and the numerical simulations was found. Generally, the resonant position and the Q factor are slightly underestimated by the model for two main reasons:

- when $x_1 \sim 1$ radiative effects become significant;
- in the thin wire approximation of the proposed model, the polarization current was imposed as uniform on the wire cross-section; this is an important approximation since, in reality, the fundamental MQS mode is more concentrated near the loop axis [39].

However, with the introduction of the radiative corrections quantitative prediction of the resonance behavior is achieved for high permittivities, and a sufficiently high accuracy on the resonance and quality factors prediction was achieved for lower permittivities.

Two interacting high-permittivity loops

The same strategy can be applied also to a pair of high-permittivity thin wire loops occupying two disjoint spatial domains Ω_1 and Ω_2 with cross sections Σ_1 and Σ_2, and wire axes denoted by the closed curves Γ_1 and Γ_2 having tangent unit vectors $\hat{\mathbf{t}}_1$ and $\hat{\mathbf{t}}_2$, respectively. The polarization current densities I_1 and I_2 in each loop, respectively, are assumed as uniformly distributed across the wires' cross-sections and directed along their axes.

By following the methodology applied for a single circular loop, the following system of equations for the intensities of the induced polarization currents can be

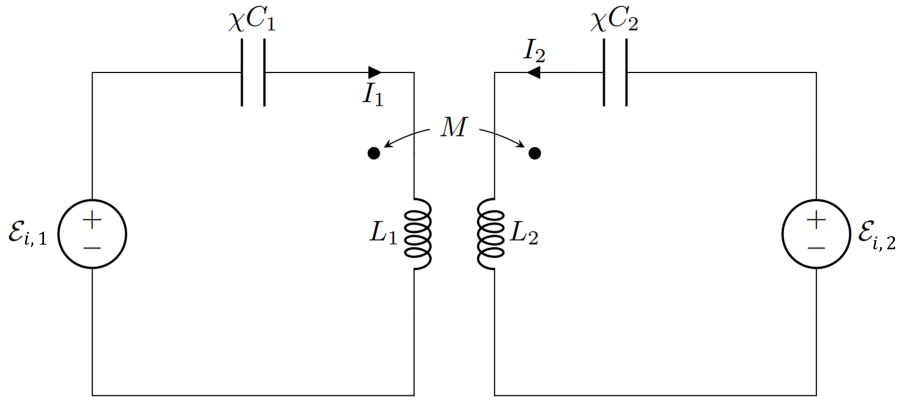

Figure 2.10: Lumped element circuit for two mutually coupled high-permittivity loops. Adapted from Ref. [44].

derived from the lumped element circuit reported in Figure 2.10):

$$\begin{aligned} i\omega L_1 I_1 + i\omega M I_2 + \frac{1}{i\chi\omega C_1} I_1 &= \mathcal{E}_{i,1}, \\ i\omega M I_1 + i\omega L_2 I_2 + \frac{1}{i\chi\omega C_2} I_2 &= \mathcal{E}_{i,2}, \end{aligned} \tag{2.155}$$

.

where

$$C_q = \varepsilon_0 \frac{\Sigma_q}{\Gamma_q} \quad q \in 1, 2, \tag{2.156}$$

L_1 and L_2 are the self-inductions of the loops, separately, while M is the mutual inductance between the two loops,

$$M = \frac{\mu_0}{4\pi} \oint_{\Gamma_1} \oint_{\Gamma_2} \frac{\hat{\mathbf{t}}_1 \cdot \hat{\mathbf{t}}_2}{|\mathbf{r} - \mathbf{r}'|} dl_1 dl_2. \tag{2.157}$$

The modes of the loop pair are solutions to the generalized eigenvalue problem

$$\underline{\underline{L}}\,\underline{u} = \frac{1}{k^{\perp}} \frac{1}{\omega_c^2} \underline{\underline{C}}^{-1}\,\underline{u} \tag{2.158}$$

where

$$\underline{\underline{L}} = \begin{pmatrix} L_1 & M \\ M & L_2 \end{pmatrix} \tag{2.159}$$

and

$$\underline{\underline{C}} = \begin{pmatrix} C_1 & 0 \\ 0 & C_2 \end{pmatrix}. \tag{2.160}$$

In this case, the generalized eigenvalue problem has two eigenvalues, denoted as $k_{\pm}^{\perp}$, and two current modes, $\underline{u}_{\pm}$. These modes exhibit equidirected and counter-directed currents, recognized as *Helmholtz* (H) and *anti-Helmholtz* (A-H) modes, respectively. They are orthogonal according to the weighted scalar product $\underline{u}_{\pm}^{\intercal}\underline{\underline{C}}^{-1}\underline{u}_{\mp} = 0$ and can be normalized as follows

$$\varepsilon_0 \ell_c \, \underline{u}_{\pm}^{\intercal}\underline{\underline{C}}^{-1}\underline{u}_{\pm} = 1. \tag{2.161}$$

Since the magnetic energy of each current mode is strictly definite positive, the matrix $\underline{\underline{L}}$ is strictly definite positive, therefore $L_1 L_2 > M^2$. The solution of the problem in Equation 2.155 written in terms of the current modes becomes

$$\underline{I} = i\varepsilon_0 \omega \chi \ell_c \sum_{h=\pm} \frac{\underline{u}_h^{\intercal}\underline{\mathcal{E}}_i}{1 - x^2\chi/k_h^{\perp}}\underline{u}_h, \tag{2.162}$$

where $\underline{I} = (I_1, I_2)^{\intercal}$, and $\underline{\mathcal{E}}_i = (\mathcal{E}_{i,1}, \mathcal{E}_{i,2})^{\intercal}$. For a loop pair, the second order corrections

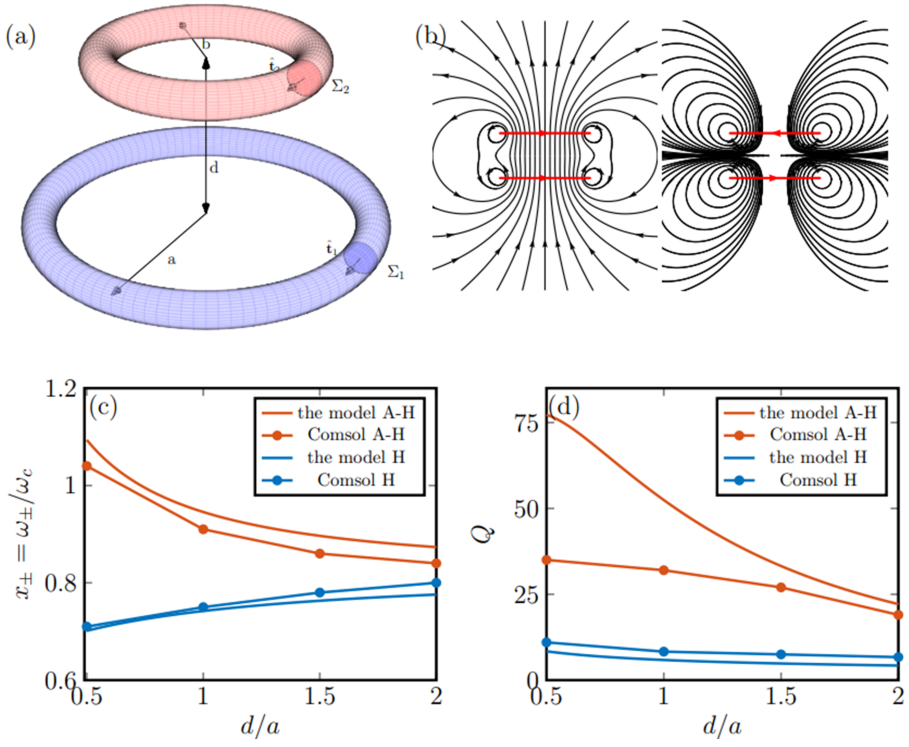

Figure 2.11: (a) Two loops with major radii a and b, distance d, sections Σ_1 and Σ_2. (b) Magnetic field lines generated by Helmholtz (H) and anti-Helmholtz (A-H) current modes for $a = b$ and $d = a/2$. Comparison between the results obtained by the proposed model and by Comsol assuming $\varepsilon_R = 100$: resonance frequency (c) normalized to $\omega_c = c_0/a$, $x_{\pm} = \omega_{\pm}/\omega_c$ and radiative quality factor (d). Reprinted from Ref. [44].

to $k_{\pm}^{\perp}$ are given by

$$k_{\pm}^{(2)} = \frac{\left(k_{\pm}^{\perp}\right)^2}{8\pi} \underline{u}_{\pm}^{\intercal} \underline{\underline{\Delta}}^{(2)} \underline{u}_{\pm}, \tag{2.163}$$

and the first non-vanishing imaginary corrections (of odd order $n_i \geq 3$) are given by

$$k_{\pm}^{(n_i)} = i(-1)^{(n_i-1)/2} \frac{\left(k_{\pm}^{\perp}\right)^2}{4\pi n_i!} \underline{u}_{\pm}^{\intercal} \underline{\underline{\Delta}}^{(n_i)} \underline{u}_{\pm}, \tag{2.164}$$

where the elements of the matrix $\underline{\underline{\Delta}}^{(n)}$ are

$$\left(\underline{\underline{\Delta}}^{(n)}\right)_{pq} = \oint_{\tilde{\Gamma_p}} \oint_{\tilde{\Gamma_q}} \hat{\mathbf{t}}_p(\tilde{\mathbf{r}}) \cdot \hat{\mathbf{t}}_q(\tilde{\mathbf{r}}) p \left|\tilde{\mathbf{r}} - \tilde{\mathbf{r}}'\right|^{n-1} dl' dl. \tag{2.165}$$

For two loops exhibiting different shapes and/or sizes, the first non-vanishing imaginary correction for both modes is 3, while, for two identical loops, the first non-vanishing imaginary correction for the A-H mode is 5. As done for the single circular loop, these corrections describe the position of the resonance frequency and the quality factor for $x \lesssim 1$. They also take into account the radiative coupling between the two loops. The polarization currents in the loop pair with the radiative corrections can be obtained by substituting $k_{\pm}^{\perp}$ with $k_{\pm} = k_{\pm}^{\perp} + k_{\pm}^{(2)} x^2 + i k_{\pm}^{(n_i)} x^{n_i}$ into Equation 2.162.

The validation of the lumped model for two interacting high-permittivity loops can be done by considering two coaxial loops with the same permittivity ε_R and circular cross-section of minor radius r_w. The two loops are assumed to be at a distance d ad have major radii a and b (Figure 2.11a). On the one hand, the self-inductances L_1 and L_2 are given by Equation 2.150, while the mutual inductance M is derived in Refs. [134, 135] is:

$$M = \mu_0 \sqrt{ab} \left[\left(\frac{2}{k'} - k' \right) K(k'^2) - \frac{2}{k'} E(k'^2) \right] \tag{2.166}$$

where $K(k)$ and $E(k)$ are the complete elliptic integrals of the first and second kinds, and

$$k' = \sqrt{\frac{4ab}{(a+b)^2 + d^2}}. \tag{2.167}$$

Figure 2.11 (b) shows the field lines of the magnetic field generated by the H $\underline{u}_-$ and A-H $\underline{u}_+$ current modes in the case of $a = b$. Figure 2.11c reports instead the resonance frequencies of these two modes normalized to ω_c, $x_{\pm} = \omega_{\pm}/\omega_c$, as a function of the normalized distance d/a between the two loops, and for $r_w = 0.1a$, and $\varepsilon_R = 100$. The red and blue full lines represent the resonance frequencies of the A-H (x_+) and

H (x_-) current modes, respectively.

The obtained resonance frequencies are compared with the peak positions of the scattering response obtained from Comsol simulations upon excitation of the two loops by an electric point dipole (red and blue lines with dots) located in the plane of the loop with radius a, at a distance $3a$ from its center, oriented along its toroidal direction $\hat{\mathbf{t}}$.

A good agreement is observed between numerical simulations and the proposed model, even though the A-H mode prediction exhibits a larger error since $x_+ \approx 1$. In Figure 2.11d, the theoretical Q factors against the inverse of the fractional bandwidth obtained from Comsol as a function of the normalized loop distance (d/a) are reported. Again, a good agreement was found for the H mode, while for the A-H mode, the overall magnetic dipole moment is vanishing, thus $k_h^{(3)} = 0$, and the quadrupole contribution ($n_i = 5$) had to be considered. For values $d/a > 1.5$, a quantitative agreement was found.

Nevertheless, as the distance d between the two loops decreases, the error increases. This is due to Equation 2.166 that does not take into account the finite size of the wires and becomes inaccurate for small values of d/a, where the two loops exhibit a strong near-field interaction. The Q-factor of the A-H mode is more sensitive to the approximations made because it depends on the fifth power of the normalized resonance frequency x_+, instead, for the H mode, it depends on the third power of x_- [43]. The resonance frequency is more robust because the quasistatic approximation alone already can predict the order of magnitude of the resonance frequencies, and the radiative corrections are only associated with the second power of the size parameter $x_\pm$.

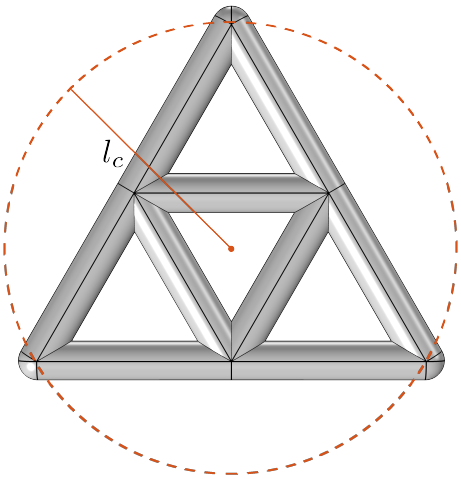

Figure 2.12: Top view of an exemplification of a dielectric network.

High-permittivity dielectric networks

The concepts introduced in this section can be generalized to an arbitrary interconnection of high-permittivity thin wires, *e.g.* Fig. 2.12. In fact, the proposed lumped element model enables the study of the main properties of the electromagnetic scattering from such structures: in particular, the induced polarization currents expressed in terms of the MQS current modes, their resonance frequencies, their radiative frequency shifts, and their radiative Q factors.

Since, in the MQS limit, the normal component of the polarization current density is null at the object's surface, it can be assumed that there is not *leakage* of polarization current density from the considered object. Therefore, at each node of the network the sum of the polarization current intensity is conserved, analogous to Kirchhoff's law for electric currents [136].

Under these hypotheses, wires extending out of a loop or connecting two disjoint loops have a weak or null influence on the scattering from high-permittivity dielectric networks. Therefore, if available, they can be disregarded before applying the following loop analysis.

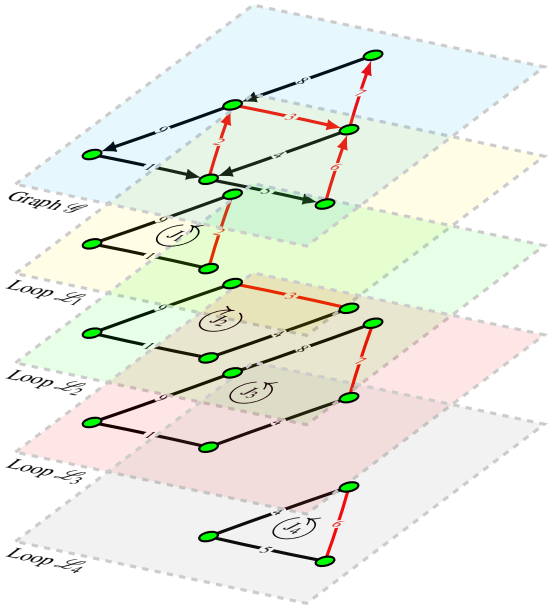

Figure 2.13: (Top Layer) Graph $\mathcal{G}$ associated to the dielectric network shown in Fig. 2.12, the chosen tree $\mathcal{T}$ is highlighted in black, the corresponding links in red. (Layers below) Fundamental loops $\mathcal{L}_1$-$\mathcal{L}_4$ are associated with the four different links. Their orientation is defined by the direction of the corresponding link. Reprinted from Ref. [44].

As for electric circuits [136], it is convenient to associate to the dielectric network a digraph $\mathcal{G}$, *i.e.* an oriented graph, with n nodes and b branches, where e_h is the h-th branch of the digraph, $\hat{\mathbf{t}}_h$ its tangent unit vector, and I_h the intensity of the branch polarization current. The digraph associated with the network of Fig. 2.12 is shown on the top layer of Fig. 2.13. For the sake of simplicity, the analysis is restricted to connected graphs. If the graph is not connected, it is possible to combine the following approach with the one carried out in the case of two disjoint circular loops.

A loop $\mathcal{L}_i$ of $\mathcal{G}$ is defined as a connected sub-graph with exactly two incident branches in each node. A tree $\mathcal{T}$ of a connected digraph $\mathcal{G}$ is instead a connected subgraph containing all the nodes of $\mathcal{G}$, but no loops.

For any given digraph $\mathcal{G}$, many possible choices of trees are possible. Given a connected digraph, and chosen a tree, the branches of $\mathcal{G}$ are partitioned in two disjoint sets: the ones belonging to $\mathcal{T}$, called *twigs*, and the ones that do not belong to $\mathcal{T}$ that is called *links*. The *fundamental theorem of graphs* [136] states that, given a connected graph with n nodes, b branches and a tree $\mathcal{T}$, there are $n-1$ twigs and $\ell = b - (n-1)$ links. Every link (e.g. the p-th link) together with a proper choice of twigs constitutes a unique loop, called the fundamental loop associated with the link.

For instance, from the graph shown in the top layer of Figure 2.13, it is possible to associate to every link of the particular tree $\mathcal{T}$ (highlighted in red), the four fundamental loops $\mathcal{L}_1, \ldots, \mathcal{L}_4$, shown in the layers bottom layers of Figure 2.13. Their orientation is defined by the direction of the corresponding link.

It is then possible to identify a set of fundamental loops through the $\ell \times b$ fundamental loop matrix $\underline{\underline{B}}$ associated with the corresponding tree. The jk occurrence is defined as follows: $b_{jk} = 1$ if branch k is in the loop j and their reference directions are the same; $b_{jk} = -1$ if branch k is in the loop j and their reference directions are opposite; $b_{jk} = 0$ if branch k is not in the loop j.

The *loop analysis* can be now applied to formulate the general electromagnetic scattering problem from the dielectric network: the b polarization current intensities of the network are expressed in terms of the ℓ fundamental loop currents. This choice ensures that the polarization currents respect Kirchhoff's law at any network node.

$\underline{I}$ now represents the (column) vector of the polarization current intensities of the branches of the circuit $\{I_1, I_2, ..., I_b\}$, and $\underline{J}$ the column vector of the current intensities of the links associated with the tree $\mathcal{T}$ of the network, $\{J_1, J_2, ..., J_\ell\}$. The conservation of the sum of the polarization currents at the nodes of the circuit [136] imposes that

$$\underline{I} = \underline{\underline{B}}^{\intercal} \underline{J}. \tag{2.168}$$

Denoted as $\underline{\mathcal{E}}$, the column vector representing the set of induced loop voltages $\{\mathcal{E}_1, \mathcal{E}_2, ..., \mathcal{E}_\ell\}$ and as $\underline{\mathcal{E}}_i$ the column vector representing the set of loop external voltages $\{\mathcal{E}_{i,1}, \mathcal{E}_{i,2}, ..., \mathcal{E}_{i,\ell}\}$, the constitutive relations of the dielectric thin wires (obtained by solving the line integral of Equation 2.133 along each fundamental loop), leads to:

$$\frac{1}{\chi}\underline{\underline{B}}\left(i\omega\underline{\underline{C}}\right)^{-1}\underline{I} = \underline{\mathcal{E}} + \underline{\mathcal{E}}_{i,}\,, \tag{2.169}$$

where $\underline{\underline{C}}$ is the diagonal matrix whose elements are $C_h = (\varepsilon_0\Sigma_h)/\Gamma_h$ with $h = 1, 2, ..., b$, Σ_h is the cross-section of the h-th wire and Γ_h is the length. On the other hand, the Faraday-Neumann law imposes that

$$\underline{\mathcal{E}} = -i\omega\underline{\underline{L}}\,\underline{J} \tag{2.170}$$

where $\underline{\underline{L}}$ is the $\ell \times \ell$ inductance matrix of the set of fundamental loops. By combining Equations 2.168-2.170, the system of equations governing the set of the link currents associated with the tree $\mathcal{T}$ is obtained:

$$i\omega\underline{\underline{L}}\,\underline{J} + \frac{1}{i\omega\chi}\underline{\underline{B}}\,\underline{\underline{C}}^{-1}\underline{\underline{B}}^{\intercal}\underline{J} = \underline{\mathcal{E}}_{\,i}. \tag{2.171}$$

The MQS current modes $\{\underline{u}_h\}$ of the network and the corresponding eigenvalues $\left\{\kappa_h^{\perp}\right\}$ are solution of the generalized eigenvalue problem:

$$\underline{\underline{L}}\,\underline{u} = \frac{1}{k^{\perp}}\frac{1}{\omega_c^2}\underline{\underline{B}}\,\underline{\underline{C}}^{-1}\underline{\underline{B}}^{\intercal}\,\underline{u}. \tag{2.172}$$

The number of MQS current modes and of resonances of a high-permittivity dielectric network is therefore equal to the number ℓ of links of the digraph $\mathcal{G}$ of the network. The matrices $\underline{\underline{L}}$ and $\underline{\underline{B}}\,\underline{\underline{C}}^{-1}\underline{\underline{B}}^{\intercal}$ are symmetric and definite positive. As a consequence, the eigenvalues $\left\{k_h^{\perp}\right\}$ are real and positive, and the current modes satisfy the following weighted orthogonality condition:

$$\varepsilon_0\ell_c\underline{u}_h^{\intercal}\left(\underline{\underline{B}}\,\underline{\underline{C}}^{-1}\underline{\underline{B}}^{\intercal}\right)\underline{u}_k = \delta_{hk}. \tag{2.173}$$

The solution of Eq. 2.171 is

$$\underline{J} = i\varepsilon_0\omega\chi\ell_c\sum_{h=1}^{\ell}\frac{\underline{u}_h^{\intercal}\underline{\mathcal{E}}_{ext}}{1 - x^2\chi/k_h^{\perp}}\underline{u}_h. \tag{2.174}$$

The direct calculation of self- and mutual- inductance of fundamental loops may not be the most efficient method to assemble the matrix $\underline{\underline{L}}$, since different loops may

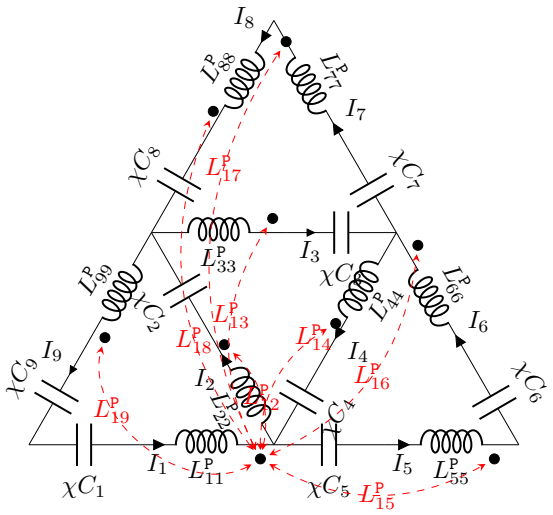

Figure 2.14: Lumped element circuit for the dielectric network in Fig. 2.12. The self-partial inductances L^{P}_{qq} of each branch of the digraph are shown. The mutual partial inductances between the first branch and any other branch are shown in red. The dotted convention commonly employed in magnetically coupled circuits is used in this case. Reprinted from Ref. [44].

share several branches, resulting in redundant and hence inefficient computations. It is instead convenient, as for electric circuits [135, 132], to preliminary assemble the partial loop inductances matrix $\underline{\underline{L}}^{\mathsf{P}}$.

Its ij occurrence is the partial inductance L^{P}_{ij} between the branches e_i and e_j. It is defined as the ratio between the magnetic flux produced by the current density flowing in the branch e_j, through the surface between the branch e_i and infinity, and the current of the branch e_j, namely:

$$L^{\mathsf{P}}_{ij} = \frac{1}{I_j} \int_{e_i} \mathbf{A}_j \cdot \hat{\mathbf{t}}_i d\tilde{l}. \tag{2.175}$$

There are $b\,(b+1)\,/2$ independent partial inductance L^{P}_{ij}, because $L^{\mathsf{P}}_{ij} = L^{\mathsf{P}}_{ji}$ by reciprocity. The loop inductance matrix $\underline{\underline{L}}$ is given by

$$\underline{\underline{L}} = \underline{\underline{B}}\,\underline{\underline{L}}^{\mathrm{P}}\,\underline{\underline{B}}^{\intercal}. \tag{2.176}$$

If the circuit is composed by an arbitrary interconnection of *straight* wires laying on the same plane, then we need formulas for calculating: i) self-partial inductance of a straight wire (Appendix A.1); ii) the mutual partial inductance between wires at an angle to each other (Appendix A.3) which includes as a limit case the mutual partial inductance between parallel wires (Appendix A.2), and the mutual partial inductance

of wires meeting in a point (given by G.A. Campbell [137]). If the circuit is not planar, then also the mutual partial inductance between skewed and displacement wires first derived by F. F. Martens and G. A. Campbell [138, 137, 135, 132] are needed.

In Figure 2.14, the lumped circuit for the dielectric network shown in Figure 2.12 is reported, where illustrations of the self-partial inductances $L^{\mathtt{P}}_{qq}$, and of only the mutual partial inductance $L^{\mathtt{P}}_{1q}$ are shown.

The generalized expression of the second-order (real) radiative correction for the h-th mode is

$$k_h^{(2)} = \frac{\left(k_h^{\perp}\right)^2}{8\pi} \underline{u}_h^{\intercal} \underline{\underline{B}}\, \underline{\underline{\Delta}}^{(2)}\, \underline{\underline{B}}^{\intercal} \underline{u}_h, \tag{2.177}$$

and the expression of the lowest non-vanishing imaginary correction order n_i (which is an odd number $n_i \geq 3$) is

$$k_h^{(n_i)} = i\,(-1)^{(n_i-1)/2}\, \frac{\left(k_h^{\perp}\right)^2}{4\pi n_i!}\, \underline{u}_h^{\intercal}\, \underline{\underline{B}}\, \underline{\underline{\Delta}}^{(n_i)}\, \underline{\underline{B}}^{\intercal} \underline{u}_h \tag{2.178}$$

where the elements of the matrix $\underline{\underline{\Delta}}^{(n)}$ are

$$\left(\underline{\underline{\Delta}}^{(n)}\right)_{ij} = \oint_{\tilde{e}_i} \hat{\mathbf{t}}_i(\tilde{\mathbf{r}}) \cdot \oint_{\tilde{e}_j} \hat{\mathbf{t}}_j(\tilde{\mathbf{r}}) |\tilde{\mathbf{r}} - \tilde{\mathbf{r}}'|^{n-1} dl' dl. \tag{2.179}$$

These corrections, also in this case, describe the position of the resonance frequencies and the Q factors for $x \lesssim 1$. They take into account the radiative coupling among the network's loops. The expression of the induced polarization currents in the links of the dielectric network taking into account the radiative corrections is obtained by substituting $k_h^{\perp}$ with $k_h = k_h + k_h^{(2)} x^2 + i k_h^{(n_i)} x^{n_i}$ for $h = 1, \ldots, \ell$, into Equation 2.174.

Sierpinski triangle

The dielectric network shown in Figure 2.13 is assumed as made by $b = 9$ high-permittivity thin wires of equal length l_w, with a circular cross-section with radius $r_w = 0.1 l_w$. The wires are interconnected accordingly to a Sierpinski triangle [139]. The minimum circle circumscribing the network is chosen as characteristic length ℓ_c.

The graph of this network is shown in the top layer of Fig. 2.13, where the twigs and links, associated with a chosen tree, are highlighted in red and black, respectively. The fundamental loops associated with each *link* are shown in the layers below.

Figure 2.14 shows the lumped element circuit. This network has 45 independent partial inductances, which are firstly evaluated, then the 10 independent elements

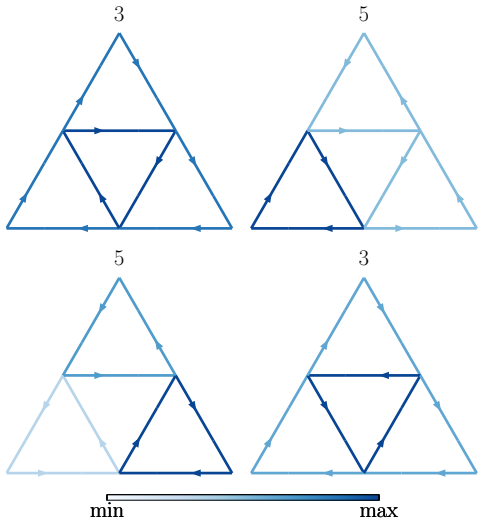

Figure 2.15: MQS current modes of the dielectric network arranged accordingly to a Sierpinsky triangle with generation number 1. Each wire has length l_w and radius $r_w = 0.1l_w$. The modes are arranged in a lexicographic order, which follows the corresponding eigenvalue. Above each mode is the order n_i of the first non-vanishing imaginary correction. Reprinted from Ref. [44]

$\kappa_h^{\perp}$	134	181	181	379
$\kappa_h^{(2)}$	-15	-5.0	-5.0	-19.0
n_i	3	5	5	3
$\kappa_h^{(n_i)}$	7.2	0.24	0.24	8.3

Table 2.1: Eigenvalues $\kappa_h^{\perp}$, second order (real) radiative correction $\kappa_h^{(2)}$, imaginary correction $\kappa_h^{(n_i)}$ of the lowest order n_i of the dielectric network of Fig. 2.12.

of the 4×4 symmetric inductance matrix $\underline{\underline{\mathrm{L}}}$ are computed. In this simple case, the calculation of the eigenvalues $k_h^{(2)}$ can be carried out with pen and paper, returning the four values listed in Tab. 2.1

The four current modes are shown in Fig. 2.15 (the second and the third mode are degenerate). These modes correspond to the MQS current density modes reported in 2.15. Then, the matrices $\underline{\underline{\Delta}}^{(2)}$ and $\underline{\underline{\Delta}}^{(n_i)}$are assembled, where $n_i = 3$ for the first and fourth mode, and $n_i = 5$ for the second and third mode. The radiative corrections $k_h^{(2)}$ and $k_h^{(n_i)}$ are provided in Tab.2.1.

Table 2.2 provides the normalized resonance frequencies and the Q factors of the four current modes of the Sierpinsky network for two different values of the permittivity, $\varepsilon_R = 100$ and $\varepsilon_R = 15.45$.

For $\varepsilon_R = 100$ the first (fundamental) resonance is located at $x_1 = 1.08$: for

$\varepsilon_R = 100$	x_1	$x_2 = x_3$	x_4	Q_1	$Q_2 = Q_3$	Q_4
the model	1.08	1.31	1.78	15	320	8.0
Comsol	1.04	1.26	–	31	280	–
$\varepsilon_R = 15.45$	x_1	$x_2 = x_3$	x_4	Q_1	$Q_2 = Q_3$	Q_4
the model	2.12	3.04	3.34	1.9	25	1.2
Comsol	2.29	2.89	–	3.9	8.3	–

Table 2.2: Normalized resonance frequencies $x_h = \omega_h/\omega_c$ and quality factors of the four modes of the dielectric network of Fig. 2.12 for $\varepsilon_R = 100$ and $\varepsilon_R = 15.45$.

$\ell_c = 10cm$ it is $\omega_1 = 3.25GHz$. The scattering peak positions and the quality factors of the four current modes have been also estimated by using Comsol Multiphysics.

The dielectric network shown in Fig. 2.12 has been excited by an electric dipole, laying on its equatorial plane, located at $3l_w$ on the left of its center, and oriented along the vertical in-plane direction. The quality factor is estimated as the inverse of the fractional bandwidth. The lumped circuit model exhibits good accuracy in locating the resonances while returning the order of magnitude of the quality factors.

The comparison is repeated for $\varepsilon_R = 15.45$, which is nearby the optical constant of crystalline Silicon. The first (fundamental) resonance is located at $x_1 = 2.12$, thus for $\ell_c = 250$nm the resonance wavelength is located within the near-infrared spectral range, $\lambda_1 = 740$nm. The relative error in the predicted resonance position (compared to its Comsol counterpart) worsens on average with respect to the previous scenario, but it remains below the 15%.

For both the investigated permittivities, in the Comsol simulation, the scattering peak associated with the fourth mode is not clearly identifiable, due to its low-quality factor. For this reason, the position of its resonance peak and its Q-factor estimate are omitted in Tab. 2.2.

The analysis of complex dielectric networks may benefit from the use of a lumped-elements approach, in terms of geometry complexity and computational costs. For example, by considering the following two networks, the first one composed of $b = 81$ thin wires interconnected accordingly to a Sierpinski triangle with generation number 3, and the second one composed of $b = 112$ thin wires, interconnected accordingly to a square grid, it is possible to evaluate all the MQS modes, resonances and Q factors of these structures in a few minutes.

The first (smallest) 21 eigenvalues of both networks are reported in Fig. 2.16. The corresponding MQS current modes are shown in Figures 2.17 and 2.18, respectively. The number reported above each mode is the order n_i of the first non-vanishing imaginary radiative correction. This number returns the power dependence of the Q factor on the size parameter, describe in Ref. [43], and it is related to the multipolar

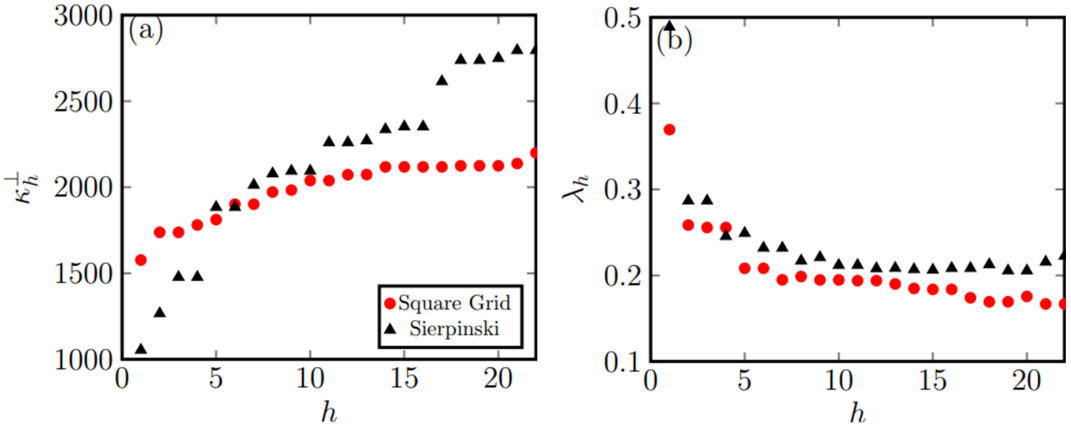

Figure 2.16: (a) First 21 eigenvalues $\kappa_h^\perp$ of a Sierpinski triangle (generation number 3) with $b = 81$, $n = 42$, $\ell = 40$, and first 21 eigenvalues $k_h^\perp$ of a 7×7 square grid with $b = 112$, $n = 64$, $\ell = 49$. (b) corresponding resonance wavelengths (in meters) assuming $\varepsilon_R = 100$ and $a = 3$cm. Reprinted from Ref. [44].

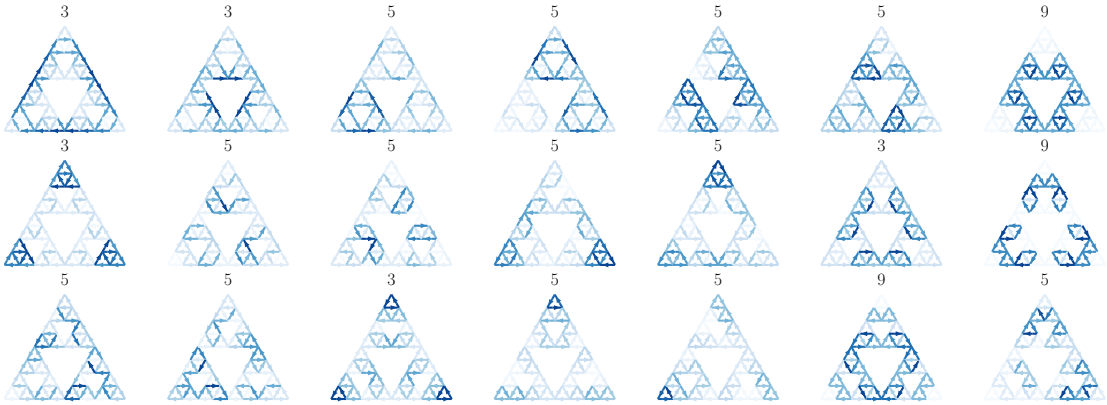

Figure 2.17: First 21 magnetoquasistatic modes of a dielectric network made of $b = 81$ thin wires interconnected accordingly to a Sierpinski triangle. Each wire has length a and radius $r_w = 0.1a$. The modes are lexicographically ordered in terms of increasing magnetoquasistatic eigenvalues. Above each mode is the order n_i of the first non-vanishing imaginary correction.Reprinted from Ref. [44].

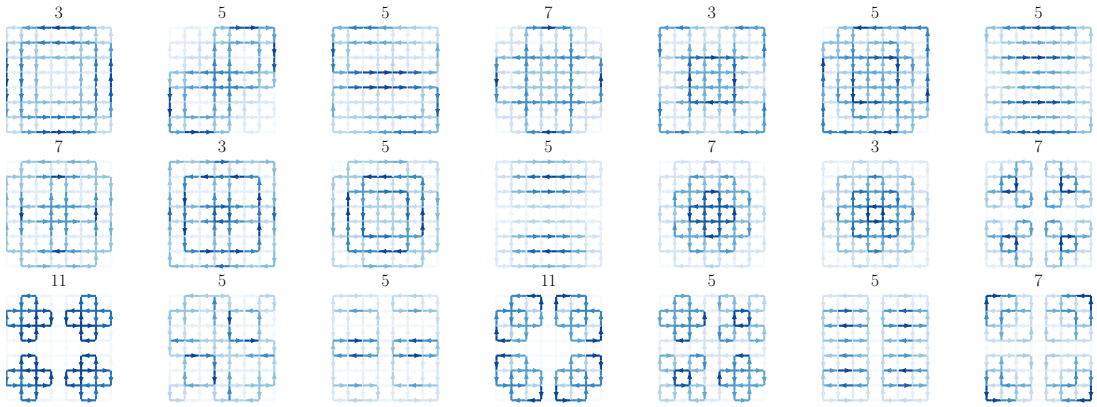

Figure 2.18: First 21 magnetoquasistatic modes of a dielectric network made of $b = 112$ thin wires arranged accordingly to a square grid. Each wire has length a and radius $r_w = 0.1a$. The modes are arranged with a lexicographic order which follows the increasing magnetoquasistatic eigenvalues. Above each mode is the order n_i of the first non-vanishing imaginary correction.Reprinted from Ref. [44].

components of the mode.

2.4 Conclusions

In this chapter, a theoretical background for the design of plasmonic and dielectric nanoresonators for biosensing applications was provided.

The first one to solve, in a closed form, the scattering problem of a sphere, was Gustav Mie in 1908. Whenever the produced particles can be assumed as spheres of radius smaller than the operating wavelength, Mie scattering theory holds true independently from the particle composition. In the last decades, novel approaches for computing Mie scattering have been developed, which, with the help of numerical calculators with high computation power, can lead to the exact prediction of the scattering from differently shaped nanomaterials.

Although the electromagnetic scattering response of an object can be fully described by Maxwell equations, it can be quite difficult to extract, with low computational efforts, preliminary predictions of the scattering behavior, in terms of modes, resonance frequencies, and quality factors of an object, which are of paramount significance in the design of new nanoresonators.

When the condition of optically/electrically small object can be applied, the complexity of Maxwell equations can be split into two more manageable units: the electroquasistatic and magneto-quasistatic approximations, *i.e.*, the same behind the mod-

eling of capacitors and inductors. The electro-quasistatic approximation covers the resonances in small particles with negative dielectric permittivity, *e.g.*, the plasmon resonances in metals at optical frequencies. The magneto-quasistatic one describes the resonance mechanism in small objects of high and positive permittivity, such as in AlGaAs and Si nanoparticles [140].

In both cases, it is possible to link the electro-quasistatic and magneto-quasistatic resonances to two linear eigenvalue problems involving compact and self-adjoint integral operators, in which the spectral parameter is the electric susceptibility χ. These eigenfunctions are the quasistatic current modes of the object, and the eigenvalues are related to its eigen-susceptibilities.

The current modes and the eigen-susceptibilities only depend on the geometry of the body, and they are material-independent. Unfortunately, both approximations are unable to predict the resonance frequency shift and the radiation Q-factor arising from the coupling with the radiation. For this purpose, closed-form expressions for the radiative corrections to the quasistatic eigenvalues and modes can be derived. These corrections only depend on the quasistatic current mode distribution.

By building on this modeling, two case studies were considered: the case of a plasmonic sphere and the case of an arbitrary connection of high-permittivity thin wires, whose EQS and MQS modes, resonance frequency shift, and Q-factors, respectively, were accurately predicted in comparison with heuristic estimates (in the EQS case) and with Comsol Multiphysics numerical simulations (in the MQS case). The quasi-static approximations with radiative corrections represent a powerful tool for the design of both plasmonic and all-dielectric nanoresonators since they provide a useful understanding of the scattering behavior of new geometries.

Chapter 3

Electromagnetic scattering by hybrid plasmonic nanoparticles

In the previous chapter, the theoretical background on the electromagnetic scattering of an object small compared to the operating wavelength was presented. When coming to the experimental practice, to achieve resonances in the visible region of the spectrum (observable to the naked eye), it is fundamental to produce objects with characteristic dimensions in the range $1 - 100\,\text{nm}$, namely *nanoparticles* (NPs).

As stated in the introduction, the fabrication of plasmonic NPs can be achieved by exploiting two different approaches: *top-down* and *bottom-up* techniques. Both approaches have their own pros and cons. In this thesis, aiming at the design, fabrication, and characterization of large-scale, low-cost, and fully predictable optical biosensors, a major focus is given to the large-scale bottom-up synthesis of plasmonic NPs. With this fabrication approach, dealing with plasmonic NPs entirely made of gold (or silver) is impractical, due to two main causes:

- the chemical reduction of gold (or silver) salts generally requires the addition of other components in the syntheses process;
- the stabilization of the synthesized NPs requires the use of chemical compounds to prevent NPs aggregation and precipitation.

Unfortunately, the concentration of these chemical species is not known *a priori* nor can it be obtained experimentally, immediately. Therefore, it is possible to introduce novel strategies by combining theory and experiments to identify the concentration of these chemical species in plasmonic NPs. As shown later, these species affect the scattering properties of the NPs.

Therefore, the term *hybrid* in this dissertation denotes plasmonic NPs synthesized in presence of, or stabilized with, other chemical compounds. Specifically, this term

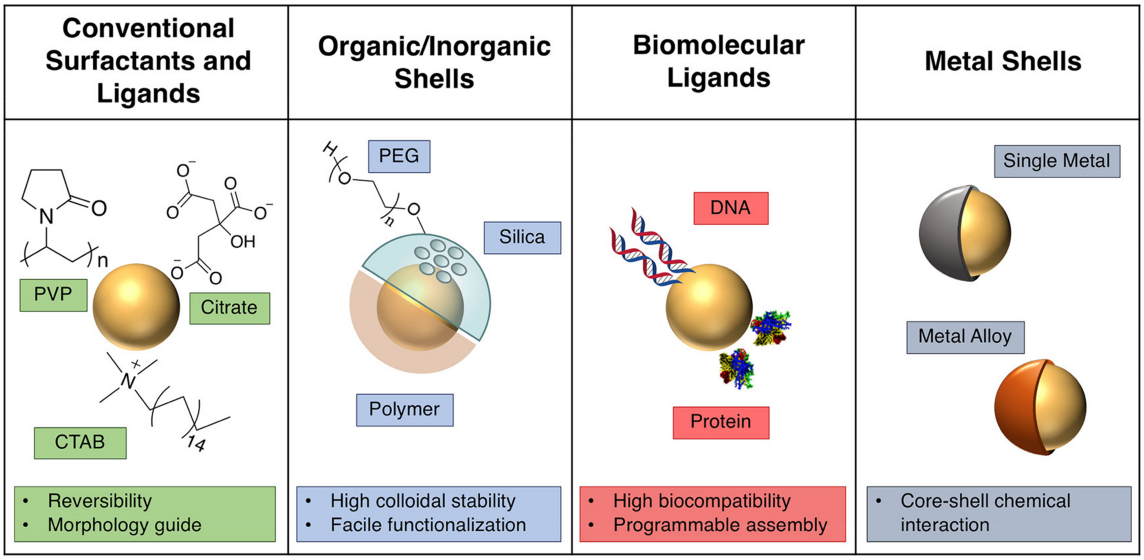

Figure 3.1: Schematic representation of different stabilizing agents involved in the preparation of *hybrid* plasmonic nanoparticles with related functions and/or characteristics. Reprinted from Ref. [141].

is used to indicate NPs obtained by the chemical reduction of a metal (inorganic) in presence of a reducing agent and/or an organic compound, or stabilizer, which interacts with or remains stacked within the NPs.

As schematized in Fig. 3.1, according to the chemical compounds adopted during the fabrication process, it is possible to classify hybrid NPs in four categories [141]:

- NPs obtained with *conventional surfactants and ligands*, for the chemical tuning of their morphology and as reversible stabilizers, such as Citrate, Polyvinylpyrrolidone (PVP), and Cetyltrimethylammonium Bromide (CTAB).
- NPs with *organic/inorganic shells*, providing them high colloidal stability and simple surface chemistry. Shells can be made of synthetic (*i.e.* Polyethylene glycol (PEG)) or natural (*e.g.*, gelatin, chitosan) polymers, or of inorganic transparent materials, such as Silica (SiO_2).
- NPs with *biomolecular ligands*, such as proteins and nucleic acids, conferring to them high biocompatibility and programmable assembly.
- NPs with metallic shells, conferring them additional optical properties (*active hybrid NPs*) or magnetic properties (*e.g.*, AuNPs with Iron shells).

In this chapter, the effects of the chemical compounds, used in the fabrication of hybrid gold NPs, on their optical properties are investigated. Mie theory, introduced in Chapter 2, is combined with the Maxwell Garnett homogenization approach,

presented in the next section, for the reverse-engineering of the electromagnetic scattering and absorption of hybrid plasmonic NPs. Moreover, also Mie-Kerker theory is introduced and applied to take into account hybrid NPs with organic/inorganic shells.

3.1 Hybrid Nanoparticles: Maxwell Garnett Theory

The determination of the average dielectric function of an object is not an easy task, since the notion of homogeneity is not always valid. In the case of hybrid NPs, the object of this chapter, the very complex interactions between reduced metal salts and molecules, involved in the chemical process, can be neglected, in favor of a simpler homogenization method.

During the past century, many different approximation strategies to derive the average dielectric function of non-homogeneous objects small compared to the wavelength have been proposed, but the most accredited and adopted one was proposed by Maxwell Garnett in 1904 [142, 13].

Consider, as a model, a two-component mixture made of a homogeneous *matrix* of dielectric permittivity ε_m with *inclusions* of dielectric permittivity ε. The inclusions are assumed identical in composition and shape but can be different in size. The electric field $\mathbf{E}$ can be obtained from a macroscopic field by averaging over many molecules.

By considering inclusions in the volume V, which still contains many inclusions, it is still possible to evaluate an average electric field $\langle \mathbf{E} \rangle$ in V around the point $\mathbf{x}$ as:

$$\langle \mathbf{E}(\mathbf{x}) \rangle = \frac{1}{V} \int_V \mathbf{E}(\mathbf{x} + \xi) d\xi. \tag{3.1}$$

In these conditions, $\langle \mathbf{E} \rangle$ still denotes a macroscopic field, but coarsely grained. The volume V is, therefore, made of the matrix volume and all its inclusions, which enables the following splitting of Equation 3.1:

$$\begin{aligned} \langle \mathbf{E}(\mathbf{x}) \rangle &= (1-f)\langle \mathbf{E}_m(\mathbf{x}) \rangle + f \sum_k w_k \langle \mathbf{E}_k(\mathbf{x}) \rangle \\ \langle \mathbf{E}_m(\mathbf{x}) \rangle &= \frac{1}{V_m} \int_{V_m} \mathbf{E}(\mathbf{x} + \xi) d\xi, \qquad \langle \mathbf{E}_k(\mathbf{x}) \rangle = \frac{1}{v_k} \int_{v_k} \mathbf{E}(\mathbf{x} + \xi) d\xi, \end{aligned} \tag{3.2}$$

where V_m is the volume of the matrix, v_k the volume of the $k-th$ inclusion, $\langle \mathbf{E}_m(\mathbf{x}) \rangle$ is the average electric field of the matrix and $\langle \mathbf{E}_k(\mathbf{x}) \rangle$ the average electric field of the

k-th inclusion, f is the volume fraction of the inclusions, w_k is f_k/f, $w_k = f_k/f$, and $f_k = v_k/V$.

The average polarization can be expressed as:

$$\langle \mathbf{P}_m(\mathbf{x}) \rangle = (1-f)\langle \mathbf{P}_m(\mathbf{x}) \rangle + f \sum_k w_k \langle \mathbf{P}_k(\mathbf{x}) \rangle. \tag{3.3}$$

Assuming that the constitutive relation in Equation 2.9 applies for both matrix and inclusions, and given the corresponding susceptibilities $\chi_m = \varepsilon_m - 1$ and $\chi = \varepsilon - 1$, it is possible to write their average polarizations as:

$$\langle \mathbf{P}_m(\mathbf{x}) \rangle = \varepsilon_0 \chi_m \langle \mathbf{E}_m(\mathbf{x}) \rangle, \qquad \langle \mathbf{P}_k(\mathbf{x}) \rangle = \varepsilon_0 \chi \langle \mathbf{E}_k(\mathbf{x}) \rangle. \tag{3.4}$$

It is possible to sum up the two constitutive equations, by introducing the average susceptibility tensor $\boldsymbol{\chi}_{av}$ of the composite medium, which does not depend on the position if the medium is statistically homogeneous:

$$\langle \mathbf{P}(\mathbf{x}) \rangle = \varepsilon_0 \boldsymbol{\chi}_{av} \cdot \langle \mathbf{E}_m(\mathbf{x}) \rangle. \tag{3.5}$$

By combining the last two equations with Equation 3.4:

$$(1-f)(\boldsymbol{\varepsilon}_{av} - \varepsilon_m \mathbf{1}) \cdot \langle \mathbf{E}_m(\mathbf{x}) \rangle + f \sum_k w_k (\boldsymbol{\varepsilon}_{av} - \varepsilon \mathbf{1}) \cdot \langle \mathbf{E}_k(\mathbf{x}) \rangle = 0, \tag{3.6}$$

with $\boldsymbol{\varepsilon}_{av}$ and $\mathbf{1}$ being the average dielectric tensor and the unit tensor, respectively.

Since the susceptibility tensor is independent of the position, also the dielectric tensor must be independent of it, therefore, $\langle \mathbf{E}_m(\mathbf{x}) \rangle$ and $\langle \mathbf{E}_m(\mathbf{x}) \rangle$ must be related by a linear relationship of the type

$$\mathbf{E}_k = \boldsymbol{\lambda}_k \cdot \mathbf{E}_m, \tag{3.7}$$

where $\boldsymbol{\lambda}_k$ is a tensor whose principal components are:

$$\lambda_j = \frac{\varepsilon_m}{\varepsilon_m + L_j(\varepsilon - \varepsilon_m)} \qquad (j = 1, 2, 3), \tag{3.8}$$

where L_j denotes the geometrical factors associated with the shape of the inclusions (for a sphere, $L_1 = L_2 = L_3$; for an ellipsoid, $L_1 = L_2 \,\&\, L_1 \neq L_3$ [13]).

Assuming that Equation 3.7 holds also for the average electric fields, namely

$\langle \mathbf{E}_k(\mathbf{x}) \rangle = \boldsymbol{\lambda}_k \langle \mathbf{E}_m(\mathbf{x}) \rangle$, Equation 3.6 becomes:

$$(1-f)(\boldsymbol{\varepsilon}_{av} - \varepsilon_m \mathbf{1}) + f(\boldsymbol{\varepsilon}_{av} - \varepsilon \mathbf{1}) \cdot \sum_k w_k \boldsymbol{\lambda}_k = 0. \tag{3.9}$$

In Equation 3.9, the only unknown is the sum over the product between the principal components of the tensor $\boldsymbol{\lambda}_k$, which depends on the shape and orientation of the inclusion, and the ratio of the $k-th$ inclusion volume over the volume of all the inclusions.

Assuming the inclusions to be ellipsoids with uncorrelated volume, shape, and/or orientation and with equally probable orientations:

$$\begin{aligned} \sum_k w_k \boldsymbol{\lambda}_k &\simeq \beta \mathbf{1}, \\ \beta &= \int\int \mathcal{P}(L_1, L_2) \frac{\lambda_1 + \lambda_2 + \lambda_3}{3} dL_1 dL_2, \end{aligned} \tag{3.10}$$

where $\mathcal{P}(L_1, L_2)$ denotes the shape probability distribution function [13].

With Equation 3.10, the average dielectric function becomes:

$$\varepsilon_{av} = \frac{(1-f)\varepsilon_m + f\beta\varepsilon}{1 - f + f\beta}. \tag{3.11}$$

Equation 3.11 must be used carefully since it requires that the dielectric functions of the matrix and of the inclusions are decided upstream.

In fact, if they are interchanged they would lead to a different average dielectric function. Moreover, to understand the physical meaning of this approximation, it is important to study the behavior in the two limit cases. In the case of $f \to 1$ (inclusions occupying the whole volume V):

$$\lim_{f \to 1} \varepsilon_{av} = \varepsilon,$$

while, if $f \to 0$ (no inclusions within the matrix in the volume V):

$$\lim_{f \to 0} \varepsilon_{av} = \varepsilon_m.$$

Equation 3.11 can be further generalized to multicomponent inhomogeneous objects, in which the average dielectric function becomes:

$$\varepsilon_{av} = \frac{(1-f)\varepsilon_m + \sum f_j \beta_j \varepsilon_j}{1 - f + \sum f_j \beta_j}. \tag{3.12}$$

where $f = \sum f_j$, β_j is obtained from Equations 3.8-3.10 by simply substituting ε with ε_j, and f_j denotes the volume fraction of the $j-th$ inclusion with dielectric function ε_j.

Finally, the Maxwell Garnett approximation can be derived by further assuming spherically-shaped inclusions. With this approximation, which still well describes the optical response of hybrid NPs, β coefficient used to describe the $\sum_k w_k \boldsymbol{\lambda}_k$ simplifies to

$$\beta = \frac{\varepsilon_m}{\varepsilon + 2\varepsilon_m}$$

and, therefore, Equation 3.9 simply becomes

$$\varepsilon_{av} = \varepsilon_m \left[1 + \frac{3f\left(\frac{\varepsilon-\varepsilon_m}{\varepsilon+2\varepsilon_m}\right)}{1 - f\left(\frac{\varepsilon-\varepsilon_m}{\varepsilon+2\varepsilon_m}\right)} \right]. \tag{3.13}$$

3.2 Identification of the optical properties of hybrid Nanoparticles

The accurate prediction of the LSPR absorption spectra and corresponding peaks of hybrid NPs is a problem of interest for biosensing applications [106]. In fact, it is possible to carefully predict the spectra of hybrid NPs after the identification of their average dielectric constant. The theoretical fitting of the experimental absorption spectrum of hybrid NPs can be performed by minimizing the norm of the difference between theoretical and experimental absorption spectra. This optimization allows the derivation of the inclusions volume fraction f in hybrid NPs. Genetic Algorithm (GA) can be used to solve the abovementioned minimization problem [12, 143]. In this section, this methodology is introduced.

3.2.1 Genetic Algorithm

Many are the available tools for solving optimization problems. Among them, the genetic algorithm (GA), useful for both constrained and unconstrained optimization problems, is based on natural selection, the process driving biological evolution. This algorithm iteratively modifies a population of individual solutions. At each step, individuals are randomly selected from the current population to be *parents* and are used to produce the *children* of the next generation. Over successive generations, the population *evolves* towards an optimal solution. The GA well applies to problems in which the objective function (function to be minimized), also denoted as *fitness*

function is discontinuous, non-differentiable, stochastic, or highly nonlinear [144]. Three main types of rules at each step are used in this algorithm to create the next generation from the current population:

- *Selection rules* select the individuals, called parents, that contribute to the population of the next generation.
- *Crossover rules* combine two parents to form children for the next generation.
- *Mutation rules* apply random changes to individual parents to form children.

The GA differs from the classical optimization algorithms, based on derivatives, for two main reasons. First, differently from classical algorithms that generate a single point for each iteration, GA generates a population of points for each iteration, whose best point approaches an optimal solution. Second, while classical algorithms select the subsequent point in the sequence in a deterministic way, the GA selects the subsequent population using random number generators. First, an initial population of elements, whose number can be opportunely decided, is randomly by the algorithm, it is always possible to set some boundaries in which they should be located. At each step, the GA derives the *children* for the next generation starting from the current population. More precisely, only some elements of the current population are selected as *parents* for the next generation. Generally, individuals that have better fitness values as parents are selected. Three are the main types of children for the next generation (Figure 3.2):

- *Elite children* are the individuals in the current generation with the best fitness values.
- *Crossover children* are created by combining the vectors of a pair of parents.
- *Mutation children* are created by introducing random changes, or mutations, to a single parent.

Elite children are obtained from the best fitness of the previous generation, and for this reason, they automatically survive to the next generation. Crossover children arise from the combination of parent pairs in the current population. At each coordinate of the child vector, there is a crossover function, which randomly selects an entry (a *gene*), at the same coordinate from one of the two parents and assigns it to the child. The crossover function is designed to create the child as a random weighted average of the parents. Finally, mutation children are created by randomly changing the genes of individual parents. By default, for unconstrained problems,

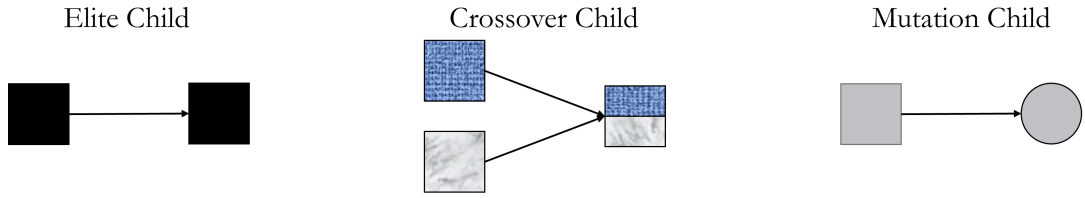

Figure 3.2: Schematic representation of the three main types of children of the GA: elite, on the left; crossover, in the middle; mutation, on the right.

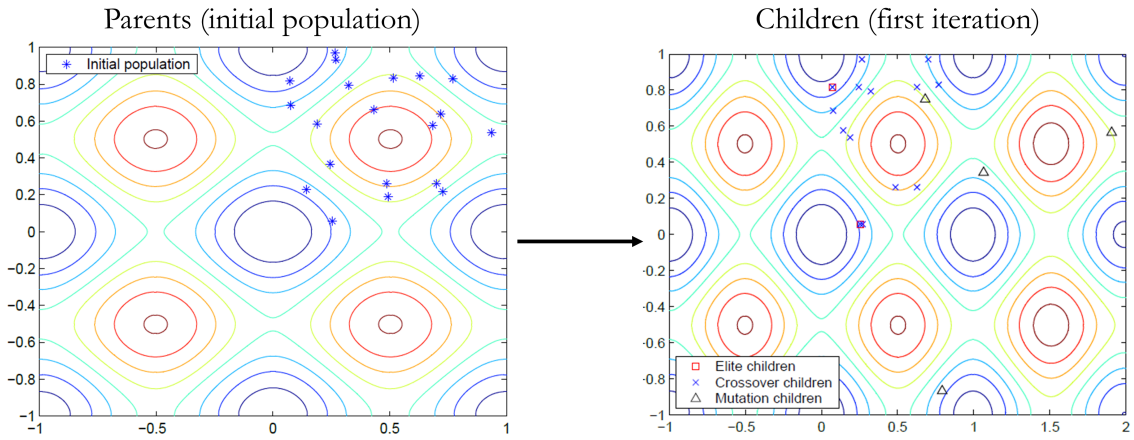

Figure 3.3: On the left, initial random population ($n = 20$) generated in Matlab® with the Optimization Toolbox for the Rastrigin's function and elite (red squares), crossover (blue crosses), and mutation (black triangles) children second generation after the first iteration. Blue and red circles denote the minima and maxima locations, respectively, of Rastrigin's function.

the algorithm adds a random vector from a Gaussian distribution to the parent. For bounded or linearly constrained problems, the child remains feasible. Figure 3.3 shows the children of the initial population (parents), that is, the population in the second generation (first iteration), and indicates whether they are elite, crossover, or mutation children. Several conditions, denoted as *stop(ping) conditions* can be imposed to halt a GA optimization:

- *Generations* — The algorithm stops when the number of generations reaches the value of Generations.
- *Time limit* — The algorithm stops after running for an amount of time in seconds equal to the Time limit.
- *Fitness limit* — The algorithm stops when the value of the fitness function for

the best point in the current population is less than or equal to the Fitness limit.

- *Stall generations* — The algorithm stops when the average relative change in the fitness function value over Stall generations is less than Function tolerance
- *Stall time limit* — The algorithm stops if there is no improvement in the objective function during an interval of time in seconds equal to the Stall time limit.
- *Stall test* — The stall condition is either average change or geometric weighted. For geometric weighted, the weighting function is $1/2n$, where n is the number of generations prior to the current. Both stall conditions apply to the relative change in the fitness function over Stall generations.
- *Function Tolerance* — The algorithm runs until the average relative change in the fitness function value over Stall generations is less than Function tolerance.
- *Nonlinear constraint tolerance* — Nonlinear constraint tolerance is not used as a stopping criterion. It is used to determine the feasibility with respect to nonlinear constraints. Also, a point is feasible with respect to linear constraints when the constraint violation is below the square root of Nonlinear constraint tolerance.

Therefore, upon verification of one of these conditions, the algorithm stops. Generally, the fitness limit condition is the criterion chosen to stop the optimization. If the algorithm stops because of one of the other conditions, it means that the parameters can be improved to achieve the desired fitness limit. It is possible to control how the GA creates the next generation in terms of *elite count*, *crossover fraction*, and *mutation fraction*. The elite count represents the number of individuals with the best fitness values in the current generation that are guaranteed to survive to the next generation. The default value of the elite count is 2. Setting the Elite count to a high value causes the fittest individuals to dominate the population, which can make the search less effective. The crossover fraction indicates the fraction of individuals in the next generation created by crossover. Finally, the mutation fraction can be evaluated from the difference between the population size and the sum of the elite count and crossover fraction.

3.2.2 Reverse Engineering based on Genetic Algorithm

The absorption of hybrid AuNPs can be theoretically predicted from the combination of Mie Theory with the Maxwell Garnett homogenization approach. This can be done under the hypothesis of *non-interacting NPs*, which, given the radius of the NP (r) and the interparticle distance (d), means $r \leq d$.

The hypothesis of non-interacting hybrid NPs holds true for diluted stabilized suspension of NPs, for non-aggregated NPs on a substrate and/or embedded in a polymeric matrix, or, more in general, for systems whose density/concentration is low enough to avoid the NPs optical interaction.

In this condition, all hybrid NPs can be modeled as complex systems made of two or more constituents, depending on the number of compounds involved in their synthesis. The identification of the average dielectric function of the hybrid NP can be made starting from the knowledge of the permittivities ε_m of the matrix, namely gold or silver, and of the molecular compounds used to stabilize them ε. The chemical compounds are modeled as spherical inclusions within the metallic matrix. Finally, given the experimental absorption spectra, it is possible to define the following objective, or fitness, function $F(f)$:

$$F(f) = \|C_{abs_{th}}(\lambda, \varepsilon_{av}(f)) - C_{abs_{exp}}(\lambda)\|, \tag{3.14}$$

where λ is the operating wavelength, $C_{abs_{th}}$ and $C_{abs_{exp}}$ are the theoretical and experimental absorption spectra, respectively, and f is the volume fraction occupied by the inclusions.

In Equation 3.14, the unknown parameter is represented by the volume fraction f of the inclusions. In the experimental practice, in fact, it is non-trivial to derive the fraction of chemical compounds, which effectively react with gold and silver salts during their chemical reduction. Therefore, by optimizing the objective function by means of the GA, the inclusions volume fraction can be derived and the experimental absorption curve can be exactly fitted.

In particular, spherical inclusions can be modeled as a gaussian distribution $N(f)$ of spheres within the single plasmonic particle, expressed as

$$N(f) = \frac{1}{\sigma\sqrt{2\pi}} e^{-\frac{(f-\mu)^2}{2\sigma^2}}, \tag{3.15}$$

where μ and σ denote the mean and standard deviation of the inclusions volume fraction. The hybrid NPs modeling is schematized in Figure 3.4. The goal of optimization is to search for the optimal values of μ and σ that minimize the standard

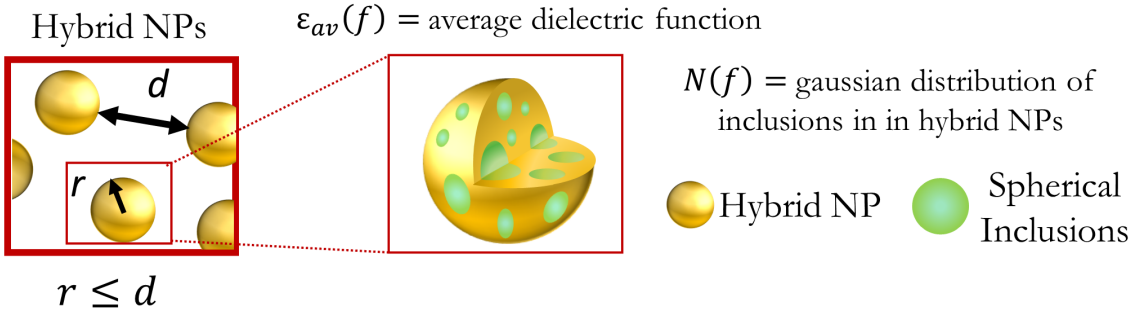

Figure 3.4: Schematic representation of the hypothesis made for the description of hybrid NPs, namely non-interacting NPs and gaussian distribution of spherical inclusions.

deviation between the theoretical solution and the experimental absorption spectra.

The condition on μ remains the same imposed by the Maxwell Garnett condition in Equation 3.13, *i.e.* $f \in [0, 1]$. The GA takes as an input a function dependent on these two parameters and returns the optimal values that minimize it. The adopted optimization algorithm, developed in Matlab ®, for the description of hybrid NPs is schematized in Figure 3.5. The input parameters are:

- hybrid NPs size/size distribution;
- experimental absorption spectrum;
- dielectric permittivity of the matrix (gold and/or silver);
- dielectric permittivity of the inclusions.

Once all these parameters are known, it is possible to run the genetic algorithm with the Matlab® global optimization toolbox as a function of a vectorial variable $[\mu, \sigma]$. T

he convergence of the algorithm is achieved when the norm of the difference between $C_{abs_{th}}$ and $C_{abs_{exp}}$ is lower or equal to the imposed fitness limit. The fitness limit imposed for this modeling is 0.1, corresponding to a difference between the predicted and the experimental absorption spectra lower or equal to 10%. This fitness limit is considered accurate enough for further studies. The outcome of this model provides an accurate estimation of the mean value and standard deviation of the inclusions volume fraction.

When the input parameters or the hypothesis are not sufficiently precise, no convergence can be reached, and returning back to them becomes a necessary step for

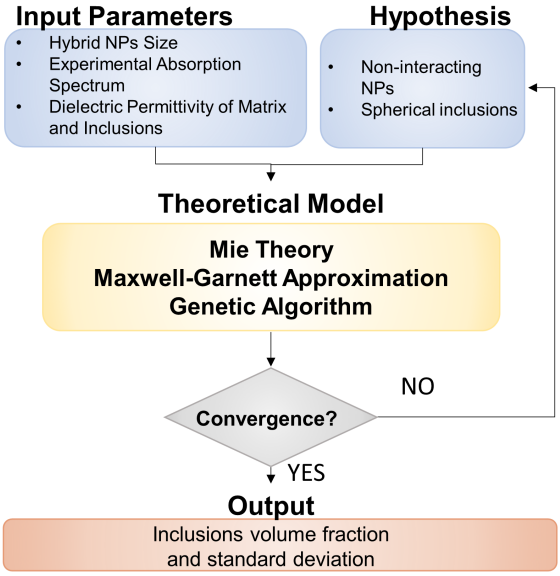

Figure 3.5: Schematic representation of the iterative optimization approach used to fit the experimental absorption spectra of Hybrid NPs.

further improvement. In the next section, two case studies are considered for the direct application of this model to the fitting of hybrid AuNPs optical spectra.

3.3 Case Studies

In this section, the abovementioned reverse engineering approach is applied to hybrid plasmonic NPs synthesized *via* bottom-up technique. More precisely, the classical Turkevich synthesis [145] for citrate-capped AuNPs and the more biocompatible pegylated AuNPs [146], which are the most common ones and whose optical response prediction can be significantly improved with the proposed method.

3.3.1 Citrate-capped gold nanoparticles

The most adopted method for the controlled synthesis of spherical plasmonic NPs is the citrate reduction method. Citrate anions operate the reduction of metal ions to atoms and stabilize them, thus forming colloidal NPs. Citrate-capped AuNPs have been largely exploited for biosensing applications since they are very stable in solution, even for long periods of time. Moreover, they represent the intermediate product before further treatments or functionalization steps [141].

In the past, the exact interaction between citrate ions and gold was not well understood. Recent studies have shown that AuNPs alone would have a positive

charge during the reduction, then this charge is neutralized and made negative by the citrate ions' adsorption on their surface [147]. The negative charges guarantee AuNPs stability thanks to the electrostatic repulsion.

Turkevich synthesis is herein proposed to effectively show the efficiency of the proposed model.

Experimental part

Chemicals - Tetrachloroauric acid trihydrate ($HAuCl_4 \cdot 3H_2O$), trisodium citrate dihydrate ($C_6H_9Na_3O_9$), were purchased from Merck KGaA (DE).

Synthesis of citrate-capped AuNPs - All glassware was cleaned with *Aqua Regia*, a mixture of nitric and hydrochloric acids (1 : 3 v/V), prior to its use. $HAuCl_4 \cdot 3H_2O$ was dissolved in MilliQ water (0.25 mM, 50 mL) and was heated under stirring on a magnetic hot plate up to boiling. After boiling *incipit* of the solution, citrate was added (0.06 M, 0.875 mL). The solution color turned from yellow to grey, then pink, and after 10 min it became red, denoting the formation of colloidal citrate-capped AuNPs.

Citrate-capped AuNPs characterization - The hydrodynamic diameter (size) and the surface charge (ζ-potential) of NPs dispersed in water, were measured by dynamic light scattering (DLS) using a Zetasizer Nano ZS instrument (Malvern Instruments, Malvern, U.K.) equipped with a He-Ne laser [633 nm, fixed scattering angle of 173°, room temperature (25°)]. The experimental absorption spectra of AuNPs were recorded using a Cary 100 (VARIAN), in the range between 400-900 nm.

Transmission Electron Microscopy - The morphology of citrate-capped AuNPs was performed by using an FEI Tecnai 12 transmission electron microscope (TEM) FEI Company, Hillsboro, OR). The NPs were purified by centrifuge and incubated for 10 min on a standard copper grid (100 mesh) covered with a Formvar film. Next, the drop was removed, and the grid was air-dried overnight at room temperature. From TEM images, a particle analysis was performed by ImageJ software to estimate the AuNPs mean radius (r).

Results

Citrate-capped AuNPs were characterized both in terms of size and ζ-potential. The obtained results are reported in Table 3.1. Moreover, TEM imaging was performed

to verify the spherical shape of the prepared AuNPs.

DLS measurements provide the NPs hydrodynamic diameter, while the average radius can be extrapolated from TEM images (see Figure 3.6). The two measured average diameters are in excellent agreement. However, the two standard deviations are significantly different. This difference finds an explanation in the different methodologies used for morphological characterization. While DLS measurements are performed on a large amount of NPs, directly in solution, TEM images of only a few particles can be acquired and analyzed by using the Image J software. Mainly, TEM characterizations are performed to confirm the spherical shape of the obtained NPs. Then DLS measurements, exhibiting one single peak, can be performed to attribute the exact average size and size distribution to the synthesized NPs.

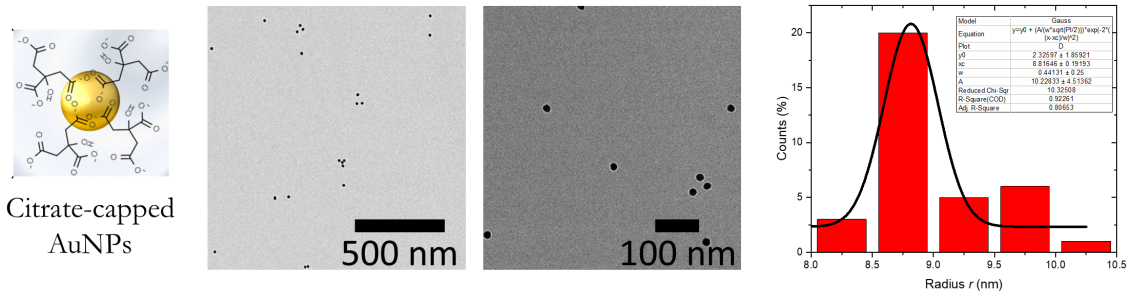

Figure 3.6: Synthesized citrate-capped AuNPs: schematic representation; TEM images at different magnifications for their morphological evaluation; size distribution histogram obtained by ImageJ freeware software, plotted in OriginPro and fitted by a gaussian curve.

Therefore, the radius $r = 7.5$ nm of the prepared AuNPs was considered for the theoretical modeling. Then, the measure of the absorption spectrum was performed by UV-Vis spectrometer in the range $400 - 900$ nm, upon suitable dilution of the NPs to avoid instrumental saturation and have maximum absorption intensity in between $[0.2, 1.0]$ (a.u.), which is the range in which the Lambert-Beer law holds.

DLS size (nm)	ζ-potential (mV)	TEM radius (nm)
15 ± 5	-29 ± 6	8.8 ± 0.2

Table 3.1: Hydrodynamic diameter, and ζ-potential of citrate-capped AuNPs (obtained from DLS) and radius r estimation by TEM images.

The measured absorption spectrum is reported in Figure 3.7 (black-dashed line). It exhibits LSPR wavelength (λ_{max}) at 524 nm. By applying the standard Mie theory to a homogeneous AuNP of radius 7.5 nm, the predicted absorption peak has $\lambda_{max} =$

519 nm, which is good in first approximation. However, the functionalization of AuNPs generally leads to a few nanometers of redshift. Therefore, a better prediction could ensure higher accuracy in the theoretical prediction of the LSPR redshift as a function of the surrounding medium refractive index.

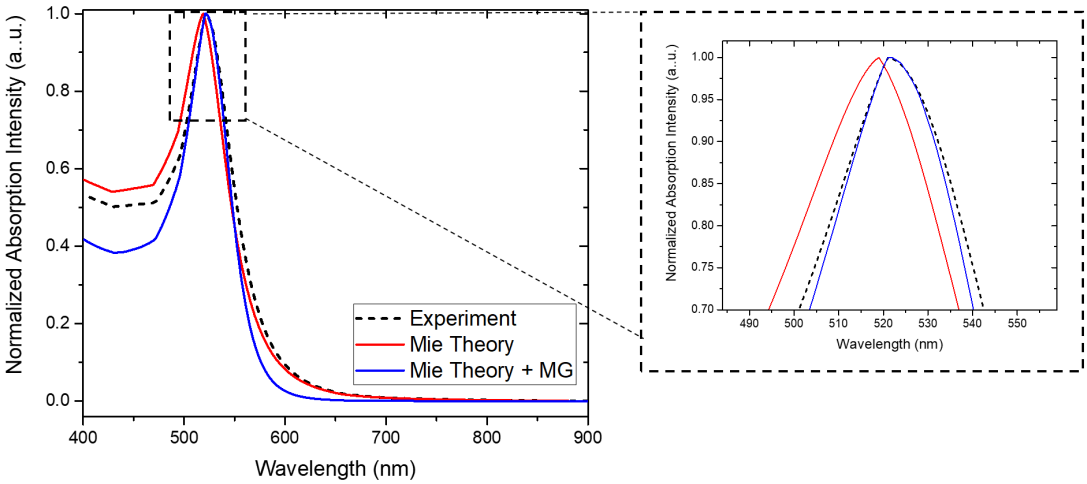

Figure 3.7: Synthesized citrate-capped AuNPs: experimental absorption spectrum (black-dashed line), Mie Theory prediction (red solid line), MG-modified Mie Theory (blue solid line).

At this stage, the application of the Maxwell Garnett (MG) homogenization in combination with Mie Theory requires the knowledge of the matrix and inclusions refractive indices.

Concerning the matrix, namely gold, the optical constants were derived by Johnson and Christie [148] in 1972, while the refractive index of citrate was assumed as ($n_{Citrate} = 1.39423$). Finally, the parameter f was derived by applying the GA.

For Turkevich citrate-capped AuNPs, the best parameters to minimize ($\%_{error} < 10\%$) the norm between the experimental and theoretical absorption spectra resulted to be $\mu = 0.05$ and $\sigma = 0.001$. Therefore, citrate-capped AuNPs can be well approximated as gold spheres containing citrate inclusions with a volume fraction $f = (5 \pm 0.1)\%$.

By applying these parameters to the Mie theory combined with the MG approximation, a more accurate prediction of λ_{max} was finally achieved (see blue solid line in Figure 3.7).

Another parameter that is important to predict is the full width at half maximum, which, as stated in the previous chapter, is inversely proportional to the quality factor Q of the nanoresonator. From the experiment, the estimated FWHM is 82 nm, which

becomes half of the estimation by Mie theory, and is quite in good agreement with the proposed approach (see Table 3.2). The mismatch between the FWHM of the experimental and theoretical absorption spectra arises from the size distribution of the synthesized spherical AuNPs. However, due to the intrinsic non-fully-homogeneous nature of bottom-up approaches, the agreement between the proposed model and the experimental observation is considered more than satisfactory. Moreover, a gaussian distribution of NPs, as done for the inclusions, can be implemented in the model to reduce the partial mismatch between theory and experiments.

	Experiment	Mie Theory	**Mie Theory+MG**
λ_{max} (nm)	524	519	524
FWHM (nm)	82	43	61

Table 3.2: LSPR wavelength (λ_{max}) and full width at half maximum (FWHM) comparison between experimental, Mie prediction, MG-modified Mie prediction for citrate-capped AuNPs.

It should be now clear the effect of citrate on hybrid AuNPs. On average, it was shown that it led to a redshift of the resonance, compared to a homogeneous AuNP of the same size. This was confirmed by the predicted absorption spectra obtained from the Mie theory and from the Mie theory combined with MG approximation. Moreover, a damping of the resonance was observed causing a broadening of the LSPR peak, as confirmed by the increased value of the FWHM.

Whether peak resonance redshift and broadening represent a disadvantage or not strongly depends on the application. Generally speaking, inherent-based LSPR optical transducers require that the peak is as sharper as possible, in order to improve the final sensitivity. On the contrary, plasmonic NPs acting as external signal amplifiers should exhibit the broadest resonances to maximize the probability of matching the localized electromagnetic field enhancement with the external signal spectral properties [17].

3.3.2 Gold nanoparticles with PEG inclusions

Besides citrate, polyethylene glycol (PEG) represents another usual chemical compound, leading to PEG-stabilized NPs for a large range of applications [146, 94]. The generally recognized advantage of PEG as a stabilizer is its biocompatibility for *in-vivo* applications. In fact, PEG improves gold biocompatibility, by imbuing resistance to protein adsorption and uptake from the phagocytic system [149]. In many

theranostic (therapeutics+diagnostics) applications, Ag and AuNPs can be functionalized with thiolated-PEG ligands, where thiol groups (-SH) can form strong metal–S bonds. These bonds enormously improve their stability even in the highly complex media [71]. Also for PEG-stabilized plasmonic spheres, it is possible to apply the MG-modified Mie theory.

Experimental part

Chemicals - Tetrachloroauric acid trihydrate ($HAuCl_4 \cdot 3H_2O$), polyethylene glycol diacid (DPEG, MW = 600 Da), and sodium borohydride ($NaBH_4$) were purchased from Merck KGaA (DE).

Synthesis of PEG-stabilized AuNPs - All glassware was cleaned with *Aqua Regia*, a mixture of nitric and hydrochloric acids (1 : 3 V/V), prior to its use. PEG-stabilized AuNPs were synthesized by using a one-pot method, in which DPEG was used as the stabilizer molecule in spite of the citrate molecules. The reduction is here performed at room temperature (RT) with the aid of a strong reducing agent, namely $NaBH_4$. Briefly, pure DPEG (600 µL) was mixed to $HAuCl_4 \cdot 3H_2O$ (0.25 mM, 25 mL) under vigorous stirring for 10 min. Afterward, $NaBH_4$ (10 mM, 20 mL) was added at once. The solution color instantaneously turned from yellow to red.

PEG-stabilized AuNPs characterization - The size and the ζ-potential of NPs dispersed in water, were measured by DLS. The experimental absorption spectra of the AuNPs were recorded in the range between 400-900 nm, as reported in section 3.3.1. The morphology of PEG-stabilized AuNPs was observed by TEM imaging (see section 3.3.1).

Results

PEG-stabilized AuNPs were synthesized by the abovementioned method and characterized both in terms of size and ζ-potential. The obtained results are summarized in Table 3.3. Moreover, to verify the spherical shape of the prepared AuNPs, TEM imaging was performed. DLS measurements provided the NPs hydrodynamic diameter, while from TEM images (see Figure 3.8), the average radius was extrapolated by image analysis.

The radius $r_{\text{PEG-AuNPs}}$ of the obtained PEG-AuNPs was 3nm. Then, the measure of the absorption spectrum was performed by UV-Vis spectrometer in the range $400 - 900$ nm, upon suitable dilution of the NPs. PEG-stabilized AuNPs resulted in

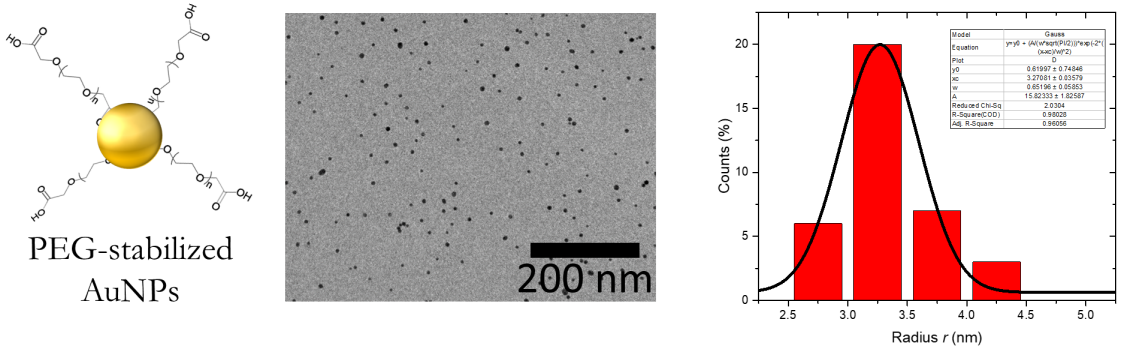

Figure 3.8: Synthesized PEG-stabilized AuNPs: schematic representation; TEM images at different magnifications for their morphological evaluation; size distribution histogram obtained by ImageJ freeware software, plotted in OriginPro and fitted by a gaussian curve.

a much smaller size than citrate NPs due to the reducing agent. One of the main drawbacks of this synthesis compared to the Turkevich method is that it leads to NPs whose size cannot be easily tuned.

DLS size (nm)	ζ-potential (mV)	TEM radius (nm)
6 ± 3	-25 ± 9	3.3 ± 0.3

Table 3.3: Hydrodynamic diameter, and ζ-potential of PEG-stabilized AuNPs (obtained from DLS) and radius r estimation by TEM images.

The measured absorption spectrum (not shown here) exhibits LSPR wavelength (λ_{max}) at 525 nm. By applying the standard Mie theory to a homogeneous AuNP of radius 3.0 nm, the predicted absorption peak has $\lambda_{max} = 519$ nm with a lower intensity than the ones of 7.5 nm reported before.

However, the functionalization of AuNPs generally leads to a few nanometers of redshift. Therefore, the 5 nm redshift is only ascribable to PEG molecules surrounding and, probably, entrapped within the AuNP during the chemical reduction. By assuming the refractive index of PEG ($n_{PEG} = 1.468$), much higher than citrate, it was finally possible to derive the parameter f with the application of the GA.

For PEG-stabilized AuNPs, the best parameters to minimize ($\%_{error} < 10\%$) the norm between the experimental and theoretical absorption spectra resulted to be $\mu = 0.1$ and $\sigma = 0.025$, which mean that PEG-stabilized AuNPs can be well approximated as gold spheres containing PEG inclusions with a volume fraction $f = (10 \pm 2.5)\%$.

By applying these parameters to the Mie theory combined with the MG approximation, a more accurate prediction of λ_{max} was finally achieved. The experimental

FWHM was 117 nm, and differently from the Mie theory as it is, its theoretical prediction resulted to be in quite good agreement with the Mie theory combined with MG approximation (see Table 3.4).

	Experiment	Mie Theory	**Mie Theory+MG**
λ_{max} (nm)	525	519	525
FWHM (nm)	117	60	93

Table 3.4: LSPR wavelength (λ_{max}) and full width at half maximum (FWHM) comparison between experimental, Mie prediction, MG-modified Mie prediction for PEG-stabilized AuNPs.

Also for PEG-stabilized AuNPs, on average, a significant redshift of the resonance, compared to a homogeneous AuNP of the same size was observed. Moreover, PEG inclusions caused a broadening of the LSPR peak, as confirmed by the increased value of the FWHM.

By using this model, further functionalization with biomolecules of these hybrid AuNPs can be in principle predicted to derive the functionalization yield, sensitivity, and figure of merit of the designed biosensor.

3.4 Coated hybrid nanoparticles: Mie-Kerker Theory

Mie-Kerker theory can be combined with the MG approximation to take into account the formation of shells around the plasmonic NPs. As shown in the first section of this chapter, the addition of an organic/inorganic/metallic shell around the plasmonic NPs can provide the hybrid NPs with increased functionalities, such as enhanced colloidal stability, additional resonances, the capability of releasing molecules, in response to an external stimulus, such as pH, temperature, ionic strength, and so on...

The first theoretical description of coated nanoparticles was provided by Kerker in 1951 [150], who provided the analytical solution to the problem of scattering from a sphere with a concentric spherical shell, known as Mie-Kerker theory. A schematic representation of a coated sphere is reported in Figure 3.9.

The coated sphere can be assumed as a core with a concentric spherical shell. The orientation of the incident plane wave is also reported in the same Figure. The inner sphere, the shell, and the surrounding medium are denoted as regions 1, 2, and 3, respectively, while the inner and outer radii of the first two regions are denoted as a

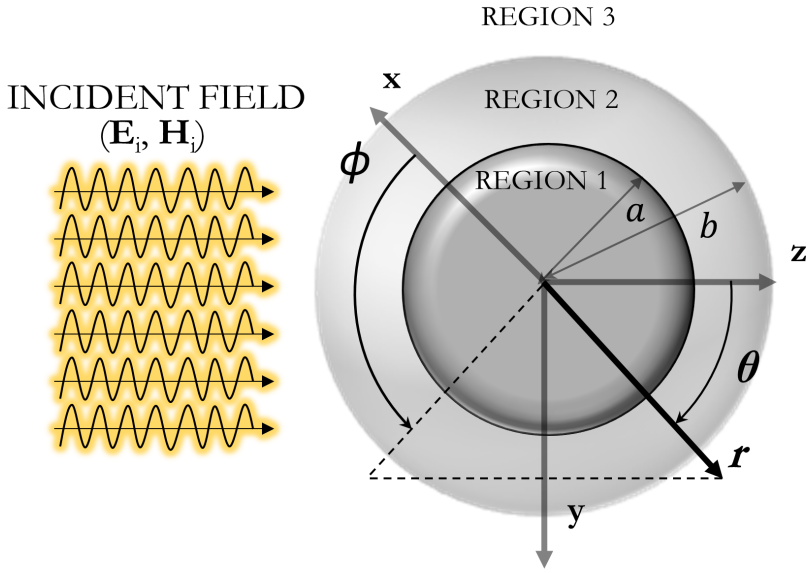

Figure 3.9: Electromagnetic plane wave incident on a sphere with a spherical shell coating.

and b, respectively.

The coated sphere is illuminated by the incident electromagnetic wave reported in Equation 2.61. The Equation of the electromagnetic field $(\mathbf{E}_1, \mathbf{H}_1)$ in the region $0 \leq r \leq a$ is reported in 2.64, while the scattered field $(\mathbf{E}_s, \mathbf{H}_s)$ is reported in Equation 2.66. By imposing the finiteness of the field at the origin, the radial part of the scalar wave equations (see Equation 2.46) is constrained to be j_n.

Differently, in the region $a \leq r \leq b (a \neq 0)$, the spherical Bessel functions (j_n and y_n) are finite. Therefore, the expansion $(\mathbf{E}_2, \mathbf{H}_2)$ can be written as:

$$\mathbf{E}_2 = \sum_{n=1}^{\infty} \mathbf{E}_n [f_n \mathbf{M}_{o1n}^{(1)} i g_n \mathbf{N}_{e1n}^{(1)} + v_n \mathbf{M}_{o1n}^{(2)} - i w_n \mathbf{N}_{e1n}^{(2)}], \tag{3.16}$$

$$\mathbf{H}_2 = -\frac{k_2}{\omega \mu_2} \sum_{n=1}^{\infty} \mathbf{E}_n [g_n \mathbf{M}_{e1n}^{(1)} + i f_n \mathbf{N}_{o1n}^{(1)} + w_n \mathbf{M}_{e1n}^{(2)} + i w_n \mathbf{N}_{o1n}^{(2)}], \tag{3.17}$$

where all the vector harmonics $\mathbf{M}$ and $\mathbf{N}$ are generated from the scalar wave equations in Equations 2.46.

The Bessel function y_n is dependent on $k_2 r$ in this region. By imposing the

boundary conditions:

$$\begin{aligned} (\mathbf{E}_2 - \mathbf{E}_1) \times \hat{\mathbf{e}}_r = 0, \qquad (\mathbf{H}_2 - \mathbf{H}_1) \times \hat{\mathbf{e}}_r = 0 \qquad r = a \\ (\mathbf{E}_s + \mathbf{E}_i - \mathbf{E}_2) \times \hat{\mathbf{e}}_r = 0, \qquad (\mathbf{H}_s + \mathbf{H}_i - \mathbf{H}_2) \times \hat{\mathbf{e}}_r = 0, \qquad r = b, \end{aligned} \tag{3.18}$$

a system of eight equations is obtained, in which the only unknowns are represented by the eight coefficients $a_n, b_n, c_n, d_n, f_n, g_n, v_n, w_n$.

$$\begin{aligned} f_n m_1 \psi_n(m_2 x) - v_n m_1 \chi_n(m_2 x) - c_n m_2 \psi_n(m_1 x) = 0, \\ w_n m_1 \chi_n'(m_2 x) - g_n m_1 \psi_n'(m_2 x) + d_n m_2 \psi_n'(m_1 x) = 0, \\ v_n \mu_1 \chi_n'(m_2 x) - f_n \mu_1 \psi_n'(m_2 x) + c_n \mu_2 \psi_n'(m_1 x) = 0, \\ g_n \mu_1 \psi_n(m_2 x) - w_n \mu_1 \chi_n(m_2 x) - d_n \mu_2 \psi_n(m_1 x) = 0, \\ m_2 \psi_n'(y) - a_n m_2 \xi_n'(y) - g_n \psi_n'(m_2 y) + w_n \chi_n'(m_2 y) = 0, \\ m_2 b_n \xi_n(y) - m_2 \psi_n(y) + f_n \psi_n(m_2 y) - v_n \chi_n(m_2 y) = 0, \\ \mu_2 \psi_n(y) - a_n \mu_2 \xi_n(y) - g_n \mu_3 \psi_n(m_2 y) + w_n \mu_3 \chi_n(m_2 y) = 0, \\ b_n \mu_2 \xi_n'(y) - \mu_2 \psi_n'(y) + f_n \mu_3 \psi_n'(m_2 y) - v_n \mu_3 \chi_n'(m_2 y) = 0, \end{aligned} \tag{3.19}$$

with m_1 and m_2 being the refractive indices of regions 1 and 2, respectively with respect to the refractive index of region 3; mu_1, mu_2, and mu_3 are the permeabilities of regions 1, 2, and 3, respectively; $x = ka$ and $y = kb$; and $\chi_n(z) = -z y_n(z)$, is the Riccati-Bessel function.

By assuming $\mu = \mu_1 = \mu_2 = \mu_3$, it is possible to solve the system of equations to find the scattering coefficients a_n and b_n:

$$\begin{aligned} a_n &= \frac{\psi_n(y)[\psi_n'(m_2 y) - A_n \chi_n'(m_2 y)] - m_2 \psi_n'(y)[\psi_n(m_2 y) - A_n \chi_n(m_2 y)]}{\xi_n(y)[\psi_n'(m_2 y) - A_n \chi_n'(m_2 y)] - m_2 \xi_n'(y)[\psi_n(m_2 y) - A_n \chi_n(m_2 y)]}, \\ b_n &= \frac{m_2 \psi_n(y)[\psi_n'(m_2 y) - B_n \chi_n'(m_2 y)] - \psi_n'(y)[\psi_n(m_2 y) - B_n \chi_n(m_2 y)]}{m_2 \xi_n(y)[\psi_n'(m_2 y) - B_n \chi_n'(m_2 y)] - \xi_n'(y)[\psi_n(m_2 y) - B_n \chi_n(m_2 y)]}, \\ A_n &= \frac{m_2 \psi_n(m_2 x) \psi_n'(m_1 x) - m_1 \psi_n'(m_2 x) \psi_n(m_1 x)}{m_2 \chi_n(m_2 x) \psi_n'(m_1 x) - m_1 \chi_n'(m_2 x) \psi_n(m_1 x)}, \\ B_n &= \frac{m_2 \psi_n(m_1 x) \psi_n'(m_2 x) - m_1 \psi_n(m_2 x) \psi_n'(m_1 x)}{m_2 \chi_n'(m_2 x) \psi_n(m_1 x) - m_1 \psi_n'(m_1 x) \chi_n(m_2 x)}. \end{aligned} \tag{3.20}$$

The obtained expressions of the scattering coefficients can be validated in the case of $m_1 = m_2$, in which the case of an isolated homogeneous sphere is recovered. In fact, for $m_1 = m_2$, it results that $A_n = B_n = 0$. Moreover, in the limit of $a \to 0$, the coefficients a_n and b_n reduce to the case of a homogeneous sphere of radius b and refractive index m_2.

3.5 Case studies

In this section, the abovementioned reverse engineering approach is combined with the Mie-Kerker theory applied to hybrid and coated plasmonic NPs synthesized *via* the bottom-up technique.

More precisely, silica-coated AuNPs are chosen as model hybrid systems. The accurate prediction of the optical response of these coated hybrid NPs can find large applications in the biosensing community.

3.5.1 Silica-coated gold nanoparticles

Silica SiO_2 has emerged as a coating material of plasmonic colloidal NPs due to its chemically inert nature and its optical transparency. It prevents the AuNPs aggregation, but at the same time, it does not affect the solid-state properties of the particles.

Gold has a very low affinity for silica because it does not form any oxide film, when in solution. Moreover, the chemical reagents involved in their bottom-up synthesis, such as citrate, make the gold surface vitreophobic.

One of the simplest ways to avoid vitreophobicity is using silane (APTES) coupling agents as surface primers, as first reported by Liz-Marzán *et al.* [151]. Moreover, many functionalization protocols, exploiting the surface of the silica coatings, have been developed to graft a biorecognition layer for biosensing applications [152].

In this subsection, the Mie-Kerker theory is combined with MG approximation to predict the optical response of citrate-capped AuNPs coated with silica shells of increasing thickness. The obtained theoretical spectra are compared with the experimental absorption spectra reported in Ref. [153].

First, Gontero and coworkers [153] synthesized citrate-capped AuNPs with a mean diameter of 41 nm ($r \sim 20.5$) nm. Then, they stabilized them with polyvinylpyrrolidone (PVP) prior to dispersion into ethanol solutions of tetraethyl-orthosilicate (TEOS) and ammonia to achieve a basic pH. They added TEOS at different percentages to achieve shells with different thicknesses. The obtained spectra are reported in Figure 3.10 (a), as a function of the silica shell thickness.

The theoretical prediction of the experimental absorption spectra reported in Ref. [153], was performed starting from the Mie Theory with MG approximation. It was applied to derive the citrate fraction for the accurate prediction of the LSPR of non-coated AuNPs. Then, the Mie-Kerker theory was implemented in Matlab®, and assuming the measured silica shell thicknesses having a refractive index $n_{SiO_2} = 1.45$,

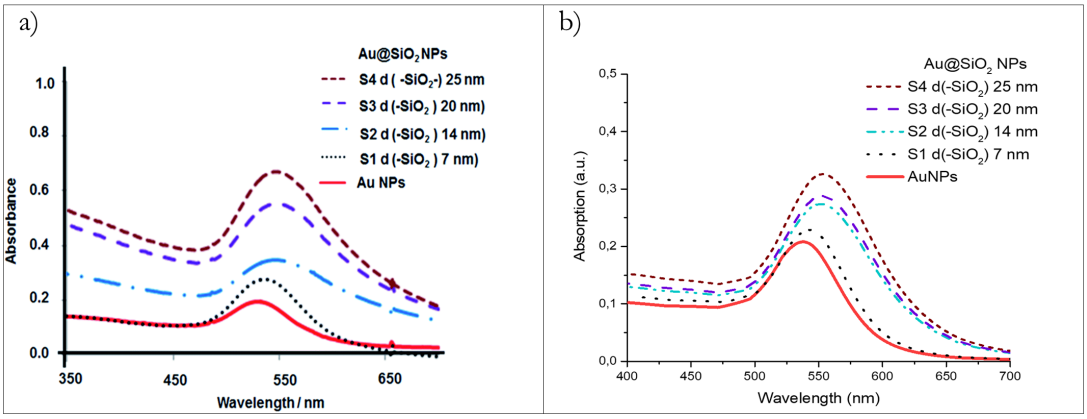

Figure 3.10: Experimental (a) and theoretical (b) absorption spectra of AuNPs and Au@SiO2 core-shell NPs with increasing SiO2 shell thicknesses: 20.5 nm -radius AuNPs (red), AuNPs with 7-nm thick SiO2 shell (blue dots), AuNPs with 14-nm thick SiO2 shell (light blue dash-dots), AuNPs with 20-nm thick SiO2 shell (violet dashes), and AuNPs with 25-nm thick SiO2 shell (magenta, short dashes). The experimental absorption spectra are reprinted from Ref. [153].

the absorbance cross-sections were calculated. The obtained theoretical predictions are reported in Figure 3.10 (b).

The very good agreement between experimental and theoretical absorption spectra further confirms the validity of the proposed model. The obtained LSPR positions as a function of the silica shell thicknesses are summarized in Table 3.5 to show the high accuracy of the proposed modeling.

t_{SiO_2} (nm)	λ_{max}^{exp} (nm)	$\lambda_{max}^{th}(nm)$
0	539	539
7	545	545
14	547	548
20	547	549
25	548	550

Table 3.5: LSPR wavelength (λ_{max}) comparison between experimental (λ_{max}^{exp})[153], and predicted (λ_{max}^{th}) of silica-coated citrate-capped AuNPs, as a function of the silica coating thickness (t_{SiO_2}).

3.6 Conclusions

In this chapter, the identification of the optical properties of hybrid plasmonic nanoparticles was proposed. The hybrid nature of the NPs resulted in a significant modification of their optical properties, compared to homogeneous AuNPs of the same size.

In particular, the Maxwell Garnett homogenization approach was adopted to derive the effective dielectric constants of hybrid NPs as a function of the stabilizer inclusion fractions. These latter were modeled as gaussian distributions of spheres within the metal matrix.

However, the experimental evaluation of the inclusions fraction within the hybrid nanoparticles is generally unfeasible or requires expensive and time-consuming equipment (*e.g.* cryo-TEM, SEM-EDX) for its efficient derivation.

Therefore, by applying a reverse-engineering approach, based on the genetic algorithm and on the experimentally measured absorption spectra of hybrid AuNPs, it was possible to achieve an accurate prediction of the LSPR position and FWHM both for citrate-capped and PEG-stabilized AuNPs. In both cases, the presence of an external chemical compound resulted in a redshift and in a broadening of the LSPR absorption peaks, caused by the increase of the average dielectric permittivity of the hybrid NPs.

Moreover, Mie-Kerker was introduced to include in the treatment of the case of coated hybrid NPs. Silica-coated citrate-AuNPs, as a case study, were used to validate the proposed modeling.

The obtained results confirmed the validity of the proposed approach that are adopted in the next chapters to model NP-based optical transducers as a function of both the stabilizing agents and coating materials. The proposed approach can have a strong impact on the analysis and design of biosensors based on large-scale assemblies of optically small nanoresonators.

Chapter 4

Gelatin-capped plasmonic/diatomite colloidal nanoparticles for drug release monitoring

Plasmonic NPs also represent valid candidates for the design of not only diagnostic, but also therapeutic, namely *theranostic*, nanodevices for *in-vivo* applications, including bioimaging [154], photo(thermal)-therapy [155], and drug delivery [156]. This is due to their low toxicity [157], ease of functionalization, and, as abovementioned, optical properties [71].

Plasmonic NPs with different sizes and shapes have been synthesized by several research groups to optimize their optical response and enhance their sensitivity [14]. However, spherical AuNPs remain the most studied for their rapid, well-understood, and controllable synthesis, which can be easily repeated in any laboratory without the need for expensive equipment [158].

Their combination with organic/inorganic materials can lead to nanodevices with multifunctional capabilities arising from the properties of the single materials involved in their fabrication. For example, the combination of AuNPs with Diatomite NPs (DNPs) and gelatin polymeric shells (Gel) has been already shown as a promising strategy for the delivery of Galunisertib (LY) to colorectal cancer cells (CRC) and real-time monitoring of its release by SERS spectroscopy [159].

DNPs are made of natural biosilica and can be obtained through a powder of diatom frustules, by mechanical crushing. Moreover, the mesoporous structure, surface tunability, and the efficient intracellular uptake of DNPs offer the possibility to

develop drug delivery systems for the controlled delivery of therapeutic compounds [160, 161].

Unfortunately, most nanocarriers, including DNPs, display a relatively low loading capacity (capability to load and keep drug molecules prior to release), hindering their clinical application [162].

To overcome this limitation, several strategies have been proposed for the production of drug delivery systems with higher loading capacity. Among them, the post-loading approach provides the drug delivery system with external *stimuli*-responsive properties [163].

As the name suggests, in the post-loading approach, NPs are loaded with the drug and then coated with, generally, an organic material (*e.g,* polymers, or proteins). This polymer forms a shell in the NPs' surroundings. As a polymer, gelatin is widely used for biomedical applications due to its biocompatibility, biodegradability, thermoresponsivity, and ease of functionalization [164].

The choice of gelatin as a polymeric shell has been shown to improve the drug loading capacity of drug delivery nanosystems avoiding burst release phenomena. Gelatin also provides the carrier with both pH and MMP-2 responsive features [165].

In the treatment of colorectal cancer (CRC), the small molecule LY represents an orally-administered molecule capable of inhibiting the metastatic progression of CRC [166]. However, the high dose of LY drug, as well as its fast metabolization, can be highly toxic for the treated patients [167].

For such therapeutic agents, nanocarriers-based drug delivery systems may offer a double benefit [168]:

- protecting LY from the liver's primary mechanism of drug metabolization
- reducing the dosing frequency

As shown in Ref. [159], the encapsulation of LY in gelatin-capped, AuNPs-DNPs (AuDNPs@Gel) provided the nanocarrier with a pH-responsive drug release profile. Moreover, it improved the capability of the drug to revert the metastatic process in CRC, re-establishing the epithelial cell phenotype.

Therefore, in this section, the identification of the optical properties of DNPs combined with gelatin-stabilized AuNPs (gel-AuNPs) is proposed for the development of an optical platform for LY delivery, as a drug molecule model.

To improve the AuDNPs loading capacity, they were capped with gelatin shells of increasing thicknesses. The optical modeling of the hybrid system was obtained by applying MG approximation combined with Mie and Mie-Kerker theories, described in Chapter 3. The model provided the nanosystem with the possibility to monitor the

gelatin shell formation, degradation, and subsequent LY release by simple absorption spectroscopy measurements.

The shell thickness was optically estimated as a function of the polymer concentration by exploiting the LSPR shifts $\Delta\lambda_{max}$ of the Gel-AuNPs immobilized on the surface of DNPs.

The proposed theoretical modeling can represent an efficient predictive tool for the design of polymer-coated nanocarriers, as drug delivery systems. Monitoring the gelatin shell formation and degradation by LSPR measurements and theoretical predictions could overcome the limitations of electron microscopy investigations, in which differences in the gelatin shell thicknesses could not be opportunely estimated.

4.1 Experimental Part

Materials and reagents

Diatomite was supplied by DEREF Spa (Castiglione in Taverina, Viterbo, Italy); 1-ethyl-3-[3-dimethylaminopropyl] carbodiimide-hydrochloride (EDC), N-hydroxysuccinimide (NHS), (3-Aminopropyl)triethoxysilane (APTES), type-B gelatin from bovine skin, tetrachloroauric acid ($HAuCl_4$), sodium borohydride ($NaBH_4$), sulfuric acid (H_2SO_4), trifluoroacetic acid (TFA), acetonitrile HPLC grade, Millex-GP syringe filter 0.22 μm, and acetone were purchased from Sigma-Merck KGaA (DE). Phosphate buffered saline (PBS) was purchased from GIBCO (IE). Hydrochloric acid (HCl) was purchased from Romil (UK). Absolute ethanol (EtOH) and hydrogen peroxide (H_2O_2) were purchased from Carlo Erba (IT). Galunisertib (LY 2157299) was purchased from Axon Medchem (Groningen, NL). All reagents were of analytical grade and all aqueous solutions were prepared with Milli-Q water.

Preparation of AuDNPs-LY@Gel nanosystem

The detailed fabrication procedure of AuDNPs-LY nanosystems is reported in Ref. [106]. Briefly, ultrasounds were applied to diatomite powder to reduce its average size to the nanometric scale, and a uniform distribution was obtained by repeating cycles of settling and recovery.

Then, the DNPs were purified with HCl and Piranha solution to remove organic and inorganic contamination. The silanization of DNPs was carried out by immersing DNPs in 10% APTES ethanol solution for 30 min. After the silanization, DNPs were recovered by centrifugation (13,500 rpm, 15 °C, 10 min) and underwent a curing process for 1 h at 40^circ C before their collection.

A dispersion of amino-modified DNPs (DNP-APT) was immersed in the $HAuCl_4$ solution for 5 min and 0.5 mL of gelatin solution 0.025% was added as a stabilizing agent (weight ratio between gold salts and gelatin 10:1). The dispersion was stirred for further 5 min and an aqueous solution of sodium borohydride 100 mM $NaBH_4$ was added dropwise to the dispersion until the color turned from yellow to purple/red.

Gold-decorated DNPs were left to rest for 30 min before purification by centrifugation (4500 rpm, 10 °C, 10 min). The supernatant was discarded and the gelatin stabilizing AuNPs was cross-linked by EDC and NHS in PBS solution (weight ratio gelatin: EDC: NHS = 10:14:7) for 90 min in mild stirring to weld Gel-AuNPs to the silica substrate firmly. At this stage, the cross-linked gelatin, used at a very low concentration (0.025%) was considered as the Gel-AuNPs stabilizer.

The as-prepared NPs dispersion is referred to as AuDNPs. For drug loading, AuDNP dispersion was shacked in a 1 mg/mL LY solution for 2 h at 37° C and the excess of the unloaded drug was discarded after centrifugation at 4500 rpm. The dispersion was washed with water and PBS solution twice. These NPs are referred to as AuDNPs-LY.

The loaded system was then re-suspended in gelatin aqueous solutions at pH 4.0 at the following concentrations: 0%, 0.125%, 0.25%, 0.5%, 0.75%, and 1.50% (w/v). The mixture was stirred for 30 min, and then EDC and NHS were added for cross-linking the gelatin matrix (weight ratio gelatin: EDC: NHS = 10:14:7) for 1 h at room temperature. At this stage, gelatin solutions, at much higher concentrations, are used to promote the growth of a shell of the cross-linked matrix surrounding the silica substrate and protect the system from drug dispersion phenomena. Finally, the dispersion was centrifuged, and NPs were washed twice in water and collected for analysis (AuDNPs-LY@Gel_x, where x denotes the different concentrations in the gelatin shell).

Apparatus and characterizations

All the characterizations were performed using 50 μg of DNPs in an aqueous solution in triplicate. Hydrodynamic diameter and surface $\zeta-$potential of bare DNPs, AuDNPs, and AuDNPs-LY@Gel_x were measured as reported in section 3.3.1.

The morphology of DNPs after each surface modification was conducted by TEM imaging (see section 3.3.1). From TEM images, a particle analysis was performed by ImageJ software to estimate the Gel-AuNPs mean radius ($r_{\text{Gel-AuNPs}}$).

Absorption spectra of amino-modified DNPs, AuDNPs-LY, and AuDNPsLY@Gel_x were recorded on Cary 100 UV-Vis double beam spectrometer (Agilent, CA, United States) using quartz cells of 10 mm path at room temperature. Samples were dis-

persed in Milli Q water immediately before the measurement. The peak analysis and first derivatives of the measured spectra were performed by OriginPro.

Numerical simulations

Each Gel-AuNP was modeled as a sphere made of two main components, namely gold, and gelatin. A schematic diagram of this identification is reported in Figure 4.2(a). Gelatin inclusions were modeled as a Gaussian distribution of spheres within the AuNP, with mean volume fraction μ_{Gel} and standard deviation σ_{Gel}. Starting from the knowledge of their permittivities, and the measured absorption spectra, as done for citrate-capped AuNPs in Chapter 3, μ_{Gel} and σ_{Gel} were obtained through the GA. The fitness function to be minimized $F(\mu_{\text{Gel}}, \sigma_{\text{Gel}})$ had the same form of Equation 3.14.

The effective relative dielectric permittivity of Gel-AuNPs was obtained by the Maxwell-Garnett homogenization theory by using experimental constants derived by Johnson and Christie for gold and gelatin refractive indices ($n_{\text{Gel}} = 1.54$). These parameters were substituted in the expression of the MG approximated average dielectric function $\varepsilon(f_{\text{Gel}})$ in Equation 3.13.

The theoretical spectrum of the Gel-AuNPs ($C_{\text{abs}_{\text{th}}}$) was predicted analytically by the Mie Theory. The radius of AuNPs (r_{Gel}) was set to 3 nm, as a result of the particle analysis carried out on TEM images, and the medium effective refractive index (n_{eff}) in the AuNPs surroundings was assumed to be made of DNPs ($n_{\text{DNPs}} = 1.45$) and water ($n_{\text{H}_2\text{O}} = 1.33$), in which the whole system (AuDNPs) was suspended during the spectroscopic measurements. The root mean square of the difference between $C_{\text{abs}_{\text{th}}}$ and $C_{\text{abs}_{\text{exp}}}$ was used as the fitness function. The GA fitness value was set to 0.1, corresponding to a 10% deviation between theory and experiments.

Then, the nanosystems made of Gel-AuNPs on DNPs were immersed in solutions with increasing concentrations of gelatin to form uniform coatings on the AuDNPs hybrid complex. The gelatin layers of increasing thickness t_{Gel} were assumed to uniformly cover the Gel-AuNPs on the DNPs described so far. The absorption spectra of AuDNPs-LY@Gel systems with increasing gelatin-coating thicknesses t_{Gel} were predicted by applying the Mie-Kerker theory (see Chapter 3). A redshift of the resonance peak was observed by increasing t_{Gel}. The first derivatives of the predicted spectra were computed to correlate the theoretical optical response as a function of t_{Gel} and the experimental optical response as a function of gelatin concentration (c_{Gel}).

In-vitro drug loading and release studies

In vitro drug release of LY was performed in PBS solution containing the proteolytic enzyme trypsin to allow the digestion of the gelatin shell. For each sample with a different gelatin shell, 0.1 mg of AuDNP-LY@Gel$_x$ were immersed in a PBS solution containing trypsin (60 μg/mL, 1 mL) and stirred at 200 rpm at 37°C. An excess of trypsin was used to guarantee that the same amount of gelatin was degraded in each sample at the same time intervals. After 5 minutes, the AuDNP-LYGel$_x$ dispersion was centrifuged (3500 rpm, 37°C, 5 minutes) to separate the nanoparticles from the release solution. At each time interval, freshly prepared PBS solution was added to the dispersion in presence of trypsin and stirred at 200 rpm, 37 37°C until the subsequent withdrawal. Release solutions were collected at time intervals of 5, 10, 20, 30, 60 minutes, and 16 hours for the quantitative analysis by Reverse-Phase-High Performance Liquid Chromatography (RP-HPLC) reported in Ref [106]. The cumulative release was calculated by using the following equation:

$$CumulativeRelease = R(t) + R(t + \Delta t) \tag{4.1}$$

where t denotes the time, and Δt the time interval from the initial one and R denotes the released drug. The loaded drug was estimated as the total drug released after 16 hours in a solution containing a large excess of trypsin (60 μg/mL).

4.2 Results and Discussion

4.2.1 Fabrication of plasmonic/diatomite nanoparticles as a drug delivery system

The development of the hybrid nanosystem (AuDNPs-LY@Gel) with increasing shells of crosslinked gelatin was performed according to the fabrication procedure reported in Ref. [106]. Briefly, the *in-situ* synthesis of Gel-AuNPs on the surface of DNPs (AuDNPs) was performed *via* a bottom-up approach. First, DNPs were modified with APTES (DNP-APT) to promote the electrostatic interactions between Au precursors and the DNPs surface. Second, DNPs were suspended in $HAuCl_4$ solutions in presence of gelatin as a stabilizing agent. After the suitable mixing of the solutions to enable interactions, sodium borohydride ($NaBH_4$) solution, as a strong reducing agent, was added drop-wise. The dispersion immediately turned from light yellow to deep red, after the effective reduction of the AuNPs. Thereafter, the cross-linking of the gelatin, as a stabilizer, was carried out *via* EDC/NHS chemistry. The complex AuDNP was

suspended in an aqueous solution of LY (1 mg/mL) and washed. Finally, AuDNPs-LY complex system was capped by a shell of gelatin to prevent the burst release effect [165].

To form gelatin shells with increasing thicknesses, AuDNPs-LY complexes were dispersed in gelatin aqueous solutions at different concentrations (0.125%, 0.25%, 0.50%, 0.75%, 1.5%) and crosslinked via EDC/NHS chemistry to achieve shells with different thicknesses. A preliminary assessment of the presence of the gelatin shell in the AuDNP-LY@Gel complex was performed *via* transmission electron microscopy (TEM), Dynamic Light Scattering (DLS), and ζ-Potential analysis, summarized in Figure 4.1.

The *in-situ* synthesis of Gel-AuNPs on the surface of the DNP-APT was observed by TEM analysis, as shown in Figure 4.1 (b-I), according to which, the irregular surface of DNPs resulted to be decorated by a uniform distribution of Gel-AuNPs with mean radius $r_{\text{Gel-AuNPs}}$ of ~ 3 nm (Figure 4.1 (c)).

The gelatin shell formation was confirmed by the color and roughness change in AuDNPs, which became darker and smoother with the increase in gelatin concentration (Figure 4.1 (b-II,b-III)) [169, 170].

DLS and ζ-potential investigations, in Figure 4.1 (d), show, on average, an increase in the average size of AuDNPs as a function of the gelatin concentration. This is mainly caused by the formation of DNPs aggregates (not Gel-AuNPs aggregates) arising from the sticky nature of the gelatin. Concerning the ζ-potential measurements, from positively charged DNPs, without gelatin shells due to the presence of positively charged APTES, the Gel-AuDNPs complexes exhibited a less-positive surface, due to the almost neutral charge of gelatin. The *zeta*-potential measurements confirmed the proper coating with gelatin and the lower stability of the complexes, in the solution.

4.2.2 Estimation of coating thickness as a function of the gelatin concentration

The morphological characterization in the previous subsection provided the first evidence of the increase in the cross-linked gelatin shell thickness on AuDNPs-LY@Gel$_x$ systems.

Unfortunately, the accurate estimation of this parameter, which is crucial in the design of polymer-coated drug delivery systems with enhanced drug loading capacity, could not be provided by classical TEM imaging due to the heterogeneity of the involved sizes, namely the gelatin shell thickness t_{Gel}, the radius of the Gel-AuNPs

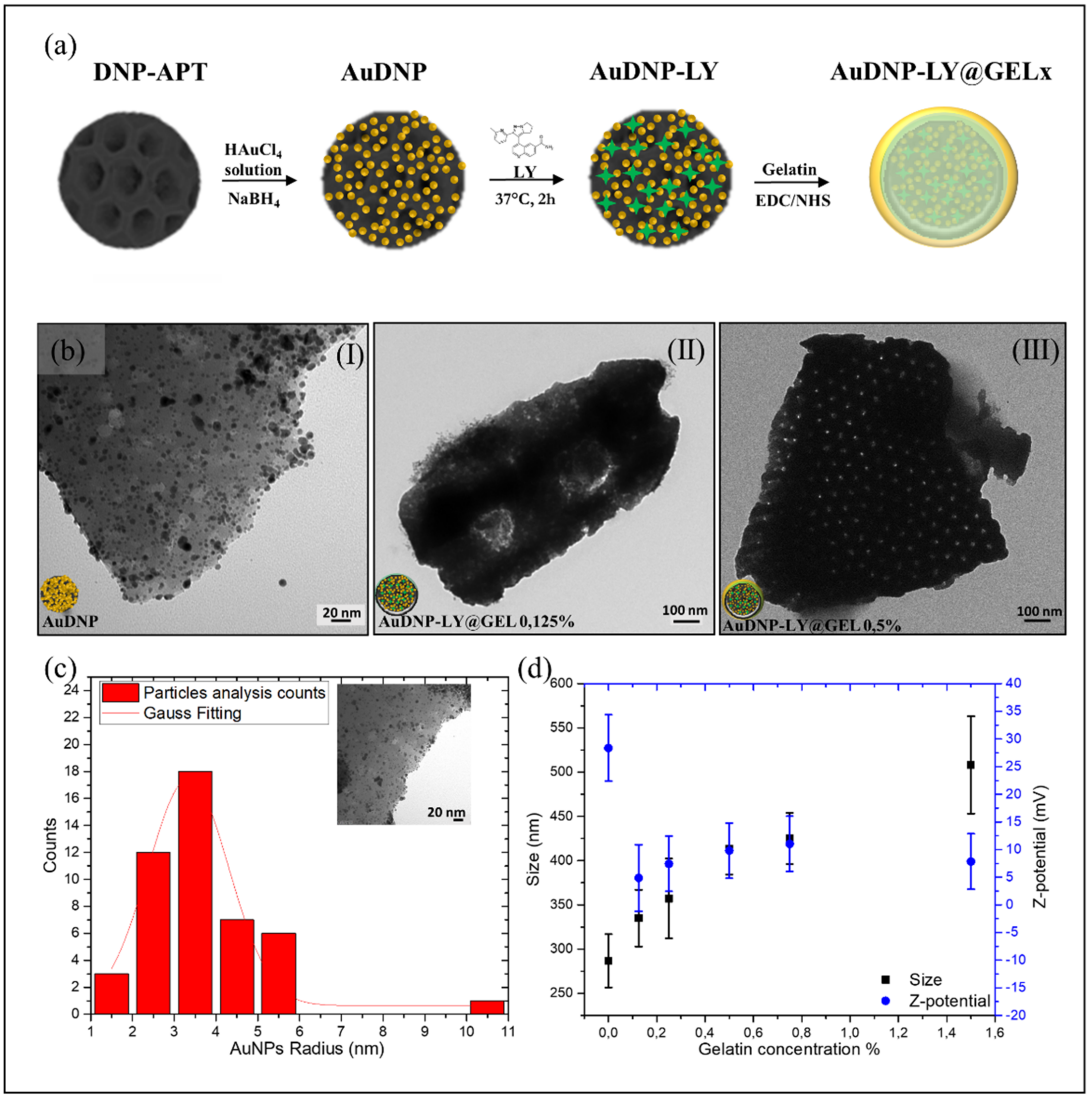

Figure 4.1: (a) Schematic representation of the fabrication procedure. (b) TEM investigations of the AuDNPs (I), AuDNP-LY@Gel$_{0.125\%}$ (II) and AuDNP-LY@Gel$_{0.5\%}$ samples (c). Particle size analysis of Gel-AuNPs decorating the surface of the DNPs fitted by a Gaussian curve. (d) Hydrodynamic diameter (black) and ζ-potential (blue) of the samples AuDNP-LY@Gel$_x$ as a function of the different gelatin concentrations in the outer shell. The vertical bars are representative of the standard deviation (SD) on a minimum of three independent measurements ($n \geq 3$). Reprinted from Ref. [106].

$r_{\text{Gel-AuNPs}}$, and the radius of DNPs r_{DNPs} ($r_{\text{Gel-AuNPs}} < t_{\text{Gel}} \ll r_{\text{DNPs}}$).

For this reason, to derive the missing information (t_{Gel}), Mie Theory and Mie-Kerker theory combined with MG approximation were adopted to predict the absorption of the hybrid nanosystem.

The small AuNPs, grown *in-situ* on the DNP surface, and stabilized by gelatin (Gel-AuNPs), had mean radius $r_{\text{Gel-AuNPs}} = 3.0 \pm 1.5$ nm. Moreover, as highlighted from TEM image in Figure 4.1 (c), on average, their spacing ($d_{\text{Gel-AuNPs}}$) resulted to be sufficiently larger than their size ($r_{\text{Gel-AuNPs}} < d_{\text{Gel-AuNPs}}$). For this reason, they were assumed as non-interacting NPs (Figure 4.2 (a)).

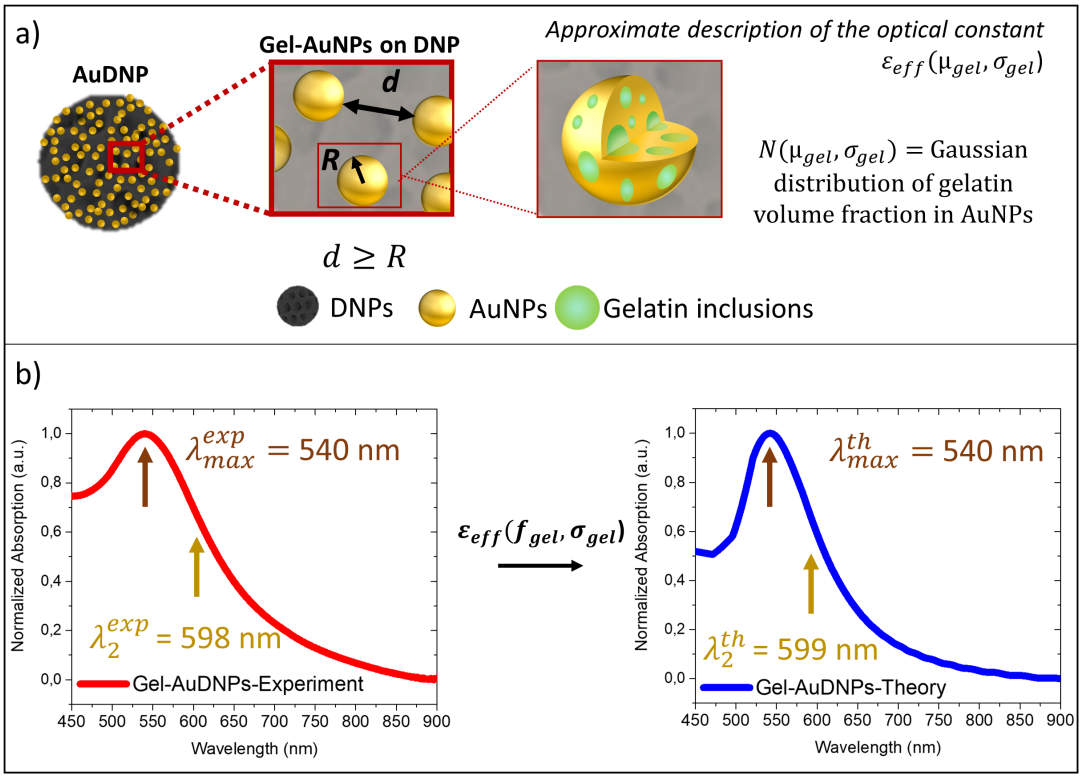

Figure 4.2: (a) Schematic representation of the approximations followed in the optical description of hybrid gel-AuDNPs. (b) The normalized experimental absorption spectrum of Gel-AuDNPs without gelatin shells (red line) exhibiting LSPR $\lambda_{max} = 540$ nm and inflection point $\lambda_2 = 598$ nm; normalized theoretical absorption spectrum of Gel-AuDNPs with no gelatin shells obtained by applying the optimized parameters $\mu_{Gel} = 0.11$ and $\sigma_{Gel} = 0.03$ (blue line). The minimized root mean square between theoretical and experimental spectra $\%_{error}$ was 0.09. Reprinted from Ref. [106].

The application of the classical Mie theory to very small AuNPs dispersed in water would result in an LSPR peak (λ_{max}) located at a wavelength of ~ 515 nm in the visible spectrum. Instead, a huge redshift of the LSPR (~ 25 nm) was observed

($\lambda_{max} \sim 540$ nm) from the experimental measurements on the AuDNPs-LY systems without gelatin coatings. This huge shift can be attributed to two main factors:

- the formation of gelatin inclusions during the reduction of gold ions, in presence of the gelatin, which remains entrapped in the Gel-AuNPs during nucleation and growth processes [96];
- the higher, as compared with water, medium effective dielectric constant due to the partial presence of DNPs in the Gel-AuNPs surroundings.

These hypotheses were validated by the comparison between theoretical and predicted absorption spectra of a 3 nm radius-AuNP, Gel-AuNP, and Gel-AuNP on DNP, as shown in Figure 4.3.

For these reasons, the effective dielectric constants $\varepsilon_{eff}(\mu_{Gel}, \sigma_{Gel})$ and $\varepsilon_{m.eff}$ were introduced to describe the absorption of the Gel-AuNPs. $\varepsilon_{eff}(\mu_{Gel}, \sigma_{Gel})$ describes the hybrid nature of Gel-AuNPs, while $\varepsilon_{m.eff}$ denotes the dielectric constant of the medium.

As highlighted in Chapter 3, and schematized in Figure 4.2, the gelatin inclusions were assumed as a Gaussian distribution of spherical particles occupying a volume fraction $f_{Gel}(\mu_{Gel}, \sigma_{Gel})$, and, by applying the GA, the parameters μ_{Gel} and σ_{Gel} were optimized. The root mean square value between theoretical and experimental absorption spectra of the AuDNPs-LY returned by GA was $0.09\,(< 0.1)$ and the optimized parameters were $\mu_{Gel} = 0.11$ and $\sigma_{Gel} = 0.03$. Therefore, in Gel-AuNPs, gelatin was occupying a volume fraction $f_{Gel} = 11 \pm 3\%$, in good agreement with the initial weight ratio (w/w) between gelatin and $HAuCl_4$ of the reaction volume.

The medium refractive index was also obtained with this optimization. It corresponded to 10% silica (DNPs) and 90% water. Finally, the accurate optical modeling of the hybrid AuDNPs-LY system immersed in water was achieved, confirming the consistency of the initial hypotheses (see Figure 4.3).

As shown in Figure 4.2 (b), the theoretical modeling of the hybrid AuDNPs system is in very good agreement with both mean LSP resonance λ_{max}^{exp} and the inflection point λ_2^{exp} of the experimental absorption spectra, corresponding to 540 nm and 598 nm, respectively. The inflection point λ_2 is nothing but the minimum of the first derivative of plasmonic absorption spectra.

The 9 % variation between theory and experiments resulting from these simulations was attributed to the different absorption intensities between 450 and 500 nm, which arose experimentally from both LY and gelatin showing non-negligible absorptions in the UV and visible region (450-500 nm) of the spectrum, as shown in Figure 4.4.

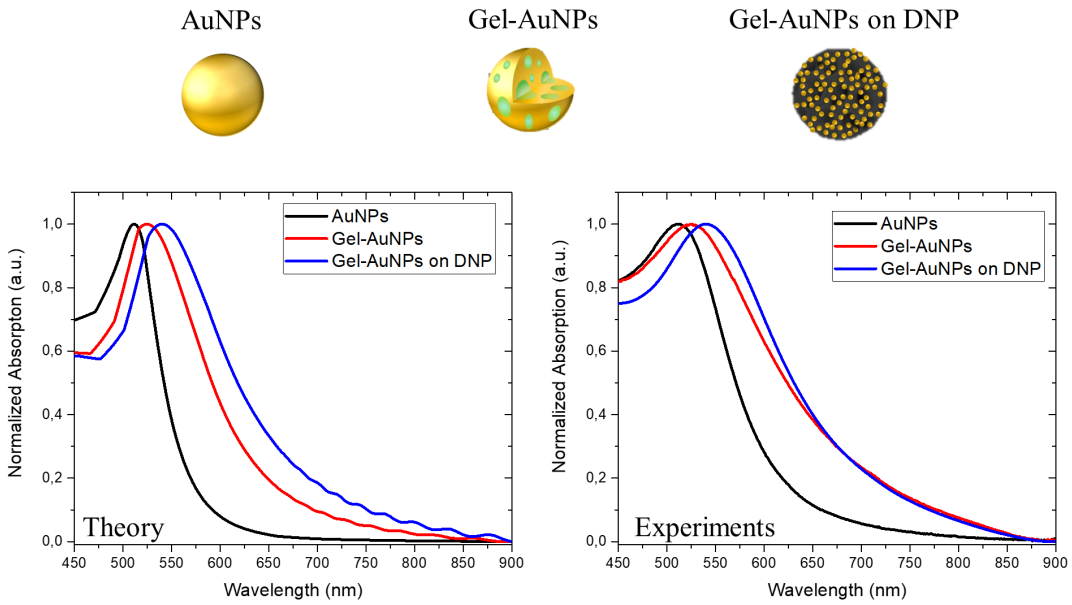

Figure 4.3: Normalized theoretical (on the left) and experimental (on the right) absorption spectra of ~ 3 nm radius AuNPs, Gel-AuNPs, and Gel-AuNPs on DNPs. Reprinted from Ref. [106].

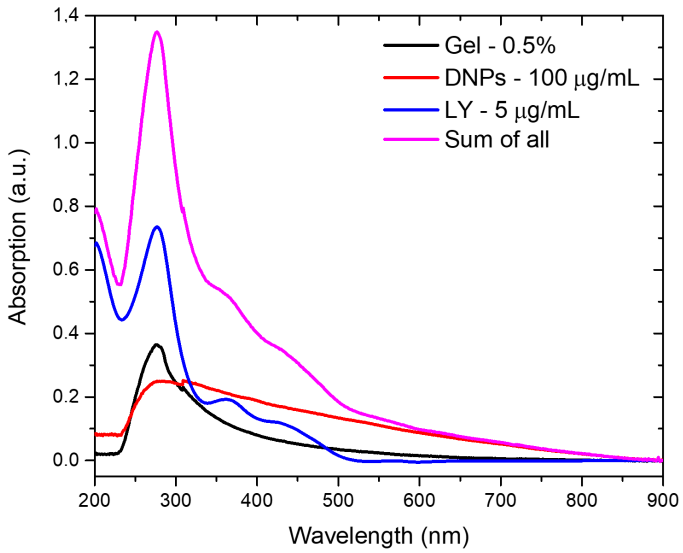

Figure 4.4: Intrinsic absorptions of the single components of the AuDNP-LY@Gel$_{0.5}$% system: absorption of Gelatin at a concentration 0.5 % (black line), DNPs at a concentration of 100 μg/mL (red line), and LY drug at a concentration of 5 μg/mL (blue line). The summation of all the contributions is also reported (purple line).

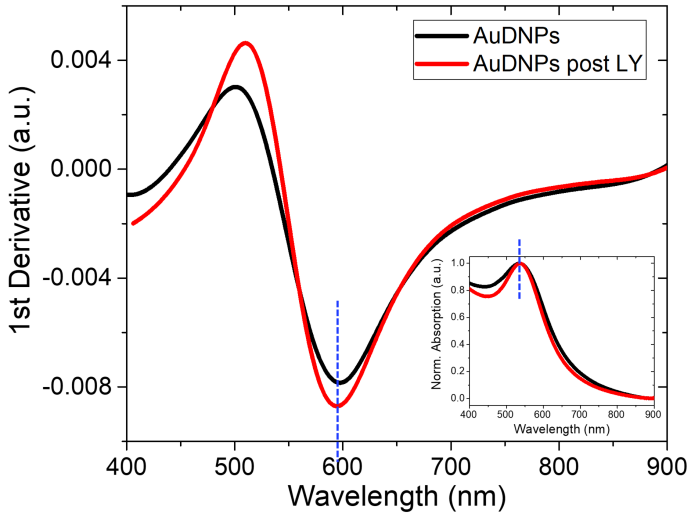

Figure 4.5: Optical monitoring of the drug loading step on the AuDNP system: Experimental first derivative and absorption spectra (in the inset) of AuDNP system before (black line) and after (red line) drug loading process.

However, both λ_{max} and λ_2 were not affected by absorption in that region, and, consequently, they could be considered negligible. The small molecule LY, with refractive index = 1.75, was not considered in the model optimization owing to its low molecular weight and tiny concentration. LY in fact did not affect the LSPR response of the system. This hypothesis was confirmed by experimental absorption measurements, in Figure 4.5.

The accurate prediction of the optical absorption in terms of λ_{max} and λ_2 of the Gel-AuNPs on DNPs in presence of LY was applied to the AuDNPs-LY@Gel$_x$ to obtain an estimation of the gelatin shell thicknesses as a function of the increasing gelatin concentrations. It was performed by using the Mie-Kerker theory presented in Chapter 3. The correlation between Gel concentrations and t_{Gel} represents a crucial design parameter to monitor the shell formation.

First, the LSPR response of the AuDNPs-LY systems with shells of increasing thicknesses in the Gel-AuNPs surroundings was simulated. An LSPR redshift was observed with the increasing gelatin shell thickness. Indeed, crosslinked gelatin possesses a refractive index higher than water and silica $n_{Gel} = 1.54$, thus causing a redshift of the LSPR λ_{max}. The simulations were performed for average t_{Gel} in the interval [0 - 20] nm. The obtained results are reported in Figure 4.6 (a).

Instead, from the experimental perspective, the chemical crosslinking of gelatin at different concentrations c_{Gel} on the AuDNPs-LY@Gel$_x$ hybrid nanosystem (Figure 4.6 (b)) was monitored spectroscopically.

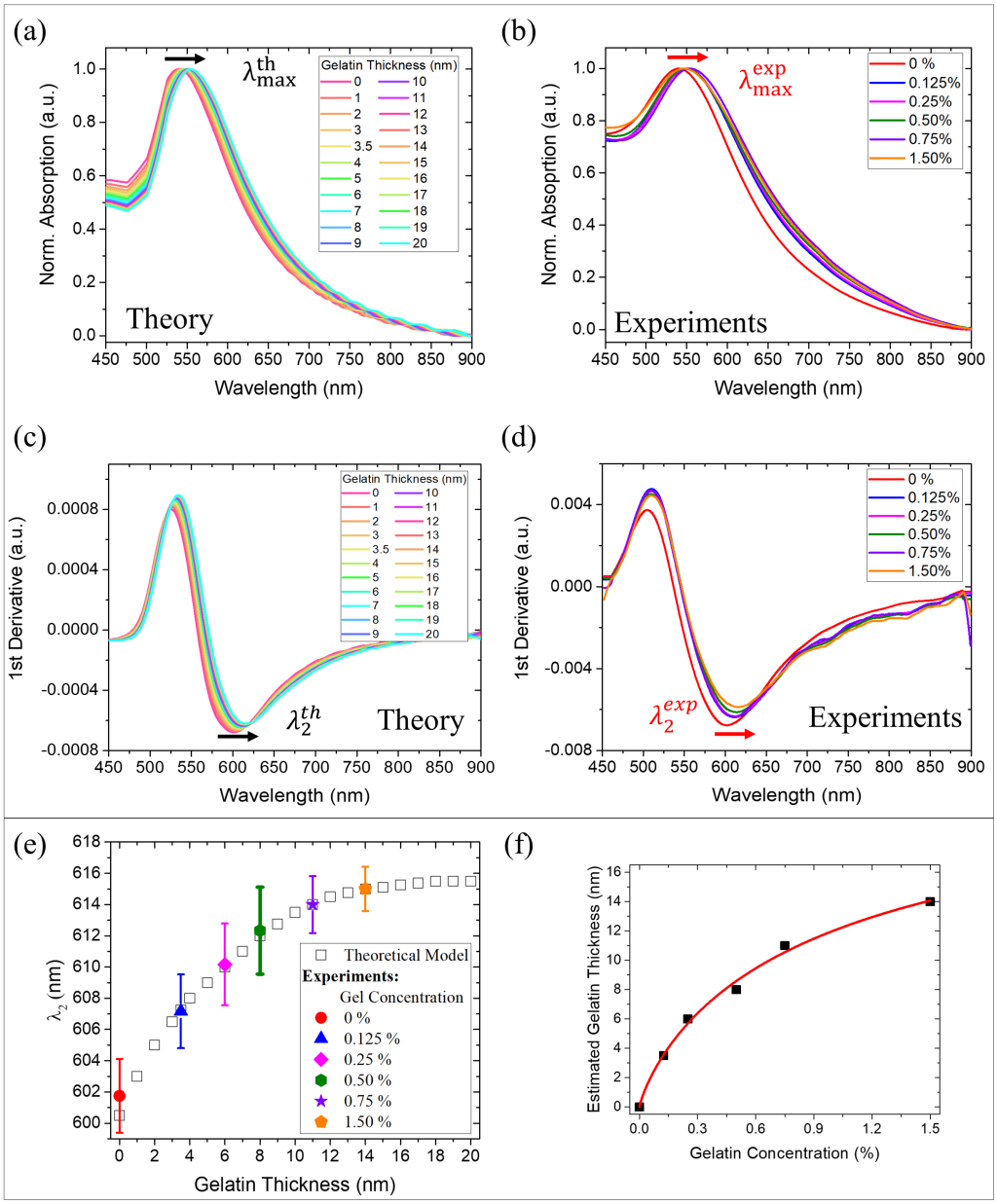

Figure 4.6: Correlation between gelatin concentration (c_{Gel}) and shell thickness (t_{Gel}): (a-c) theoretical absorption spectra and first derivatives of AuDNPs with increasing t_{Gel}. The black arrows (redshifts of (a) λ_{max}^{th} and (c) λ_2^{th}) correspond to increasing t_{Gel}. (b-d) Experimental absorption spectra and first derivatives of AuDNPs with increasing c_{Gel}: 0 % (red), 0.125 % (blue), 0.25 % (purple), 0.5 % (green), 0.75 % (violet), 1.50 % (orange). The red arrows (redshifts of (b) λ_{max}^{exp} and (d) λ_2^{exp}) correspond to increasing c_{Gel}. (e) Comparison between λ_2^{th} versus t_{Gel} (theoretical model, white squares) and λ_2^{exp} versus c_{Gel} (experimental data, colored squares). (f) Correlation between the gelatin concentration and estimated coating thickness. The red line is a fitting of the scatter plot (Equation 4.2). Reprinted from Ref. [106].

However, the redshift of tiny AuNPs LSPR, exhibiting very poor sensitivity to refractive index variations, was better visualized by considering the inflection point λ_2 in both theoretical and experimental absorption spectra. The use of the second inflection point of the absorption spectra significantly enhances the plasmonic response sensitivity [171, 172]. Therefore, the first derivatives of the spectra were computed and the minima of the curves in Figure 4.6 (c-d) were considered as λ_2.

Another inflection point (λ_1), corresponding to the maxima of the first derivatives, could have been evaluated. However, it has been already demonstrated that the highest sensitivity for refractive index sensing can be obtained by considering the λ_2 values [171, 172]. Moreover, the first inflection points are affected by the *a-specific* absorption of the other chemicals involved in the nanocarrier fabrication, thus hindering the accuracy of their theoretical prediction (recall Figure 4.4). For these reasons, from here on, only λ_2 points are considered for further analysis.

The λ_2^{th} underwent a redshift as a function of the t_{Gel}. More precisely, λ_2^{th} redshift from 600 to 616 nm was observed, following a saturation curve with a linear range from 0 to $\sim$ 11 nm of t_{Gel} and achieving saturation at $t_{\mathrm{Gel,max}} \sim 18$ nm (white squares in Figure 4.6 (e)). The saturation behavior, herein observed, finds an explanation from the rapidly decaying field enhancement of Gel-AuNPs, whose plasmon resonance is localized within the NPs' surroundings. Therefore, even if thicker gelatin shells could be easily simulated, the inflection points of the absorption spectra would have been not affected anymore by the increase of the t_{Gel}. For this reason, the simulations were stopped at $t_{\mathrm{Gel}} = 20$ nm.

Meanwhile, the experimental evaluation of λ_2^{exp} was performed by measuring the absorption spectra of the AuDNP-LY@Gel systems obtained by different c_{Gel}, namely, 0%, 0.125%, 0.25%, 0.5%, 0.75% and 1.50% on the AuDNP-LY systems. Accordingly, a redshift of λ_2^{exp} was observed for the different c_{Gel}.

The theoretical and experimental results reported in Figures 4.6(c-d-e) enabled the correlation between c_{Gel} and t_{Gel} on the hybrid AuDNPs-LY nanosystem. This relationship could be described by a Michaelis-Menten-like kinetics in the investigated thickness range [173], whose representation is reported in Figure 4.6(f):

$$t_{\mathrm{Gel}} = t_{\mathrm{Gel,max}} \frac{c_{\mathrm{Gel}}}{k_t + c_{\mathrm{Gel}}} \tag{4.2}$$

where $t_{\mathrm{Gel,max}} \sim 18$ nm is the maximum gelatin thickness at which a redshift of λ_2 in the first derivatives of absorption spectra was still detectable and $k_t = 0.63$ % is the gelatin concentration at which the c_{Gel} on the AuDNP-LY@Gel system corresponds to half of the $t_{\mathrm{Gel,max}}$ ($\sim$ 9 nm).

The modeling for the estimation of the average gelatin thickness of the proposed drug delivery system was crucial for the nanocarrier design since it provided the reverse design of a hybrid system in which the gelatin concentration could be tuned to achieve the desired average coating thickness.

4.2.3 Evaluation of the loading capacity of the nanosystem AuDNP-LY@Gel$_x$

The capability of gelatin polymeric shells to guarantee a sustained release, demonstrated in Ref. [159], enabled the investigation of the benefits arising from the increase in the gelatin concentration c_{Gel} in the proposed AuDNP hybrid nanosystems. Among them, the loading capacity increase to enhance the effects of the drug with a lower dose was the targeted objective.

To prove this, *in vitro*-drug release studies were performed to quantify the amount of drug released through Reversed-Phase High-Performance Liquid Chromatography (RP-HPLC) (Figure 4.7 (a). The loading capacity (LC) of AuDNP-LY@Gel with increasing gelatin concentration was compared with the AuDNP control sample to evaluate the influence of the shell thickness (estimated in the previous subsection) on the nanosystem LC.

In Figure 4.7 (a), the increase of gelatin concentration/thickness resulted in a higher amount of LY entrapped in the system and available for delivery. Indeed, the control sample AuDNP exhibited a lower LC of LY 2.4 ± 0.2 μg per 100 μg of DNPs (LC_{min}) When the gelatin concentration increased to 1.5%, the released drug was about 5.6 ± 0.6 μg of LY (LC_{max}).

The different drug LC displayed by the samples in response to increasing c_{Gel} followed a typical sigmoidal behavior, as shown in Figure 4.7(b). As obvious from Figure 4.7 (c), the drug LC of AuDNP-LY@Gel$_x$ systems followed the same sigmoidal curve as a function of the estimated t_{Gel}.

No significant enhanced LC was observed for $t_{\text{Gel}} \leq 5$ nm. At $5 \leq t_{\text{Gel}} \leq 11$ nm instead, a direct proportionality with the nanosystem drug LC was observed, finally reaching a plateau region in the sample with $c_{\text{Gel}} = 1.5\%$ and $t_{\text{Gel}} \geq 11$ nm. The increment of the LY LC in the nanosystem was explained by considering the non-covalent interactions between the gelatin molecules and LY. Moreover, by increasing the c_{Gel}, the larger polymeric shell slowed down the diffusion of the drug molecules out of the system.

The sigmoidal relationship between the drug Loading Capacity (LC, μg) of AuDNPs-LY@Gel$_x$ systems, and the estimated gelatin shell thickness (t_{Gel}, nm) can

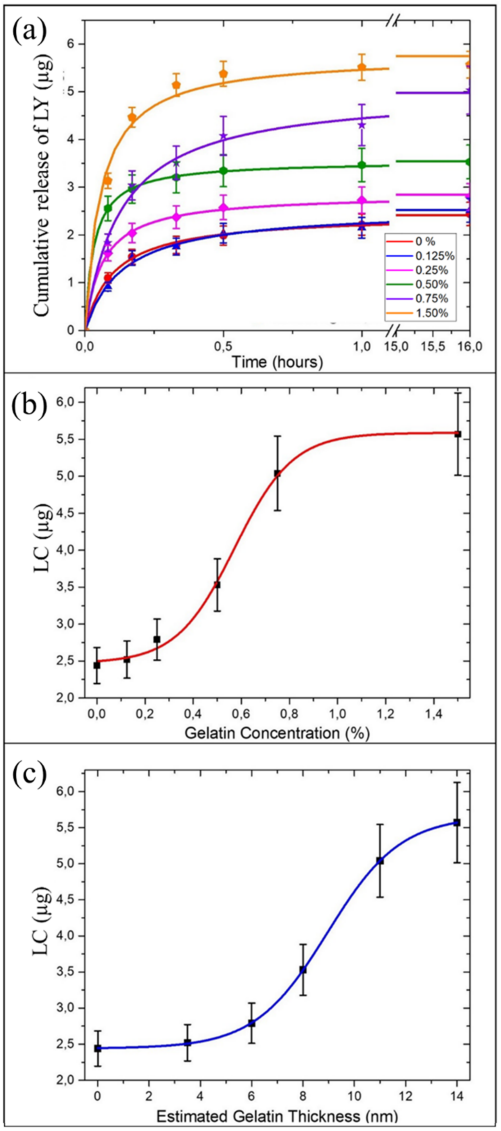

Figure 4.7: (a) Cumulative release of LY from AuDNP-LY@Gel samples with increasing concentration of the gelatin shell. (b) Experimental estimation of the drug LC as a function of c_{Gel}. (c) Theoretical estimation of the drug LC as a function of the estimated t_{Gel}. The vertical bars are representative of the SD on a minimum of three independent measurements ($n \geq 3$). Reprinted from Ref. [106].

be fitted by a Boltzmann-type equation:

$$LC = LC_{max} + (LC_{min} - LC_{max})/(1 + e^{(}t_{\mathrm{Gel}} - (t_{\mathrm{Gel,m}}/2))/\Delta t_{\mathrm{Gel}}) \tag{4.3}$$

where LC_{max} and LC_{min} are the maximum and minimum amounts of LY loaded on the AuDNP-LY@Gel$_x$ systems reported previously, t_{Gel} is the estimated gelatin thickness, $t_{\mathrm{Gel,m}} \sim 18$ nm, and Δt_{Gel} can be expressed as:

$$\Delta t_{\mathrm{Gel}} = \frac{LC_{max} - LC_{min}}{4\frac{d(LC)}{dt_{\mathrm{Gel}}}\Big|_{t_{\mathrm{Gel}}=\frac{t_{\mathrm{Gel,m}}}{2}}} \tag{4.4}$$

The LC trend of the AuDNP-LY@Gel$_x$ systems as a function of t_{Gel} reported in Figure 4.7 (c) exhibited three different regimes: a toe region in which the t_{Gel} did not affect the LC capacity of the system (0-5 nm); a linear region in which the LC was directly proportional to the t_{Gel} (5-11 nm) due to the increase of the interactions between the drug and gelatin molecules; and a saturation region (11-14 nm) in which the drug, whose experimental concentration was kept constant (1 mg/mL), represented the limiting factor of the entrapment efficiency in the gelatin matrix. It is worth mentioning that the drug LC enhancement due to the t_{Gel} could be fully considered in the estimation model we described earlier.

4.2.4 Application of the model to the monitoring of *in vitro* drug release

As discussed in the previous sections, the complete optical modeling of the AuDNPs-LY@Gel system enabled the monitoring of the gelatin shell formation on the surface of the nanocarrier. Furthermore, the presence of Gel-AuNPs on DNPs provided the nanosystem with another useful functionality: the possibility to directly monitor the gelatin degradation in presence of an external stimulus directly, such as trypsin enzyme (Figure 4.8 (a), and indirectly monitoring the drug release of LY.

As an example, once half of the gelatin thickness was degraded by trypsin, about half of the drug loaded in the nanocarrier is expected to have been released. This could be evaluated by a spectroscopic measurement without the need for expensive equipment. As a proof of concept, the blue shift associated with the gelatin degradation of the AuDNP-LY@Gel$_{0.125\%}$ system was reported in Figure 4.8 (b).

From the theoretical point of view, the Trypsin enzyme used during the release studies reduced the medium effective refractive index from 1.54 (in presence of gelatin) to 1.33 (water refractive index) in the surroundings of AuNPs on the DNPs. For this

reason, 100 % of gelatin shell degradation would result in a blueshift in both λ_{max}) and λ_2 of the Gel-AuNPs absorption spectra.

Ideally, the blueshift due to the gelatin degradation should be equal and opposite to the redshift caused by the gelatin shell formation on the AuDNP system. To show this, in Figure 4.8 (b), the theoretical first derivatives of the absorption spectra highlighting the perfect overlapping between blue and purple lines corresponding to the AuDNP system before the gelatin shell formation and after gelatin degradation, respectively, are reported.

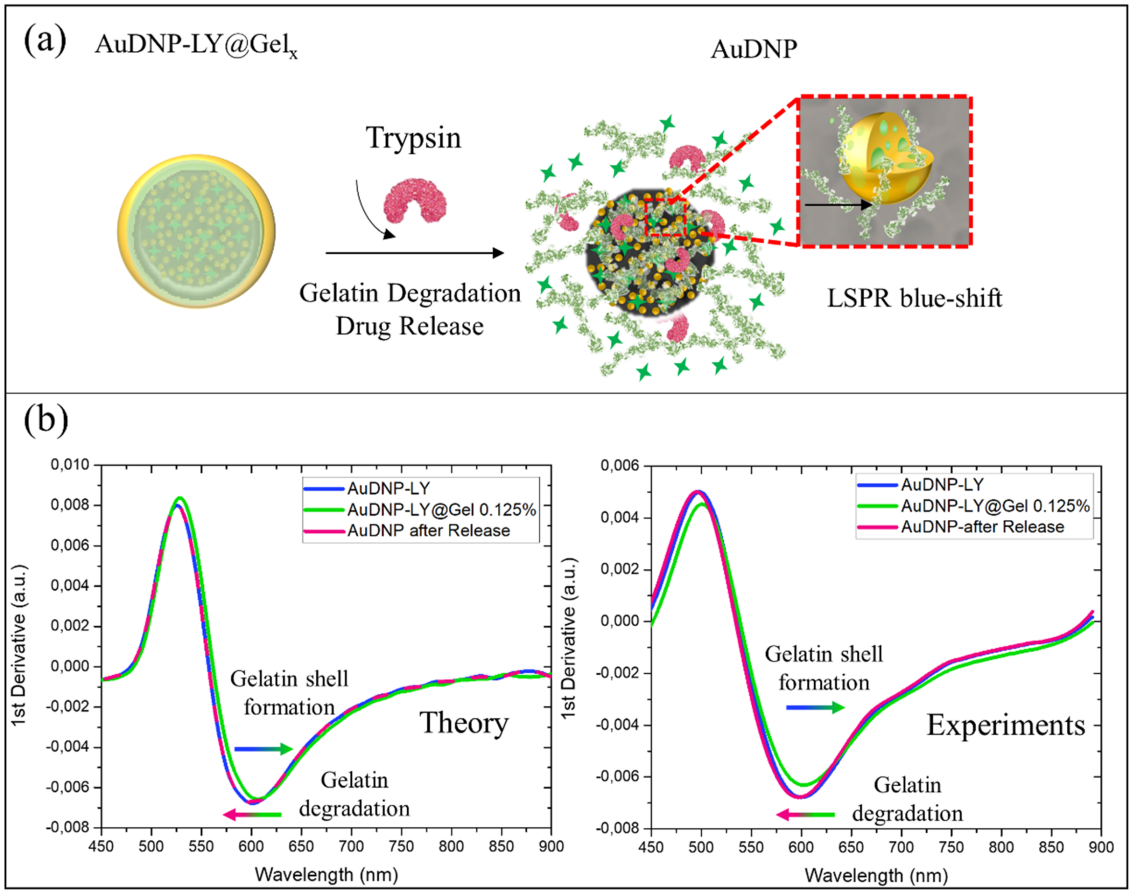

Figure 4.8: (a) Schematic representation of the *in-vitro* gelatin degradation and drug release in a solution containing the Trypsin enzyme. (b) Theoretical and experimental first derivatives of the absorption spectra of the AuDNP-LY system (blue lines), AuDNP-LY@Gel$_{0.125\%}$ (green lines), and after drug release test, during which gelatin degradation occurs (purple lines). Reprinted from Ref. [106].

To validate the proposed model for the prediction of the gelatin degradation, the AuDNP-LY@Gel$_{0.125\%}$ system after the *in-vitro* release, in presence of the trypsin enzyme, was optically monitored. The experimental first derivatives of the absorption

spectra were accurately predicted by the model, as shown in Figure 4.8 (b), since a blue shift of the inflection point in the first derivative occurred.

However, from the experimental point of view, the perfect overlapping between the AuDNP-LY system (blue line) and AuDNP system after the drug release study (purple line), was not achieved. The inflection wavelength of the AuDNPs system underwent a slighter blue shift compared with its initial position, after gelatin degradation. This phenomenon was attributed to the intrinsic hybrid nature of the Gel-AuNPs, which was theoretically hypothesized and experimentally validated in this study.

Indeed, as highlighted in the inset of Figure 4.8 (a), the AuNPs synthesized on DNPs contained gelatin inclusions, which could be partially available, on the surface, to trypsin degradation. Therefore, since the effective relative dielectric constant of Gel-AuNPs was strictly dependent on the gelatin volume fraction, also their optical properties could be affected by gelatin degradation. However, due to the very slight variation in root mean square between theoretical and experimental results, this unwanted effect could be safely neglected.

4.3 Conclusions

The recent trends in nanobiotechnology have led to the development of numerous porous drug-loaded nanoparticles for therapeutic applications. To face challenges such as low drug loading efficiency, these nanoparticles can be coated by a polymeric shell that acts as a gatekeeper enhancing the carrier drug loading capacity.

In this chapter, it is shown that the drug loading capacity of diatomite-based carriers can be significantly enhanced by means of polymeric shells made of natural gelatin *via* post-loading modifications. Herein, the Galunisertib loading capacity of the proposed nanocarrier AuDNP-LY@Gel displayed a sigmoidal growth from 2.4 to 5.6 $\mu g \cdot mg$ of AuDNPs in response to the amount of gelatin in the outer shell.

Moreover, the presence of Gel-AuNPs provided the proposed nanocarrier with optical features suitable for the monitoring of the generation of growing gelatin shells on the nanocarrier. The LSPR of the Gel-AuNPs offered an additional and valid means to monitor the functionalization, thus overcoming the limitations of the standard methods. The formation of the gelatin shell embedding the hybrid nanocarrier AuDNP-LY@Gel, indeed, was confirmed by absorption spectroscopy investigations, and the shell thickness was estimated through numerical simulations.

First, the optical modeling was performed by reverse engineering of the optical response of Gel-AuNPs to extract the gelatin volume fraction in the NPs by applying

Mie theory combined with the Maxwell-Garnett homogenization approach. Secondly, the correlation between theoretically estimated average shell thickness, and the experimental concentrations of gelatin on AuDNP was found by monitoring the variations in the inflection points of both simulated and experimental absorption spectra. Finally, the gelatin degradation and subsequent drug release were confirmed from both theoretical and experimental points of view.

The proposed platform suggests the possibility of directly monitoring gelatin degradation and indirectly monitoring the drug release with an optically modeled system that may be exploited for *in-vivo* applications. Indeed, the LSPR response of differently shaped AuNPs could be tuned to exhibit LSPR position in the invisibility region of human tissues, namely in the range 700-1100 nm.

In this way, the optical response of plasmonic nanoparticles could be followed by simple spectroscopic measurements with no need for expensive equipment. Similarly, the gelatin degradation profile - directly correlated to the drug loading capacity - could be optically monitored to evaluate drug release within the targeted tissues. Finally, since the overexpression of gelatin-degrading enzymes is altered in the tumor microenvironment, the choice of gelatin as a capping material offers two advantages: it improves the nanocarrier loading capacity and makes the drug release triggerable by external *stimuli*.

Chapter 5

Hydrogel-based plasmonic transducers for biomolecular interactions monitoring

With the advent of *flexible* electronics, several conventional fabrication techniques, generally adopted for the large-scale fabrication of electronic components on rigid substrates, have been shifted and re-adapted to polymeric substrates [174]. The same applies to nanophotonics and optical biosensors, in which the capability of polymers to adapt to non-planar substrates [59] directly finds application in wearable sensors, conforming to the skin [175, 176], food-packaging (sensors for food monitoring) [177], real-time monitoring of healing processes [178].

From the combination of polymers with plasmonic NPs hybrid nanocomposite transducers can be designed. These platforms are generally low-cost, highly processable, and relatively simple to fabricate. Moreover, with their ease of integration within microfluidic and microelectronic devices, they represent a promising alternative toward always more smart and efficient technologies due to the following reasons:

- rigid substrates are difficult to employ as wearable sensors since they cannot easily adapt to the skin, as they would not find patient's compliance [179];
- point-of-Care Testing (POCT) optical devices generally possess a microfluidic polymeric component to reduce sample volumes and enhance the capability of an analyte to interact with the bioprobe, therefore a polymeric transducer could be much easier integrated within [180, 181, 182];
- in food quality assessment, polymeric optical devices can be easily integrated into food packaging and interrogated remotely or to the naked eye, without the

need for electronic components [183, 184];

- the mechanical properties of polymers (elasticity, bending capability, and stretchability) over/in which plasmonic NPs can be immobilized open novel fundamental studies on the coupling mechanisms between plasmonic NPs that can be exploited for novel transducing mechanisms (optomechanics) [185];

These polymeric plasmonic transducers can be classified into 2D and or 3D optical sensors according to the fabrication strategy employed to combine the plasmonic NPs on/within the selected polymer. In 2D architectures, the NPs are immobilized on a surface, usually by grafting them on the polymeric substrate with physicochemical strategies. In 3D platforms, the NPs are all distributed within a volume, typically embedding nanomaterials within a pre-polymer precursor [59].

Even though most of the biosensing platforms are 2D architectures with their biorecognition elements immobilized on the top, the effective amount of biomolecules, which can be immobilized in the sensing area, strongly depends on the surface area and surface-area-to-volume ratio. These two parameters are generally very small when dealing with 2D nanostructured devices thus causing important limitations, such as bioprobe instability, narrow dynamic range, and high LODs due to surface rapid saturation [88]. In this context, polymers offer the possibility to obtain 3D miniaturized architectures, which significantly enhance the available surface area and surface-area-to-volume *ratio* to achieve higher analytical performances. In fact, polymer characteristic dimensions can be tailored in a volumetric context from the nanometer scale to the mesoscopic scale with a large variety of techniques such as UV-photolithography, 3D bioprinting, and stencil lithography, among others, [186]. Figure 5.1 provides a summary of the main fabrication strategies (*i.e.*, soft lithography, stencil lithography, nanospheres lithography, electrospinning), polymers properties and types (*i.e.*, natural *vs* synthetic, transparent *vs* large-area), plasmonic NPs composition, size and shape, and potential biomedical applications (*i.e.*, wearable (bio)sensors, POCT, and food quality assessment).

Among all the polymers, hydrogels represent the ideal candidates for 3D optical biosensors since both plasmonic NPs and biomolecules can be embedded in a highly tunable 3D network and optically investigated. Hydrogels are, in fact, highly hydrophilic regular networks obtained from the crosslinking reaction of specific polymer chains, which can be of synthetic or natural origin [187]. They have been extensively used in biomedical applications, ranging from tissue engineering [188, 189] to drug delivery [190, 191]. Their swelling behavior (*i.e.*, capability of absorbing big amounts of water, up to 99 % of their volume) arises from the strong hydrophilic nature of the

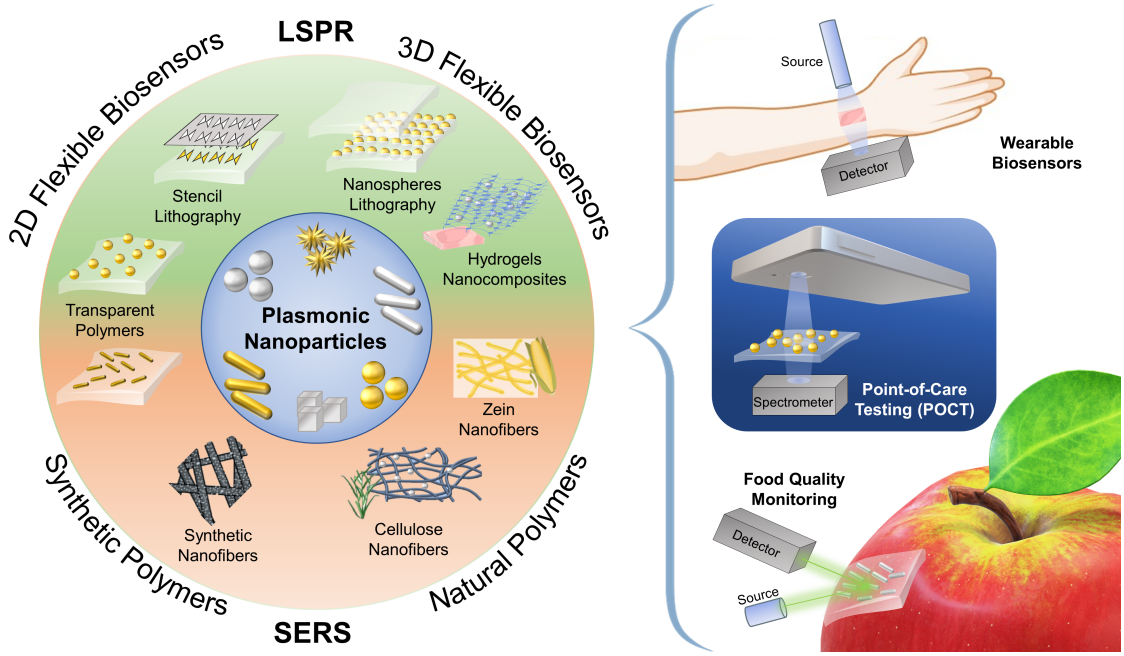

Figure 5.1: Summary of the fabrication strategies, polymer types, plasmonic NPs, and applications of plasmonic polymer nanocomposites. Reprinted from Ref. [59].

polymeric chains, conferring them appealing properties also in the biosensing field.

Recent studies have demonstrated the role of hydrogels as 3D matrices for the entrapment of plasmonic NPs since they are usually anti-fouling, biocompatible, and biodegradable. Moreover, they preserve the activity and functionality of biomolecules within their network [99, 100].

Hydrogel plasmonic nanocomposites that are functionalized with bioprobes can undergo significant variations in response to target analytes becoming *bio-responsive hydrogels*.

The fabrication processes of these particular polymers are generally very simple and straightforward. Starting from a pre-polymer solution of the selected monomer, a crosslinking reaction transforming the monomers into a polymeric network is generally performed. The crosslinking reaction can be made according to several procedures: polymer-polymer bonding or the use of crosslinkers, photo-responsive agents, and/or enzymes. The crosslinking reaction leads to a polymeric network that can be tuned in terms of patterning, mesh size, and crosslinking density. The mesh size and crosslinking density are strongly affected by the monomer molecular weight (MW) and the selected curing agent concentration [192].

In this chapter, hydrogel nanocomposites transducers made of polyethylene glycol diacrylate (PEGDA) and AuNPs are presented as novel optical platforms for both inherent resonance-based biosensors and external signal amplification-based biosen-

sors.

A state-of-the-art of the currently available hydrogel nanocomposites for low-cost, large-scale biosensing is presented, followed by a full description of the fabrication, characterization, and physicochemical properties description of PEGDA and AuNPs, separately.

Then, the investigation of the hybrid properties obtained from the combination of these two materials is described together with their application to different sensing schemes. More in detail, a low MW PEGDA is used for refractive index sensing of small molecules, while a high MW PEGDA is exploited for big molecules sensing in both label-free and MEF modes.

5.1 Towards low-cost, large-scale hydrogel nanocomposites for biosensing applications

Biosensors made of nanocomposite hydrogels have been shown to possess all the requirements to become a great alternative to the common rigid 2D biosensors since they exhibit distinguishable performance and minimized platform cost. Depending on the polymer composition, hydrogels can be classified as natural, synthetic, or composite polymer hydrogels. Natural polymer hydrogels show great biocompatibility and biodegradability, and hence they find large applications in biomedicine (*i.e.*, drug delivery, tissue engineering, and repairing).

On the contrary, synthetic components also possess excellent properties and are extremely tunable in terms of mesh size, crosslinking degree, and, as a consequence, swelling capability. These properties make them the ideal candidates for *ex-vivo* biosensing applications, in which the target analyte to be tested may possess from very low MW (*i.e.*, small molecules, such as sugars, amino acids, and hormones) to very high MW (*i.e.* large molecules, such as enzymes, antibodies, and proteins in general).

More often, hydrogels are required to simultaneously possess many properties such as biocompatibility, biodegradability, controllable hydrophilicity, sufficient mechanical strength, availability of functional groups, and, in the case of biosensors, optical and/or electrical properties too. However, many natural or synthetic polymers do not fulfill all the requirements, as they are.

Therefore, it is possible to design multifunctional composites by selecting the proper combination of natural and synthetic polymers or by *doping* the selected polymer with optical or electrical nanomaterials (*i.e.*, AuNPs). Mechanical properties

should be opportunely designed according to the required specifications. Hydrogels that possess high mechanical strength can be obtained by improving the degree of cross-linking [193], or by reducing the monomer MW. On the contrary, hydrogels possessing large-swelling capability can be obtained by reducing the crosslinking degree and increasing the monomer MW.

To provide hydrogels with multiparametric functionalities one of the key strategies is the nanoscale dispersion of different materials within the polymeric network to form nanocomposite hydrogels [194]. In this context, nanomaterials ranging from 1 to hundreds of nm in size can be dispersed within the polymeric branched and/or crosslinked network with different approaches. The uniform dispersion of inorganic components within the hydrogels goes under different names, such as nanocomposite hydrogels and hybrid hydrogels. Therefore, plasmonic nanocomposite hydrogels are nanocomposite hydrogels in which plasmonic NPs are integrated.

There are three main fabrication strategies with which plasmonic NPs can be integrated within a hydrogel network:

- *in-situ* chemical reduction of plasmonic NPs within a pre-polymerized hydrogel;
- immobilization of pre-synthesized plasmonic NPs on a pre-polymerized hydrogel by surface functionalization;
- polymerization of a pre-polymer hydrogel solution containing pre-synthesized plasmonic NPs.

In the first case, noble-metal salts precursors, such as silver nitrate ($AgNO_3$) and Gold(III) chloride trihydrate ($HAuCl_4 \cdot 3H_2O$) are diffused within a physically or chemically crosslinked hydrogel and then reduced by reducing agents, including sodium borohydride and trisodium citrate. It is the case of Thomas and coworkers that demonstrated the *in-situ* reduction of silver NPs within swollen poly(acrylamide-*co*-acrylic acid. The presence of the plasmonic NPs was confirmed by Transmission Electron Microscopy (TEM) and Uv-Vis spectroscopy by obtaining an LSPR typical absorption spectrum at 406 nm. They optimized the silver nitrate concentration to achieve the best antimicrobial activity on *Escherichia Coli* [195]. Similarly, Zhu *et al.*, proposed the *in-situ* synthesis of thermosensitive poly(*N*-isopropylascrylamide)(PNIPAM)/AuNPs nanocomposite hydrogels by gamma radiation. In this case, AuNPs and hydrogel network were formed simultaneously under the action of gamma radiation. The size of the synthesized AuNPs resulted to be correlated to the monomer concentration so that bigger NPs could be obtained by increasing the monomer concentration. The proposed nanocomposite exhibited

a temperature-dependent catalytic activity in the reduction of *o*-nitroaniline [196]. Even though the *in-situ* chemical reduction represents a fast fabrication strategy for hydrogel nanocomposites, the main limiting factor in its application is the lack of control on the generated NPs size distribution and shapes. In fact, in the proposed examples, only spherical and very tiny NPs have been obtained and when coming to larger spherical NPs, almost always a large size distribution was reported. Due to these motivations, despite being largely applied to antimicrobial and catalytic activity, their application to biosensing is generally limited. Moreover, their optical response is not easily predictable and suffers from reproducibility issues.

A second fabrication strategy to obtain hydrogel nanocomposites is to immobilize plasmonic NPs on the surface of a hydrogel film or microparticle. Choe *et al.*, demonstrated the fabrication of a stretchable and wearable colorimetric patch based on plasmonic NPs immobilized on thermoresponsive microgel particles [197]. Based on the hydrogel swelling/shrinkage behavior, they exploited plasmon decoupling/coupling to achieve a colorimetric temperature sensor. To avoid the instability issue of large colloidal plasmonic microgels, they incorporated them in a flexible film made of polyacrylamide (PAAm). The immobilization of plasmonic NPs requires several stabilization and functionalization procedures to selectively and permanently fix them on the surface of a hydrogel with a uniform distribution and reproducible optical signal. Unfortunately, this can be time-consuming and generally not straightforward because the surface chemistry of plasmonic NPs requires several trials to avoid their non-specific aggregation. For example, citrate AuNPs are generally not stable in saline buffers (*i.e.* PBS buffer, NaCl solutions), strong basic or acidic pH, and organic solvents [76, 77, 78]. For these reasons, the functionalization steps are strongly limited by the medium properties that must keep NPs stable.

Finally, pre-synthesized plasmonic NPs can be incorporated in the monomer solution prior to polymerization in a way that the size distribution, shape, and composition of the plasmonic NPs can be selected *ab-initio* and the incorporation does not require any significant chemical procedure to enable the interaction between the two components. With this technique, large-scale, low-cost, and highly reproducible plasmonic hydrogel nanocomposites can be obtained and fabricated at the industrial level. The crucial parameters here are the concentration and volume *ratios* of NPs and monomers, the mixing time to achieve uniform NPs dispersion, the polymerization approach, and time. Randriantsilefisoa *et al.*, reported on the use of AuNPs embedded in polyol-based hydrogels for influenza A virus detection. Briefly, they started from a pre-polymer solution of dendritic polyglycerol cyclooctyne (dPG) and diazide-poly(ethylene) glycol (PEG) and sialic acid-stabilized AuNPs, the latter

showing high specificity and affinity with the hemagglutinin (HA) protein in influenza A virus (IAV). The naked-eye detection of the virus was made by monitoring the colorimetric variation of the hydrogel as a function of the virus concentration [103]. Analogously, a quantitative LSPR enzyme biosensor obtained from AgNPs embedded in a pre-polymer polyvinyl-pyrrolidone (PVP) hydrogel solution was used for glucose sensing. The platform was functionalized with glucose oxidase enzyme (GOx), and upon the soaking of the platform in a glucose solution, a decrease in the absorbance spectrum of AgNPs was observed due to the proportional hydrogel swelling [65].

The high flexibility and transparency together with the intrinsic mechanical properties of hydrogels can be combined with plasmonic NPs. From this combination, low-cost, large-scale optical transducers can be obtained, which can work both in label-free and non-label-free modes. Their biosensing applications span from drug release monitoring, *ex-vivo* and *in-vitro* biomarkers monitoring, to food quality assessment [59].

Hydrogels do provide physical entrapment and enhanced stability of plasmonic NPs. Moreover, within the matrix, the NPs surface is still partially exposed, allowing the chemical immobilization of a biorecognition element.

5.2 Hydrogels physicochemical properties: the case of polyethylene glycol diacrylate

Due to the large applicability of hydrogels in the biomedical field, their synthesis and physicochemical characterization have been the focus of extensive research [198]. Concerning their fabrication, despite many other methods that have been implemented for the gelation, curing, or crosslinking of the hydrogel monomer solutions, the most commonly used is photopolymerization.

Photopolymerization is a light-induced reaction converting liquid monomers into a crosslinked hydrogel, by means of an appropriate photoinitiator. A photoinitiator, as the word suggests, is a light-sensitive molecule capable of producing an active species upon irradiation with UV, visible, or infrared light. Differently from thermal polymerization, which usually requires elevated temperatures, photopolymerization can be performed at or below room temperature, which is of paramount importance in biology and biochemistry to preserve the integrity of biomolecules, such as proteins and enzymes [199]. Moreover, light-induced polymerization enables the fabrication of complex geometries directly *in-situ*, by exploiting soft photolithographic techniques without the need for expensive molds.

Polyethylene glycol (PEG) has a simple molecular structure, as reported in Figure 5.2 (a). Such a chemical structure confers to this polymer's unique characteristics: high hydrophilicity, non-toxicity, and flexibility. It has found large applications in tissue engineering and drug delivery systems alone or in combination with other materials. As reported in Chapter 3, this polymer is generally used to coat or cap plasmonic NPs to improve their biocompatibility.

PEG diacrylate (PEGDA) is a chemical derivative of PEG. It contains two acrylate groups at the two terminations, which allow the formation of chemical gels by themselves or with other co-polymers (Figure 5.2 (b)). The photopolymerization of PEGDA, schematized in Figure 5.2 (c), involves the preparation of a pre-polymer solution containing the PEGDA monomer and the photoinitiator. Under the action of light (UV-light for Darocur 1173), the photoinitiator dissociates and forms a free radical, which breaks the acrylate double bond forming two crosslinking functionalities, which are free to interact with other broken functionalities. Therefore, a cascade free radical reaction is activated and a polymeric network is formed. Many studies have unrevealed the effect of the PEGDA MWs on the final mechanical properties and morphological microstructure of hydrogels starting from the same polymer concentration [198].

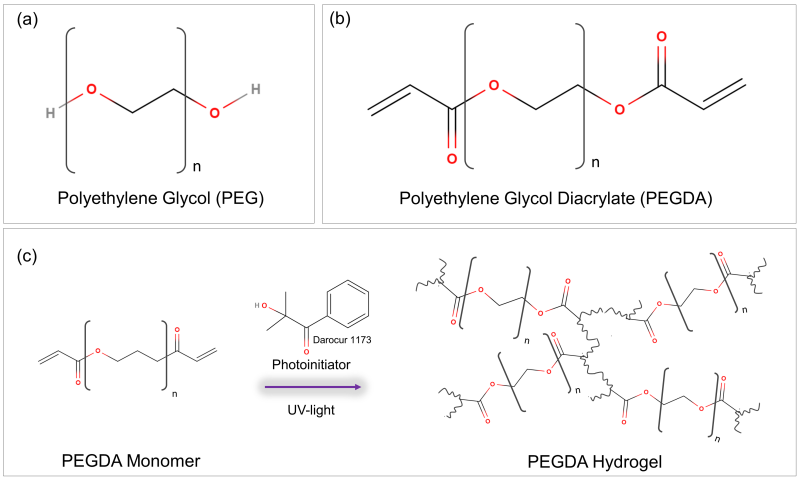

Figure 5.2: Chemical structure of PEG (a) and PEGDA (b). Photopolymerization chemical schematization from PEGDA monomer to PEGDA hydrogel by using a photoinitiator as Darocur 1173. n stands for the repetition number of units associated with the monomer molecular number or molecular weight. The chemical structures are obtained from the online version of MolView software.

The increase in the PEGDA MW generally results in an increase in the swelling capability and a decrease in the crosslinking density and elastic modulus [199]. The

swelling *ratio* (SR) definition chosen for this thesis is:

$$SR = \frac{W_s - W_d}{W_d}, \tag{5.1}$$

where W_s is the weight of the swollen hydrogel, while W_d is the weight of the dried hydrogel. The crosslinking density (CD) is measured in [mol/mL] and can be obtained from the Flory-Renher equation [200]:

$$CD = -\frac{\ln(1 - v_2) + v_2 + \chi_{12} v_2^2}{V_1(v_2^{1/3} - 2v_2/f)}, \tag{5.2}$$

where χ_{12} is a coefficient associated to the polymer-solvent interaction ($\chi_{12} = 0.45$ for PEGDA), V_1 is the molar volume of water ($V_1 = 18.062$ mL/mol), f is the crosslinking functionality ($f = 4$ for PEGDA), and v_2 is the polymer volume fraction at the swelling equilibrium. As expected, while the SR increases with hydrogel MW, the CD decreases since, at fixed polymer weight, the available number of double bonds decreases with the MW.

Also, the microstructures and permeability of PEGDA hydrogels are affected by the monomer MW and must be taken into account for biosensing purposes according to the target analyte molecular weight. In this chapter, four PEGDA monomers are investigated, namely PEGDA 700, 2000, 6000, and 10000, where these numbers denote the final molecular weight of the hydrogel due to the repetition number of the units n in the brackets in Figure 5.2.

5.2.1 Thin film hydrogels preparation

The comparison between PEGDA hydrogels with different MWs was performed by preparing transparent pre-polymer solutions with the same polymer mass, curing agent (PI) amount, and final volume, as schematized in Table 5.1. The prepared

#	PEGDA MW	Polymer Mass	PI Fraction	Final Volume
1	700	108 mg	10% (w/w)	270 μL
2	2000	108 mg	10% (w/w)	270 μL
3	6000	108 mg	10% (w/w)	270 μL
4	10000	108 mg	10% (w/w)	270 μL

Table 5.1: Pre-polymer solutions composition for the preparation of transparent PEGDA hydrogel thin films

solutions were poured in between two 24×24 mm coverslips and cured by UV-Light for 5 minutes to allow full polymerization of the monomers. After the removal of the coverslips, the obtained thin films of hydrogels were soaked in MilliQ water for 24 hours to remove eventual unreacted PEGDA monomers and Darocur (PI) moieties, prior to further characterizations of the material.

5.2.2 Chemical properties

A correct polymerization of a monomer can be validated by performing Fourier Transform InfraRed (FTIR) spectroscopy, which provides information on the chemical structure of the materials.

Instead of measuring the absorption of the materials at each wavelength, with this technique many frequencies at once are shined on the sample to measure how the material absorbs that combination of light frequencies. The same is repeated for different combinations of frequencies. Then, a Fourier Transform algorithm is applied to produce an interferogram. This technique can be applied to both PEGDA monomers and dried polymers, and the differences between the obtained interferograms can provide information on the chemical structure of the prepared materials, in terms of stretching vibrations.

In particular, in Figure 5.3, the FTIR spectra of the PEGDA monomers at different MWs and the dried hydrogels are reported. As marked out in purple, the peaks centered around $1635\,\mathrm{cm}^{-1}$, $985\,\mathrm{cm}^{-1}$, and $810\,\mathrm{cm}^{-1}$ denote the $C = C$ double bonds of the acrylates, which greatly reduce after the polymerization step. While the peaks at $1730\,\mathrm{cm}^{-1}$, and $1110\,\mathrm{cm}^{-1}$, marked in blue, denote the $C = O$ stretching vibration and $C-O$ asymmetric stretching vibration, respectively. The intensity of these peaks in thin film hydrogels decreased in intensity, suggesting that the UV-light intensity for polymerization was proper but weak since no significant damages were provided to the inherent structure of PEGDA, with exception of the $C = C$ double bonds [198].

It must be also noticed, as anticipated above, that the peaks associated with $C = C$ double bonds significantly reduce from low MW weight hydrogels to high MW hydrogels, thus denoting a lower CD due to the lower probability of breaking a double bond during polymerization.

Therefore, from the chemical point of view, the structural integrity, after polymerization and incubation in water for 24 hours, makes these polymers the ideal matrices to embed plasmonic NPs for biosensing purposes, which generally require several functionalization steps prior to target recognition.

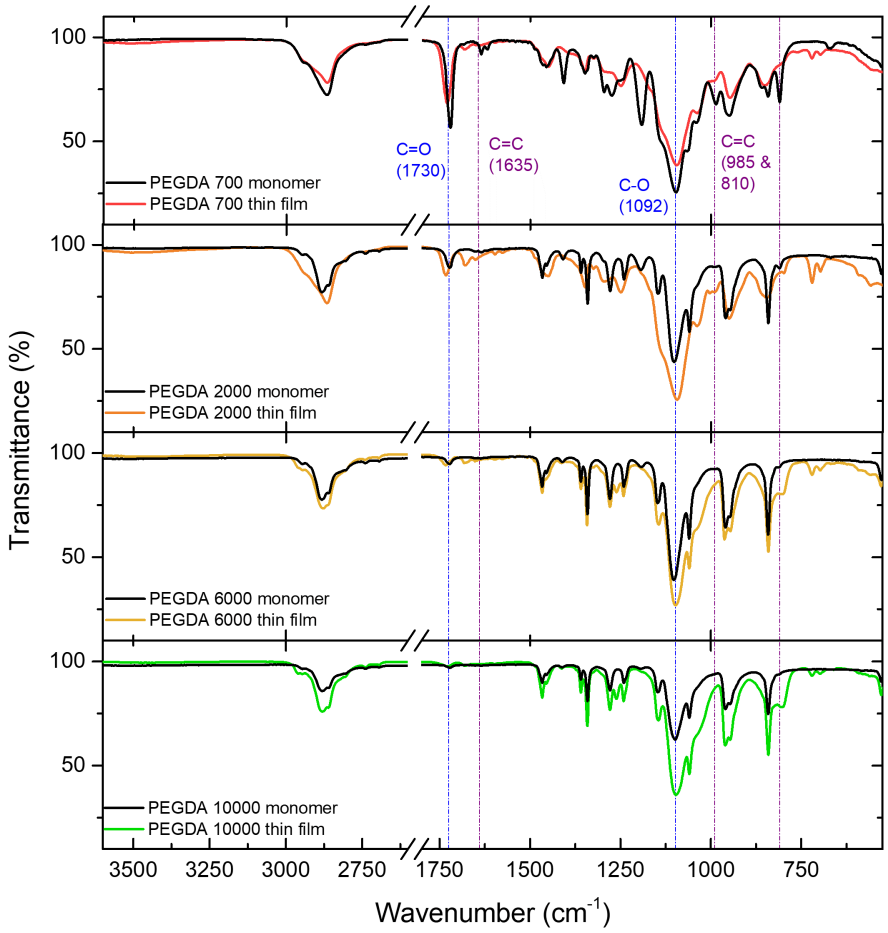

Figure 5.3: FTIR spectra of PEGDA 700, 2000, 6000, 10000 before (monomers) and after photopolymerization (thin film).

5.2.3 Mechanical properties

The mechanical properties of PEGDA hydrogel thin films with different MW were evaluated in terms of SR, mechanical deformation, and elastic modulus.

The measure of the swelling *ratio*, *i.e.*, the absorbency capacity of the hydrogel thin films, measurements at fixed time intervals of 24 hours, after fabrication and immersion in MilliQ water of the hydrogels, were performed. The as-synthesized hydrogel thin films with different MWs were dipped in an exceeding amount of MilliQ water for 24 h and weighed. Prior to each weighing step, the nanocomposites were placed on a dry cloth and gently wiped with another dry cloth to remove excess and weakly bound water. Finally, the hydrogel nanocomposites were put in a vacuum oven at 40°C overnight to achieve their complete drying and measure the W_d value, as reported in Equation 5.1.

In Figure 5.4 (a), the SR histogram of the different hydrogels is reported. As expected, an increase in the swelling capability with the increase in the MW is achieved. While, PEGDA 700 exhibits a $SR = 2 \pm 0.2$, PEGDA 10000 exhibits a $SR = 12 \pm 0.8$, denoting its six times larger capability of absorbing water compared to PEGDA 700.

To further characterize the hydrogels from a mechanical point of view, the thin films were cut into 6×24 rectangles, which were used to perform tensile tests on them to derive maximum deformation and elastic modulus of the material. The elastic modulus and deformation at the break of hydrogel thin films were evaluated by means of quasistatic mechanical tests, performed with a TA-DMA Q800 equipped with tension film clamps. The used standard system was ASTM D-882 for the tensile testing of thin films having thicknesses lower than 1 mm, widths greater than 5 mm, and a width-to-thickness ratio greater than 8. The Young modulus was evaluated at RT in displacement-ramp mode, according to the stress–strain slope up to 2 % strain.

Figures 5.4 (b-c) report the deformation at break ε and Young Modulus E of the thin films. As expected, the larger the molecular weight of the hydrogel, the larger the maximum deformation and the lower the elastic modulus. Generally speaking, higher deformation means higher deformability and adaptability to non-planar substrates, which is a must for flexible biosensors. However, higher deformation also means lower handling possibility and mechanical instability of the material, especially when it absorbs large amounts of water. This explains the larger standard deviations of the box chart in Figure 5.4 (b) with the increase in the MW. Therefore, according to the desired application of the hydrogel as an optical platform, it is important to take into account its mechanical properties. By looking more in detail at the elastic *moduli*, it is important to recognize that even if the elastic modulus decreases from

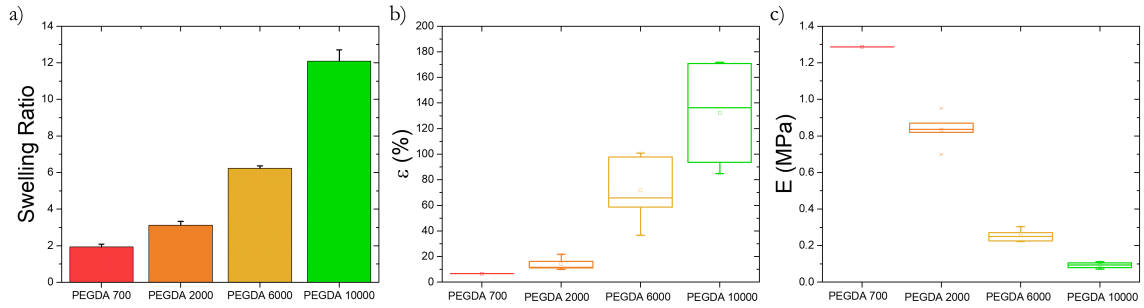

Figure 5.4: (a) Swelling ratio at 24 hours, (b) maximum tensile deformation ε (%), and (c) elastic modulus E (MPa) of PEGDA 700, 2000, 6000, 10000 thin films.

$\sim$ 1.3 MPa, for PEGDA 700, to $\sim$ 0.1 MPa, for PEGDA 10000, it is still possible to handle this material, since its mechanical modulus is still high enough to be included in the following analysis.

Therefore, from these data, all the selected hydrogels are still in consideration to become excellent substrates for AuNPs for plasmonic biosensing purposes.

5.2.4 Optical properties

Finally, a good polymeric substrate for 3D plasmonic transducers must have good optical transparency to allow the investigation of the optical properties of the NPs embedded within it and known optical constants (refractive index) to allow the theoretical fitting of the plasmonic response, as done in Chapter 3.

Therefore, the transmission spectra of PEGDA hydrogel thin films after 24 hours of swelling, were evaluated by using a customized transmission optical setup. A halogen light source covering the visible and near-IR spectrum (400–900 nm) was connected to a Thorlabs optic fiber conveying light to the sample through a collimator. The transmitted light was collected by another Thorlabs optic fiber connected to a spectrometer (Filmetrics F20). The thin films were placed on a coverslip, whose background was subtracted, and wiped with a tissue to remove the excess water.

The spectra were collected in the range 400–900 nm with a resolution of $\sim$ 0.5 nm and are reported in Figure 5.5 (a). As it can be observed, all the PEGDA exhibit excellent transparency between 500 and 900 nm, which is a bit lost in the range 400 - 550 nm, as it generally happens for all organic compounds. However, all the selected hydrogels can be considered sufficiently transparent for the monitoring of the optical signal of a suitable density of plasmonic NPs.

Moreover, when performing absorption measurements of plasmonic NPs, the background coming from the non-perfect transparency of the substrate can be subtracted

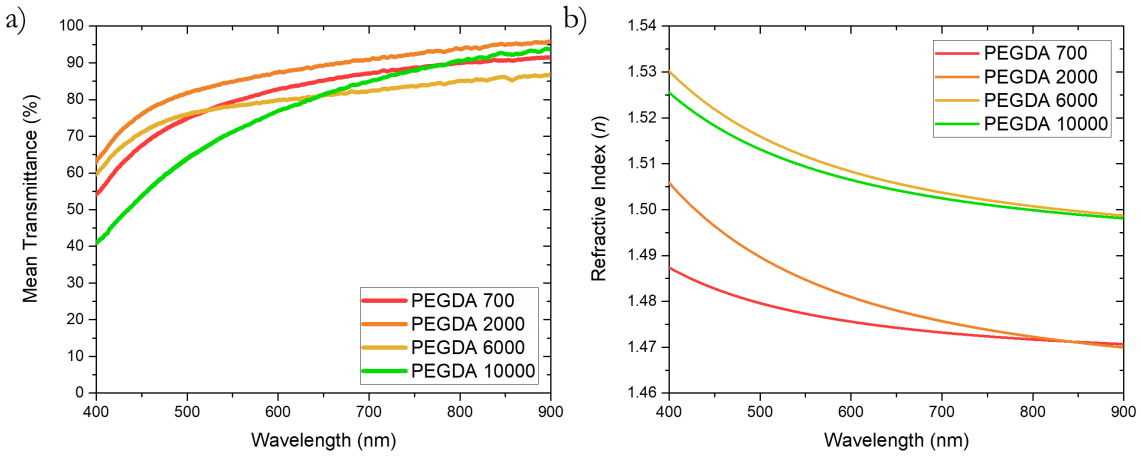

Figure 5.5: (a) Transmission, and (b) refractive index of PEGDA 700, 2000, 6000, 10000 thin films measured at wavelengths in between 400 and 900 nm.

by using a naked (without NPs) thin film as a reference standard, as shown in the next sections.

Also, the refractive index of the substrate was characterized as shown in Figure 5.5 (b). While the refractive indices of the PEGDA monomers generally come with a datasheet, the refractive indexes of the polymerized hydrogels dried on silicon were measured by variable angle spectroscopic ellipsometry (UVISEL, Horiba, Jobin–Yvon). The spectra were recorded in the spectra range $300 - 1600$ nm, and only the range $400 - 900$ was selected, to be in agreement with the other recorded spectra. The measurements were performed at five different incident angles ($50°, 55°, 60°, 65°$, and $70°$). The Sellmeier transparent model [201] was used:

$$n^2(\lambda) = A + \frac{B\lambda^2}{\lambda^2 - \lambda_0^2} \qquad k(\lambda) = 0 \tag{5.3}$$

where n is the real part of the refractive index and k is the imaginary part of the refractive index, generally associated with materials' intrinsic absorption and, therefore, set to 0, as imposed from the Sellmeier transparent model. A, B, and λ_0 are empirical parameters that are derived from the fitting of the measured dispersion curves.

The curves in Figure 5.5 (b), show a slight increase in the refractive index n as a function of the hydrogel MW. More precisely, PEGDA 700 and 2000 (red and orange curves) show similar behavior with exception of the range $400 - 550$ nm, while the refractive indices of PEGDA 6000 and 10000, are significantly higher than the

others, and mostly overlap between them (yellow and green curves). All of them are significantly larger than the PEGDA monomers. This significant difference may be attributed to the formation of the crosslinked network operated by the photoinitiator (PI), which makes the hydrogel network more dense and viscous than the uncrosslinked monomers.

5.3 Bottom-up synthesis of citrate-capped AuNPs with controlled size

In this section, the synthesis and characterization of the AuNPs to be embedded in the PEGDA hydrogel thin films are reported. During the past decades, tremendous efforts have been made to achieve good control of the size and shape of plasmonic NPs. Despite Turkevich method [145] for the synthesis of citrate-stabilized AuNPs remains the most common (see Chapter 3) to obtain AuNPs from 5 to 150 nm, the size and size distribution (but also the shape) of the obtained NPs is quite non-uniform.

More recently, seed-mediated synthetic strategies have represented the most efficient strategies to achieve good control of AuNPs quality, since nucleation and growth processes are temporally separated. Based on this, Bastus *et al.*, proposed a modification of the Turkevich method, namely *seeded-growth method*, to achieve great control over the size and shape of the spherical NPs. Their strategy focuses on the inhibition of secondary nucleation during the growth process. This latter is kinetically controlled by adjusting the reaction conditions in terms of temperature, seed concentration, and pH level [95]. The obtained AuNPs are quasi-spherical, highly monodispersed, and highly concentrated. These three main properties are highly desirable to achieve ease of predictability of the AuNPs optical response, stable optical signals, and reduced centrifugation steps to achieve the desired optical density in plasmonic nanocomposites.

Experimental part

Chemicals - Tetrachloroauric acid trihydrate ($HAuCl_4 \cdot 3H_2O$), trisodium citrate dihydrate ($C_6H_9Na_3O_9$), were purchased from Merck KGaA (DE).

Synthesis of monodisperse AuNPs - AuNPs from $\approx$ 20 to $\approx$ 70 nm were obtained by adapting the protocol reported in Ref. [95]. All glassware was cleaned with *Aqua Regia*, a mixture of nitric and hydrochloric acids (1 : 3 V/V), prior to its use. Briefly, a citrate solution (2.2 mM, 150 mL) was heated up to 100 °C.

Thereafter, $HAuCl_4$ (1 mL, 25 mM) was added to the boiling solution to obtain the Au seeds ($\sim$ 10 nm, $\sim 3 \cdot 10^{12}$ NPs/mL). In 10 minutes, the color of the solution changed from yellow to bluish-gray and finally to soft pink. In the same flask, the solution was cooled down to 90 °C.Then, 1 mL of $HAuCl_4$ solution (25 mM) was injected. After 30 min reaction time, the injection was repeated. After 30 min, part (55mL) of the obtained solution was picked up and the remaining part was diluted with 53 mL MilliQ water and 2 mL of 60 mM sodium citrate. The diluted solution represented the new seed for the subsequent growth step. The 55 mL solution that was picked up represented the 1^{st} growth step, corresponding to AuNPs with mean diameter of $\sim$ 20 nm. The synthesis proceeded until the 9^{th} growth step, corresponding to nanoparticles of $\sim$ 70 nm. Since evaporation was prevented during the reaction process, the final volume was kept constant. Therefore the final concentrations of all the NPs solutions (from the 1^{st} to the 9^{th} growth step) were approximately equal to the ones reported in Ref. [95].

5.3.1 AuNPs Characterization

Freshly synthesized AuNPs were characterized in terms of size distribution and absorbance spectra. The size and size distribution measurements were performed by DLS, as reported in section 3.3.1. The UV-Vis absorbance spectra were measured from 400 to 900 nm. The samples were opportunely diluted in order to obtain absorbance peaks between 0 and 1 (see section 3.3.1). Finally, a peak analysis was performed. Both DLS and UV-Vis characterization are reported in Figure 5.6.

In Figures 5.6 (a-b), the AuNPs size and LSPR wavelength λ_{max} are reported as a function of the growth step. DLS measurements confirmed the presence of monodisperse and stable NPs colloidal suspensions with a single scattering peak both in intensity and volume, having a polydispersity index (PDI) always well below 0.2. As a result of the seeded-growth reaction, the mean diameter of the NPs increased from $\sim$ 20, for the 1st growth step, to $\sim$ 70 nm, for the 9th step. As a comparison, starting from SEM images of Figure 5.6 (c), particle analysis was performed and, as a result, the measured mean NPs diameters well-agree with the values obtained from DLS. The differences in the standard deviations can be certainly ascribed to the number of particles that can be optically detected by DLS, which is higher than the number of imaged particles. On the contrary, DLS produces higher standard deviations since also bigger and smaller NPs that were not resolved in SEM images are considered. For this reason, DLS results were taken into account for the following sections.

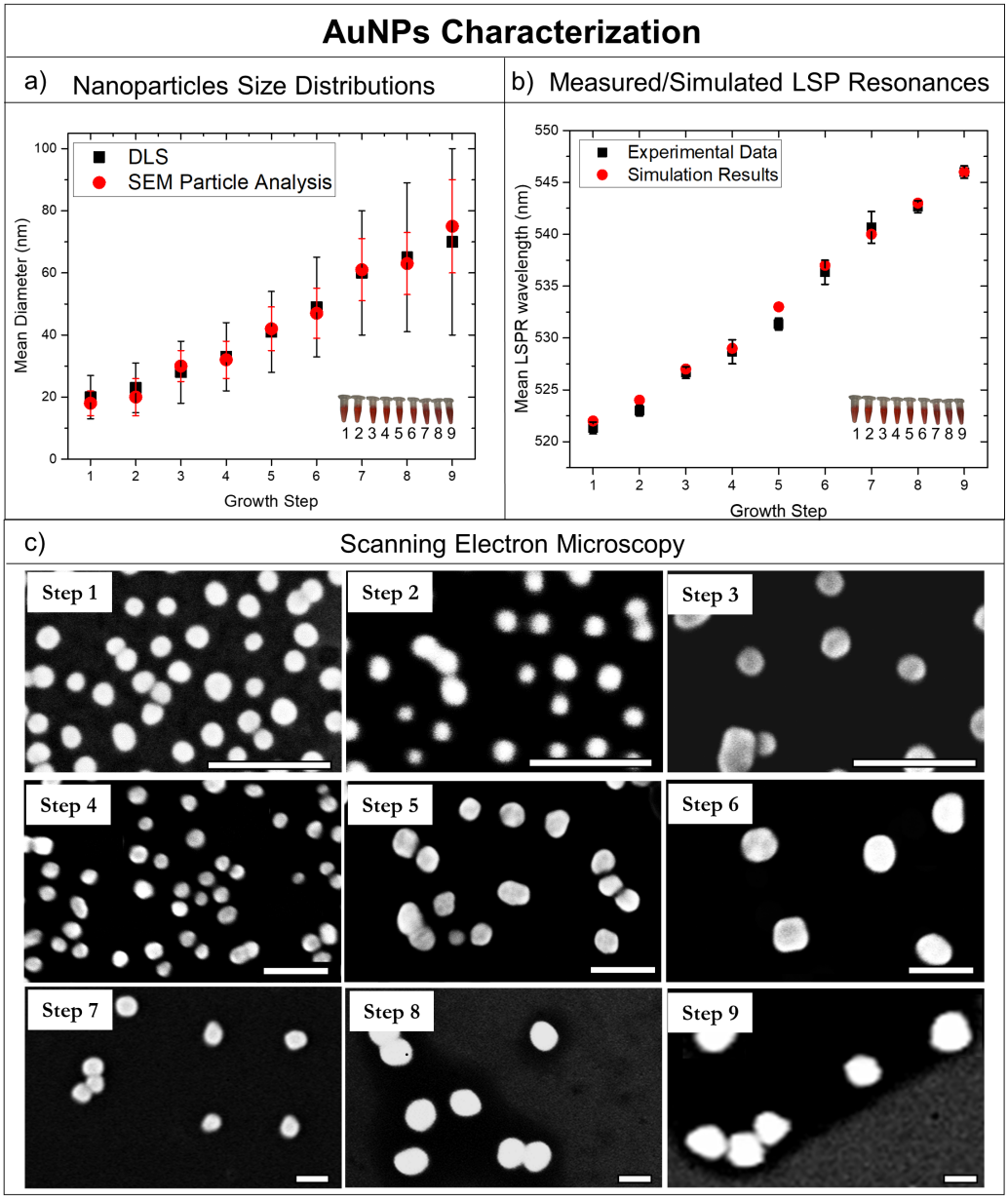

Figure 5.6: Characterization of colloidal gold nanoparticles, synthesized by the seeded-growth method reported in Ref.[95]. a)Comparison of Dynamic light scattering (DLS) size measurements (black squares) and particle analysis by SEM images (red circles) revealing an increasing mean diameter of AuNPs as a function of the growth step. b) LSP resonances (λ_{max}) as a function of the growth step are obtained via a peak analysis of absorbance spectra measured by UV-Vis spectroscopy (black squares). The vertical bars represent the standard deviations on a minimum of three independent measurements. The simulated extinction cross-section resonance peaks of the distributions of gold nanoparticles in water (n=1.33) are reported (red circles). (c) SEM images of the 9 populations of gold nanoparticles, showing spherical or quasi-spherical gold nanoparticles with increasing size as a function of the growth step. The reported scale bars correspond to 100 nm. Adapted from Ref. [60].

The increasing size distribution of AuNPs was also confirmed by UV-Vis spectroscopy (Figure5.6 (b), in which a red-shift of the λ_{max} from $\sim$ 522 nm to $\sim$ 547 nm can be observed. The very low standard deviations highlight the good reproducibility of the NPs synthesis. In Figure5.6 (b), the simulated λ_{max}, starting from DLS size distributions, are also reported. They are obtained by using the Mie Theory combined with MG approximation presented in Chapter 3. The hypothesis of *non-interacting* NPs holds true also for this modified Turkevich synthesis since no absorption peaks were observed at wavelengths between 600 and 800 nm. Moreover, the presence of dimers, or trimers, would have caused huge resonance shifts both for smaller and larger particles, as reported in refs. [202, 203]. The simulation results are in very good agreement with the measured spectra, confirming both DLS and UV-Vis spectroscopy measurements. The SEM images, in Figure5.6 (c), are further proof of the controlled growth of the AuNPs, which appear spherical, or quasi-spherical, and with few clusters, which can be mainly attributed to the drying process on the silicon wafer.

5.4 PEGDA/AuNPs nanocomposites: fabrication and characterization

Chemicals - Tetrachloroauric acid trihydrate ($HAuCl_4 \cdot 3H_2O$), trisodium citrate dihydrate ($C_6H_9Na_3O_9$), PEGDA with MWs of 700, 2000, 6000, and 10000 Da, 2-Hydroxy-2-methyl-1-phenyl-propan-1-one (Darocur 1173), and cysteamine (C_2H_7NS) were purchased from Merck KGaA (DE).

Fabrication, Functionalization, and Characterization - Once the PEGDA hydrogel thin films and the AuNPs have been selected and characterized, it is possible to study the optical performances arising from their combination. In this section, the effect of the PEGDA on AuNPs with fixed size (60 ± 20 nm) is unrevealed. The all-solution fabrication strategy, ensuring high reproducibility of the optical signal, is schematized in Figure 5.7. The nanocomposites with different PEGDA were prepared by following Table 5.2 where the AuNPs weight per mL was obtained by drying the AuNps in a calibrated plastic tube. The amount of polymer, AuNPs, PI, and final volume were kept constant to study the different behaviors of hydrogel nanocomposites obtained from PEGDA monomers with different MW.

The thin films embedding AuNPs were characterized by the customized transmission mode setup at normal incidence included in Section 5.2.4. A schematic represen-

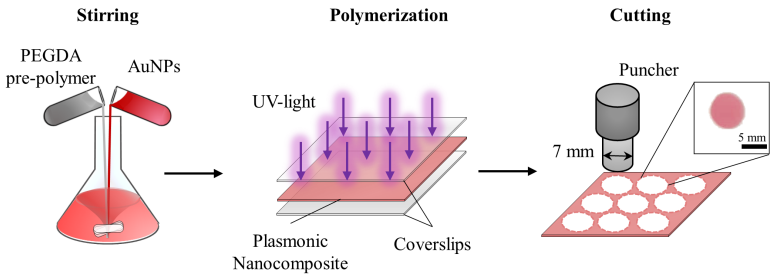

Figure 5.7: Schematic representation of the all-solution fabrication strategy consisting of: stirring of a PEGDA pre-polymer solution with a suitable concentration of AuNPs; polymerization by exposing the solution in between two coverslips to UV-light; and cutting by a puncher to ensure controlled samples sizes. Adapted from Ref. [66].

PEGDA MW	PEGDA Mass	PI fraction	AuNPs (60nm)	Volume
700	108 mg	10% w/w	0.3% w/w	270 μL
2000	108 mg	10% w/w	0.3% w/w	270 μL
6000	108 mg	10% w/w	0.3% w/w	270 μL
10000	108 mg	10% w/w	0.3% w/w	270 μL

Table 5.2: Pre-polymer/AuNPs solutions composition for the preparation of PEGDA/AuNPs hydrogel nanocomposites

tation of the optical setup is reported in Figure 5.8 (a). The absorption spectra were

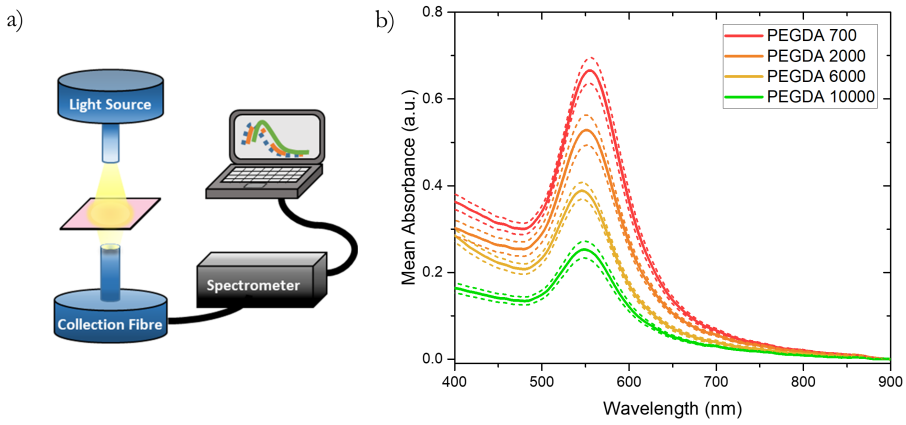

Figure 5.8: (a) Schematic representation of the customized transmission mode optical setup to identify the optical properties of PEGDA/AuNPS nanocomposite transducers. Adapted from Ref. [60]. (b) Mean absorption spectra (solid lines) with confidence interval (dashed lines) of PEGDA/AuNPs (60 nm) nanocomposites obtained from hydrogels with increasing MW.

collected in the range of $400 - 900$ nm, after dipping the nanocomposites in MilliQ water, whose excess was removed before measurements.

The spectra reported in Figure 5.8 (b) show very low standard deviations, owing to the high reproducibility of the all-solution fabrication strategy. Moreover, a decrease in the LSPR signal with the increasing MW of the hydrogel can be observed. This is due to the optical density of the AuNPs, which decreases as the hydrogels undergo swelling, and to the light beam spot, which was kept constant during all the measurements.

The chemical stability of the AuNPs within the PEGDA hydrogels was assessed by incubating the nanocomposites for 15 days in buffers at different pH (2.5, 4.5, 6.5, 8.5, and 11) and different NaCl concentrations (from 0.01 mM to 1 M). The pH was adjusted by using sodium hydroxide (NaOH) and hydrochloric acid (HCl). The experiments were performed at room temperature in sealed multiwells to avoid solvent evaporation. The nanocomposites were finally washed with water to restore the swelling equilibrium. The results of this investigation are summarized in Figure 5.9. The mean absorption intensity spectra demonstrate the chemical stability of AuNPs. No significant variation of the absorption nor shift of the plasmonic response was registered after 15 days of incubation.

To have an idea of the hydrogel nanocomposite sensing performances a small molecule, namely the cysteamine, was used to monitor the LSPR signal variation as a function of this model molecule concentration.

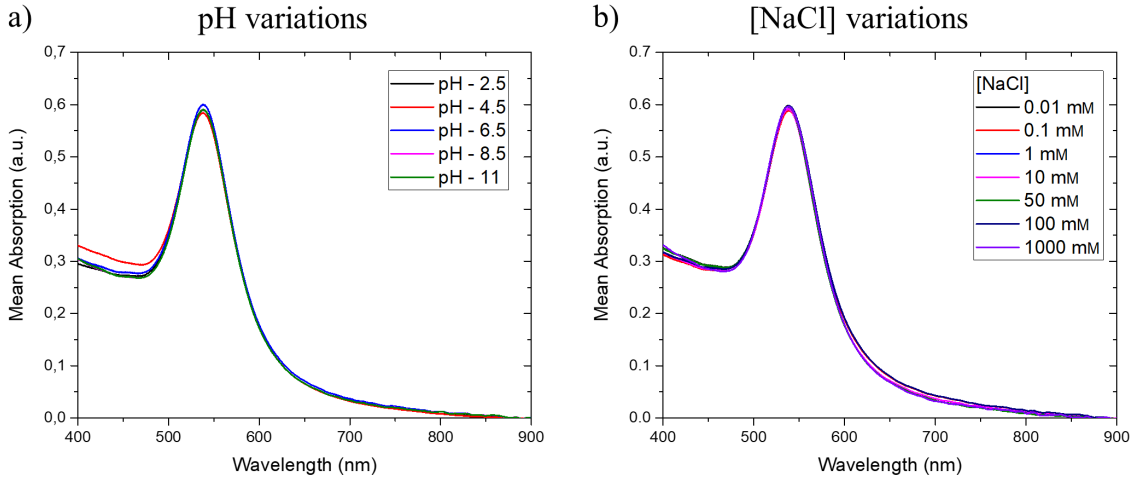

Figure 5.9: (a) Mean absorption spectra of the nanocomposites after 15 days incubation in buffers with increasing pH (from 2.5 to 11). (b) Mean absorption spectra of the PEGDA/AuNPs nanocomposites after 15 days of incubation in water with increasing salt concentrations (from 0.01 mM to 1 M). The optical measurements are obtained from a minimum of three independent samples ($n \geq 3$)..

Cysteamine, having a $MW = 77.15$ Da is a chemical compound that can be biosynthesized in mammals, including humans, from the degradation of coenzyme A [204]. It is a very advantageous compound to screen the sensing capabilities of a new platform, due to its $-SH$ thiol group, which can be exploited for S-metal bonds.

Cysteamine solutions at different concentrations, ranging from 0 mM to 2.0 mM, were prepared and the different hydrogel nanocomposite samples were incubated overnight in these solutions at room temperature.

After washing, the optical spectra of the AuNPs within the hydrogels were recorded and the variations of the LSPR both in terms of position and intensity were monitored as compared to the hydrogels in water. The obtained results are summarized in Figure 5.10.

Interesting behaviors were observed for the different hydrogels. First, it must be noticed that the variation in absorption intensity, denoted as $|\Delta Abs.|$, is actually a decrease in the absorption intensity from an initial state (hydrogels in water) to a final state (after the incubation of the hydrogels within cysteamine solutions). The variation in intensity was recorded at λ_{max} and it increased, in absolute value, as a function of cysteamine concentration following saturation kinetics (Michaelis-Menten type). In particular, the highest $|\Delta Abs.|$, corresponding to a relative decrease of the $\sim 50\%$ ([cysteamine] = 2.0 mM) was achieved for the PEGDA with the highest MW, while only a 5% variation was observed for the PEGDA 700 nanocomposites. This

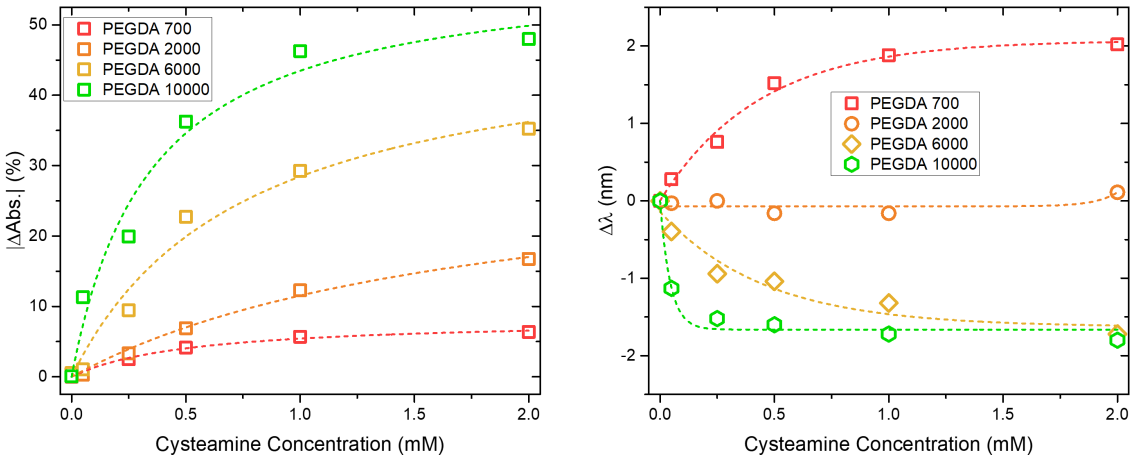

Figure 5.10: On the left, absorption intensity variations $|\Delta Abs.|$ at a fixed wavelength λ_{max} as a function of the cysteamine concentration for hydrogel nanocomposites with increasing MW. On the right, LSPR shift $\Delta\lambda_{max}$ as a function of the cysteamine concentration for hydrogel nanocomposites with increasing MW.

behavior arises from the hydrophilic nature of the cysteamine, which, ones linked to the AuNPs within the hydrogel, tends to favor the absorption of water from the hydrogel. Then, since the swelling capability increases almost linearly with the MW, the hydrogel that mostly benefits from this behavior is PEGDA 10000.

Contrarily, concerning LSPR position variations, denoted as $\Delta\lambda_{max}$, the exact opposite behavior is observed. In this case, a significant redshift is achieved only for low MW hydrogel nanocomposites (PEGDA 700), where a small molecule as cysteamine, led to a 2 nm redshift. The other hydrogels, instead, because of their larger swelling capability, tended to restore the refractive index variations in the surrounding of the NPs with water, and therefore, no significant shift, or even blueshift (for PEGDA 6000 and 10000), in the LSPR signal was observed. The blueshift in high MW hydrogels was caused by the reduction of the effective medium refractive index.

Therefore, at this stage, it is clear that low MW hydrogel can be used as refractometric plasmonic biosensors, with the classical approach of monitoring $\Delta\lambda_{max}$ as a function of a target analyte concentration, while high MW hydrogels can be exploited as a new paradigm of plasmonic biosensors, dominated by a *swelling-dependent* response.

For small molecules, such as hormones and small oligonucleotides, both approaches can be adopted. Contrarily, for large molecules, such as antibodies and big proteins, a large-swelling hydrogel is required to ensure the diffusion of the molecules within the network [60, 66, 59]. In the next sections, these statements are further clarified.

For low MW PEGDA, a study also on the AuNPs size on the sensing performance will be reported; while for high MW the optical intensity achieved with 60 nm AuNPs will be shown to be sufficient enough for the design of an excellent optical transducer.

5.5 Low MW PEGDA nanocomposites as refractometric biosensors

In this section, a 3D plasmonic sensing platform combining the properties of citrate-capped AuNPs and low MW PEGDA hydrogels is described as a nanocomposite hybrid material for refractive index-based biosensing.

In particular, the optical properties and sensitivity were tuned by varying the AuNPs' mean size and accurately predicted by the Mie theory modified with the MG approximation (Chapter 3). The increased stability of citrate-capped AuNPs, when embedded in the hydrogel network, and compared to the colloidal aqueous solutions, is also, herein, demonstrated.

Low MW PEGDA hydrogel physically entraps the AuNPs even after their full swelling, thus overcoming the aggregation effects usually seen in colloidal aqueous solutions. Such property was confirmed by dipping the hydrogel nanocomposites in organic solvents and buffers, which would generally cause the aggregation of the same AuNPs if they were in solution. Moreover, biotin, as a small molecule model, was captured, and optically detected with the transmission mode customized setup reported in Figure 5.8 (a). The final result was a hybrid device, which can be functionalized with a bio-recognition element for specific detection of a target.

5.5.1 Experimental Part

PEGDA/AuNPs nanocomposites fabrication - The synthesized citrate-capped AuNPs with controlled size were embedded with low MW hydrogel thin films (PEGDA 700). To achieve a suitable optical density of all the AuNPs sizes within the hydrogel, they were all centrifuged and concentrated 10× (*e.g.*, $\sim 1.9 \cdot 10^{13}$ NPs/mL for the 1^{st} growth step). AuNPs were centrifuged at 1920 g at 10° C for time intervals ranging from 10 minutes for bigger nanoparticles ($\sim$ 70 nm) to 60 minutes for smaller ones ($\sim$ 20 nm). PEGDA 700, with Darocur 1173 as photoinitiator (2% v/v), was prepared and gently mixed with the concentrated AuNPs in a volume ratio 2:1, respectively, by means of a magnetic stirrer. All the 9 pre-polymer solutions containing nanoparticles with increasing size (from 20 to 70 nm), from the 1^{st} to 9^{th} growing step, were obtained with the same procedure. A

part from the size and concentration of AuNPs, the fabrication procedure is the same reported in Section 5.4 and schematized in Figure 5.7. This fabrication resulted in hydrogel thin films (24 mm × 24 mm × 0.47 mm) embedding AuNPs and having the typical coloration of colloidal AuNPs (from pinkish to reddish, for smaller NPs; from purplish to violetish for bigger NPs), as shown in Figure 5.11 (a).

Optical Characterization of PEGDA/AuNPs hydrogels - The low MW hydrogel thin films embedding AuNPs were characterized as reported in Section 5.2.4, after removal of PEGDA and Darocur moieties. The spectra were collected in the range of 400-900 nm with a resolution of 0.2 nm. The spectra were zoomed in the range of $475 - 650$ nm for better visualization of the LSPR peak. The absorption of hydrogel nanocomposites was evaluated by using naked PEGDA 700 thin films (with no AuNPs) as a reference standard. The raw absorbance spectra were fitted with a polynomial curve and the resonance wavelength λ_{max} was measured through a peak analysis, performed in OriginPro.

Scanning Electron Microscopy - Scanning Electron Microscopy characterizations were performed using a Carl Zeiss NTS GmbH 1500 Raith Field Emission Scanning Electron Microscope (Carl Zeiss, Oberkochen, Germany), equipped with an InLens detector. The voltage was set at 5 kV and the aperture at 10 μm. The imaging was performed on PEGDA embedding AuNPs with a size distribution of 65 ± 20 nm.

Sensitivity Analysis - To obtain information about the sensing performance of the fabricated LSPR refractive index-based transducers, different sensitivity measurements, involving dipping of the nanocomposites into different organic solvents with known refractive index (RI) were performed. Briefly, the thin hydrogel patches were cut into disks and placed in cuvettes. The disks were immersed in Water ($n = 1.33303$), Ethanol ($n = 1.3617$), and Isopropanol ($n = 1.3776$), and the LSPR variations $\Delta\lambda_{max}$ were measured by using the optical setup reported in Section 5.2.4. To confirm the data and being sure of negligible swelling effects, the same analysis was performed with glycerol-water mixtures with percentage weight ratios $0\%, 20\%, 40\%, 60\%, 80\%$ and 100%, and whose refractive index is proportional to the concentration of glycerol, namely $n = 1.33303, 1.35749, 1.38413, 1.41299, 1.44290, 1.47399$, respectively. A linear fitting of the collected λ_{max} was performed, and the slopes of the obtained straight lines were taken as Sensitivity values and plotted as a function of the growth step,

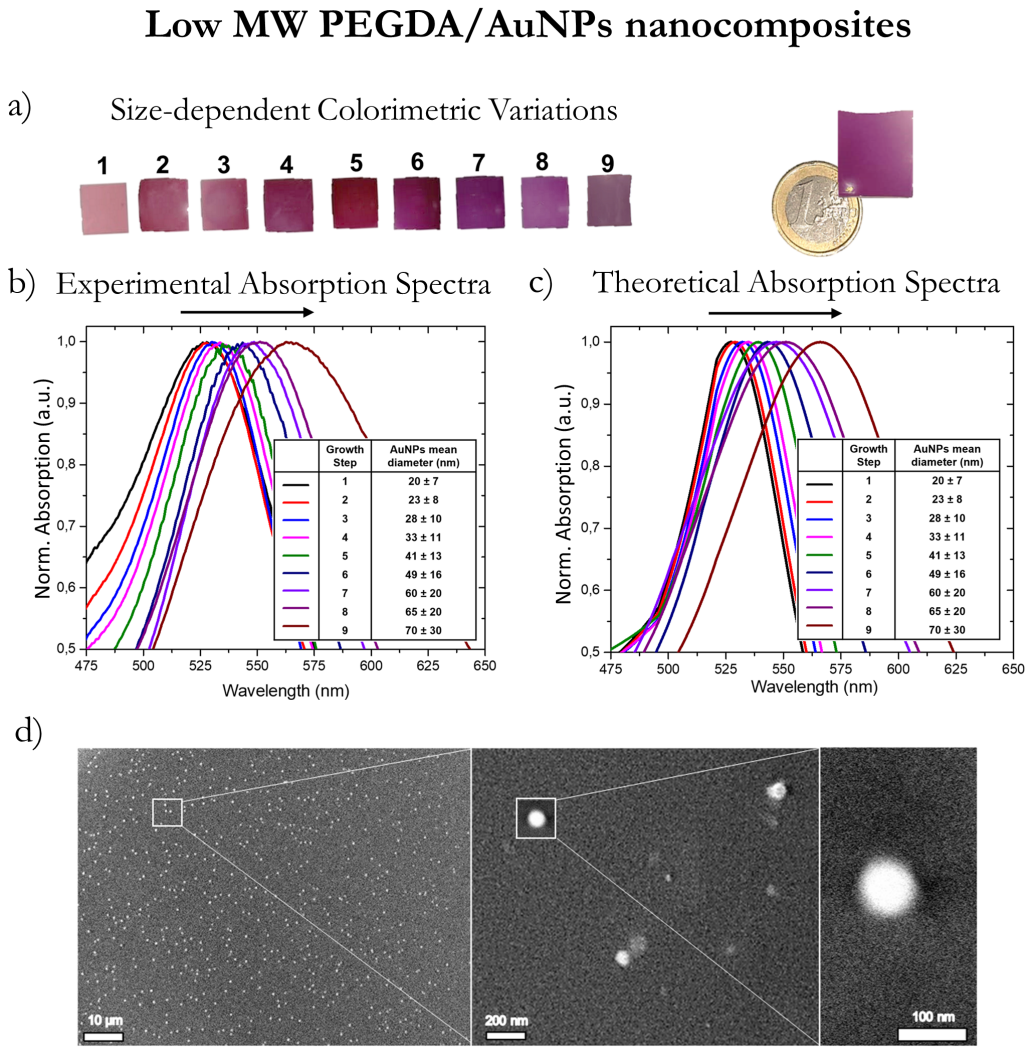

Figure 5.11: (a) Colorimetric variation of low MW PEGDA/AuNPs nanocomposites as a function of the citrate-capped AuNPs growing step shown. (b) Normalized absorption spectra from 475 nm to 650 nm; in the legend, the growth step and the mean diameter of the synthesized AuNPs. (c) Predicted absorption spectra of PEGDA/AuNP patches, by using MG-modified Mie Theory, and a surrounding medium effective refractive index obtained as the weighted average of PEGDA and Water refractive indexes, respectively. (d) SEM images of the PEGDA hydrogel nanocomposites with size distribution 65 ± 20 nm at different magnitudes. A good dispersion of the AuNPs on the hydrogel surface can be observed. The scale bars correspond to 10 μm, 200 nm and 100 nm, respectively.

Performance Parameters Comparison					
Sample	**Medium**	**RI Range**	**S (nm/RIU)**	**FWHM (nm)**	**FOM**
AuNPs	Org. Solvents	1.33 - 1.37	N/D	95	N/D
PEGDA/AuNPs	Org. Solvents	1.33 - 1.37	110	80	1.4
AuNPs	Gly/Water	1.33 - 1.47	110	95	1.2
PEGDA/AuNPs	Gly/Water	1.33 - 1.47	70	80	0.9

Table 5.3: Comparison of Sensitivity (S), Full Width at Half Maximum (FWHM) and Figure of Merit (FOM) of AuNPs (65 ± 20 nm) in solution and after their embedding in PEGDA. The analysis is performed both for organic solvents (RI range = [1.33 - 1.37]) and glycerol/water solutions of w/w 0%, 20%, 40%, 60%, 80%, and 100% (RI range = [1.33 - 1.47]). Due to AuNPs spontaneous aggregation in organic solvents (Ethanol and Isopropanol) S and FOM cannot be defined (N/D).

as reported in Figure 5.12. The highest sensitivity of low MW PEGDA/AuNPs nanocomposites was compared with the sensitivity of a colloidal solution AuNPs of the same size. The analysis was performed for both organic solvents and glycerol/water mixtures. The results are briefly schematized in Table 5.3 and Figure 5.13.

Numerical Simulations - Numerical optimization was performed by combining the genetic algorithm (GA) and the Mie Theory modified with MG approximation, as done in Chapter 3 for citrate-capped AuNPs, under the hypothesis of non-interacting NPs. The diameter of the AuNPs was described through a Gaussian distribution, with mean value and standard deviation obtained by DLS measurements (section 5.3.1). The optical absorption spectra were predicted after the inclusion of the AuNPs in PEGDA hydrogel. In this case, the refractive index of the medium was assumed to be the arithmetic mean of water and PEGDA refractive indices. The refractive index of PEGDA 700 with Darocur (2% V/V) was measured by variable angle spectroscopic ellipsometry (UVISEL, Horiba, Jobin–Yvon), and is reported in Figure 5.5 (b - red solid line).

Low MW PEGDA/AuNPs functionalization The low MW PEGDA with ~ 65 nm AuNPs was pre-swollen in MilliQ water for 24 h and then soaked into a water solution of cysteamine with concentrations varying from 10 μM to 2 mM (ON, RT) to allow the interaction of cysteamine with AuNPs. After accurate washing in MilliQ water, a peak analysis was performed on the monitored absorption spectra. Then, biotin, as a small molecule model, was allowed to interact with cysteamine-capped AuNPs. To do this, hydrogel nanocomposites were soaked into sulfo-NHS-Biotin in Dimethyl Sulfoxide (DMSO) and 0.01 M PBS (pH = 7.4) in a ratio $1 : 1 V/V$

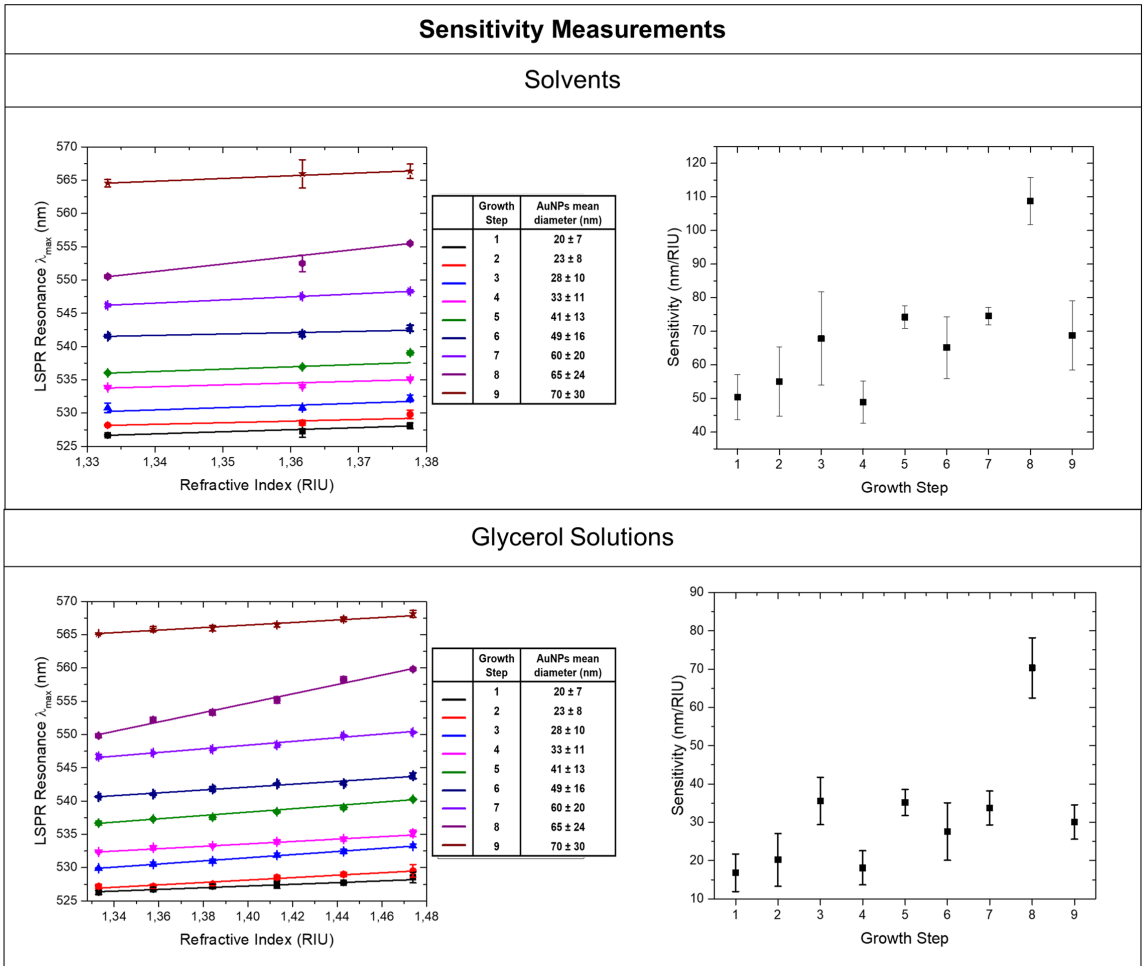

Figure 5.12: PEGDA/AuNPs nanocomposite sensitivity measurements. a) PEGDA/AuNPs composite mean LSP Resonance with respect to water ($n = 1.3303$), ethanol ($n = 1.3617$), and isopropanol ($n = 1.3776$). b) A linear fitting of the scatter plot is performed and the slope of the straight line (S) is reported as a function of the growth step. To be noticed the 8th growth step corresponding to a mean NPs diameter of $\sim$ 65 nm shows a sensitivity $S \sim 110 nm/RIU$). c)PEGDA/AuNPs composite mean LSP Resonance with respect to glycerol/water solutions of 0% w/w ($n = 1.33303$), 20% w/w ($n = 1.35749$), 40% w/w ($n = 1.38413$), 60% w/w ($n = 1.41299$), 80% w/w ($n = 1.44290$), 100% w/w ($n = 1.47399$). d) A linear fitting of the scatter plot is performed and the slope of the straight line (S) is reported as a function of the growth step. All the sensitivity values are lower compared to the previous refractive index interval, but follow nearly the same trend confirming the patch with AuNPs having a mean diameter of $\sim$ 65 nm as the most sensitive and suitable for refractive index sensing.

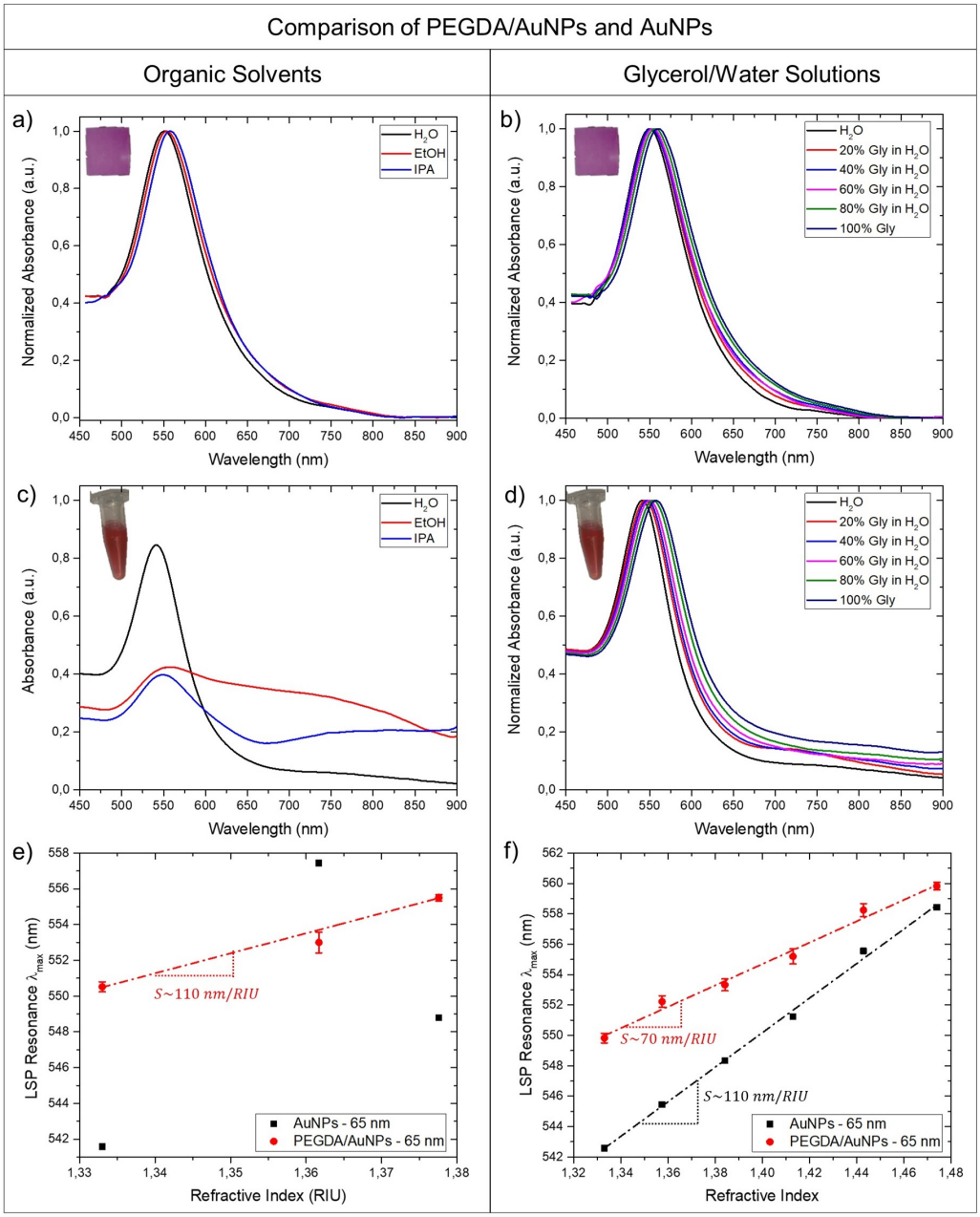

Figure 5.13: a-c) PEGDA/AuNPs nanocomposites and AuNPs mean LSPR in H_2O ($n = 1.3303$), EtOH ($n = 1.3617$) and IPA ($n = 1.3776$). b-d) PEGDA/AuNPs nanocomposites and AuNPs mean LSPR in glycerol/water solutions. e) Sensitivities comparison of PEGDA/AuNPs and AuNPs in solvents. f) Sensitivities comparison of PEGDA/AuNPs and AuNPs in glycerol/water solutions.

at RT for 2h. The tested concentrations varied from 25 μM to 10 mM, followed by three washing steps in MilliQ water. The same optical analysis was performed on the patches to monitor the $\Delta\lambda_{max}$ as a function of the biotin concentration. A dose-response curve was used to fit the λ_{max} variations in biotin concentration. The functionalization strategy approach and the results are reported in Figure5.14 and discussed in the next section.

5.5.2 Results and Discussion

In this section, the optical response of citrate-capped AuNPs in terms of stability, sensitivity, and bio-functionalization into a low-MW PEGDA hydrogel thin film is reported. By varying the AuNPs size distribution, the optimal combination of PEGDA and AuNPs size distributions was selected to achieve the highest sensitivity (S) as a refractive index-based biosensor, with S being defined as:

$$S = \frac{d\lambda_{max}}{dn} \tag{5.4}$$

where n is the medium effective refractive index. PEGDA with $MW = 700$ Da provided AuNPs with enhanced stability. The PEGDA/AuNPs volume ratio (2:1 V/V) and the thickness were accurately defined to obtain a good compromise between having a sufficiently large number of AuNPs and adequate transparency to allow the optical characterization in transmission mode.

The nine thin films, shown in Figure5.11 (a), exhibited the typical coloration of AuNPs with increasing size; they were optically characterized at normal incidence. Their normalized absorption spectra are shown in Figure 5.11 (b).

In agreement with the LSPR λ_{max} of the AuNPs in solution, reported in Figure 5.6 (b), a resonance red-shift, due to the growing AuNPs, was measured also for PEGDA/AuNPs nanocomposites (Figure 5.11 (b)). This is the first evidence of the AuNPs stability within the hydrogel since no other peaks could be optically detected at higher frequencies. Moreover, the absorption spectra exhibited a further redshift, compared to the counterpart colloidal suspensions, due to the hydrogel environment.

By increasing the NPs size, a continuous broadening of the absorption spectra of the nanocomposites was observed. This is due to two mechanisms:

- the wider size distribution of the colloidal AuNPs, shown in Figure 5.6, which implies that the scattering response is a superposition of many contributions arising from nanoparticles of different radius, exhibiting a different resonance frequency,

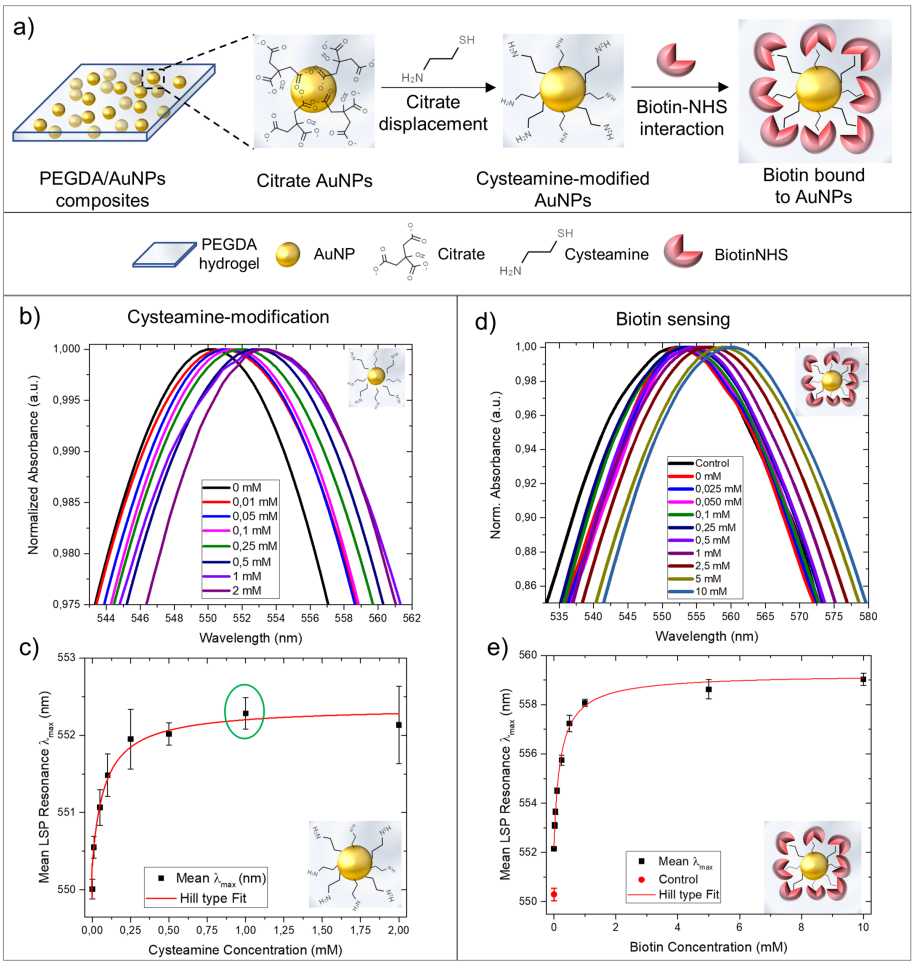

Figure 5.14: (a) Citrate displacement by cysteamine modification of AuNPs and Biotin grafting. (b) Absorption spectra of PEGDA/AuNPs nanocomposites as a function of cysteamine concentrations in the range between 10 μM and 2 mM; milliQ water was used as control. (c) LSP resonance λ_{max} as a function of the cysteamine concentrations from 0.01 to 2 mM; the red line represents the Hyll Type curve used to fit the data. (d) Absorption spectra of PEGDA/AuNPs nanocomposites with cysteamine-capped AuNPs as a function of the Biotin concentrations in the range between 25 μM to 10 mM; a patch without cysteamine, soaked into a 10 mM biotin-NHS concentration was used as control (black curve). e) LSP resonance λ_{max} (black squares) as a function of the biotin concentration (from 25 μM to 10 mM); the red line represents the Hyll Type curve used to fit the data, while the red circle is the LSP resonance λ_{max} of the negative control. The black square referring to a 0 mM biotin concentration has to be considered the one with 1 mM cysteamine with no biotin.

- the increase of the FWHM of the absorption power spectra of each individual NP as its size increases, due to the coupling with the radiation [43, 205].

This could be detrimental for applications requiring very narrow absorbance bands, however, in our case, we were principally interested in the peak shift as a function of the medium refractive index (n).

The broadening and redshift of the plasmon resonances observed in the experiments were consistent with the numerical simulations reported in Figure5.11 (c). For accurate prediction, a Gaussian distribution of non-interacting AuNPs diameters was assumed, which were immersed in a homogeneous medium, whose refractive index was chosen as the average between the ones of the PEGDA hydrogel and water. The hypothesis of non-interacting nanoparticles was confirmed both by SEM images and by absorbance spectra measurements. Further, the sensing capabilities as a function of the refractive index variations were analyzed by monitoring the shifts of the LSPR λ_{max} with respect to the refractive index n of the surrounding medium, as reported in Equation 5.4.

The sensitivity analysis is reported in Figure 5.12. The analysis was performed for all obtained nanocomposites, by dipping them in solvents with different refractive indexes, *e.g.* water, ethanol, and isopropanol, and also in glycerol mixtures at several concentrations, as described in the experimental part.

In Figure 5.12 (b), it is apparent that there was not a clear trend of the sensitivity with respect to the AuNPs size. In fact, after a sudden increase for the first three growth steps, there was a decrease in sensitivity for the 4^{th} step (mean diameter of 33 nm). After this, from the 5^{th} to the 9^{th} growth step, there was an approximately constant sensitivity of $\sim$ 70 nm/RIU, except for the 8^{th} growth step, which exhibited the highest sensitivity of $\sim$ 110 nm/RIU.

The sensitivity trend shown in Figure 5.12 (b) was different from the corresponding trends of the 2D AuNPs platform reported in the literature [206, 207, 208], showing an increase of the sensitivity up to a certain threshold, followed by a sudden decrease. To exclude that the trend in Figure 5.12 (b) was not due to a different swelling behavior with different solvents, the same analysis was repeated with glycerol/water solutions, as reported in Figure 5.12 (c). In this case, a larger refractive index interval was investigated, spanning from 1.33 to 1.47, nevertheless, the same trend was observed (Figure 5.12 d). This different behavior arises from the 3D hydrogel architecture, which exhibits a complex dependence on the swelling capability, crosslinking density, refractive index, and on AuNPs concentration and size. Therefore, it can be concluded that the nanocomposite embedding $\sim$ 65 nm AuNPs is the most promising substrate for refractive index sensing, and for this reason, only

this patch was considered for the subsequent analysis, functionalization, and sensing experiments.

First, a direct comparison of the performance parameters of AuNPs in solution and PEGDA/AuNPs thin films, in terms of Sensitivity (S), Full Width at Half Maximum (FWHM), and Figure of Merit (FOM), was performed, where the FOM can be defined as:

$$FOM = \frac{S}{FWHM}. \tag{5.5}$$

The results of this comparison are summarized in Table 5.3, while the absorption spectra are reported in Figure 5.13.

A direct comparison in the refractive index range from 1.33 to 1.37 was not possible, since, as expected, a colloidal suspension of citrate-capped AuNPs spontaneously aggregated in both Ethanol and Isopropanol. This confirmed that AuNPs in hydrogels are much more stable. The nanocomposites exhibited a sensitivity $S \sim 110$ nm/RIU in this RI interval and a FOM ~ 1.4, which is very competitive with many reported flexible LSPR-based platforms.

On the contrary, by using glycerol/water mixtures, a direct comparison was achieved. The analysis revealed better performances of AuNPs with respect to PEGDA/AuNPs in the RI range from 1.33 to 1.47. In particular, a FOM of ~ 1.2 was measured for AuNPs and ~ 0.9 for PEGDA/AuNPs. This result can be explained by simply considering the effective medium refractive index, which undergoes a jump from NPs in solution and PEGDA/AuNPs. The medium RI is not anymore due to 100% water content ($RI = 1.33$), but is higher, on average, due to PEGDA refractive index (see Figure 5.5 (b)). Despite this 25% decrease in the FOM of the platform, it still resulted to be very competitive also in this very broad RI range.

Ensuring NPs stability can enable many functionalization schemes that would have been unfeasible in colloidal suspensions. To demonstrate the possibility of functionalizing the AuNPs also when they are already embedded within the hydrogel network, a surface modification *via* citrate displacement in favor of cysteamine was performed. Thereafter, biotin, as a small molecule model, was easily anchored to the amino groups of cysteamine and successfully recognized.

The performed functionalization and biotin recognition are briefly schematized in Figure 5.14 (a). Measurements of the absorption spectra as a function of the different cysteamine concentrations (from 10 μM to 2 mM) were performed to evaluate the efficiency of the surface modification. The results are shown in Figures 5.14 (b-c). The absorption spectra revealed the saturation achievement at a 1 mM cysteamine concentration with a $2nm$ redshift (in agreement with Figure 5.10).

Finally, the nanocomposites modified with 1 mM cysteamine were soaked in

DMSO/PBS solutions of biotin and the optical signals were recorded. The results, reported in Figures 5.14 (d-e), show that saturation is achieved starting from a 1 mM biotin concentration, where an LSPR shift of $\sim$ 5 nm is measured. It is important to notice that small molecules, such as biotin, of size much smaller than the AuNPs, do not lead to large resonance shifts, because they weakly couple with the LSPRs of AuNPs. The LOD of the proposed platform was evaluated by the consolidated linear regression intercepting the control data plus three times the SD.

The possibility to effectively detect the biotin interaction with low MW PEGDA hydrogel/AuNPs nanocomposites offers promising opportunities for novel biosensing platforms based on refractometric sensing. The achieved results, with a $LOD = 25\mu$M, are definitely competitive with other well-performing 2D randomly assembled plasmonic platforms on rigid substrates [26, 209], as well as flexible substrates[210, 211]. This hybrid device could be further improved by exploiting tip-shape effects by embedding differently shaped NPs within the polymer (*e.g.* nanostars, nanotriangles, ...) to achieve better optical response and performance.

5.6 High MW PEGDA nanocomposites as swelling-dependent biosensors

In this section, hybrid plasmonic transducers made of high MW PEGDA (PEGDA 10000) hydrogel thin films and 60 nm citrate-capped AuNPs are described. They were exploited for the chemical sensing of a high MW protein, namely streptavidin (SA), as a model molecule. SA was specifically recognized by a biotin-based biorecognition layer, immobilized on the AuNPs within the hydrogel. LSPR absorption signals were exploited to quantify the biorecognition process in the 3D architecture.

The proposed platform is label-free and can represent a low-cost, flexible, and easy-to-use platform for sensing applications in biomedical or environmental diagnostics [66]. In the previous section, the description of a low MW PEGDA (700) hydrogel embedding AuNPs, for refractometric biosensing, was proposed, resulting in a flexible transparent film that could be chemically functionalized to selectively interact with biotin, achieving a sensitivity up to 110 nm/RIU and a LOD of 25 μM [60]. However, low MW PEGDA exhibits a poor swelling capability, as shown in Figure 5.4 (a), thus limiting their application to small molecules. *Vice versa*, high-MW PEGDA can be exploited, as a matrix, to obtain a hydrogel-based, high-sensitivity, hybrid transducer to be used as a label-free optical biosensor, even in case of high MW target analytes, such as the streptavidin (SA) protein.

SA is a protein secreted by Streptomyces avidinii. It can specifically bind up to four biotin molecules with very high affinity. Biotin/streptavidin interactions are recognized as the strongest non-covalent interactions available in nature and have been extensively employed in the detection of target analytes in biomedical applications [212, 213, 214]. For this reason, this type of interaction is generally used as a proof-of-concept for the validation of a novel platform in the biosensing field [215, 216].

The large swelling capability of a high-MW PEGDA is exploited to monitor the absorption variations of the AuNPs within the hydrogel as a function of the SA concentration ([SA]) in label-free mode. Indeed, the swelling ratio of the hydrogel is demonstrated to increase as a function of the [SA], with a consequent decrease in the absorption of the AuNPs within the transducer, achieving a LOD of 1.6 nM. These promising results are achieved by exploiting the high reproducibility, flexibility, and stability of the nanocomposite and to the possibility of functionalizing the AuNPs directly within the hydrogel matrix, which prevents their spontaneous aggregation or degradation [60].

5.6.1 Experimental Part

Chemicals and Reagents - Trisodium citrate ($Na_3C_6H_5O_7$), tetrachloroauric acid ($HAuCl_4$), Poly(Ethylene Glycol) Diacrylate (PEGDA, average Mn 10000), 2-Hydroxy-2-methylpropiophenone (Darocur 1173), cysteamine, sulfo-N-hydroxysuccinimide biotin (biotin-NHS) water-soluble, Bovine Serum Albumin (BSA), Phosphate Buffered Saline (PBS), Tween20, Streptavidin (SA) from Streptomyces avidinii, and Streptavidin−Cy3^{TM} (Cy3-SA) from *Streptomyces avidinii*, Protein G from Streptococcus *sp.* were purchased from Merck KGaA (DE); Wheat Germ Agglutinin (WGA), Alexa Fluor^{TM} 555 Conjugate was purchased from Thermo Fisher Scientific.

High MW PEGDA/AuNPs nanocomposites fabrication- The freshly synthesized citrate-capped AuNPs (60 ± 20 nm) were centrifuged at 1920 g at 10° C for 10 min and concentrated 10×. Poly(ethylene glycol) diacrylate (average Mn 10000), with Darocur as photoinitiator (1% v/v), was prepared and gently mixed with the concentrated AuNPs in a volume ratio of 2:1, respectively, using a magnetic stirrer at 300 rpm. The polymerization was performed as schematized in Figure 5.7.

Absorption spectroscopy - The thin hydrogel patches embedding AuNPs

were characterized by the customized transmission mode setup at normal incidence Figure 5.8. The samples were placed on a coverslip, whose background was removed in the reference measurements. The raw absorption spectra were smoothed to remove noise and the absorption increasing and decreasing were evaluated at the peak position ($\sim$ 540 nm). All the measurements were performed by removing the excess water with delicate text wipes to avoid light scattering during the measurements and minimize noise. The size of the collimated light spot conveyed on the samples and the distance between the two optical fibers were kept constant for all the measurements.

SEM imaging of AuNPs and H3 transducer - SEM images have been performed at 5 kV accelerating voltage and 20 μm wide aperture by a Field Emission Scanning Electron Microscope (Carl Zeiss NTS GmbH 1500 Raith FESEM). Secondary Emission and InLens detectors have been used.

Fluorescence Microscopy and Image Analysis - Fluorescence images were acquired by using a Leica AF6000LX-DM6M-Z microscope (Leica Microsystems, Mannheim, Germany), controlled by LAS-X (Leica Application Suite; rel. 3.0.13) software and equipped with a Leica Camera DFC7000T. Both BF and Fluorescence images were acquired by focusing on the hydrogel surface with a 10× objective. Fluorescence images were obtained by using a Quad-band LED filter cube and setting the excitation filter at 535(25) nm, the dichromatic mirror at 555 nm, and the suppression filter at 575(30) nm. Exposure time and contrast were set at 1.0 s and to 1.0, respectively. Before imaging, the excess water from H3 transducers exposed to or functionalized with Cy3-SA was removed. A minimum of three images was acquired on three independent samples. The obtained images were analyzed by the ImageJ freeware software by measuring the fluorescence intensity values from fixed regions of interest (ROI = 300 pixels × 300 pixels). Mean fluorescence intensity values ± SD were calculated and normalized according to the minimum and maximum fluorescence values of each measurement session.

High MW PEGDA/AuNPs Functionalization - Before use, the fabricated nanocomposites were pre-swollen in MilliQ water for 24 h to remove the excess Darocur and some eventual unreacted PEGDA. The hydrogel disks were placed in 24-well plates and each reaction was carried out separately. First, they were soaked into a water solution of cysteamine (1 mL) with concentrations varying from 50 μM to 2 mM (overnight, $4^{c}irc$ C). After one washing step in a Tween20

buffer (0.2 % v/v, 10 min, 25^{c}irc C), to remove the unreacted moieties, and three washing steps in MilliQ water, to restore the swelling equilibrium, the absorption spectra were measured and the variation in the absorption intensity as a function of the cysteamine concentration was analyzed. Secondly, the covalent interaction of cysteamine-capped AuNPs with biotin was performed by soaking the hydrogel in biotin water solutions (0.25 mL) with concentrations ranging from 0.1 mM to 4.0 mM (2 h, at RT). The same washing steps and optical analysis were performed on the patches to detect the absorption intensity variations to increasing biotin concentrations. A dose-response type equation was used to fit both the absorption intensity decrease as a function of the cysteamine concentration and the absorption intensity increase as a function of the biotin concentration. The variation of the absorption intensity was denoted as the absolute value of the difference of the current absorption intensity compared to the reference value ($|\Delta Abs.|$). Then, the nanocomposites were soaked in a BSA-PBS (1×, pH 7.4) solution (0.1 μM, 1 mL) to reduce non-specific interactions (2 h at RT). Finally, fixed volumes (0.25 mL) of PBS solutions of SA (from 0.375 nM to 750 nM) and with increasing concentrations were incubated in the biotinylated PEGDA/AuNPs nanocomposites (2 h at RT). The dose-response curves obtained, after the washing steps, were fitted by the four-parameter Hill equation (Equation 5.6). The negative controls were performed by incubating SA (750 nM), in absence of biotin (2 h at RT). The specificity tests were performed by incubating the biotin-modified transducers with PrG (750 nM) for label-free mode and AlexaFluor555-WGA (150 nM) for MEF mode (2 h at RT).

Numerical Simulations - The optimization of the optical response of the high MW/AuNPs nanocomposites was carried out as done in previous chapters. Also for high MW hydrogels, the hypothesis of *non-interacting* nanoparticles was assumed valid to predict the experimental absorption spectra. This approximation was made starting from the SEM images, which confirm that the interparticle distance is always less than or comparable with the size of the AuNPs. The effective medium refractive index was assumed as a weighted average of water and PEGDA 10000 optical constants (Figure 5.5).

Statistical Analysis - Mean absorption spectra were calculated as the average of 5 spectra collected on different substrate positions on 10 different samples treated in the same way ($n \geq 10$). The plots of the absorption spectra were obtained by smoothing and, when specified, normalization by using OriginPro. The absorption variations $|\Delta$Abs.$|$ as a function of cysteamine, biotin, and SA concentrations are

reported by considering the peak position of the absorption spectra. The mean ± SD is representative of at least three independent experiments ($n \geq 3$). For fluorescence analysis, a minimum of 3 images on 3 independent samples was acquired in the same conditions ($n \geq 3$). Fluorescence intensity was evaluated by using ImageJ software. Mean fluorescence intensities were analyzed and normalized by using OriginPro. The obtained data are reported as mean ± SD. The difference in data between groups for specificity tests was analyzed by ANOVA by using OriginPro. $p < 0.001$ were considered statistically significant. Unless otherwise stated, the other data were expressed as mean ± SD. SD is reported as vertical bars and is representative of at least three independent experiments ($n \geq 3$).

5.6.2 Results and Discussion

The high MW PEGDA/AuNPs transducer was fabricated by following the same approach reported in Figure 5.7. The obtained hydrogel thin films ($24 \times 24 \times 0.47$ mm^3) were cut by a puncher into disks (7 mm in diameter), which were easier to handle and could be functionalized in multiwells with controlled volumes. One run of this process generated nine transducers.

Since PEGDA 10000 is a transparent polymer, as shown in Figure 5.5, also the resulting nanocomposites were transparent. Therefore, straightforward optical characterization in transmission mode with the same optical setup in Figure 5.8 was feasible.

High MW PEGDA transducers revealed a well-detectable swelling (shrinkage) behavior once the AuNPs, within the network, were functionalized with hydrophilic (hydrophobic) molecules. The two phenomena had opposite effects on the optical properties of the patch, in particular on its absorption (Figure5.15).

The LSPR peak at 540 nm, due to the $\sim$ 60 nm AuNPs inside the polymeric film, decreased its intensity on swelling. In fact, the number of AuNPs intercepted by the probe light beam, which was kept constant for all the measurements, was diluted in a greater 3D volume. On the contrary, the absorption peak value increased on shrinkage due to the AuNPs density increase in a smaller volume. The swelling *ratio* of the high-MW PEGDA was affected by the hydrophilicity/hydrophobicity of the molecules immobilized on the surface of the AuNPs within the hydrogel, which overall made the effective transducer surface more hydrophilic/hydrophobic, accordingly [217, 218]. At the equilibrium, after soaking the nanocomposites in water for the washing steps, a decrease in the absorption intensity was observed, together with an increase in the size and swelling ratio of the hydrogel disk in presence of hydrophilic molecules

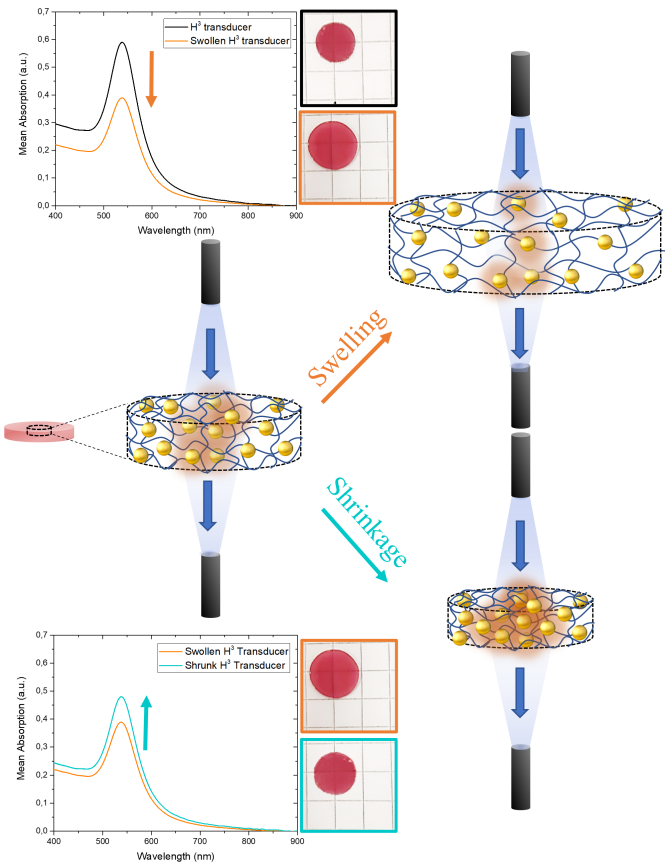

Figure 5.15: Absorption intensity variations due to shrinkage/swelling capability of the hydrogel when the embedded AuNPs are functionalized with hydrophobic/hydrophilic molecules. The functionalization of the high MW PEGDA/AuNPs nanocomposites with hydrophobic molecules leads to an increase in the absorption spectrum intensity due to the hydrogel shrinkage (blue line) compared to the bare transducer (black line). On the contrary, the modification of the nanocomposites with hydrophilic molecules results in a decrease in the absorption spectrum intensity due to the hydrogel swelling (orange line).

(cysteamine and SA). On the contrary, an increase in the absorption intensity, and a decrease in the size and swelling ratio, in presence of hydrophobic molecules (biotin) were observed, as reported in Figure 5.16.

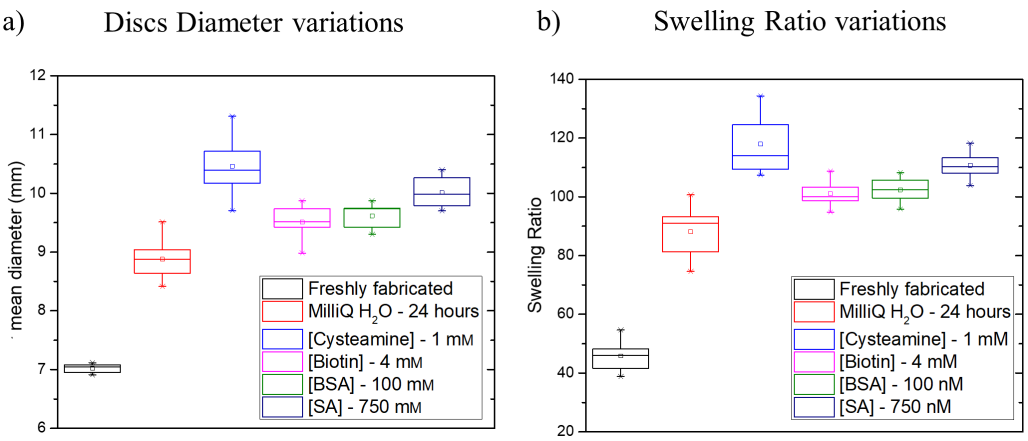

Figure 5.16: a) Discs diameter variations and b) swelling ratio variations as a function of the functionalization step. The measurements are obtained from a minimum of three independent samples ($n \geq 3$).

Both the effects were dose-response, *i.e.*, and they depended on the concentration of the hydrophilic/hydrophobic molecules used in the functionalization steps and the label-free detection of SA. On the one hand, the AuNPs acted as transducing elements and enabled the very well-known functionalization schemes reported in the literature for liquid plasmonic assays, on the other, high MW PEGDA acted as a stabilizer for the AuNPs and as a responsive matrix, allowing the diffusion of the analytes of interest. Moreover, the high flexibility and stretchability of the PEGDA could be exploited for their application to non-planar substrates (Figure 5.17).

SEM imaging of the AuNPs was performed before (on a flat Si wafer) and after embedding them within the polymeric network (Figures 5.18(a-b), respectively). No aggregation nor degradation of AuNPs was observed. They preserved their size distribution after their embedding in the hydrogel. The images show that the AuNPs ($\sim$ 60 nm in size) preserved their spherical shape and homogeneity even after the embedding within the hydrogel.

The optical characterizations revealed an LSPR peak positioned around 540 nm (Figure 5.18 (c)). The spectroscopic measurements were performed on a minimum of 3 hydrogel disks ($n \geq 3$) after their stabilization in MilliQ water for 24 hours. The resulting optical signal always confirmed the high reproducibility of the platform. The theoretical fit in Figure 5.18 (c) was performed by applying the MG-modified Mie Theory, as done in Chapter 3. The assumption of non-interacting nanoparticles

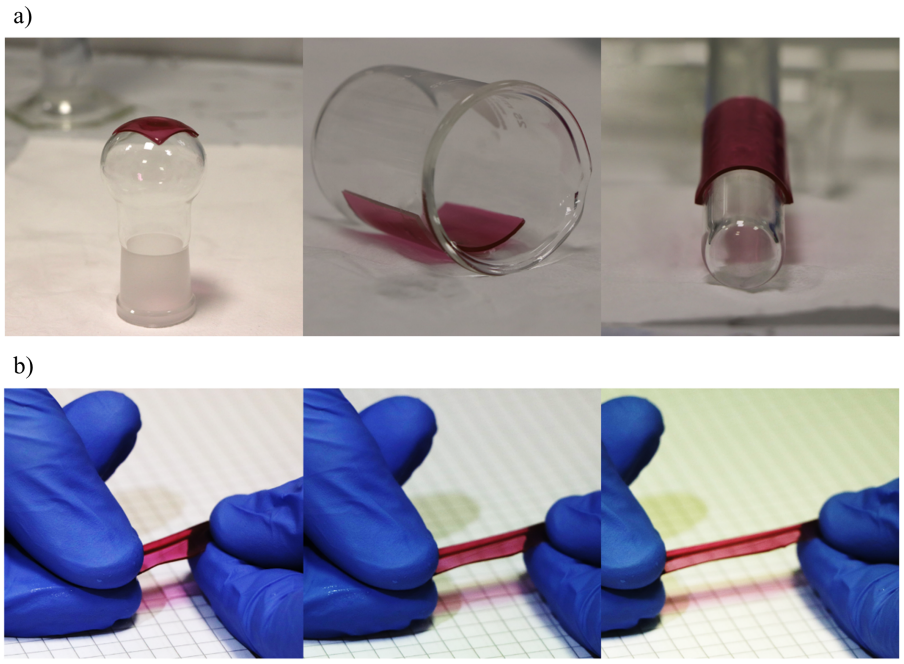

Figure 5.17: (a) Digital photographs showing the adaptability (flexibility) of the high MW PEGDA/AuNPs nanocomposites to non-planar (concave and convex) substrates. b) Digital photographs obtained by applying tensile stress to the nanocomposites, which show the strong deformation that it can undergo before rupture.

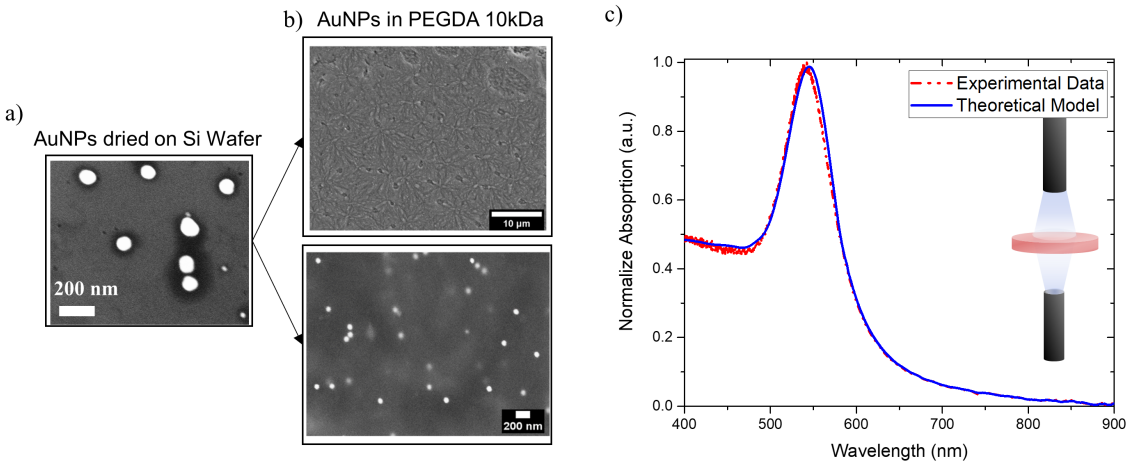

Figure 5.18: SEM images of freshly synthesized AuNPs before (a) and after (b) embedding in PEGDA 10000 hydrogel. No aggregation nor degradation of AuNPs was observed. (c) Experimental and theoretical absorption spectra of high MW PEGDA/AuNPs nanocomposites.

held also in this case, as confirmed by the SEM images. An excellent between the experimental results and the numerical simulation was obtained.

Therefore, the first step for the chemical functionalization of the high MW was thus the substitution of the citrate molecules with a proper linker, the cysteamine, able to bind the bioprobe molecule, in this case, the biotin.

Schematized in Figure 5.19 (a), the process was developed acting directly on the AuNPs when embedded into the polymeric layer. Being hydrophilic, cysteamine caused, at the equilibrium, an enhanced swelling ratio of the high MW PEFDA, with a consequent decrease in the absorption intensity Figure 5.19 (b). By quantifying the relative absorption intensity variations $|\Delta\text{Abs.}|$, as a function of the cysteamine concentration, the proper amount of the linker to be used was again found to be equal to 1 mM.

After citrate displacement and cysteamine anchoring, the biotin was covalently bound to the AuNPs within the hydrogel. The hydrophobic nature of the biotin on the AuNPs surface caused a volumetric shrinkage depending on the biotin concentration (Figure 5.19 (c)). The shrinkage was caused by the tendency of the hydrophobic molecule within the hydrogel to repel the aqueous component. Consequently, an increase in the absorption intensity was measured, compared to the absorption of the patch functionalized by cysteamine (1 mM). A dose-response curve was used to fit the data as a function of the biotin concentration and a saturation value was achieved at a biotin concentration of 4 mM (inset in Figure Figure 5.19 (c)). The correct functionalization of the nanocomposites was also confirmed by fluorescence microscopy (Figure 5.19 (d)), using a fixed concentration of Cy3-labeled SA. The dose-response curve reported in the right panel of Figure Figure 5.19 (e) shows the same saturation behavior as in Figure 5.19 (c).

This result validated the absorption measurements and confirmed the chosen biotin concentration (4 mM) as the most suitable to achieve the optimal immobilization of the biorecognition layer. The curve in Figure 5.19 (e) was obtained by measuring the fluorescence of a minimum of three independent hydrogel disks ($n \geq 3$) at different biotin concentrations (from 0 mM to 4 mM) after interaction with the same concentration of Cy3-labeled SA (150 pM). From the same figure, a first control on the specificity of the platform can be also argued. Indeed, no significant fluorescence was observed in absence of biotin, meaning that the non-specific interaction of the Cy3-SA with the platform was prevented. However, to further reduce non-specific interactions, a blocking step was added between biotin and SA incubations, as reported in the following sections.

Once the best biotin concentration for the AuNPs functionalization was fixed, the

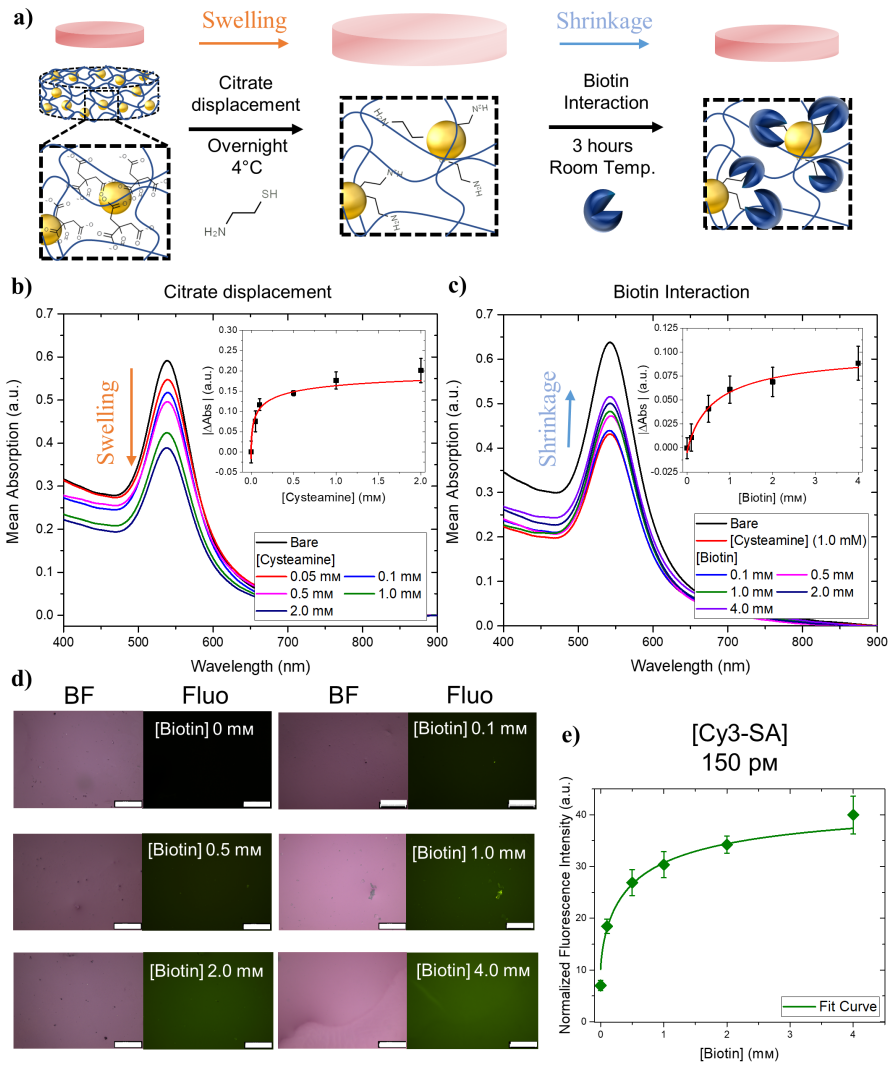

Figure 5.19: (a) *In-situ* functionalization of high MW PEGDA/AuNPs nanocomposites: citrate-displacement by cysteamine, enabling an enhanced SR; biotin interaction, responsible for the reduction of the SR. (b) Absorption spectra of the nanocomposites as a function of the cysteamine concentration. In the inset, the absolute value of the mean absorption variation ($|\Delta$Abs.$|$) at λ_{max} against cysteamine concentration (from 0.05 mM to 2.0 mM). (c) Absorption spectra of the nanocomposites as a function of the biotin concentration. In the inset, the $|\Delta$Abs.$|$ at λ_{max} against biotin concentration (from 0.1 mM to 4.0 mM). The optical measurements are obtained from a minimum of three independent samples ($n \geq 3$). SD is reported as vertical bars. (d) Validation of the functionalization by fluorescence imaging at a fixed concentration of Cy3-SA (150 pM). Scale bars are 250 μm. (e) Fluorescence intensity as a function of the biotin concentration on a minimum of three independent images ($n \geq 3$). SD is reported as vertical bars.

interaction with solutions having different content of SA was monitored by LSPR absorption variations by using non-labeled SA molecules. Figure 5.20 (a) shows a schematic representation of the functionalization approach: the nanocomposites containing biotin-modified AuNPs were incubated for two hours in a BSA solution to block the remaining active sites, which could have been not saturated on the AuNPs surfaces. Then they were soaked in solutions at different concentrations of SA to obtain a dose-response calibration curve of the transducer. In Figure 45.20 (b-d), the experimental results are shown. Since SA is a hydrophilic molecule, its biorecognition by the biotin molecules resulted again in an enhancement of the SR.

More water permeated inside the hydrogel, thus causing a volume increase of the nanocomposites and, as an optical consequence, the decrease of the absorption value measured at the LSPR wavelength (Figure 5.20 (b)) compared to the patch blocked by BSA. Again, this phenomenon was correlated to the SA concentration ([SA]) according to the dose-response curve shown in Figure 5.20 (c), from which the sensitivity and the LOD of the platform in the LSPR mode could be quantified.

More precisely, the experimental data were fitted by the common four-parameters Hill equation:

$$|\Delta\text{Abs.}([SA])| = |\Delta\text{Abs.}_1| + \frac{(|\Delta\text{Abs.}_2| - |\Delta\text{Abs.}_1|)}{(1 + \left(\frac{k}{[SA]}\right)^n} \tag{5.6}$$

where $|\Delta\text{Abs.}_1| = 0.002 \pm 0.001$ (a.u.), $|\Delta\text{Abs.}_2| = 0.08 \pm 0.01$ (a.u.), $k = 6 \pm 1$ nM, and the Hill coefficient $n = 0.9 \pm 0.2$. The dynamic range of the transducer extended from 1.5 nM to 750 nM, a LOD of 1.6 nM was estimated by considering the $|\Delta\text{Abs.}|$ threshold as three times the standard deviation (SD) of the control value, while the sensitivity of $(3.0 \pm 0.3) \times 10^{-}3$ nM^{-1} could be quantified by considering the linear region of the fitting curve.

Additionally, the negative control experiment and the specificity test are reported in Figure 5.20 (d). The functionalized high MW transducer generated a higher response than the patch without biotin on exposure to the highest SA concentration (750 nM). An almost four-time percentile variation in the absorption was achieved, thus confirming the *in-situ* functionalization. Also, the specificity test performed against a random target, Protein G (PrG, 750 nM), did not lead to significant absorption variation compared to the SA. The results obtained with the proposed transducer were very promising and competitive with other platforms, which have been recently reported [215, 216, 219].

The high MW PEGDA hydrogel combined with AuNPs enabled the design of

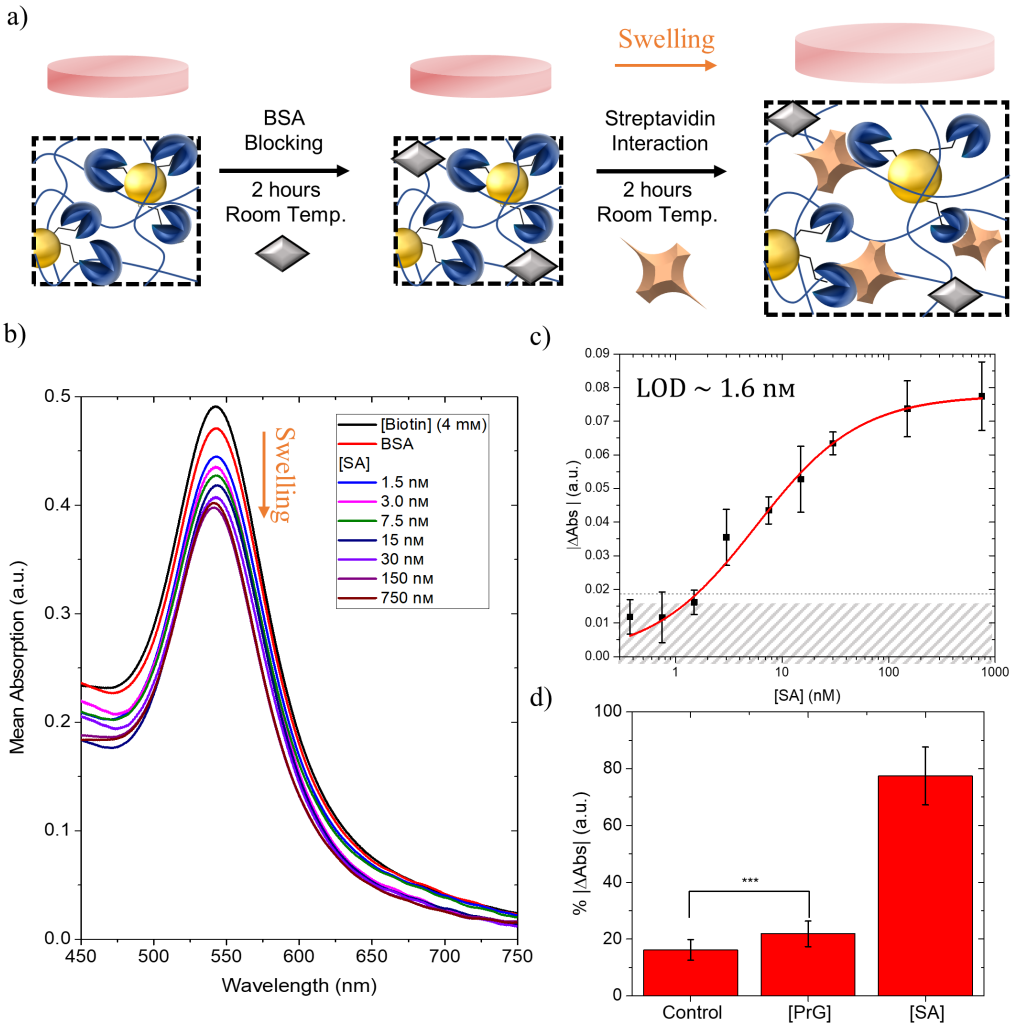

Figure 5.20: (a) Schematics of the biotin-SA interaction for LSPR sensing associated with the SR variation. BSA blocking does not cause significant swelling variations, while non-labeled SA interaction with biotin causes a further increase of the swelling in the nanocomposites. (b) Mean absorption spectra of the as a function of the SA concentration (from 0.375 nM to 750 nM). (c) Absolute value of the mean absorption variation (|ΔAbs.|) at λ_{max} is plotted against [SA]. A four-parameter Hill model is used to fit the data. The optical measurements are obtained from a minimum of three independent samples ($n \geq 3$). (d) Control and specificity test against a random target (PrG). The control is performed in absence of biotin ([SA] = $750nM$). The specificity test is performed by incubation with PrG ([PrG] = 750 nM). The percent absolute value of the mean absorption variation (|ΔAbs.|) at λ_{max} associated with the control and with PrG is monitored and compared with its corresponding value in presence of biotin ([SA] = 750 nM). The experiment is performed on a minimum of three different samples ($n \geq 3$) and the results are reported as mean ± SD (reported as vertical bars). $^{***}p < 0.001$ resulting from ANOVA test were considered statistically significant.

a simple and efficient platform with a good LOD in label-free mode and a broad dynamic range, which could be mainly ascribed to the 3D nature of our platform. 3D architectures possess, in fact, the advantage of increasing the contact area between the biorecognition element and the target analyte, and this interaction was easily readable by simple spectroscopic measurements due to the swelling capability of the hydrogel and its high transparency [66].

5.7 Metal-Enhanced Fluorescence in hydrogel nanocomposites

Plasmonic nanomaterials have found large interest also in the amplification of external signals, such as Fluorescence, Raman signals, and Infrared Absorption [14].

The phenomena for which, plasmonic NPs act as nanoantennas for the amplification of external signals are known as Metal- (or Plasmon-) Enhanced Fluorescence (MEF) [26], Surface-Enhanced Raman Scattering (SERS) [220], and Surface-Enhanced InfraRed Absorption (SEIRA) [221].

When proposing novel biosensing platforms, based on optical nanoresonators, such as plasmonic NPs, a winning strategy to further reduce the achieved LODs and sensitivity is to exploit immunoassays for which an external molecule, such as a fluorescent dye, or a Raman reporter, is used to push the detection limits down to the single-molecules levels [17, 59].

In this section, for the first time, hydrogel nanocomposites based on PEGDA and citrate-capped AuNPs are exploited to design a MEF-based biosensor.

The detection of biomolecular interactions through fluorescence avoids the handling of radioactive tracers. In fact, for this technology, fluorescent dyes are employed. In nature, many fluorescent dyes have been recognized and utilized. The main characteristic that joins all the fluorescent dyes is the possession of a couple of aromatic rings structure [20].

When these fluorescent molecules are excited by light, they collect energy from the photons, passing from a ground state (basal state S_0) to unstable excited states (S_1 and S_2). Being in an unstable condition, the molecules will tend to lose the excess energy and return back to the ground state. There are several ways in which this process happens, according to the excited molecule configuration.

For the most part of the molecules, two phenomena happen at the same time: emission of photons at the identical wavelength as that of the initial light irradiation and release of the excess energy through molecular rotations and/or vibrations (inter-

nal energy U), or production of heat (Q). Due to the energy loss, the emitted light is attenuated, and so there will be different absorption values at different wavelengths, giving rise to a spectrum. This is due to the fact that the energy conversion, from the photons, is higher at certain wavelengths and lower at others. For the fluorescent dyes, the phenomenon is instead quite different: they absorb more photons at a specific wavelength, and the excited electrons return back to S_0 just emitting photons and without internal energy or heat exchange [222].

The energy loss of these molecules happens in two phases: the Stokes shift, in which the excited electrons shift to the less excited state, and a secondary shift at lower energy, in which a large amount of energy is lost until the ground state. From this, the emitted light carries less energy than the incident light. The energy of light, but in general of an electromagnetic wave, is related to the wavelength[20]:

$$E = \frac{\hbar c}{\lambda} \tag{5.7}$$

where E = energy, $\hbar$ = Planck's constant = $6.6 \cdot 10^{-34} Js$, c = speed of light = $3 \cdot 10^8$ m/s, λ = wavelength. Given this equation, the emitted light results in a longer wavelength than the incident (excited) light.

A schematic representation of the reported phenomenon has been given by Jablonski diagrams that explain, in a synthetic way, how the molecules do respond to excitation from light (Figure 5.21). The emission of the fluorescent dyes is generally associated with a *thermally equilibrated excited state* that corresponds to the vibrational state of S_1 at the lowest energy. The absorption phenomenon happens on a very fast scale (femtosecond regime), while the emission from an isolated fluorophore is described through two parameters: *Quantum yield* Q_0 and *lifetime* τ. These optical variables are defined in terms of the radiative decay (k_r) and nonradiative decay rate (k_{nr}). In particular,

$$Q_0 = \frac{k_r}{k_r + k_{nr}} \tag{5.8}$$

and

$$\tau = \frac{1}{k_r + k_{nr}} \tag{5.9}$$

are the expressions used for the computation of these two parameters [20].

In Equations 5.8 and 5.9, the radiative decay rate (k_r) is the one associated with the emission (from S_1 to S_0), while the non-radiative decay rate is associated to the internal conversions (from excited singlet states higher than S_1 to the first excited singlet state S_1).

The radiative decay (in a scale of nanoseconds) corresponds to a light emission

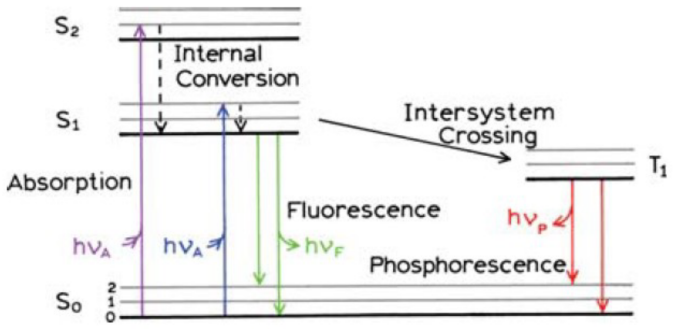

Figure 5.21: One form of a Jablonski diagram (Reprinted from Ref. [20]).

specular to the absorption just from S_0 to S_1 and not of the total absorption (see also Figure 5.21).

For dilute solutions, Beer's law has been proven to be valid and so the measured absorbance is:

$$A = \epsilon \ell c = \log P_0 - \log P \tag{5.10}$$

where ℓ is the optical path length of the sample, c is the analyte concentration, P_0 is the excitation power (photons/s), and ϵ is the analyte molar absorption coefficient $(M^{-1}cm^{-1})$[26].

The measured signal F (photons/s) is finally computed as:

$$F = QP_0(1 - 10^{\epsilon bc}) \approx QP_0\epsilon bc, \tag{5.11}$$

so fluorescence increases linearly with concentration and excitation power, before saturation.

These types of measurements depend on the used imaging techniques and microscopes, and, for this reason, F intensity is usually expressed as arbitrary units. Fluorescence detection is quite easy by using fluorescence microscopy. Nowadays, one of the most used approaches for fluorescence microscopes is *epi-illumination*[223]: the objective works both for imaging and as a condenser that illuminates the specimen.

The physics behind fluorescence enhancement induced by metallic nanomaterials is still an object of study [224]. It represents one of the most interesting topics in fluorescence-based bio-medical and biochemical applications, in which quantum yield, lifetime, and photostability are observable quantities.

Given the distance z between fluorophore and nanostructures, three are the most recognized mechanisms that actually contribute to the MEF phenomenon. First, if the fluorescent dye is in close proximity to the NPs surface ($1 \leq z \leq 10$ nm), the local field of one dipole can excite the second one. This phenomenon is recognized

as Förster resonance energy transfer (FRET) mechanism. FRET is favored when the LSPR of the nanostructure and the excitation of the fluorescent dye are matching [20, 225] (Figure 5.22 (a)).

Second, the LSPR can enhance the radiative rate of the fluorophore via the Purcell effect, which dominates at distances far from the FRET region ($z > 10$ nm), when the LSPR matches with the emission of the fluorescent dye (Figure 5.22 (b)).

Finally, a combination of both at distances $10 \leq z \leq 15$ nm, known as dual-mechanism can be observed [17] (Figure 5.22 (c)).

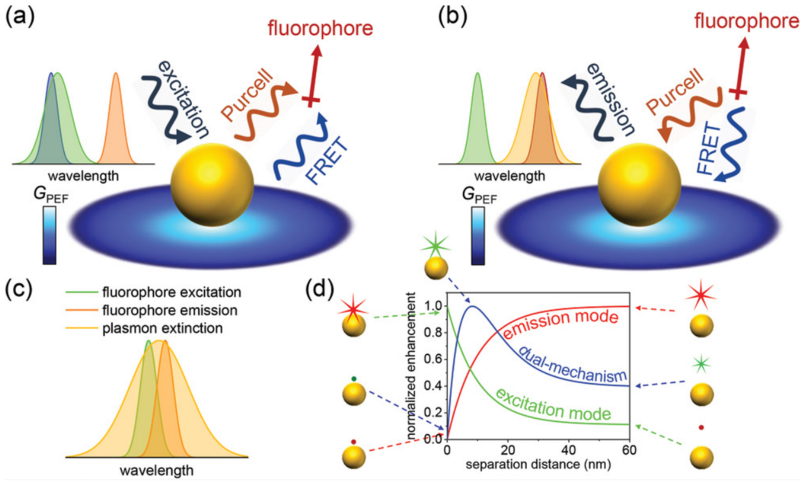

Figure 5.22: a) Excitation mode enhancement due to the spectral overlap between the plasmon extinction and the fluorophore absorption. b) Emission mode enhancement due to the spectral overlap between the plasmon extinction and the fluorophore emission. c) If the plasmon extinction encompasses both the absorption and emission peaks of the fluorophore, a dual-mechanism enhancement takes place. d) Excitation (solid green line), emission (solid red line), and dual-mechanism (solid blue line) enhancement as a function of the nanostructure-fluorophore separation distance. Reprinted with permission from Ref. [17]

The capability of a nanostructure to amplify the fluorescence signal can be measured through a parameter known as EF, defined as:

$$\mathrm{EF_{MEF}} = \left[\frac{E_p(\omega)}{E_0(\omega)}\right]^2 \frac{Q_p(\omega')}{Q_0(\omega')} \frac{\kappa_p(\omega')}{\kappa_0(\omega')}, \tag{5.12}$$

where, E, Q, and κ denote the electric field, quantum yield, and collection efficiency of the fluorescent dye. The suffix 'p' denotes the presence of the nanostructure, while the suffix '0' denotes the absence of the nanostructure (vacuum). Finally, ω and ω' are the excitation and emission frequencies, respectively.

To significantly enhance the sensing capabilities of PEGDA/AuNPs nanocomposites, the excitation of a fluorescent dye (Cy3) was coupled with its absorption. The detection of Cy3-labelled SA molecules (Cy3-SA) is, therefore, proposed. A fluorescence EF of ~ 10 and a LOD of ~ 0.1 pM were achieved. The 10-fold EF is obtained by working in excitation mode enhancement (FRET mechanism), where the non-interacting AuNPs enhance the fluorescence signal of Cy3 in their close proximity ($1 \leq z \leq 10$ nm).

5.7.1 Results and Discussion

Having selected a Cy3-SA molecule for the MEF-based sensing mechanism, only the high MW hydrogels were explored. The fabrication and characterization of high MW PEGDA/AuNPs nanocomposites was performed as reported in section 5.6.

Figure 5.23 (b) shows the excitation/emission spectra of the selected Cy3 fluorophore. The spectral overlapping of the fluorescent dye excitation with the absorption of the fabricated transducer can be immediately visualized in Figure 5.23 (a).

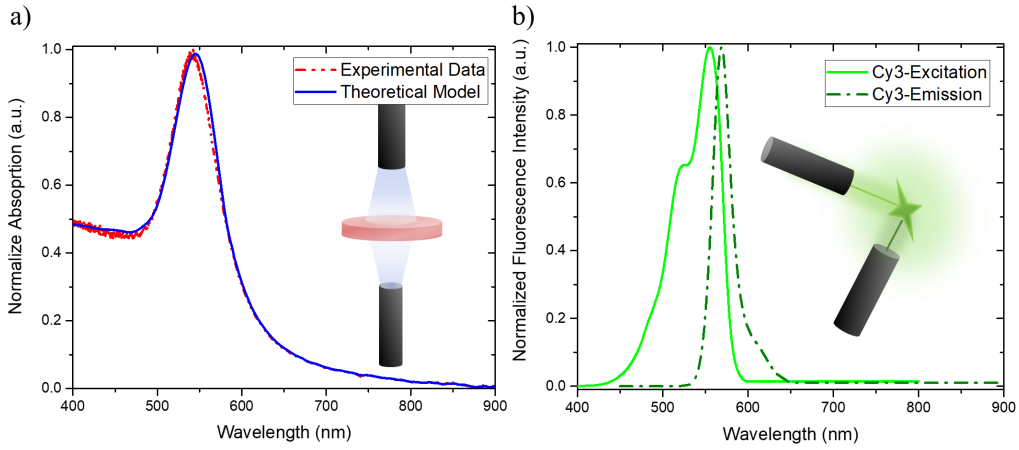

Figure 5.23: (a) Experimental and theoretical absorption spectra of H3 nanocomposites confirm the hypothesis of non-interacting NPs. (b) Fluorescence excitation and emission spectra of the Cy3-SA show a good overlap between Cy3 excitation (peaks at 530 and 550 nm) and H3 transducer absorption (peak at 540 nm).

In particular, the fluorescent dye excitation spectrum exhibited two peaks located at $\sim$ 530 and $\sim$ 550 nm, while the nanocomposites absorption peak was located around 540 nm, making Cy3 a suitable candidate for MEF in excitation enhancement mode.

Moreover, SA labeled by Cy3 was selected as the target molecule to prove the

sensing approach with MEF in excitation enhancement mode. Indeed, the hydrodynamic radius of SA has been reported to be ~ 5 nm [226], and, for this reason, even in presence of the biotin small molecule, as a biorecognition element, the value of z was reasonably expected to be well below 10 nm.

To experimentally evaluate the possibility of using the hydrogel nanocomposites as a MEF substrate, Cy3-SA (150 nM, 1 mL), was simply allowed to diffuse overnight into a high-MW PEGDA photopolymerized in absence of AuNPs (Figure 5.24 (a)) and into PEGDA/AuNPs nanocomposite transducer (Figure 5.24 (b)) having the same physical volume and processing conditions. For this comparison, no functionalization steps were performed since PEGDA without AuNPs did not possess any functional group to be used to link a biorecognition layer for SA.

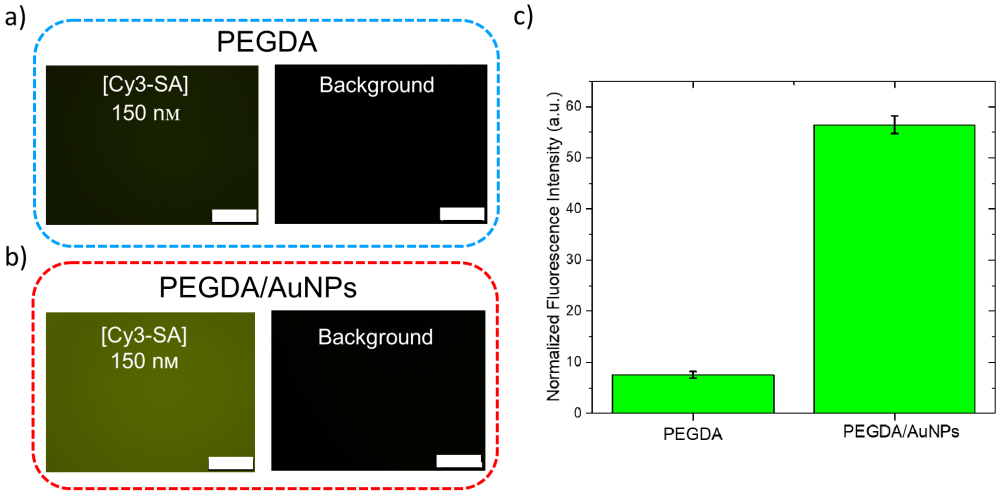

Figure 5.24: (a) Fluorescence images of PEGDA without AuNPs in presence of Cy3-SA (150 nM) and its corresponding background. (b) Fluorescence images of the PEGDA/AuNPs transducer in the presence of Cy3-SA (150 nM) and its corresponding background. (c) Fluorescence intensity counts of Cy3-SA diffused in pure PEGDA and in the transducer to evaluate the fluorescence EF are expressed as mean $\pm$ SD on a minimum of three independent experiments ($n \geq 3$). Scale bars are 250 μm.

Therefore, this preliminary study on the enhancement factor (EF) evaluation was performed with no chemical modification of the transducer. Fluorescence images were acquired on the two samples (PEGDA and PEGDA/AuNPs nanocomposite) and on their counterpart with non-labeled SA, in the same conditions, to collect information also on the auto-fluorescence of the material. Fluorescence EF was evaluated as the *ratio* of the fluorescence intensity measured in presence of the AuNPs and the one measured in absence of the AuNPs, both normalized to their corresponding backgrounds, as shown in Figure 5.24 (c). An EF of ~ 10 was obtained due to the in-

teraction between the fluorophore and the AuNPs surface, compared to the PEGDA hydrogel thin films without AuNPs. Moreover, the nanocomposites did not suffer from auto-fluorescence, when excited at 530 nm, thus confirming their applicability in fluorescence-based sensing strategies in this optical range.

The optical characterizations and the fluorescence EF determination reported in Figure 5.24 were exploited for the monitoring of the *in-situ* functionalization of the AuNPs and the selective detection of a labeled target analyte. Fluorescence spectroscopy is the generally adopted method to boost the sensitivity of many platforms when, for a certain target, the required clinically-relevant LODs are very low. Moreover, labeling target molecules has become a standardized and straightforward technique for many biomolecules, including DNAs, RNAs, proteins, and aptamers [227]. For this reason, based on the achieved EF, the investigation of the sensing performance of the platform in MEF mode was performed by directly screening a Cy3-labelled SA as the target element. The proper functionalization until biotin is reported in the previous section. The results of this detection mode are reported in Figure 5.25.

Figure 5.25 (a) is a schematic representation of the proposed approach starting from the biotinylated AuNPs within the hydrogel at the optimized biotin concentration reported in the previous section (4 mM). Even in this case, the nanocomposite was first passivized by BSA to minimize non-specific interactions and then used for the quantification of different Cy3-SA concentrations. A much lower LOD was achieved, due to the enhancement of the fluorophore-metallic NPs interaction.

The fluorescence images in Figure 5.25 (b), which were all acquired in the same experimental conditions were analyzed by ImageJ to derive the fluorescence intensity counts. The dose-response curve, in Figure 5.25 (c), was obtained by reporting the average intensity counts, of at least three different and independent images for each SA concentration ($n \geq 3$). The experimental data were fitted by the same standard four-parameter Hill curve used for the label-free case, according to the following equation:

$$F([Cy3-SA]) = F_1 + \frac{F_2 - F_1}{(1 + \left(\frac{k}{[Cy3-SA]}\right)^n} \tag{5.13}$$

where $F_1 = 0.4 \pm 0.2$ (a.u.), $F_2 = 56 \pm 3$ (a.u.), $k = (2.5 \pm 1.2) \times 10^2$ pM and the Hill coefficient $n = 0.37 \pm 0.04$ are the four fitting parameters. The dynamic range of the transducer extended from 0.01 pM to 150 nM, and a LOD of 0.1 pM was achieved by considering the fluorescence threshold as three times the SD of the control value (Figure 5.25(c)), while a sensitivity value of $(8.8 \pm 0.5) \times 10^{-1}$ pM^{-1} was estimated by considering the linear region of the Hill Curve.

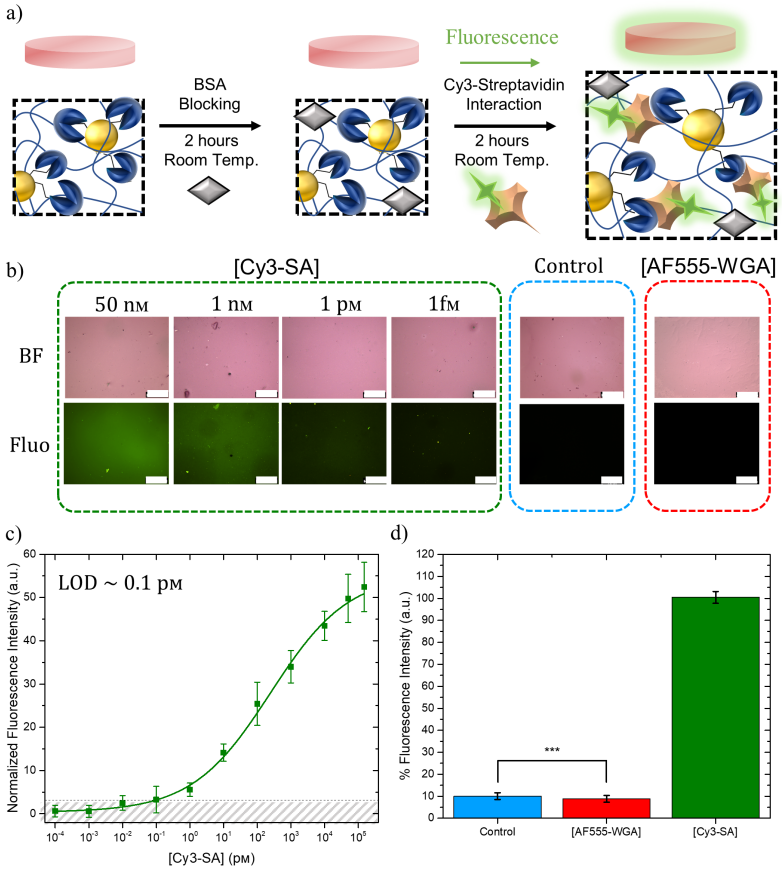

Figure 5.25: (a) Schematic representation of the biotin/Cy3-SA interaction for MEF sensing. (b) Representative bright-field and corresponding fluorescence images of the nanocomposites incubated with 50 nM, 1 nM, 1 pM, and 1 fM of Cy3-SA (dashed green). The control is performed by incubating Cy3-SA (150 nM) in absence of biotin (dashed blue). The specificity test is performed against a random target (WGA) labeled with a Cy3 equivalent fluorescent dye (AF555) at a concentration of 150 nM (dashed red). Scale bars are 250 μm. (c) The dose-response curve is obtained by measuring the mean $\pm$ SD of the fluorescence intensity on a minimum of three independent images on three independent samples ($n \geq 3$). A four-parameter Hill model is used to fit the data. A LOD of 0.1 pM is achieved. (d) The percent fluorescence intensity associated with the control (no biotin and [SA] = 150 nM) and with AF555-WGA (150 nM) is monitored and compared with its corresponding value in presence of biotin ([SA] = 750 nM). The experiment is performed on a minimum of three different samples ($n \geq 3$) and the results are reported as mean $\pm$ SD (reported as vertical bars). $^{***}p < 0.001$ resulting from the ANOVA test were considered as statistically significant.

Also in MEF-based sensing modality, the negative control experiment and the specificity test against a random target (Wheat Germ Agglutinin – WGA protein labeled with Alexa Fluor 555) (Figure 5.25 (d) confirmed the relevance of the *in situ* AuNPs functionalization. When properly biotin-modified, the AuNPs within the hydrogel generated a $\sim 10\times$ higher fluorescence response than the non-functionalized one and the one with a random target. The significantly lower LOD achieved in fluorescence mode was mainly due to the FRET mechanism described earlier, confirming the hypothesized threshold of the fluorophore-NPs distance z below 10 nm.

5.8 Conclusions

In this chapter, the design, fabrication, and characterization of hybrid transducers made of PEGDA hydrogels, and spherical citrate-capped AuNPs were proposed.

First, the physicochemical properties of PEGDA hydrogels as polymeric matrices to embed and stabilize plasmonic NPs were examined. PEGDA resulted in a chemically stable, inert polymer with excellent optical transparency and mechanical properties that could be tuned as a function of the MW.

Then, monodispersed citrate-capped AuNPs were chemically synthesized by following the seeded-growth method proposed by Bastus *et al.* [95]. The optimization of the fabrication technique took advantage of the high reproducibility, large scalability, and simplicity of an all-solution fabrication strategy, as pre-polymer solution photocuring under UV light.

Interestingly, it was found that the diverse nature of PEGDA hydrogels with different MW had an effect on the optical properties of the hybrid materials. More precisely, low MW hydrogel nanocomposites exhibited an optical dependency of the LSPR wavelength position (λ_{max}) on the effective refractive index of the AuNPs surrounding medium. On the contrary, high MW hydrogels exhibited an optical dependency of the LSPR absorption intensity (Abs.) on the large swelling behavior, which in turn was affected by the hydrophilic/hydrophobic nature of the molecules used for its functionalization. The proposed nanocomposites exhibited a fully predictable optical response based on the Mie Theory modified with the Maxwell-Garnett homogenization approach and ensured high stability of the AuNps as compared to their colloidal counterpart.

As proof of concept, low-MW hydrogel nanocomposites were used as refractometric biosensors for the detection of a small molecule as biotin, achieving a LOD of 25 μM, while high MW hydrogel nanocomposites were used for the label-free detection of a large molecule, namely the streptavidin, by exploiting its highly specific

interaction with biotin, achieving a LOD of 1.6 nM. The obtained results are very competitive with the flexible biosensors reported in the literature.

Finally, to further boost the sensing capabilities of the proposed platforms, for the first time, it was tested as an amplifier of the external fluorescence of the Cy3 fluorescent dye, by exploiting FRET-based MEF sensing. A 10-fold enhancement factor was achieved, pushing the LOD of a fluorescent streptavidin molecule down to the picomolar level, this representing an unprecedented result. The hybrid combination of these two simple materials was optimized and can now find applications in several fields of the biosensing community. Such a 3D flexible platform offers challenging opportunities in the design of real-time optical biosensors for cell cultures [228, 229], and in diagnostics, exploiting the capability of hydrogels of adapting to non-planar surfaces to design wearable sensors [179]. Moreover, they could find large applications in wound healing [230], drug-release [106], and food-quality monitoring [59].

Further improvements could be provided to the proposed system by exploiting, tip-shape plasmonic effects (for example by using nanostars, nanobipyramids, ...), which would confer to the nanocomposites higher sensitivity to refractive index variations and multiple resonances to be simultaneously monitored, spectroscopically, for multiplexed detection (sensing of multiple targets). Moreover, it could be possible to integrate the sensing element with polymer-based light-emitting diodes (LEDs) and photodetectors to obtain a fully-integrated portable system, as point-of-care testing (POCT) devices. By basing on the achieved results, new outcomes in biosensing research are, therefore, envisaged.

Conclusions and Future Perspectives

In this thesis, the design, fabrication, and characterization of multifunctional hybrid nanoresonators have been proposed.

The theoretical background describing the electromagnetic scattering of optically small objects has been briefly introduced. It is based on the electroquasistatic and magnetoquasistatic approximations of the Maxwell equations and allows the prediction of the resonance positions and quality factors of both plasmonic and dielectric nanoresonators. This theory has been applied to plasmonic spherical nanoparticles and networks of high-permittivity thin wires. These analytical tools are very powerful since they require very low computational costs and provide a clear idea of the scattering behavior of homogeneous nanoresonators. Second, the main fabrication techniques for the production of nanoresonators have been described, with a main focus on the bottom-up techniques, which better meet the demand for large-scale, low-cost, and highly reproducible optical devices for biosensing applications.

However, when coming to experimental practice, rarely bottom-up synthesized (mainly plasmonic) nanoresonators result in their homogeneous composition. Indeed, the reduction and stabilization procedures of the colloids require the addition of *impurities* within or around the nanoparticles, namely hybrid nanoparticles. To accurately predict the material composition of hybrid nanoparticles, a genetic optimization method based on the combination of the classical Mie and Mie-Kerker theory with Maxwell-Garnett homogenization was introduced. This proposed novel approach can be exploited for the analysis and design of multifunctional hybrid nanosystems.

In particular, for the first time, the engineering of the optical properties of a hybrid drug delivery system has been proposed. It is made of porous biosilica nanoparticles, gelatin-stabilized gold nanoparticles, and gelatin polymeric shells In this nanosystem, porous biosilica acted as a nanocarrier for a model drug, gold nanoparticles as the transducing element, and gelatin shell as a pH-responsive polymer capable of retaining the drug for long times at neutral conditions and releasing it in acidic environments

(*e.g.*, a tumor site). A correlation between polymer concentration and polymer shell thickness has been achieved starting from theoretical predictions. This enables the monitoring of gelatin shell formation, degradation, and indirectly, drug release by simple spectroscopic techniques.

With a similar approach, hybrid nanocomposite transducers have been optimized for biomolecular interaction monitoring. They are made of plasmonic nanoparticles and polyethylene glycol diacrylate hydrogels with increasing molecular weights. The mechanical properties of the hydrogel matrix allow the use of this device in both refractive-index-based and swelling-dependent optical biosensors, depending on the hydrogel molecular weight. The sensing of both small and large molecules with high accuracy and relatively low LODs has been demonstrated. Moreover, the simple, low-cost, large-scale fabrication of these nanocomposites enables their application to a wide range of biomedical applications, since their chemical and optical properties can be tailored to specific applications.

By basing on the results of this thesis, it is possible to appreciate the impact that bottom-up synthesized hybrid nanoresonators can have in biomedicine when properly engineered. It is possible to achieve extremely competitive large-scale, low-cost nanosystems with no need for expensive and time-consuming equipment upon an accurate prediction of their optical features.

It is envisaged that hybrid nanocarriers embedding plasmonic nanoresonators could find large applications for drug formulation, drug discovery, and patient treatment. For example, differently shaped plasmonic nanoparticles could be introduced as nanoresonators in the near-infrared region, known as the *invisibility region* of the tissues. They could enable simple spectroscopic monitoring of the release of a drug directly *in-vivo*, at the accumulation site.

Concerning hybrid hydrogel nanocomposites, they could find large applications in the fields of wearable sensing, food quality assessment, and environmental monitoring, owing to the flexible nature of the polymeric matrix. Moreover, such a 3D platform could offer opportunities in the design of real-time optical biosensors for cell cultures, exploiting the high percentage water content of hydrogel, which makes them the ideal candidates for the design of scaffolds. Finally, they could be easily integrated within microsystems, such as microneedles for the monitoring of the dermal interstitial fluid; microfluidic devices, for optofluidic platforms; and with microelectronics components, such as integrated LEDs and photodiodes, for the fabrication of fully portable devices.

The current limitations of the proposed model are associated with the dielectric counterpart. At the moment, the bottom-up synthesis of all-dielectric nanoparticles, exhibiting lower losses and extremely narrow Mie resonances, is still an active and

not standardized research field. However, with the recent nanotechnology and inorganic chemistry advances, it is envisaged that some controlled synthetic routes to produce high-index nanoparticles with controlled sizes will be reached, and, at that stage, the description of their hybrid optical properties will benefit from the proposed approaches and will enable their large-scale application in biomedicine.

Appendix A

Partial Inductances Calculation

For the prediction of the electromagnetic scattering from high-permittivity dielectric networks, instead of solving Maxwell equations, it is possible to import concepts and formulas that have been produced by scientists and engineers working on electric inductive network [132], in particular the analytic formulas produced in the first twenty years of the XX century and summarized in the manuscripts of Rosa [231], Grover [135], and Weber [232]. These concepts can be applied to the polarization current densities, rather than to the electric currents, consistently with the framework proposed by Engheta and co-workers in Refs. [233, 234, 235, 236]. In particular, one of the main strengths of the proposed model lies in its simplicity: when the network consists of only a few loops, the calculation of the magneto-quasistatic current modes and the associated resonances can be carried out with just paper and pencil, together with their radiative frequency shifts and quality factors. It also enucleates the connection between the current modes, resonances, radiative corrections, and the topology of the underlying graph. It may also help the comprehension of lasing in complex photonic graphs and networks [237, 238, 239, 240].

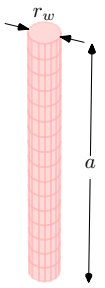

Figure A.1: Self partial inductance of a wire of length a and circular cross section of radius r_w.

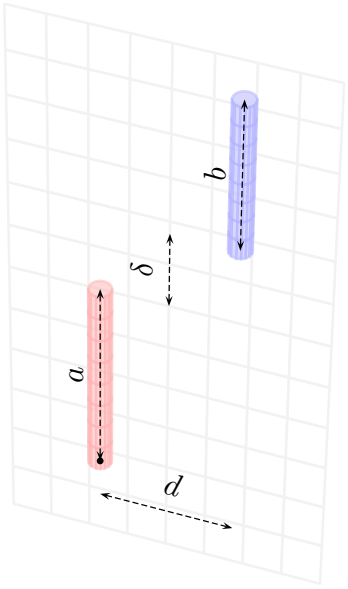

Figure A.2: Mutual partial inductance of two wires of lengths a and b, equal circular cross section of radius r_w, at distance d and offset z.

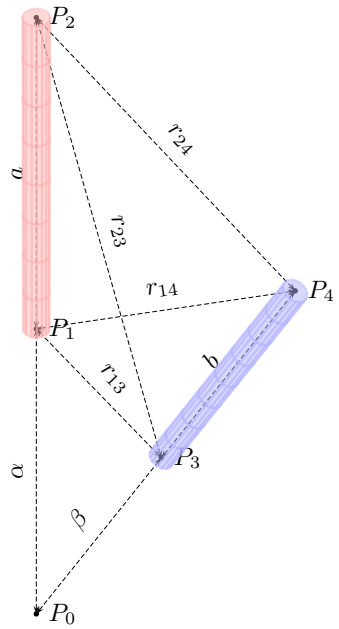

Figure A.3: Mutual partial inductance of two wires of lengths a and b, at an angle to each other.

A.1 Self partial inductance of a straight wire

The self partial inductance L^{P} of the wire of Fig. A.1 with radius r_w and length a is

$$L^{\mathrm{P}} = \frac{a\mu_0}{2\pi}\left[\ln\left(\frac{a}{r_{\mathrm{w}}}+\sqrt{\left(\frac{a}{r_{\mathrm{w}}}\right)^2+1}\right) -\sqrt{1+\left(\frac{r_{\mathrm{w}}}{a}\right)^2}+\frac{r_{\mathrm{w}}}{a}\right]+\frac{\mu_0}{8\pi}a. \quad \text{(A.1)}$$

A.2 Mutual partial inductance between two unequal parallel wires that are offset

The mutual partial inductance M_p between the two wires shown in Fig. A.2 of negligible cross section, length a and b. at a distance d, with an offset δ, is given by [241, 135]:

$$\begin{aligned} M^{\mathrm{P}} = \frac{\mu_0}{4\pi}\Bigg[& z_2\sinh^{-1}\frac{z_2}{d} - z_1\sinh^{-1}\frac{z_1}{d} - (z_2-a)\sinh^{-1}\frac{z_2-a}{d} \\ & + (z_1-a)\sinh^{-1}\frac{z_1-a}{d} - \sqrt{z_2^2+d^2}+\sqrt{z_1^2+d^2} \\ & + \sqrt{(z_2-a)^2+d^2}-\sqrt{(z_1-a)^2+d^2}\Bigg] \end{aligned} \quad \text{(A.2)}$$

where $z_2 = a+b+\delta$ and $z_1 = a+\delta$.

A.3 Mutual partial inductance between wires at an angle to each other

Let us consider the two wires of Fig. A.3, of length a and b, of negligible cross section (filaments). The wires are coplanar, forming an angle θ to each other [137, 135, 132]. Their mutual inductance has the following expression:

$$\begin{aligned} M^{\mathrm{P}} = \frac{\mu_0}{4\pi}\Bigg[& (\beta+b)\ln\frac{r_{24}+r_{14}+a}{r_{24}+r_{14}-a} - \beta\ln\frac{r_{23}+r_{13}+a}{r_{23}+r_{13}-a} \\ & + (a+\alpha)\ln\frac{r_{24}+r_{23}+b}{r_{24}+r_{23}-b} - \alpha\ln\frac{r_{14}+r_{13}+b}{r_{14}+r_{13}-b}\Bigg] \end{aligned} \quad \text{(A.3)}$$

if the two wires are touching in P_0 then the above equation reduces to [137]:

$$M^{\mathrm{P}} = \frac{\mu_0}{4\pi} \cos\theta \left(a \ln \frac{r_{24} + a + b}{r_{24} + a - b} + b \ln \frac{r_{24} + a + b}{r_{24} + b - a} \right). \tag{A.4}$$

Appendix B

List of Publications, Book Chapters, Proceedings, and Attended Conferences

Publications included in this thesis

J1. Carlo Forestiere, Giovanni Miano, and Bruno Miranda."Electromagnetic Scattering by Networks of High-Permittivity Thin Wires". In: *Physical Review Applied* 16.1 (2021), p. 014015.

J2. Bruno Miranda, Rosalba Moretta, Selene De Martino, Principia Dardano, Ilaria Rea, Carlo Forestiere, and Luca De Stefano. "A PEGDA hydrogel nanocomposite to improve gold nanoparticles stability for novel plasmonic sensing platforms". In: *Journal of Applied Physiscs* 129.3 (2021), p. 033101.

J3. Bruno Miranda, Ilaria Rea, Principia Dardano, Luca De Stefano, and Carlo Forestiere. "Recent advances in the fabrication and functionalization of flexible optical biosensors: Toward smart life-sciences applications". In: *Biosensors* 11.4 (2021), p. 107.

J4. Chiara Tramontano & Bruno Miranda, Giovanna Chianese, Luca De Stefano, Carlo Forestiere, Marinella Pirozzi, and Ilaria Rea. "Design of gelatin-capped plasmonic-diatomite nanoparticles with enhanced galunisertib loading capacity for drug delivery applications". In: *International Journal of Molecular Sciences* 22.19 (2021), p. 10755.

J5. Bruno Miranda, Rosalba Moretta, Principia Dardano, Ilaria Rea, Carlo

Forestiere, and Luca De Stefano. "H^3 (Hydrogel-Based, High-Sensitivity, Hybrid) Plasmonic Transducers for Biomolecular Interactions Monitoring". In: *Advanced Materials Technologies* 7.9 (2022), p. 2101425.

J6. Valeria Nocerino & Bruno Miranda, Chiara Tramontano, Giovanna Chianese, Principia Dardano, Ilaria Rea, and Luca De Stefano. "Plasmonic Nanosensors: Design, Fabrication, and Applications in Biomedicine". In: *Chemosensors* 10.5 (2022), p. 150.

Publications *not* included in this thesis

J7. Bruno Miranda, Vincenzo D'Ambrosio, Giovanni Miano, Luca De Stefano, and Carlo Forestiere. "Enhancing Electric Fields in High-Index Resonators by Flux Conservation of the Displacement Current Density". In: *arXiv* 2005 (2020), p. 10358.

J8. Principia Dardano, Selene De Martino, Mario Battisti, Bruno Miranda, Ilaria Rea, and Luca De Stefano. "One-Shot Fabrication of Polymeric Hollow Microneedles by Standard Photolithography". In: *Polymers* 13.4 (2021), p. 520.

J9. Mario Battisti, Selene De Martino, Bruno Miranda, Chiara Tammaro, Principia Dardano, Stefania Dello Iacono, and Luca De Stefano. "Oxygen indicator films of acrylate photopolymers and TiO_2 nanoparticles with tunable response times". In: *Optical Materials Express* 11.7 (2021), p. 2244-2255.

J10. Bruno Miranda, Mario Battisti, Selene De Martino, Valeria Nocerino, Principia Dardano, Luca De Stefano, and Giancarlo Cangiano. "Hollow Microneedle-based Plasmonic Sensor for on Patch Detection of Molecules in Dermal Interstitial Fluid". *under review* In: *Advanced Materials Technologies* (2023).

Book Chapters (not included in this thesis)

B1. Principia Dardano, Mario Battisti, Selene De Martino, Ilaria Rea, Bruno Miranda, Luigi Nicolais, and Luca De Stefano. "Theranostic Microneedle Devices: Innovative Biosensing and Transdermal Drugs Administration". In: *Biosensors-Current and Novel Strategies for Biosensing, IntechOpen* 129.3 (2020), p. 033101.

B2. Monica Terracciano, Chiara Tramontano, Rosalba Moretta, Bruno Miranda, Nicola Borbone, Luca De Stefano, and Ilaria Rea. "Protein-modified porous silicon optical devices for biosensing". In: *Porous Silicon for Biomedical Applications* (2021), p. 113-148.

Proceedings

P1. Bruno Miranda, Rosalba Moretta, Principia Dardano, Ilaria Rea, Carlo Forestiere, and Luca De Stefano. "Hydrogel-based Nanocomposite Plasmonic Sensors for Biomedical Applications". In: *Italian Conference on Optics and Photonics* (ICOP) (2020), p. 1-4.

P2. Bruno Miranda, Rosalba Moretta, Selene De Martino, Principia Dardano, Ilria Rea, Carlo Forestiere, and Luca De Stefano. "Plasmonic hydrogel nanocomposites with combined optical and mechanical properties for biochemical sensing". In: *Chemistry Proceedings* 5.1 (2021), p. 34.

Attended Conferences

C1. Bruno Miranda, Vincenzo D'Ambrosio, Giovanni Miano, Luca De Stefano, and Carlo Forestiere."Enhancing Electric Field in High-Index Resonators by Flux Conservation of the Displacement Current Density". In: *Physics Onlyne Meetup* (POM2020), Poster Presentation.

C2. Bruno Miranda, Selene De Martino, Rosalba Moretta, Principia Dardano, Ilaria Rea, Carlo Forestiere, and Luca De Stefano. " Nanocomposite Plasmonic Sensors for Biomedical Applications". In: *Italian Conference on Optics and Photonics* (ICOP) (2020), Oral Presentation.

C3. Bruno Miranda, Selene De Martino, Rosalba Moretta, Principia Dardano, Ilaria Rea, Carlo Forestiere, and Luca De Stefano. "3D nanocomposite bio-responsive hydrogels for multiplexed sensing". In: *Sensors in Medicine* (2020), Poster Presentation.

C4. Bruno Miranda, Selene De Martino, Rosalba Moretta, Principia Dardano, Ilaria Rea, Carlo Forestiere, and Luca De Stefano. "Towards Low-Cost Metal-Enhanced Fluorescence Biosensor based on 3D bio-responsive hydrogels". In: *Applied Nanotechnology and Nanoscience International Conference* ANNIC (2021), Oral Presentation.

C5. Bruno Miranda, Rosalba Moretta, Selene De Martino, Principia Dardano, Ilaria Rea, Carlo Forestiere, and Luca De Stefano. "Plasmonic Hydrogel Nanocomposites with Combined Optical and Mechanical Properties for Biochemical Sensing". In: 1^{st} *International Electronic Conference on Chemical Sensors and Analytical Chemistry* CSAC (2021), Oral Presentation.

C6. Bruno Miranda, Ilaria Rea, Principia Dardano, Carlo Forestiere, and Luca De Stefano. "Hybrid Plasmonic Nanomaterials: Functional Platforms for Bio and Food". In: 11^{th} *International Conference on Metamaterials, Photonic Crystals, and Plasmonics* META (2021), Invited Oral Presentation.

C7. Bruno Miranda, Rosalba Moretta, Selene De Martino, Principia Dardano, Ilaria Rea, Carlo Forestiere, and Luca De Stefano. "Hydrogel-based Plasmonic Nanocomposites for Biosensing Applications". In: *Research on (Bio)sensors for Infectious Disease in Italy* RBID (2021), Oral Presentation.

C8. Bruno Miranda, Rosalba Moretta, Selene De Martino, Principia Dardano, Ilaria Rea, Carlo Forestiere, and Luca De Stefano. "Plasmonic Hydrogel Nanocomposites for Biosensing Applications". In: *European Optical Society Annual Meeting* EOSAM (2021), Oral Presentation.

C9. Carlo Forestiere, Giovanni Miano, and Bruno Miranda."Electromagnetic Scattering by Networks of High-Permittivity Thin Wires". In: *European Optical Society Annual Meeting* EOSAM (2021), Oral Presentation.

C10. Bruno Miranda, Chiara Tramontano, Giovanna Chianese, Carlo Forestiere, Ilaria Rea, and Luca De Stefano."Design of Engineered Porous Biosilica Nanoparticles with Enhanced Galunisertib Loading Capacity for Drug Delivery Applications". In: *Porous Semiconductors - Science and Technology* PSST (2022), Oral Presentation.

C11. Bruno Miranda, Stefania Dello Iacono, Principia Dardano, Ilaria Rea, and Luca De Stefano."Hybrid Strain Sensors based on Hydrogel Plasmonic Nanocomposites". In: *Italian Conference of Optics and Photonics* ICOP (2022), Poster Presentation.

C12. Bruno Miranda, Rosalba Moretta, Stefania Dello Iacono, Principia Dardano, Ilaria Rea, Carlo Forestiere, and Luca De Stefano."Hydrogel-based Plasmonic Nanocomposites for Biochemical Sensing". In: *Italian Conference of Optics and Photonics* ICOP (2022), Oral Presentation.

C13. Bruno Miranda, Rosalba Moretta, Stefania Dello Iacono, Principia Dardano, Ilaria Rea, Carlo Forestiere, and Luca De Stefano."Large-scale, Hydrogel-based, Plasmonic Nanocomposites for Biomolecular Interactions Monitoring". In: *Quantum & Biomedical Applications Technologies and Sensors* qBATS (2022), Oral Presentation.

C14. Bruno Miranda, Selene De Martino, Rosalba Moretta, Principia Dardano, Ilaria Rea, Carlo Forestiere, and Luca De Stefano."Novel Nanocomposite Plasmonic Sensors for Biomedical Applications". In: 15^{th} *International Conference on Modern Materials and Technologies* CIMTEC (2022), Oral Presentation.

C15. Bruno Miranda, Rosalba Moretta, Stefania Dello Iacono, Principia Dardano, Ilaria Rea, Carlo Forestiere, and Luca De Stefano."Hydrogel-based Plasmonic Nanocomposites for label-free and non-label-free Biomolecular Interactions Monitoring". In: *Plasmonica* (2022), Oral Presentation.

Bibliography

[1] Rakesh Kumar, Mohit Kumar, and Gaurav Luthra. “Fundamental approaches and applications of nanotechnology: A mini review”. In: *Materials Today: Proceedings* (2023).

[2] A Femius Koenderink, Andrea Alù, and Albert Polman. “Nanophotonics: Shrinking light-based technology”. In: *Science* 348.6234 (2015), pp. 516–521.

[3] Samantha Bordy, Jiuk Byun, and Lisa V Poulikakos. “Nanophotonic materials: enabling targeted cancer diagnostics and therapeutics with light”. In: *Current Opinion in Chemical Engineering* 37 (2022), p. 100852.

[4] Qian Zhao, Ji Zhou, Fuli Zhang, and Didier Lippens. “Mie resonance-based dielectric metamaterials”. In: *Materials today* 12.12 (2009), pp. 60–69.

[5] Ramón Paniagua-Domınguez, Boris Luk’yanchuk, Andrey Miroshnichenko, and José A Sánchez-Gil. *Dielectric nanoresonators and metamaterials*. 2019.

[6] Feng Wang and Y. Ron Shen. “General Properties of Local Plasmons in Metal Nanostructures”. In: *Phys. Rev. Lett.* 97 (20 Nov. 2006), p. 206806.

[7] Vasily Klimov. *Nanoplasmonics*. CRC press, 2014.

[8] Kuiru Li, Mark I. Stockman, and David J. Bergman. “Self-Similar Chain of Metal Nanospheres as an Efficient Nanolens”. In: *Phys. Rev. Lett.* 91 (22 Nov. 2003), p. 227402.

[9] David J. Bergman and Mark I. Stockman. “Surface Plasmon Amplification by Stimulated Emission of Radiation: Quantum Generation of Coherent Surface Plasmons in Nanosystems”. In: *Phys. Rev. Lett.* 90 (2 Jan. 2003), p. 027402.

[10] D. R. Fredkin and I. D. Mayergoyz. “Resonant Behavior of Dielectric Objects (Electrostatic Resonances)”. In: *Phys. Rev. Lett.* 91 (25 Dec. 2003), p. 253902.

[11] Jon A Schuller, Edward S Barnard, Wenshan Cai, Young Chul Jun, Justin S White, and Mark L Brongersma. “Plasmonics for extreme light concentration and manipulation”. In: *Nature materials* 9.3 (2010), pp. 193–204.

[12] Carlo Forestiere, Alyssa J Pasquale, Antonio Capretti, Giovanni Miano, Antonello Tamburrino, Sylvanus Y Lee, Björn M Reinhard, and Luca Dal Negro. "Genetically engineered plasmonic nanoarrays". In: *Nano letters* 12.4 (2012), pp. 2037–2044.

[13] Craig F Bohren and Donald R Huffman. *Absorption and scattering of light by small particles*. John Wiley & Sons, 2008.

[14] Valeria Nocerino, Bruno Miranda, Chiara Tramontano, Giovanna Chianese, Principia Dardano, Ilaria Rea, and Luca De Stefano. "Plasmonic Nanosensors: Design, Fabrication, and Applications in Biomedicine". In: *Chemosensors* 10.5 (2022), p. 150.

[15] Wan Qi Lim and Zhiqiang Gao. "Plasmonic nanoparticles in biomedicine". In: *Nano Today* 11.2 (2016), pp. 168–188.

[16] Kathryn M Mayer and Jason H Hafner. "Localized surface plasmon resonance sensors". In: *Chemical reviews* 111.6 (2011), pp. 3828–3857.

[17] Antonio Minopoli, Adriano Acunzo, Bartolomeo Della Ventura, and Raffaele Velotta. "Nanostructured surfaces as plasmonic biosensors: A review". In: *Advanced Materials Interfaces* 9.2 (2022), p. 2101133.

[18] Adriano Acunzo, Emanuela Scardapane, Maria De Luca, Daniele Marra, Raffaele Velotta, and Antonio Minopoli. "Plasmonic nanomaterials for colorimetric biosensing: a review". In: *Chemosensors* 10.4 (2022), p. 136.

[19] Konstantin Sokolov, George Chumanov, and Therese M Cotton. "Enhancement of molecular fluorescence near the surface of colloidal metal films". In: *Analytical Chemistry* 70.18 (1998), pp. 3898–3905.

[20] Joseph R Lakowicz. *Principles of fluorescence spectroscopy*. Springer, 2006.

[21] Martin Fleischmann, Patrick J Hendra, and A James McQuillan. "Raman spectra of pyridine adsorbed at a silver electrode". In: *Chemical physics letters* 26.2 (1974), pp. 163–166.

[22] Daniela Lospinoso, Adriano Colombelli, Mauro Lomascolo, Roberto Rella, and Maria Grazia Manera. "Self-assembled metal nanohole arrays with tunable plasmonic properties for SERS single-molecule detection". In: *Nanomaterials* 12.3 (2022), p. 380.

[23] Niccolò Paccotti, Alessandro Chiadò, Chiara Novara, Paola Rivolo, Daniel Montesi, Francesco Geobaldo, and Fabrizio Giorgis. "Real-Time Monitoring of the In Situ Microfluidic Synthesis of Ag Nanoparticles on Solid Substrate for Reliable SERS Detection". In: *Biosensors* 11.12 (2021), p. 520.

[24] Stefano Fornasaro, Fatima Alsamad, Monica Baia, Luis AE Batista de Carvalho, Claudia Beleites, Hugh J Byrne, Alessandro Chiadò, Mihaela Chis, Malama Chisanga, Amuthachelvi Daniel, et al. "Surface enhanced Raman spectroscopy for quantitative analysis: results of a large-scale European multi-instrument interlaboratory study". In: *Analytical chemistry* 92.5 (2020), pp. 4053–4064.

[25] Am Hartstein, JR Kirtley, and JC Tsang. "Enhancement of the infrared absorption from molecular monolayers with thin metal overlayers". In: *Physical Review Letters* 45.3 (1980), p. 201.

[26] Bruno Miranda, Kang-Yu Chu, Pier Luca Maffettone, Amy Q Shen, and Riccardo Funari. "Metal-Enhanced Fluorescence Immunosensor Based on Plasmonic Arrays of Gold Nanoislands on an Etched Glass Substrate". In: *ACS Applied Nano Materials* (2020).

[27] A Chiadò, C Novara, A Lamberti, F Geobaldo, F Giorgis, and P Rivolo. "SERS-active metal-dielectric nanostructures integrated in microfluidic devices for ultra-sensitive label-free miRNA detection". In: *Procedia technology* 27 (2017), pp. 37–38.

[28] Peng Si, Nasrin Razmi, Omer Nur, Shipra Solanki, Chandra Mouli Pandey, Rajinder K Gupta, Bansi D Malhotra, Magnus Willander, and Adam de la Zerda. "Gold nanomaterials for optical biosensing and bioimaging". In: *Nanoscale Advances* 3.10 (2021), pp. 2679–2698.

[29] Xiaowen Ou, Yuqi Liu, Mingxing Zhang, Li Hua, and Shenshan Zhan. "Plasmonic gold nanostructures for biosensing and bioimaging". In: *Microchimica Acta* 188.9 (2021), p. 304.

[30] Stephan Link and Mostafa A El-Sayed. "Shape and size dependence of radiative, non-radiative and photothermal properties of gold nanocrystals". In: *International reviews in physical chemistry* 19.3 (2000), pp. 409–453.

[31] Xiaohua Huang, Prashant K Jain, Ivan H El-Sayed, and Mostafa A El-Sayed. "Plasmonic photothermal therapy (PPTT) using gold nanoparticles". In: *Lasers in medical science* 23 (2008), pp. 217–228.

[32] Yun-Ling Luo, Yi-Syun Shiao, and Yu-Fen Huang. "Release of photoactivatable drugs from plasmonic nanoparticles for targeted cancer therapy". In: *ACS nano* 5.10 (2011), pp. 7796–7804.

[33] Majid Sharifi, Farnoosh Attar, Ali Akbar Saboury, Keivan Akhtari, Nasrin Hooshmand, Anwarul Hasan, Mostafa A El-Sayed, and Mojtaba Falahati. "Plasmonic gold nanoparticles: Optical manipulation, imaging, drug delivery and therapy". In: *Journal of Controlled Release* 311 (2019), pp. 170–189.

[34] Aitzol Garcıa-Etxarri, Raquel Gómez-Medina, Luis S Froufe-Pérez, Cefe López, Laura Chantada, Frank Scheffold, J Aizpurua, Manuel Nieto-Vesperinas, and Juan José Sáenz. "Strong magnetic response of submicron silicon particles in the infrared". In: *Optics express* 19.6 (2011), pp. 4815–4826.

[35] Andrey B Evlyukhin, Sergey M Novikov, Urs Zywietz, René Lynge Eriksen, Carsten Reinhardt, Sergey I Bozhevolnyi, and Boris N Chichkov. "Demonstration of magnetic dipole resonances of dielectric nanospheres in the visible region". In: *Nano letters* 12.7 (2012), pp. 3749–3755.

[36] Arseniy I Kuznetsov, Andrey E Miroshnichenko, Yuan Hsing Fu, JingBo Zhang, and Boris Luk'Yanchuk. "Magnetic light". In: *Scientific reports* 2.1 (2012), pp. 1–6.

[37] Arseniy I Kuznetsov, Andrey E Miroshnichenko, Mark L Brongersma, Yuri S Kivshar, and Boris Luk'yanchuk. "Optically resonant dielectric nanostructures". In: *Science* 354.6314 (2016), aag2472.

[38] Mikhail V Rybin, Kirill L Koshelev, Zarina F Sadrieva, Kirill B Samusev, Andrey A Bogdanov, Mikhail F Limonov, and Yuri S Kivshar. "High-Q supercavity modes in subwavelength dielectric resonators". In: *Physical review letters* 119.24 (2017), p. 243901.

[39] Carlo Forestiere, Giovanni Miano, Guglielmo Rubinacci, Mariano Pascale, Antonello Tamburrino, Roberto Tricarico, and Salvatore Ventre. "Magnetoquasistatic resonances of small dielectric objects". In: *Phys. Rev. Research* 2.1 (Feb. 2020), p. 013158.

[40] John B Pendry, AJ Holden, DJ Robbins, and WJ Stewart. "Low frequency plasmons in thin-wire structures". In: *Journal of Physics: Condensed Matter* 10.22 (1998), p. 4785.

[41] Georgia T Papadakis, Dagny Fleischman, Artur Davoyan, Pochi Yeh, and Harry A Atwater. "Optical magnetism in planar metamaterial heterostructures". In: *Nature Communications* 9.1 (2018), p. 296.

[42] MS Mirmoosa, S Yu Kosulnikov, and CR Simovski. "Magnetic hyperbolic metamaterial of high-index nanowires". In: *Physical Review B* 94.7 (2016), p. 075138.

[43] Carlo Forestiere, Giovanni Miano, and Guglielmo Rubinacci. "Resonance frequency and radiative Q-factor of plasmonic and dieletric modes of small objects". In: *Phys. Rev. Research* 2.4 (Nov. 2020), p. 043176.

[44] Carlo Forestiere, Giovanni Miano, and Bruno Miranda. "Electromagnetic Scattering by Networks of High-Permittivity Thin Wires". In: *Physical Review Applied* 16.1 (2021), p. 014015.

[45] Emilija Petronijevic, Alessandro Belardini, Grigore Leahu, Roberto Li Voti, and Concita Sibilia. "Nanostructured materials for circular dichroism and chirality at the nanoscale: towards unconventional characterization". In: *Optical Materials Express* 12.7 (2022), pp. 2724–2746.

[46] Ozlem Yavas, Mikael Svedendahl, Paulina Dobosz, Vanesa Sanz, and Romain Quidant. "On-a-chip Biosensing Based on All-Dielectric Nanoresonators". In: *Nano Letters* 17.7 (2017). PMID: 28616986, pp. 4421–4426. eprint: `https://doi.org/10.1021/acs.nanolett.7b01518`.

[47] Ozlem Yavas, Mikael Svedendahl, and Romain Quidant. "Unravelling the role of electric and magnetic dipoles in biosensing with Si nanoresonators". In: *ACS nano* 13.4 (2019), pp. 4582–4588.

[48] Jose Garcia-Guirado, Mikael Svedendahl, Joaquim Puigdollers, and Romain Quidant. "Enhanced chiral sensing with dielectric nanoresonators". In: *Nano letters* 20.1 (2019), pp. 585–591.

[49] Ershad Mohammadi, Ahad Tavakoli, Parisa Dehkhoda, Yasaman Jahani, Kosmas L Tsakmakidis, Andreas Tittl, and Hatice Altug. "Accessible superchiral near-fields driven by tailored electric and magnetic resonances in all-dielectric nanostructures". In: *Acs Photonics* 6.8 (2019), pp. 1939–1946.

[50] Gleb I Tselikov, Georgy A Ermolaev, Anton A Popov, Gleb V Tikhonowski, Daria A Panova, Alexey S Taradin, Andrey A Vyshnevyy, Alexander V Syuy, Sergey M Klimentov, Sergey M Novikov, et al. "Transition metal dichalcogenide nanospheres for high-refractive-index nanophotonics and biomedical

theranostics". In: *Proceedings of the National Academy of Sciences* 119.39 (2022), e2208830119.

[51] Vasyl Kilin, Gabriel Campargue, Ina Fureraj, Sim Sakong, Tarek Sabri, Florian Riporto, Alice Vieren, Yannick Mugnier, Christophe Mas, Davide Staedler, et al. "Wavelength-Selective Nonlinear Imaging and Photo-Induced Cell Damage by Dielectric Harmonic Nanoparticles". In: *ACS nano* 14.4 (2020), pp. 4087–4095.

[52] Richard Feynman. "There's plenty of room at the bottom". In: *Feynman and computation*. CRC Press, 2018, pp. 63–76.

[53] Parvez Iqbal, Jon A Preece, and Paula M Mendes. "Nanotechnology: the "top-down" and "bottom-up" approaches". In: *Supramolecular chemistry: from molecules to nanomaterials* (2012).

[54] Boon K Teo and XH Sun. "From top-down to bottom-up to hybrid nanotechnologies: road to nanodevices". In: *Journal of cluster science* 17 (2006), pp. 529–540.

[55] H-J van Manen, Tommaso Auletta, Barbara Dordi, Holger Schönherr, Gyula J Vancso, Frank CJM van Veggel, and David N Reinhoudt. "Non-Covalent Chemistry on Surface-Confined, Isolated Dendrimers". In: *Advanced functional materials* 12.11-12 (2002), pp. 811–818.

[56] Jesús del Barrio and Carlos Sánchez-Somolinos. "Light to shape the future: from photolithography to 4D printing". In: *Advanced Optical Materials* 7.16 (2019), p. 1900598.

[57] R Seisyan. "Nanolithography in microelectronics: A review." In: *Technical Physics* 56.8 (2011).

[58] Mark A McCord and Michael J Rooks. "Handbook of microlithography, micromachining, and microfabricaiton Vol." In: *Rai-Choudhury, ed.,(IEE, London, 1997)* (1997), pp. 139–249.

[59] Bruno Miranda, Ilaria Rea, Principia Dardano, Luca De Stefano, and Carlo Forestiere. "Recent Advances in the Fabrication and Functionalization of Flexible Optical Biosensors: Toward Smart Life-Sciences Applications". In: *Biosensors* 11.4 (Apr. 2021), p. 107. ISSN: 2079-6374.

[60] B Miranda, R Moretta, S De Martino, P Dardano, I Rea, C Forestiere, and LJJOAP De Stefano. "A PEGDA hydrogel nanocomposite to improve gold nanoparticles stability for novel plasmonic sensing platforms". In: *Journal of Applied Physics* 129.3 (2021), p. 033101.

[61] Nikhil Bhalla, Yuwei Pan, Zhugen Yang, and Amir Farokh Payam. "Opportunities and challenges for biosensors and nanoscale analytical tools for pandemics: COVID-19". In: *ACS nano* 14.7 (2020), pp. 7783–7807.

[62] Jeong-Yeol Yoon and Jeong-Yeol Yoon. "Lab-on-a-chip biosensors". In: *Introduction to Biosensors: From Electric Circuits to Immunosensors* (2016), pp. 257–297.

[63] Tuan Vo-Dinh and Brian Cullum. "Biosensors and biochips: advances in biological and medical diagnostics". In: *Fresenius' journal of analytical chemistry* 366 (2000), pp. 540–551.

[64] Stefan Alexander Maier. *Plasmonics: fundamentals and applications*. Springer Science & Business Media, 2007.

[65] Tatsuro Endo, Ryuzoh Ikeda, Yasuko Yanagida, and Takeshi Hatsuzawa. "Stimuli-responsive hydrogel–silver nanoparticles composite for development of localized surface plasmon resonance-based optical biosensor". In: *Analytica chimica acta* 611.2 (2008), pp. 205–211.

[66] Bruno Miranda, Rosalba Moretta, Principia Dardano, Ilaria Rea, Carlo Forestiere, and Luca De Stefano. "H3 (Hydrogel-Based, High-Sensitivity, Hybrid) Plasmonic Transducers for Biomolecular Interactions Monitoring". In: *Advanced Materials Technologies* (2022), p. 2101425.

[67] Anil Desireddy, Brian E Conn, Jingshu Guo, Bokwon Yoon, Robert N Barnett, Bradley M Monahan, Kristin Kirschbaum, Wendell P Griffith, Robert L Whetten, Uzi Landman, et al. "Ultrastable silver nanoparticles". In: *Nature* 501.7467 (2013), pp. 399–402.

[68] Nikhil Bhalla, Afshan Jamshaid, Mandy HM Leung, Noriko Ishizu, and Amy Q Shen. "Electrical contact of metals at the nanoscale overcomes the oxidative susceptibility of silver-based nanobiosensors". In: *ACS Applied Nano Materials* 2.4 (2019), pp. 2064–2075.

[69] Moon Sung Kang, So Yun Lee, Ki Su Kim, and Dong-Wook Han. "State of the art biocompatible gold nanoparticles for cancer theragnosis". In: *Pharmaceutics* 12.8 (2020), p. 701.

[70] João Conde, Jorge T Dias, Valeria Grazú, Maria Moros, Pedro V Baptista, and Jesus M de la Fuente. "Revisiting 30 years of biofunctionalization and surface chemistry of inorganic nanoparticles for nanomedicine". In: *Frontiers in chemistry* 2 (2014), p. 48.

[71] J Christopher Love, Lara A Estroff, Jennah K Kriebel, Ralph G Nuzzo, and George M Whitesides. "Self-assembled monolayers of thiolates on metals as a form of nanotechnology". In: *Chemical reviews* 105.4 (2005), pp. 1103–1170.

[72] Zhiyang Zhang, Han Wang, Zhaopeng Chen, Xiaoyan Wang, Jaebum Choo, and Lingxin Chen. "Plasmonic colorimetric sensors based on etching and growth of noble metal nanoparticles: Strategies and applications". In: *Biosensors and Bioelectronics* 114 (2018), pp. 52–65.

[73] Jingwei Sun, Yuexiang Lu, Liuying He, Jiawei Pang, Fengyi Yang, and Yueying Liu. "Colorimetric sensor array based on gold nanoparticles: Design principles and recent advances". In: *TrAC Trends in Analytical Chemistry* 122 (2020), p. 115754.

[74] Jane Politi, Jolanda Spadavecchia, Gabriella Fiorentino, Immacolata Antonucci, and Luca De Stefano. "Arsenate reductase from Thermus thermophilus conjugated to polyethylene glycol-stabilized gold nanospheres allow trace sensing and speciation of arsenic ions". In: *Journal of The Royal Society Interface* 13.123 (2016), p. 20160629.

[75] Marzia Iarossi, Chiara Schiattarella, Ilaria Rea, Luca De Stefano, Rosalba Fittipaldi, Antonio Vecchione, Raffaele Velotta, and Bartolomeo Della Ventura. "Colorimetric immunosensor by aggregation of photochemically functionalized gold nanoparticles". In: *ACS omega* 3.4 (2018), pp. 3805–3812.

[76] AD Levin, A Ringaci, MK Alenichev, EB Drozhzhennikova, KG Shevchenko, VR Cherkasov, MP Nikitin, and PI Nikitin. "Dynamic light scattering biosensing based on analyte-induced inhibition of nanoparticle aggregation". In: *Analytical and Bioanalytical Chemistry* (2020), pp. 1–9.

[77] Santosh Aryal, Remant Bahadur KC, Narayan Bhattarai, Chul Ki Kim, and Hak Yong Kim. "Study of electrolyte induced aggregation of gold nanoparticles capped by amino acids". In: *Journal of colloid and interface science* 299.1 (2006), pp. 191–197.

[78] Shengqiang Hu, Po-Jung Jimmy Huang, Jianxiu Wang, and Juewen Liu. "Dissecting the Effect of Salt for more Sensitive Label-free Colorimetric Detection of DNA Using Gold Nanoparticles". In: *Anal Chem. [published online ahead of print, 2020 Aug 28]. 2020; 10.1021/acs.analchem.0c02688. doi:10.1021/acs.analchem.0c02688* ().

[79] NL Kazanskiy, SN Khonina, and MA Butt. "Plasmonic sensors based on Metal-insulator-metal waveguides for refractive index sensing applications: A brief review". In: *Physica E: Low-dimensional systems and nanostructures* 117 (2020), p. 113798.

[80] S Barizuddin, S Bok, and S Gangopadhyay. "Plasmonic sensors for disease detection-a review". In: *J. Nanomed. Nanotechnol* 7.3 (2016), p. 1000373.

[81] J Spadavecchia, MG Manera, F Quaranta, P Siciliano, and R Rella. "Surface plasmon resonance imaging of DNA based biosensors for potential applications in food analysis". In: *Biosensors and Bioelectronics* 21.6 (2005), pp. 894–900.

[82] Maura Cesaria, Antonietta Taurino, Maria Grazia Manera, Maria Minunni, Simona Scarano, and Roberto Rella. "Gold nanoholes fabricated by colloidal lithography: novel insights into nanofabrication, short-range correlation and optical properties". In: *Nanoscale* 11.17 (2019), pp. 8416–8432.

[83] Stephanie L Dodson, Cuong Cao, Hamed Zaribafzadeh, Shuzhou Li, and Qihua Xiong. "Engineering plasmonic nanorod arrays for colon cancer marker detection". In: *Biosensors and Bioelectronics* 63 (2015), pp. 472–477.

[84] Gayatri K Joshi, Samantha Deitz-McElyea, Merrell Johnson, Sonali Mali, Murray Korc, and Rajesh Sardar. "Highly specific plasmonic biosensors for ultrasensitive microRNA detection in plasma from pancreatic cancer patients". In: *Nano letters* 14.12 (2014), pp. 6955–6963.

[85] Gerardo A Lopez, M-Carmen Estevez, Maria Soler, and Laura M Lechuga. "Recent advances in nanoplasmonic biosensors: applications and lab-on-a-chip integration". In: *Nanophotonics* 6.1 (2017), pp. 123–136.

[86] Chengjun Huang, Kristien Bonroy, Gunter Reekmans, Wim Laureyn, Katarina Verhaegen, Iwijn De Vlaminck, Liesbet Lagae, and Gustaaf Borghs. "Localized surface plasmon resonance biosensor integrated with microfluidic chip". In: *Biomedical microdevices* 11 (2009), pp. 893–901.

[87] Chengjun Huang, Kristien Bonroy, Gunter Reekman, Kris Verstreken, Liesbet Lagae, and Gustaaf Borghs. "An on-chip localized surface plasmon resonance-based biosensor for label-free monitoring of antigen–antibody reaction". In: *Microelectronic Engineering* 86.12 (2009), pp. 2437–2441.

[88] Rita Rebelo, Ana I Barbosa, David Caballero, Il Keun Kwon, Joaquim M Oliveira, Subhas C Kundu, Rui L Reis, and Vitor M Correlo. "3D biosensors in advanced medical diagnostics of high mortality diseases". In: *Biosensors and Bioelectronics* 130 (2019), pp. 20–39.

[89] Glenda Biasotto, Alessandro Chiadò, Chiara Novara, Marco Fontana, Marco Armandi, Maria Aparecida Zaghete, Fabrizio Giorgis, and Paola Rivolo. "Graphenic aerogels decorated with Ag nanoparticles as 3D SERS substrates for biosensing". In: *Particle & Particle Systems Characterization* 37.7 (2020), p. 2000095.

[90] Elizabeth Ellis, Kangyi Zhang, Qianyu Lin, Enyi Ye, Alessandro Poma, Giuseppe Battaglia, Xian Jun Loh, and Tung-Chun Lee. "Biocompatible pH-responsive nanoparticles with a core-anchored multilayer shell of triblock copolymers for enhanced cancer therapy". In: *Journal of Materials Chemistry B* 5.23 (2017), pp. 4421–4425.

[91] Nina Jiang, Xiaolu Zhuo, and Jianfang Wang. "Active Plasmonics: Principles, Structures, and Applications". In: *Chemical Reviews* 118.6 (2018). PMID: 28960067, pp. 3054–3099. eprint: `https://doi.org/10.1021/acs.chemrev.7b00252`.

[92] A Colombelli, MG Manera, A Taurino, M Catalano, A Convertino, and R Rella. "Au nanoparticles decoration of silica nanowires for improved optical bio-sensing". In: *Sensors and Actuators B: Chemical* 226 (2016), pp. 589–597.

[93] Dokyoon Kim, Kwangsoo Shin, Soon Gu Kwon, and Taeghwan Hyeon. "Synthesis and biomedical applications of multifunctional nanoparticles". In: *Advanced Materials* 30.49 (2018), p. 1802309.

[94] Joanne Manson, Dhiraj Kumar, Brian J Meenan, and Dorian Dixon. "Polyethylene glycol functionalized gold nanoparticles: the influence of capping density on stability in various media". In: *Gold bulletin* 44.2 (2011), pp. 99–105.

[95] Neus G Bastús, Joan Comenge, and Vıctor Puntes. "Kinetically controlled seeded growth synthesis of citrate-stabilized gold nanoparticles of up to 200 nm: size focusing versus Ostwald ripening". In: *Langmuir* 27.17 (2011), pp. 11098–11105.

[96] MP Neupane, SJ Lee, IS Park, MH Lee, TS Bae, Y Kuboki, M Uo, and F Watari. "Synthesis of gelatin-capped gold nanoparticles with variable gelatin concentration". In: *Journal of Nanoparticle Research* 13.2 (2011), pp. 491–498.

[97] Y Battie, A Resano-Garcia, N Chaoui, Y Zhang, and A En Naciri. "Extended Maxwell-Garnett-Mie formulation applied to size dispersion of metallic nanoparticles embedded in host liquid matrix". In: *The Journal of chemical physics* 140.4 (2014), p. 044705.

[98] Vadim A Markel. "Introduction to the Maxwell Garnett approximation: tutorial". In: *JOSA A* 33.7 (2016), pp. 1244–1256.

[99] Daniel Buenger, Fuat Topuz, and Juergen Groll. "Hydrogels in sensing applications". In: *Progress in Polymer Science* 37.12 (2012), pp. 1678–1719.

[100] Linjie Feng, Liwei Wang, Zhichao Hu, Yuan Tian, Yuezhong Xian, and Litong Jin. "Encapsulation of horseradish peroxidase into hydrogel, and its bioelectrochemistry". In: *Microchimica acta* 164.1 (2009), pp. 49–54.

[101] Piet J Driest, Iris E Allijn, Dick J Dijkstra, Dimitrios Stamatialis, and Dirk W Grijpma. "Poly (ethylene glycol)-based poly (urethane isocyanurate) hydrogels for contact lens applications". In: *Polymer international* 69.2 (2020), pp. 131–139.

[102] Chien-Chi Lin and Kristi S Anseth. "PEG hydrogels for the controlled release of biomolecules in regenerative medicine". In: *Pharmaceutical research* 26 (2009), pp. 631–643.

[103] Rotsiniaina Randriantsilefisoa, Chuanxiong Nie, Badri Parshad, Yuanwei Pan, Sumati Bhatia, and Rainer Haag. "Double trouble for viruses: a hydrogel nanocomposite catches the influenza virus while shrinking and changing color". In: *Chemical Communications* 56.24 (2020), pp. 3547–3550.

[104] Ji Eun Song and Eun Chul Cho. "Dual-responsive and multi-functional plasmonic hydrogel valves and biomimetic architectures formed with hydrogel and gold nanocolloids". In: *Scientific reports* 6.1 (2016), pp. 1–10.

[105] Harald Ian Muri, Andon Bano, and Dag Roar Hjelme. "A single-point, multiparameter, fiber optic sensor based on a combination of interferometry and LSPR". In: *Journal of Lightwave Technology* 36.4 (2018), pp. 1159–1167.

[106] Chiara Tramontano, Bruno Miranda, Giovanna Chianese, Luca De Stefano, Carlo Forestiere, Marinella Pirozzi, and Ilaria Rea. "Design of gelatin-capped plasmonic-diatomite nanoparticles with enhanced galunisertib loading capacity for drug delivery applications". In: *International journal of molecular sciences* 22.19 (2021), p. 10755.

[107] Bruno Miranda, Rosalba Moretta, Principia Dardano, Ilaria Rea, Carlo Forestiere, and Luca De Stefano. "Hydrogel-based Nanocomposite Plasmonic Sensors for Biomedical Applications". In: *2020 Italian Conference on Optics and Photonics (ICOP)*. IEEE. 2020, pp. 1–4.

[108] Bruno Miranda, Rosalba Moretta, Selene De Martino, Principia Dardano, Ilaria Rea, Carlo Forestiere, and Luca De Stefano. "Plasmonic hydrogel nanocomposites with combined optical and mechanical properties for biochemical sensing". In: *Chemistry Proceedings* 5.1 (2021), p. 34.

[109] Principia Dardano, Selene De Martino, Mario Battisti, Bruno Miranda, Ilaria Rea, and Luca De Stefano. "One-shot fabrication of polymeric hollow microneedles by standard photolithography". In: *Polymers* 13.4 (2021), p. 520.

[110] Mario Battisti, Selene De Martino, Bruno Miranda, Chiara Tammaro, Principia Dardano, Stefania Dello Iacono, and Luca De Stefano. "Oxygen indicator films of acrylate photopolymers and TiO 2 nanoparticles with tunable response times". In: *Optical Materials Express* 11.7 (2021), pp. 2244–2255.

[111] M Terracciano, C Tramontano, R Moretta, B Miranda, N Borbone, L De Stefano, and I Rea. "Protein-modified porous silicon optical devices for biosensing". In: *Porous Silicon for Biomedical Applications*. Elsevier, 2021, pp. 113–148.

[112] Yu-lin Xu and Ru T Wang. "Electromagnetic scattering by an aggregate of spheres: Theoretical and experimental study of the amplitude scattering matrix". In: *Physical Review E* 58.3 (1998), p. 3931.

[113] Roger G Newton. "Optical theorem and beyond". In: *American Journal of Physics* 44.7 (1976), pp. 639–642.

[114] R Courant and D Hilbert. *Methods of Mathematical Physics*. Interscience Publishers, New York, 1953, pp. 326–327.

[115] Mariano Pascale, Giovanni Miano, Roberto Tricarico, and Carlo Forestiere. "Full-wave electromagnetic modes and hybridization in nanoparticle dimers". In: *Scientific reports* 9.1 (2019), pp. 1–21.

[116] Julius Adams Stratton. *Electromagnetic theory*. Vol. 33. John Wiley & Sons, 2007.

[117] I. D. Mayergoyz, D. R. Fredkin, and Z. Zhang. "Electrostatic (plasmon) resonances in nanoparticles". In: *Phys. Rev. B* 72 (2005).

[118] Isaak D Mayergoyz. *Plasmon Resonances in Nanoparticles*. _eprint: https://www.worldscientific.com/doi/pdf/10.1142/8158. WORLD SCIENTIFIC, 2013.

[119] Jean G Van Bladel. *Electromagnetic fields*. Vol. 19. John Wiley & Sons, 2007.

[120] D. Schaubert, D. Wilton, and A. Glisson. "A tetrahedral modeling method for electromagnetic scattering by arbitrarily shaped inhomogeneous dielectric bodies". In: *IEEE Transactions on Antennas and Propagation* 32.1 (Jan. 1984), pp. 77–85.

[121] G. Miano, G. Rubinacci, and A. Tamburrino. "Numerical Modeling for the Analysis of Plasmon Oscillations in Metallic Nanoparticles". In: *IEEE Transactions on Antennas and Propagation* 58.9 (Sept. 2010), pp. 2920–2933. ISSN: 1558-2221.

[122] David J Bergman and D Stroud. "Theory of resonances in the electromagnetic scattering by macroscopic bodies". In: *Physical Review B* 22.8 (1980), p. 3527.

[123] J. Van Bladel. "The Excitation of Dielectric Resonators of Very High Permittivity". In: *IEEE Transactions on Microwave Theory and Techniques* 23.2 (Feb. 1975), pp. 208–217. ISSN: 0018-9480.

[124] Hermann A Haus and James R Melcher. *Electromagnetic fields and energy*. Vol. 107. Prentice Hall Englewood Cliffs, NJ, 1989.

[125] Harold Jeffreys, Bertha Jeffreys, and Bertha Swirles. *Methods of mathematical physics*. Cambridge University Press, 1999.

[126] Dimitrios C. Tzarouchis, Pasi Yla-Oijala, and Ari Sihvola. "Unveiling the scattering behavior of small spheres". In: *Physical Review B* 94.14 (Oct. 12, 2016). Publisher: American Physical Society, p. 140301.

[127] Dimitrios Tzarouchis and Ari Sihvola. "Light Scattering by a Dielectric Sphere: Perspectives on the Mie Resonances". In: *Applied Sciences* 8.2 (Feb. 2018). Number: 2 Publisher: Multidisciplinary Digital Publishing Institute, p. 184.

[128] J. Van Bladel. "On the Resonances of a Dielectric Resonator of Very High Permittivity". In: *IEEE Transactions on Microwave Theory and Techniques* 23.2 (1975), pp. 199–208.

[129] Eric W Weisstein. *CRC concise encyclopedia of mathematics*. Chapman and Hall/CRC, 2002.

[130] RD Richtmyer. "Dielectric resonators". In: *Journal of Applied Physics* 10.6 (1939). Publisher: AIP, pp. 391–398.

[131] M. Verplanken and J. Van Bladel. "The Magnetic-Dipole Resonances of Ring Resonators of Very High Permittivity". In: *IEEE Transactions on Microwave Theory and Techniques* 27.4 (Apr. 1979). Conference Name: IEEE Transactions on Microwave Theory and Techniques, pp. 328–333. ISSN: 1557-9670.

[132] Clayton R Paul. *Inductance: loop and partial*. John Wiley & Sons, 2011.

[133] M. Abramowitz and I. A. Stegun. *Handbook of Mathematical Functions with Formulas, Graphs, and Mathematical Tables*. ninth Dover printing. New York: Dover, 1964.

[134] James Clerk Maxwell. *A treatise on electricity and magnetism*. Vol. II. Oxford: Clarendon Press, 1873.

[135] Frederick W Grover. *Inductance calculations: working formulas and tables*. Courier Corporation.

[136] Leon O. Chua, Charles A. Desoer, and Ernest S. Kuh. *Linear and Nonlinear Circuits*. en. Google-Books-ID: hl0pAAAACAAJ. McGraw-Hill, 1987. ISBN: 978-0-07-100167-0.

[137] George A Campbell. "Mutual inductances of circuits composed of straight wires". In: *Physical Review* 5.6 (1915). Publisher: APS, p. 452.

[138] FF Martens. "Über die gegenseitige Induktion und ponderomotorische Kraft zwischen zwei stromdurchflossenen Rechtecken". In: *Annalen der Physik* 334.10 (1909). Publisher: Wiley Online Library, pp. 959–970.

[139] Waclaw Sierpinski. "Sur une courbe dont tout point est un point de ramification". In: *Compt. Rend. Acad. Sci. Paris*. 160 (1915), pp. 302–305.

[140] A. B. Evlyukhin. "Demonstration of magnetic dipole resonances of dielectric nanospheres in the visible region". In: *Nano letters* 12 (2012).

[141] Hyunho Kang, Joseph T Buchman, Rebeca S Rodriguez, Hattie L Ring, Jiayi He, Kyle C Bantz, and Christy L Haynes. "Stabilization of silver and gold nanoparticles: preservation and improvement of plasmonic functionalities". In: *Chemical reviews* 119.1 (2018), pp. 664–699.

[142] JC Maxwell Garnett. "XII. Colours in metal glasses and in metallic films". In: *Philosophical Transactions of the Royal Society of London. Series A, Containing Papers of a Mathematical or Physical Character* 203.359-371 (1904), pp. 385–420.

[143] RL Haupt and DH Warner. *Genetic algorithms in electromagnetics, 1wiley & Sons Ltd*. 2007.

[144] Oliver Kramer. "Genetic algorithms". In: *Genetic algorithm essentials*. Springer, 2017, pp. 11–19.

[145] John Turkevich, Peter Cooper Stevenson, and James Hillier. "A study of the nucleation and growth processes in the synthesis of colloidal gold". In: *Discussions of the Faraday Society* 11 (1951), pp. 55–75.

[146] Torben Gillich, Canet Acikgoz, Lucio Isa, A Dieter Schlüter, Nicholas D Spencer, and Marcus Textor. "PEG-stabilized core–shell nanoparticles: Impact of linear versus dendritic polymer shell architecture on colloidal properties and the reversibility of temperature-induced aggregation". In: *ACS nano* 7.1 (2013), pp. 316–329.

[147] Benito Rodrıguez-González, Paul Mulvaney, and Luis M Liz-Marzán. "An electrochemical model for gold colloid formation via citrate reduction". In: *Zeitschrift für Physikalische Chemie* 221.3 (2007), pp. 415–426.

[148] P Johnson. "B and Christy RW 1972". In: *Phys. Rev. B* 19 (), p. 4370.

[149] Francesca Baletto and Riccardo Ferrando. "Structural properties of nanoclusters: Energetic, thermodynamic, and kinetic effects". In: *Reviews of modern physics* 77.1 (2005), p. 371.

[150] Arthur L Aden and Milton Kerker. "Scattering of electromagnetic waves from two concentric spheres". In: *Journal of Applied Physics* 22.10 (1951), pp. 1242–1246.

[151] Luis M Liz-Marzán, Michael Giersig, and Paul Mulvaney. "Synthesis of nanosized gold- silica core- shell particles". In: *Langmuir* 12.18 (1996), pp. 4329–4335.

[152] SH Liu and MY Han. "Synthesis, functionalization, and bioconjugation of monodisperse, Silica-Coated gold nanoparticles: Robust bioprobes". In: *Advanced Functional Materials* 15.6 (2005), pp. 961–967.

[153] D Gontero, Alicia Viviana Veglia, Angel Guillermo Bracamonte, and Denis Boudreau. "Synthesis of ultraluminescent gold core–shell nanoparticles as nanoimaging platforms for biosensing applications based on metal-enhanced fluorescence". In: *RSC advances* 7.17 (2017), pp. 10252–10258.

[154] Mohammad Javed Ansari, Saade Abdalkareem Jasim, Talib Zeedan Taban, Dmitry Olegovich Bokov, Mohammed Nader Shalaby, Moaed E Al-Gazally, Hamzah H Kzar, Maytham T Qasim, Yasser Fakri Mustafa, and M Khatami. "Anticancer drug-loading capacity of green synthesized porous magnetic iron nanocarrier and cytotoxic effects against human cancer cell line". In: *Journal of Cluster Science* (2022), pp. 1–11.

[155] Arshadul Hak, Vinod Ravasaheb Shinde, and Aravind Kumar Rengan. "A review of advanced nanoformulations in phototherapy for cancer therapeutics". In: *Photodiagnosis and Photodynamic Therapy* 33 (2021), p. 102205.

[156] Himali Horo, Srirupa Bhattacharyya, Bishnupada Mandal, and Lal Mohan Kundu. "Synthesis of functionalized silk-coated chitosan-gold nanoparticles and microparticles for target-directed delivery of antitumor agents". In: *Carbohydrate Polymers* 258 (2021), p. 117659.

[157] Yan-Peng Jia, Bu-Yun Ma, Xia-Wei Wei, and Zhi-Yong Qian. "The in vitro and in vivo toxicity of gold nanoparticles". In: *Chinese Chemical Letters* 28.4 (2017), pp. 691–702.

[158] Li Shi, Eric Buhler, François Boué, and Florent Carn. "How does the size of gold nanoparticles depend on citrate to gold ratio in Turkevich synthesis? Final answer to a debated question". In: *Journal of colloid and Interface Science* 492 (2017), pp. 191–198.

[159] Stefano Managò, Chiara Tramontano, Donatella Delle Cave, Giovanna Chianese, Gianluigi Zito, Luca De Stefano, Monica Terracciano, Enza Lonardo, Anna Chiara De Luca, and Ilaria Rea. "SERS Quantification of Galunisertib Delivery in Colorectal Cancer Cells by Plasmonic-Assisted Diatomite Nanoparticles". In: *Small* 17.34 (2021), p. 2101711.

[160] Chiara Tramontano Giovanna Chianese, Monica Terracciano, Luca de Stefano, and Ilaria Rea. "Nanostructured Biosilica of Diatoms: From Water World to Biomedical Applications." In: *Applied Sciences* 10.19 (2020), pp. 6811–6831.

[161] Monica Terracciano, Mohammad-Ali Shahbazi, Alexandra Correia, Ilaria Rea, Annalisa Lamberti, Luca De Stefano, and Hélder A Santos. "Surface bioengineering of diatomite based nanovectors for efficient intracellular uptake and drug delivery". In: *Nanoscale* 7.47 (2015), pp. 20063–20074.

[162] Yun Liu, Guangze Yang, Song Jin, Letao Xu, and Chun-Xia Zhao. "Development of high-drug-loading nanoparticles". In: *ChemPlusChem* 85.9 (2020), pp. 2143–2157.

[163] Thashini Moodley and Moganavelli Singh. "Current stimuli-responsive mesoporous silica nanoparticles for cancer therapy". In: *Pharmaceutics* 13.1 (2021), p. 71.

[164] Yi Liu, Sai Cheong Ng, Jiashing Yu, and Wei-Bor Tsai. "Modification and crosslinking of gelatin-based biomaterials as tissue adhesives". In: *Colloids and Surfaces B: Biointerfaces* 174 (2019), pp. 316–323.

[165] Kuldeep K Bansal, Deepak K Mishra, Ari Rosling, and Jessica M Rosenholm. "Therapeutic potential of polymer-coated mesoporous silica nanoparticles". In: *Applied Sciences* 10.1 (2019), p. 289.

[166] Stephan Herbertz, J Scott Sawyer, Anja J Stauber, Ivelina Gueorguieva, Kyla E Driscoll, Shawn T Estrem, Ann L Cleverly, Durisala Desaiah, Susan C Guba, Karim A Benhadji, et al. "Clinical development of galunisertib (LY2157299 monohydrate), a small molecule inhibitor of transforming growth factor-beta signaling pathway". In: *Drug design, development and therapy* 9 (2015), p. 4479.

[167] Kenneth C Cassidy, Ivelina Gueorguieva, Colin Miles, Jessica Rehmel, Ping Yi, and William J Ehlhardt. "Disposition and metabolism of [14C]-galunisertib, a TGF-β RI kinase/ALK5 inhibitor, following oral administration in healthy subjects and mechanistic prediction of the effect of itraconazole on galunisertib pharmacokinetics". In: *Xenobiotica* 48.4 (2018), pp. 382–399.

[168] Israel Perez. "Reducing the effective dose of cisplatin using gold nanoparticles as carriers". In: *Instituto de Ingeniería y Tecnología* (2020).

[169] Shengtao Wang, Anhe Wang, Yuqi Ma, Qingquan Han, Yang Chen, Xin Li, Songyuan Wu, Jieling Li, Shuo Bai, and Jian Yin. "In situ synthesis of superorganism-like Au NPs within microgels with ultra-wide absorption in visible and near-infrared regions for combined cancer therapy". In: *Biomaterials Science* 9.3 (2021), pp. 774–779.

[170] Barnabás Horváth, Melinda Rigó, Sándor Guba, István Szalai, and Réka Barabás. "Magnetic field response of aqueous hydroxyapatite based magnetic suspensions". In: *Heliyon* 5.4 (2019), e01507.

[171] Peng Chen, Nhung Thi Tran, Xinglin Wen, Qihua Xiong, and Bo Liedberg. "Inflection point of the localized surface plasmon resonance peak: a general method to improve the sensitivity". In: *ACS sensors* 2.2 (2017), pp. 235–242.

[172] Kyeong Rim Ryu and Ji Won Ha. "Influence of shell thickness on the refractive index sensitivity of localized surface plasmon resonance inflection points in silver-coated gold nanorods". In: *RSC advances* 10.29 (2020), pp. 16827–16831.

[173] Athel Cornish-Bowden. "One hundred years of Michaelis–Menten kinetics". In: *Perspectives in Science* 4 (2015), pp. 3–9.

[174] Yasser Khan, Arno Thielens, Sifat Muin, Jonathan Ting, Carol Baumbauer, and Ana C Arias. "A new frontier of printed electronics: flexible hybrid electronics". In: *Advanced Materials* 32.15 (2020), p. 1905279.

[175] Jun Chang Yang, Jaewan Mun, Se Young Kwon, Seongjun Park, Zhenan Bao, and Steve Park. "Electronic skin: recent progress and future prospects for skin-attachable devices for health monitoring, robotics, and prosthetics". In: *Advanced Materials* 31.48 (2019), p. 1904765.

[176] Muamer Dervisevic, Maria Alba, Beatriz Prieto-Simon, and Nicolas H Voelcker. "Skin in the diagnostics game: Wearable biosensor nano-and microsystems for medical diagnostics". In: *Nano Today* 30 (2020), p. 100828.

[177] Fatima Mustafa and Silvana Andreescu. "Chemical and biological sensors for food-quality monitoring and smart packaging". In: *Foods* 7.10 (2018), p. 168.

[178] John Jackson, Helen Burt, Dirk Lange, In Whang, Robin Evans, and David Plackett. "The Design, Characterization and Antibacterial Activity of Heat and Silver Crosslinked Poly (Vinyl Alcohol) Hydrogel Forming Dressings Containing Silver Nanoparticles". In: *Nanomaterials* 11.1 (2021), p. 96.

[179] Duarte Dias and João Paulo Silva Cunha. "Wearable health devices—vital sign monitoring, systems and technologies". In: *Sensors* 18.8 (2018), p. 2414.

[180] Caterina Dallari, Caterina Credi, Elena Lenci, Andrea Trabocchi, Riccardo Cicchi, and Francesco Saverio Pavone. "Nanostars—decorated microfluidic sensors for surface enhanced Raman scattering targeting of biomolecules". In: *Journal of Physics: Photonics* 2.2 (2020), p. 024008.

[181] Qusai Alkhalaf, Sarang Pande, and Ritesh Ramesh Palkar. "Review of polydimethylsiloxane (pdms) as a material for additive manufacturing". In: *Innovative Design, Analysis and Development Practices in Aerospace and Automotive Engineering* (2021), pp. 265–275.

[182] Prashanth Reddy Konari, Yung-Dai Clayton, Melville B Vaughan, Morshed Khandaker, and Mohammad Robiul Hossan. "Experimental analysis of laser micromachining of microchannels in common microfluidic substrates". In: *Micromachines* 12.2 (2021), p. 138.

[183] Bruna Agrillo, Marco Balestrieri, Marta Gogliettino, Gianna Palmieri, Rosalba Moretta, Yolande TR Proroga, Ilaria Rea, Alessandra Cornacchia, Federico Capuano, Giorgio Smaldone, et al. "Functionalized polymeric materials with bio-derived antimicrobial peptides for "active" packaging". In: *International Journal of Molecular Sciences* 20.3 (2019), p. 601.

[184] K Narsaiah, Shyam Narayan Jha, Rishi Bhardwaj, Rajiv Sharma, and Ramesh Kumar. "Optical biosensors for food quality and safety assurance—a review". In: *Journal of food science and technology* 49.4 (2012), pp. 383–406.

[185] Chloé Minnai, Marcel Di Vece, and Paolo Milani. "Mechanical-optical-electro modulation by stretching a polymer-metal nanocomposite". In: *Nanotechnology* 28.35 (2017), p. 355702.

[186] Ana I Barbosa and Nuno M Reis. "A critical insight into the development pipeline of microfluidic immunoassay devices for the sensitive quantitation of protein biomarkers at the point of care". In: *Analyst* 142.6 (2017), pp. 858–882.

[187] Desireé Alesa Gyles, Lorena Diniz Castro, José Otávio Carréra Silva Jr, and Roseane Maria Ribeiro-Costa. "A review of the designs and prominent biomedical advances of natural and synthetic hydrogel formulations". In: *European Polymer Journal* 88 (2017), pp. 373–392.

[188] Pascal Bertsch, Mani Diba, David J Mooney, and Sander CG Leeuwenburgh. "Self-healing injectable hydrogels for tissue regeneration". In: *Chemical Reviews* (2022).

[189] Jian Yang, Haojie Yu, Li Wang, Jian Liu, Xiaowei Liu, Yichuan Hong, Yudi Huang, and Shuning Ren. "Advances in adhesive hydrogels for tissue engineering". In: *European Polymer Journal* (2022), p. 111241.

[190] Vesna Teofilović, Busra Agan, Jelena Pavličević, Davut Lacin, and Ayse Zehra Aroguz. "Synthesis, characterization and kinetics of sustained pantoprazole release studies of interpenetrated poly (acrylic acid)-chitosan-bentonite hydrogels for drug delivery systems". In: *Reaction Kinetics, Mechanisms and Catalysis* (2022), pp. 1–15.

[191] Rogelio Rodrıguez-Rodrıguez, Hugo Espinosa-Andrews, and Zaira Yunuen Garcıa-Carvajal. "Stimuli-Responsive Hydrogels in Drug Delivery". In: *Functional Biomaterials*. Springer, 2022, pp. 75–103.

[192] Pedro Lavrador, Marco R Esteves, Vıtor M Gaspar, and João F Mano. "Stimuli-responsive nanocomposite hydrogels for biomedical applications". In: *Advanced Functional Materials* 31.8 (2021), p. 2005941.

[193] Shanghui Huang, Xiangqian Hong, Mingyi Zhao, Nanbo Liu, Huiling Liu, Jun Zhao, Longquan Shao, Wei Xue, Han Zhang, Ping Zhu, et al. "Nanocomposite hydrogels for biomedical applications". In: *Bioengineering & Translational Medicine* (2022), e10315.

[194] Ke Wang, Yuting Hao, Yingna Wang, Jinyuan Chen, Lianzhi Mao, Yudi Deng, Junlin Chen, Sijie Yuan, Tiantian Zhang, Jiaoyan Ren, et al. "Functional hydrogels and their application in drug delivery, biosensors, and tissue engineering". In: *International Journal of Polymer Science* 2019 (2019).

[195] V Thomas, Murali Mohan Yallapu, B Sreedhar, and SK Bajpai. "A versatile strategy to fabricate hydrogel–silver nanocomposites and investigation of their antimicrobial activity". In: *Journal of colloid and interface science* 315.1 (2007), pp. 389–395.

[196] Chun-Hua Zhu, Zi-Bin Hai, Chun-Hua Cui, Hui-Hui Li, Jia-Fu Chen, and Shu-Hong Yu. "In situ controlled synthesis of thermosensitive poly (N-isopropylacrylamide)/Au nanocomposite hydrogels by gamma radiation for catalytic application". In: *Small* 8.6 (2012), pp. 930–936.

[197] Ayoung Choe, Jeonghee Yeom, Ravi Shanker, Minsoo P Kim, Saewon Kang, and Hyunhyub Ko. "Stretchable and wearable colorimetric patches based on thermoresponsive plasmonic microgels embedded in a hydrogel film". In: *NPG Asia Materials* 10.9 (2018), pp. 912–922.

[198] Hongbin Zhang, Lei Wang, Li Song, Guoguang Niu, Hui Cao, Guojie Wang, Huai Yang, and Siquan Zhu. "Controllable properties and microstructure of hydrogels based on crosslinked poly (ethylene glycol) diacrylates with different molecular weights". In: *Journal of Applied Polymer Science* 121.1 (2011), pp. 531–540.

[199] Kytai Truong Nguyen and Jennifer L West. "Photopolymerizable hydrogels for tissue engineering applications". In: *Biomaterials* 23.22 (2002), pp. 4307–4314.

[200] PJ Flory and J Rehner. "Statistical mechanics of crosslinked polymers. Rubber like elasticity". In: *J. Chem. Phys* 11 (1943), p. 521.

[201] Wilhelm Sellmeier. "Ueber die durch die Aetherschwingungen erregten Mitschwingungen der Körpertheilchen und deren Rückwirkung auf die ersteren, besonders zur Erklärung der Dispersion und ihrer Anomalien". In: *Annalen der Physik* 223.12 (1872), pp. 525–554.

[202] Ana Sánchez-Iglesias, Nathalie Claes, Diego M Solıs, Jose M Taboada, Sara Bals, Luis M Liz-Marzán, and Marek Grzelczak. "Reversible clustering of gold nanoparticles under confinement". In: *Angewandte Chemie* 130.12 (2018), pp. 3237–3240.

[203] Adele De Lucia, Ilaria Rea, Rosalba Moretta, Monica Terracciano, Jolanda Spadavecchia, Gabriella Fiorentino, Carlo Forestiere, and Luca De Stefano. "Optical modelling of hybrid nanoparticles for theranostic applications". In: *Proceeding of 19th Italian National Conference on Photonic Technologies (Fotonica 2017)* (2017).

[204] Martine Besouw, Rosalinde Masereeuw, Lambert van den Heuvel, and Elena Levtchenko. "Cysteamine: an old drug with new potential". In: *Drug Discovery Today* 18.15-16 (2013), pp. 785–792.

[205] Carlo Forestiere, Giovanni Miano, Mariano Pascale, and Roberto Tricarico. "Quantum theory of radiative decay rate and frequency shift of surface plasmon modes". In: *Physical Review A* 102.4 (2020), p. 043704.

[206] Nidhi Nath and Ashutosh Chilkoti. "Label-free biosensing by surface plasmon resonance of nanoparticles on glass: optimization of nanoparticle size". In: *Analytical Chemistry* 76.18 (2004), pp. 5370–5378.

[207] Mathieu Francoeur, Pradeep Garudadri Venkata, and M Pinar Mengüç. "Sensitivity analysis for characterization of gold nanoparticles and agglomerates via surface plasmon scattering patterns". In: *Journal of Quantitative Spectroscopy and Radiative Transfer* 106.1-3 (2007), pp. 44–55.

[208] Huanjun Chen, Xiaoshan Kou, Zhi Yang, Weihai Ni, and Jianfang Wang. "Shape-and size-dependent refractive index sensitivity of gold nanoparticles". In: *Langmuir* 24.10 (2008), pp. 5233–5237.

[209] Nikhil Bhalla, Aditya Jain, Yoonjoo Lee, Amy Q Shen, and Doojin Lee. "Dewetting Metal Nanofilms—Effect of Substrate on Refractive Index Sensitivity of Nanoplasmonic Gold". In: *Nanomaterials* 9.11 (2019), p. 1530.

[210] S Scarano, MG Manera, A Colombelli, M Minunni, and R Rella. "Nano structures and polymers: Emerging nanocomposites for plasmonic resonance transducers". In: *Thin Solid Films* 698 (2020), p. 137859.

[211] Hamid SadAbadi, Simona Badilescu, Muthukumaran Packirisamy, and Rolf Wüthrich. "Integration of gold nanoparticles in PDMS microfluidics for lab-on-a-chip plasmonic biosensing of growth hormones". In: *Biosensors and Bioelectronics* 44 (2013), pp. 77–84.

[212] Samuel Bearden, Fanny Wang, and Adam R Hall. "Simple and efficient room-temperature release of biotinylated nucleic acids from streptavidin and its application to selective molecular detection". In: *Analytical chemistry* 91.13 (2019), pp. 7996–8001.

[213] Thangavel Lakshmipriya, Subash CB Gopinath, and Thean-Hock Tang. "Biotin-streptavidin competition mediates sensitive detection of biomolecules in enzyme linked immunosorbent assay". In: *PLoS One* 11.3 (2016), e0151153.

[214] Ying Yan, Tingting Hu, Xinying Xiang, Wenkai Li, and Changbei Ma. "Fluorometric Detection of Streptavidin with a Cationic Conjugated Polymer and Hairpin DNA Probe". In: *ChemistrySelect* 6.21 (2021), pp. 5248–5253.

[215] Monica Focsan, Andreea Campu, Ana-Maria Craciun, Monica Potara, Cosmin Leordean, Dana Maniu, and Simion Astilean. "A simple and efficient design to improve the detection of biotin-streptavidin interaction with plasmonic nanobiosensors". In: *Biosensors and Bioelectronics* 86 (2016), pp. 728–735.

[216] Donggee Rho and Seunghyun Kim. "Demonstration of a Label-Free and Low-Cost Optical Cavity-Based Biosensor Using Streptavidin and C-Reactive Protein". In: *Biosensors* 11.1 (2020), p. 4.

[217] G Roshan Deen and Vivien Chua. "Synthesis and properties of new "stimuli" responsive nanocomposite hydrogels containing silver nanoparticles". In: *Gels* 1.1 (2015), pp. 117–134.

[218] Talaial B Alina, Victoria A Nash, and Kara L Spiller. "Effects of biotin-avidin interactions on hydrogel swelling". In: *Frontiers in chemistry* 8 (2020), p. 593422.

[219] R Bruck, E Melnik, P Muellner, R Hainberger, and M Lämmerhofer. "Integrated polymer-based Mach-Zehnder interferometer label-free streptavidin biosensor compatible with injection molding". In: *Biosensors and Bioelectronics* 26.9 (2011), pp. 3832–3837.

[220] Anna Chiara De Luca, Peter Reader-Harris, Michael Mazilu, Stefania Mariggio, Daniela Corda, and Andrea Di Falco. "Reproducible surface-enhanced Raman quantification of biomarkers in multicomponent mixtures". In: *ACS nano* 8.3 (2014), pp. 2575–2583.

[221] Valentina Di Meo, Massimo Moccia, Gennaro Sanità, Alessio Crescitelli, Annalisa Lamberti, Vincenzo Galdi, Ivo Rendina, and Emanuela Esposito. "Probing denaturation of protein a via surface-enhanced infrared absorption spectroscopy". In: *Biosensors* 12.7 (2022), p. 530.

[222] George G Guilbault. *Practical fluorescence*. CRC Press, 2020.

[223] Jeff W Lichtman and José-Angel Conchello. "Fluorescence microscopy". In: *Nature methods* 2.12 (2005), pp. 910–919.

[224] Eric Lucas, Rachael Knoblauch, Mandie Combs-Bosse, Sheldon E Broedel Jr, and Chris D Geddes. "Low-concentration trypsin detection from a metal-enhanced fluorescence (MEF) platform: Towards the development of ultra-sensitive and rapid detection of proteolytic enzymes". In: *Spectrochimica Acta Part A: Molecular and Biomolecular Spectroscopy* 228 (2020), p. 117739.

[225] Palash Bharadwaj and Lukas Novotny. "Plasmon-enhanced photoemission from a single Y3N@ C80 fullerene". In: *The Journal of Physical Chemistry C* 114.16 (2010), pp. 7444–7447.

[226] Jugal P Dhandhukia, Dab A Brill, Aida Kouhi, Martha K Pastuszka, and J Andrew MacKay. "Elastin-like polypeptide switches: A design strategy to detect multimeric proteins". In: *Protein Science* 26.9 (2017), pp. 1785–1795.

[227] De-en Sun, Xinqi Fan, Yujie Shi, Hao Zhang, Zhimin Huang, Bo Cheng, Qi Tang, Wei Li, Yuntao Zhu, Jinyi Bai, et al. "Click-ExM enables expansion microscopy for all biomolecules". In: *Nature Methods* 18.1 (2021), pp. 107–113.

[228] Xuan Zhou, Sara Tenaglio, Timothy Esworthy, Sung Yun Hann, Haitao Cui, Thomas J Webster, Hicham Fenniri, and Lijie Grace Zhang. "Three-Dimensional Printing Biologically Inspired DNA-Based Gradient Scaffolds for Cartilage Tissue Regeneration". In: *ACS Applied Materials & Interfaces* 12.29 (2020), pp. 33219–33228.

[229] Clara Garcıa-Astrain, Elisa Lenzi, Dorleta Jimenez de Aberasturi, Malou Henriksen-Lacey, Marco R Binelli, and Luis M Liz-Marzán. "3D-Printed Biocompatible Scaffolds with Built-In Nanoplasmonic Sensors". In: *Advanced Functional Materials* (2020), p. 2005407.

[230] Luigia Serpico, Stefania Dello Iacono, Luca De Stefano, Selene De Martino, Mario Battisti, Principia Dardano, Silvana Pedatella, and Mauro De Nisco. "pH-sensitive release of antioxidant Se-glycoconjugates through a flexible polymeric patch". In: *European Polymer Journal* 178 (2022), p. 111486.

[231] Edward Bennett Rosa. *The self and mutual inductances of linear conductors*. 80. US Department of Commerce and Labor, Bureau of Standards, 1908.

[232] Ernst Weber. "Electromagnetic Fields : Theory and Applications". In: (1950). Publisher: Wiley.

[233] Nader Engheta, Alessandro Salandrino, and Andrea Alu. "Circuit elements at optical frequencies: nanoinductors, nanocapacitors, and nanoresistors". In: *Physical Review Letters* 95.9 (2005). Publisher: APS, p. 095504.

[234] Andrea Alú and Nader Engheta. "Optical 'Shorting Wires'". In: *Opt. Express* 15.21 (Oct. 2007). Publisher: OSA, pp. 13773–13782.

[235] Andrea Alú, Alessandro Salandrino, and Nader Engheta. "Parallel, series, and intermediate interconnections of optical nanocircuit elements. 2. Nanocircuit and physical interpretation". In: *J. Opt. Soc. Am. B* 24.12 (Dec. 2007). Publisher: OSA, pp. 3014–3022.

[236] Alessandro Salandrino, Andrea Alú, and Nader Engheta. "Parallel, series, and intermediate interconnections of optical nanocircuit elements. 1. Analytical solution". In: *J. Opt. Soc. Am. B* 24.12 (Dec. 2007). Publisher: OSA, pp. 3007–3013.

[237] Stefano Lepri, Cosimo Trono, and Giovanni Giacomelli. "Complex Active Optical Networks as a New Laser Concept". In: *Phys. Rev. Lett.* 118.12 (Mar. 2017). Publisher: American Physical Society, p. 123901.

[238] Michele Gaio, Dhruv Saxena, Jacopo Bertolotti, Dario Pisignano, Andrea Camposeo, and Riccardo Sapienza. "A nanophotonic laser on a graph". In: *Nature communications* 10.1 (2019). Publisher: Nature Publishing Group, pp. 1–7.

[239] Andreas Lubatsch and Regine Frank. "A Self-Consistent Quantum Field Theory for Random Lasing". In: *Applied Sciences* 9.12 (2019). Publisher: Multidisciplinary Digital Publishing Institute, p. 2477.

[240] Loredana M. Massaro, Silvia Gentilini, Alberto Portone, Andrea Camposeo, Dario Pisignano, Claudio Conti, and Neda Ghofraniha. "Heterogeneous Random Laser with Switching Activity Visualized by Replica Symmetry Breaking Maps". In: *ACS Photonics* (Jan. 2021). Publisher: American Chemical Society.

[241] WH Eccles. *Wireless telegraphy and telephony*. Publication Title: A Handbook of formulae, data and information. 1918.